TECHNISCHE UNIVERSITÄT WIEN

Non-invasive Beam Diagnostic Development for FCC using Cherenkov Diffraction Radiation in Dielectric Materials

Dissertation

zur Erlangung des akademischen Grades

Doktor der technischen Wissenschaften

im Fachbereich Technische Physik

eingereicht von

Dipl.-Ing. Andreas Schlögelhofer
Matrikelnummer 01426875

ausgeführt am
Atominstitut der Fakultät für Physik der Technischen Universität Wien (TU Wien)

in Zusammenarbeit mit der
Europäischen Organisation für Kernforschung (CERN)

unter der Anleitung von
Privatdoz. Dipl.-Ing. Dr.techn. Michael Benedikt (TU Wien, CERN)
und
Dr. Stefano Mazzoni (CERN)

Genf, Februar 2024

Kurzfassung

Čerenkov-Diffraktionsstrahlung bezeichnet die Emission von elektromagnetischer Strahlung, wenn sich ein geladenes Teilchen in der Nähe von dielektrischer Materie bewegt und die Geschwindigkeit des Teilchens größer ist, als die Phasengeschwindigkeit der elektromagnetischen Strahlung im Dielektrikum. Im Gegensatz zur besser bekannten Čerenkov-Strahlung beschreibt Čerenkov-Diffraktionsstrahlung eine nichtinvasive Methode der Strahlungserzeugung, da sich das geladene Teilchen nicht direkt durch das Dielektrikum bewegt. Das macht Čerenkov-Diffraktionsstrahlung zu einem vielversprechenden Strahlungsmechanismus für die Strahldiagnostik, besonders in Kreisbeschleunigern mit hohen Strahlintensitäten beziehungsweise, wenn es erforderlich ist, die Emittanz des Teilchenstrahls zu erhalten. Čerenkov-Diffraktionsstrahlung besitzt überdies weitere vorteilhafte Eigenschaften für die Anwendung in der Strahldiagnostik, wie ein breitbandiges Emissionsspektrum, die Möglichkeit große Emissionswinkel relativ zur Teilchenbahn zu realisieren und eine vergleichsweise hohe Lichtausbeute, die mit der Ausdehnung des Dielektrikums in longitudinaler Richtung in Bezug auf die Teilchenbahn skaliert. Darüber hinaus erleichtert der kleine Formfaktor von Radiatoren für Čerenkov-Diffraktionsstrahlung deren Implementierung und reduziert gleichzeitig die Komplexität des finalen Instruments. Die Messung des longitudinalen Strahlprofils mithilfe von Čerenkov-Diffraktionsstrahlung könnte eine einfachere Alternative zu Synchrotronstrahlung darstellen. Die Extraktion und Verwendung von Synchrotronstrahlung in Großbeschleunigern wie dem Future Circular Collider für Elektronen und Positronen (FCC-ee) würde viele Herausforderungen mit sich bringen, wie entsprechend lange Distanzen für die Extraktion und die hohen kritischen Energien der Photonen.

Diese Dissertation nützt Čerenkov-Diffraktionsstrahlung, um spezifische Herausforderungen in der Diagnostik von Teilchenstrahlen im FCC-ee zu lösen, wobei das Hauptaugenmerk auf der bündelweisen Messung des Längsprofils der Teilchenstrahlen mit einer Auflösung im Sub-Pikosekundenbereich liegt. Je nach Betriebsweise des FCC-ee variiert die vorhergesehene Bündeldauer zwischen 6 und 52 ps ($1\,\sigma$).

Zahlreiche Eigenschaften von Čerenkov-Diffraktionsstrahlung werden im Zuge dieser Dissertation zum ersten Mal untersucht. Dazu wurde ein Prototyp eines Vakuum-

kompatiblen dielektrischen Radiators in einem 200 MeV-Linearbeschleuniger für Elektronen installiert. Dieser Energiebereich bringt mit sich, dass alle präsentierten Messungen im kohärenten Spektrum der Čerenkov-Diffraktionsstrahlung durchgeführt wurden. Umfangreiche numerische Simulationen der spezifischen Radiatorgeometrie werden präsentiert und anschließend mit den Daten aus verschiedenen experimentellen Messungen verglichen. Die kohärenten Eigenschaften der Čerenkov-Diffraktionsstrahlung, ihre Polarisation, sowie ihre Abhängigkeit von der Distanz zwischen Teilchenbahn und Oberfläche des Dielektrikums, werden dargelegt. Die Grenzfrequenz des Radiators, sowie verzögerte Strahlungsanteile aufgrund von Reflexionen im Radiator werden identifiziert. Der Absolutbetrag der elektrischen Feldstärke von Čerenkov-Diffraktionsstrahlung wird erstmalig bestimmt und die gleichmäßige Verteilung der Strahlung an der Außenfläche des Radiators präsentiert. Schließlich wird die Strahlung mit einer zeitlichen Auflösung im Pikosekundenbereich erfasst, und somit die kürzesten Echtzeit-Messungen von Čerenkov-Diffraktionsstrahlung durchgeführt. Überdies wird dadurch die zeitliche Unterscheidung zwischen Pulsen der Čerenkov-Diffraktionsstrahlung und diversen Komponenten der Diffraktionsstrahlung aufgezeigt.

Abstract

Cherenkov diffraction radiation (ChDR) refers to the emission of electromagnetic radiation when a charged particle travels in the vicinity of dielectric matter, and the particle's velocity exceeds the phase velocity of electromagnetic radiation in the dielectric. Unlike the better-known Cherenkov radiation, ChDR can be utilized as a non-invasive technique, as the charged particle beam does not directly traverse the material. This feature makes ChDR an appealing emission mechanism for beam diagnostics applications in circular accelerators, particularly those with intense beams and whenever preserving the beam's emittance is crucial. ChDR exhibits several more features, which are advantageous for beam diagnostic purposes, including a broadband emission spectrum, the ability to achieve a large emission angle relative to the beam trajectory, and a relatively high light yield which is proportional to the length of the dielectric exposed to the beam field. Additionally, the small form factor of ChDR radiators facilitates their implementation and reduces the overall complexity of the final instrument. Measuring the longitudinal beam profiles with ChDR could represent a simpler, viable alternative to synchrotron radiation, whose extraction and utilisation in large-scale facilities, like the Future Circular Collider for electrons and positrons (FCC-ee), would imply many challenges, such as long extraction lines as well as high critical photon energies.

This thesis exploits ChDR to address a specific diagnostics problem in the context of FCC-ee, explicitly focusing on the bunch-by-bunch measurement of the beam's longitudinal profile with sub-picosecond resolution. Depending on the FCC-ee operation mode, the design bunch duration varies between 6 and 52 ps ($1\,\sigma$).

Several key characteristics of ChDR are investigated for the first time within the framework of this thesis. A prototype of a vacuum-compatible dielectric radiator was installed at a 200 MeV linear electron accelerator. Due to this energy range, all presented measurements were conducted within the coherent spectrum of ChDR. Numerical simulations of the specific radiator design are shown and benchmarked against experimental data from multiple campaigns. The coherent nature of ChDR, its polarisation and its dependency on the distance between the particle trajectory and radiator surface are demonstrated. The low-frequency cutoff

of the dielectric radiator, as well as trailing fields due to reflections within the radiator, are identified. The absolute value of the electric field strength of ChDR is measured for the first time, and its uniform distribution on the radiator's exit surface is presented. Finally, real-time measurements with a resolution in the picosecond range demonstrate the shortest real-time measurement of the ChDR pulse and indicate the temporal discrimination between the ChDR pulse and various diffraction radiation components.

Contents

1

Future Circular Collider for Electrons and Positrons

The following chapter introduces the Future Circular Collider for electrons (e^-) and positrons (e^+), abbreviated as FCC-ee. The framework and development of the FCC study are presented, and the current status of the accelerator layout is introduced. The expected beam parameters are provided as a necessity for beam instrumentation development, and several aspects of beam instrumentation systems are discussed. Current bunch length diagnostics are introduced, leading to the motivation behind Cherenkov diffraction radiation (ChDR) as a potential tool for bunch length diagnostics in the FCC-ee.

1.1 Introduction to FCC-ee

Following the European Strategy for Particle Physics, the Future Circular Collider for electrons and positrons was proposed as part of the Future Circular Collider Study [1]. This international study was launched in 2014 and aimed to study high-energy lepton and hadron circular colliders in order to push the energy frontier even further after the High-Luminosity Large Hadron Collider (HL-LHC) operation ends in 2041. The long-term goal was identified as a hadron collider with a centre-of-mass energy of 100 TeV. This must be compared to the centre-of-mass energy of 14 TeV targeted with HL-LHC. A lepton collider was included in the study effort as a possible intermediate step, utilising, first and foremost, the tunnel needed to host the hadron machine and large parts of the surface infrastructure. This approach would be a retake of the previous Large Electron-Positron Collider (LEP), which was then followed by the Large Hadron Collider (LHC), both of which were installed in the same 27 km long tunnel [2]. The Future Circular Collider Study is a collaboration with more than 1350 contributors from 350 institutes, and the global effort resulted in the publication of four conceptual design reports, namely FCC physics opportunities, the lepton collider (FCC-ee), the hadron collider (FCC-hh) and the high energy large hadron collider (HE-LHC) [1, 3–5].

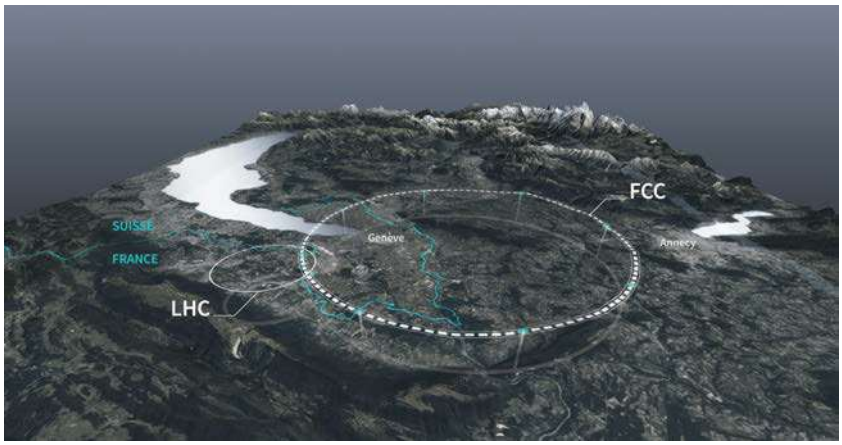

Figure 1.1: Illustration of the 91 km FCC baseline, located around Geneva in the border region between France and Switzerland. The footprint of the 27 km long LHC is shown on the left [6].

The European Strategy for Particle Physics in 2020 confirmed the approach of investigating the technical and financial feasibility of a future hadron collider, whereas, at the same time, the lepton collider was identified as the highest-priority next collider to serve the European particle physics community as a Higgs factory for high precision measurements. This decision led to the launch of the FCC

Feasibility Study in 2021. The feasibility study follows the European Strategy for Particle Physics by prioritising the lepton collider, followed by the hadron collider in the second stage. This option was also chosen to optimise the general timeline and overall cost of physics output. The current timeline for this combined approach would foresee the start of the FCC-ee operation around 2045 and the start of FCC-hh operation around 2070. Whereas these dates are in the far future, as seen from today, it has to be noted that in order to achieve these milestones, the construction of the tunnel would need to begin in the early 2030s during HL-LHC operation [7]. The FCC Feasibility Study aims to publish its final report in 2025. As of writing this report, the last international collaboration meeting was the FCC week 2023 in London, Great Britain, where the most recent developments of the feasibility study were presented.

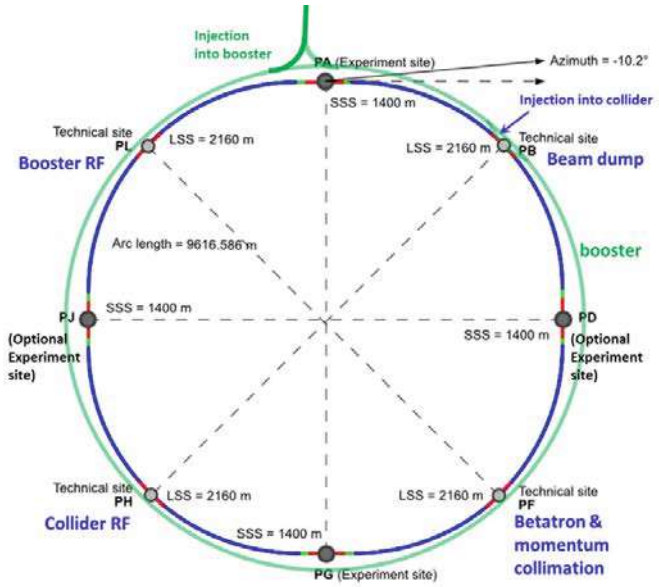

Figure 1.2: Layout of the FCC-ee accelerator. The booster is shown in green, and the collider is shown in blue [8].

1.2 Accelerator Layout

The FCC-ee layout and parameters were modified and optimised during the course of its planning several times. Table 1.1 summarises some of the changes since the conceptual design report (CDR) in 2018. The most prominent feature of the FCC-ee is the unprecedented circumference of the accelerator complex, which allows the realisation of unparalleled particle energies in a collider. The ring placement was optimised considering geology and surface constraints, as well as environmental

and infrastructure aspects [6]. This resulted in the total circumference of 97.76 km from the conceptual design report in 2019 to be changed to 90.66 km. An updated layout of the FCC-ee footprint is shown in fig. 1.2. A four-fold super-periodicity was introduced to have the possibility of four interaction points (IPs), located about 10.2 m outwards from the lattice [9]. Having several experiments would benefit measurements' robustness and engage an even larger community. Therefore, four surface sites are considered for experiments. As the total number of surface sites was reduced to eight compared to the previous 12 in the design report, only four more surface sites remain. Two of those are used for the collider and booster ring's radio frequency infrastructure, respectively. One surface point will provide access to the beam dump and another one to the collimators. The number of straight sections has remained the same in the current layout. However, their lengths had to be adapted to respect the four-fold super-periodicity. The long, straight sections were shortened by nearly a third compared to the design report, and their number has been increased from two to four.

		CDR (2018)	**Optimised (2023)**
Total circumference	km	97.756	90.657
Total arc length	km	83.75	76.93
Arc bending radius	km	13.33	12.24
Arc lengths (and number)	km	8.869 (8), 3.2 (4)	9.617 (8)
Number of surface sites		12	8
Number of straights		8	8
Straights lengths (and number)	m	1450 (6), 2760 (2)	1400 (4), 2032 (4)
Super-periodicity		2	4

Table 1.1: Overview of the FCC-ee accelerator layout from the conceptual design report in 2018 versus the optimised parameters in 2023 [6, 9].

In fig. 1.3, one of the proposed cross-sections of the FCC-ee tunnel with a diameter of 5.5 m is shown. In the shown configuration, the booster ring would be placed 103 cm above the collider ring. The top-up injection scheme was chosen to increase the beam lifetime and maintain the bunch charge of the colliding bunches in the collider ring. The separation between the electron and positron beam in the arc has been enlarged to 35 cm since the CDR. Also, the beam pipe radius might change to 30 mm instead of the previous 35 mm [9].

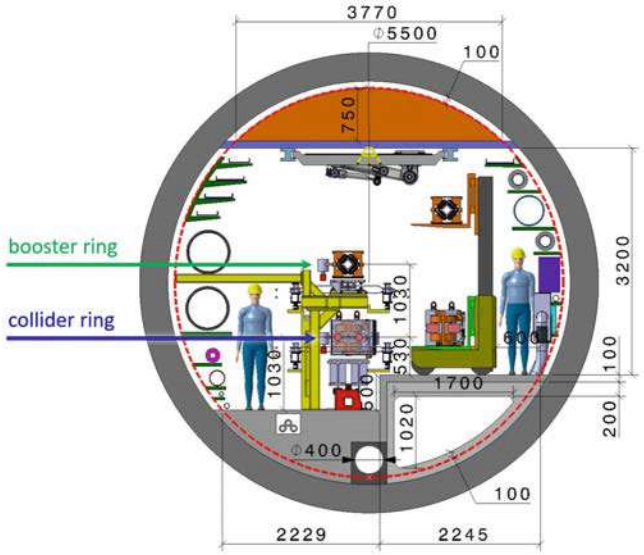

Figure 1.3: One of the proposed cross-sections of the FCC-ee tunnel. The booster (green arrow) is located on top of the collider ring (blue arrow) [10].

1.3 Beam Parameters

An overview of the beam parameters is given in table 1.2. The different operation modes are sorted by particle energy, starting from Z up to $t\bar{t}$ operation. The run plan for the FCC-ee foresees to start operation at the lowest energy of 45.6 GeV (Z) and then increasing to 80 GeV (W), 120 GeV (ZH) and up to an energy of 182.5 GeV for $t\bar{t}$ operation. However, the possibility of starting with Higgs operation at 120 GeV is still being considered. The beam parameters are optimised to maximise luminosity by keeping the beam lifetime longer than 4000 seconds for each operation mode. The shorter circumference of approximately -7% and the reduction of damping between the IPs reduce the luminosity per IP significantly compared to the CDR [9]. The expected integrated luminosity would still deliver a number of particles which surpass the ones from LEP operation by several orders of magnitude. Four years of Z operation would deliver $> 10^{12}$ Z bosons, which is 10^5 more than during LEP operation. Two years of W operation would deliver $> 10^8$ W bosons, which is 10^4 more than generated with LEP [8].

1.4 Beam Instrumentation for FCC-ee

The following paragraphs outline some of the criteria to be fulfilled in relation to beam instrumentation needs for the FCC-ee. Even though some are not directly

linked to the possible application of ChDR, they have been included to provide the reader with an overview of various challenges to be addressed from a beam instrumentation perspective. Many of those challenges apply to a large variety of devices. A subset of beam diagnostic devices, along with their characteristic challenges, is presented to serve as examples. The information draws from a dedicated chapter on beam diagnostics in the FCC-ee conceptual design report from 2018 [1, Chapter 3.6] and a presentation given by T. Lefèvre at FCC Week 2023 [11].

Beam Position Monitors

With over 300 km of beamlines to be equipped, large distances make distributed systems like Beam Position Monitors (BPM) challenging to operate and maintain. For the collider, booster and injector complex, more than 10000 BPMs are expected to be needed. One major challenge of these distributed systems will be the time delays and, consequently, long latencies for the feedback systems. With synchrotron radiation power limited to a total of 50 MW per beam, synchrotron radiation will still significantly impact all devices installed, especially in the arcs. In locations where cabling and electronics are typically located, the yearly dose is estimated to vary from 150 kGy up to 600 kGy. The electricity consumption is dominated by synchrotron radiation and the yearly consumption during beam operation is estimated to vary from 1.07 to 1.77 TWh for the different operation modes. This would correspond to about 1.9 to 3.1% of the yearly electricity consumption of Switzerland in 2022 [12]. The high beam current during Z operation makes it necessary to reduce the coupling impedance of the BPMs to a minimum to avoid beam heating related issues. Their impact on the stability and precision of the BPMs still needs to be investigated. Figure 1.4 shows that in the current design, the electrodes are mounted at 45° with respect to the horizontal plane where the winglets of the vacuum chamber are present. With the help of absorbers placed within the winglets, contributions from synchrotron radiation, which is peaking close to the horizontal plane, will be mitigated.

Transverse Beam Profile

The transverse beam profile is needed bunch-by-bunch in order to determine the beam emittance. Current machines with small transverse beam sizes typically use X-ray imaging of synchrotron radiation [13] and visible light interferometry [14] to measure the beam size. However, with the unprecedented energies at the FCC-ee, these techniques might be limited by diffraction effects or even impossible to realise due to the synchrotron radiation spectrum, with critical wavelengths in the hard

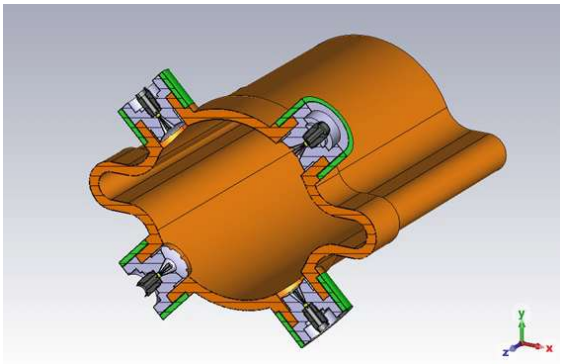

Figure 1.4: Proposed cross-section of the FCC-ee vacuum chamber including four electrodes mounted at 45° with respect to the horizontal plane to measure the beam position [11].

X-ray regime. At the highest energy of 182.5 GeV, the diffraction limit at 0.1 nm would be approximately 15 μm, whereas the vertical beam size is typically $< 10\,\mu$m.

Possible alternatives are under investigation. For example, X-ray interferometers using a two-slit setup push the visible light interferometry principle to smaller wavelengths [15]. Another approach is to use X-ray near field speckles, which use the interferometric pattern generated by nanospheres exposed to X-rays [16].

Longitudinal Beam Profile

The bunch length measurements are especially important to monitor the strength of beamstrahlung and for energy calibration. To determine the impact of beamstrahlung, which occurs at all the IPs, the bunch length has to be provided for every turn. This leads to the requirement of a bunch-by-bunch, turn-by-turn acquisition system. The resolution of this fast acquisition system must be in the order of one picosecond. The shortest bunch lengths occur during $t\bar{t}$ operation, where they vary from 5.6 ps up to 8.5 ps, including beamstrahlung. The longest bunch lengths are expected during Z operation, varying from 18.7 ps up to 52.0 ps, including beamstrahlung.

The energy spread within the bunches must be measured with a sub-ps resolution for energy calibration. These longitudinal bunch profiles need to be measured bunch-by-bunch. However, these fine-resolution measurements are not required on a turn-by-turn basis. They need to be available on a time scale of several minutes, which allows for the accumulation and averaging over many turns. The same bunch in the FCC tunnel passes approximately 3300 times per second.

		Z	W	ZH	$t\bar{t}$
Beam energy	GeV	45.6	80	120	182.5
Number of bunches/beam		11200	1780	440	60
Beam current	mA	1270	137	26.7	4.9
Luminosity/IP	$10^{34}\text{cm}^{-2}\text{s}^{-1}$	140	20	5.0	1.25
Luminosity/IP (CDR, 2 IP)	$10^{34}\text{cm}^{-2}\text{s}^{-1}$	230	28	8.5	1.8
Synchrotron radiation power / beam	MW		50		
Bunch population	10^{11}	2.14	1.45	1.15	1.55
Bunch length with sync. radiation	mm	5.60	3.47	3.40	1.81
Bunch length with beamstrahlung	mm	15.5	5.41	4.70	2.17
Bunch spacing	ns		25		
Hor. emittance $\varepsilon_{x,y}$	nm	0.71	2.17	0.71	1.59
Vert. emittance $\varepsilon_{x,y}$	pm	1.4	2.2	1.4	1.6
Energy spread with sync. radiation	%	0.039	0.070	0.104	0.160
Energy spread with beam strahlung	%	0.089	0.109	0.143	0.192
Lifetime (q + BS + lattice)	s	15000	4000	6000	6000
Max. power during beam operation	MeV	222	247	273	357
Total yearly consumption	TWh	1.07	1.21	1.33	1.77

Table 1.2: Overview of several FCC-ee beam parameters [6, 8, 9].

1.5 Current Longitudinal Beam Profile Diagnostics

1.5.1 Streak Camera

During the operation of the Large Electron-Positron Collider at CERN in the 1990s, synchrotron radiation emitted in the visible spectrum was used to acquire the bunch length using a streak camera [17]. At the University of Tokyo, Japan, it was demonstrated in 1997 that streak camera measurements using beam-generated signals can reach sub-ps resolution [18]. Reflective optics were used to avoid dispersion and to avoid a broad velocity distribution of the generated photoelectrons, a narrow bandwidth optical filter was necessary. For a large machine like the FCC-ee with an arc bending radius of 12.24 km, the separation distance between synchrotron light and the beam trajectory becomes non-negligible and would require designated infrastructure. The high critical frequency $\omega_c = 3\gamma^3 c/(2r)$ of the synchrotron radiation photons proposes substantial challenges to beam diagnostic devices, which would need to be overcome by designated dipoles in the lattice for utilising the visible spectrum. Compared to the operation during LEP, another large

disadvantage of streak cameras is that current-day streak cameras can not keep up with the high repetition rates to provide online bunch-by-bunch, turn-by-turn monitoring for the FCC-ee filling pattern.

1.5.2 Longitudinal Density Monitor

The Longitudinal Density Monitor (LDM) uses the principle of time-correlated single photon counting. It is a device currently installed in the Large Hadron Collider (LHC) at CERN and is primarily designed to provide a high dynamic range of particle density within the collider rings. After integration times of several minutes, a dynamic range in the order of 10^5 can be obtained. This allows for clearly identifying satellite and ghost bunches during proton and lead ion operations. It tracks single photon events generated by synchrotron radiation in the visible spectrum. The single photons are measured with an avalanche photodiode and binned in time steps of 50 ps using a time-to-digital converter. The time resolution achievable is limited by the time-to-digital converter and the timing jitter in the acquisition system. Even though the LDM was developed for its high dynamic range, time-correlated single photon counting can also be used to measure bunch length. As the bunch population is much greater in the main particle bunches than in the satellite bunches, profiles of the main bunches can be obtained within several seconds [19]. Besides incoherent synchrotron radiation, also other beam-generated radiation might be used for this technique. Incoherent ChDR in the visible spectrum might be a promising candidate. However, its photon yield in the incoherent regime still requires further studies.

1.5.3 Electro-optical Techniques

Electro-optical measurement techniques are of great interest for particle bunch lengths as short as hundreds of femtoseconds [20]. They rely on the Pockels effect, which introduces a birefringence in electro-optical crystals when exposed to an external electric field. Frequent crystal types used for electro-optical measurements and their respective largest electro-optic coefficient r_{ij} include Gallium phosphide (GaP, $r_{41} \approx 1.2\,\mathrm{pm/V}$), Zinc telluride (ZnTe, $r_{41} \approx 4.0\,\mathrm{pm/V}$), Lithium niobate ($LiNbO_3$, $r_{33} \approx 30.8\,\mathrm{pm/V}$) and Barium borate ($BaB_2O_4$, $r_{11} \approx 2.7\,\mathrm{pm/V}$) [21–24]. Typically, a short, beam-induced pulse is measured, allowing various beam properties to be derived from the measurement. An invasive technique for producing short pulses is using coherent transition radiation. If bunch lengths are sufficiently short, sending the beam through a transition radiation screen will emit coherent backward transition radiation up to the terahertz regime. A non-invasive technique, especially suitable for synchrotrons, is using coherent synchrotron radiation.

A non-invasive signal source that can also be utilised in LINACs is the direct beam field of the particle bunch.

Electro-optical Sampling

An electro-optical sampling of terahertz pulses was demonstrated in the mid-1990s with a subpicosecond resolution [25]. By the end of the second millennium, the possibility of using those techniques for electron bunch length measurements had already been investigated and demonstrated with a subpicosecond resolution [26–28]. Sampling the direct beam field of the particle bunch requires the electro-optical crystal to be close to the particle beam in the vacuum chamber, where also wakefields need to be considered, not only because the crystal itself might introduce wakefields, but also due to the fact that the crystal is sensitive enough to measure wakefields present in the beamline. Sampling the terahertz field of transition radiation outside the vacuum chamber is an alternative approach, where the crystal is not subject to introducing and sensing wakefields. No matter which signal source is used, the main limitation of an electro-optical sampling setup is the need for sampling the pulses with a probing laser. This requires the temporal jitter between the probing laser and signal to be minimised and requires a stable signal shape, as the final profile is sampled over many shots.

Electro-optical Spectral Decoding

Electro-optic spectral decoding (EOSD) of terahertz pulses was demonstrated in 1998 [29]. No introduced time delay is needed to sample the pulse with the probing laser, which gives rise to the possibility of single-shot measurements. For this variation of electro-optical detection, a laser pulse is linearly chirped, introducing a frequency-to-time relation within the laser pulse. Figure 1.5 illustrates the direct beam field sensing principle. The laser pulse is stretched to a length longer than the signal length. As for electro-optical sampling, the intensity of the laser pulse is modulated under the presence of the signal. However, instead of delaying the laser pulse and introducing a different modulation of the pulse depending on the temporal offset between the laser pulse and signal, a time-dependent modulation is introduced at different locations within the laser pulse. Those different locations correspond to an optical frequency, which can be read out using a grating to disperse the chirped laser pulse.

The EOSD scheme was pioneered with particle beams at the FELIX facility at the Radboud University Nijmegen [31]. Since then, electro-optical spectral decoding setups have been installed at various accelerators. Notably, at the VUV-FEL and European XFEL at DESY (Deutsches Elektronen-Synchrotron) [32], SwissFEL at PSI (Paul Scherrer Institute) [33] and the ANKA storage ring at KIT (Karlsruhe

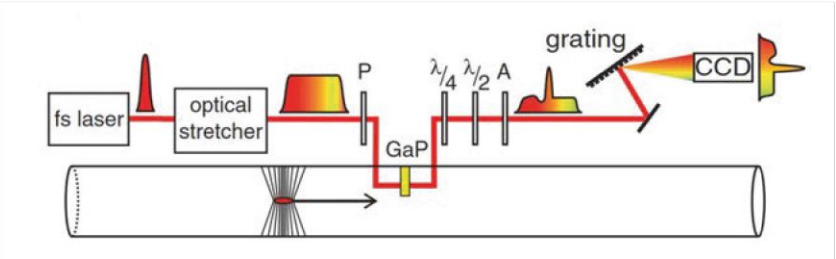

Figure 1.5: Schematic of an electro-optical spectral decoding scheme for measuring the direct beam field. The birefringence induced in the crystal (GaP) by the beam field is sensed with a chirped laser pulse and read out using a spectrometer (grating + CCD) [30].

Institute of Technology) [34]. With ANKA being a storage ring, EOSD could be used to analyse the longitudinal phase space of electron bunches in a synchrotron [35]. More recently, the EOSD scheme was extended by a new method of encoding the terahertz field into the crystal. By this new approach, the previous resolution limit of EOSD can be overcome [36].

In the framework of the FCC-ee, the adaptation of the electro-optical spectral decoding setup as currently implemented at ANKA is being investigated [37]. One main goal is to reduce the impedance of the in-vacuum detector and adapt the crystal geometry for FCC-ee bunch lengths. Moreover, at KIT, a fast line array for read-out speeds up to 2.7 MHz was developed, which is currently improved to allow for acquisition at even higher repetition rates [38, 39]. Considering a bunch spacing of 25 ns at the FCC-ee, a repetition rate of 40 MHz would be needed to monitor all bunches continuously.

Photonic Time-Stretch

Photonic time-stretch techniques are used to stretch an obtained signal to longer time frames, which are then analysed with photodetectors, which have much smaller bandwidth than the original signal. A chirped laser pulse is modulated in intensity just as for the EOSD scheme. However, instead of then analysing the frequency content of the laser pulse, the laser pulse is dispersed in several kilometres of fibre to much longer laser pulse durations. Typically, the laser pulse is stretched from picoseconds at the encoding position to nanoseconds at the read-out location. The modulated laser pulse intensity is then digitised with photodiodes and oscilloscopes with a bandwidth of several GHz [40, 41].

1.6 Motivation of using Cherenkov Diffraction Radiation

ChDR refers to the emission of Cherenkov radiation by charged high-energy particles propagating in close vicinity to a dielectric medium. ChDR has gained considerable attention as a potential tool for beam instrumentation applications in recent years [42]. Both the incoherent [43, 44] and the coherent spectrum [45, 46] of the induced radiation were measured in different experimental campaigns and increased the interest in utilising ChDR for beam diagnostic devices. Most recently, this led to the research on a high-frequency beam position monitor utilising ChDR [47, 48] as well as a bunch length monitor based on ChDR [49], both of which are studied for operation at the Advanced Proton Driven Plasma Wakefield Acceleration Experiment (AWAKE) hosted at CERN [50].

The main feature of ChDR compared to the well-established Cherenkov radiation phenomenon is the distance between the particle trajectory and the dielectric material. As the material does not intercept the particle's trajectory directly, it is the charged particle's field at a given distance from the particle's trajectory, which induces the emission of ChDR at the surface of a dielectric material. The field of the charged particle decreases over distance, so ChDR intrinsically has a lower yield than Cherenkov radiation. However, this gap between particle and dielectric allows for non-invasive measurements, making it of great interest for beam diagnostic purposes. As the generation mechanism is similar, ChDR shares several properties with Cherenkov radiation. One of them is the well-defined angle at which the radiation propagates within the dielectric medium, commonly referred to as the Cherenkov angle. This characteristic has several benefits for use in future diagnostic devices. The Cherenkov angle can be tuned by choosing the refractive index of the dielectric accordingly. Consequently, the relative angle between the beam trajectory and the emission of ChDR can be tuned by selecting an appropriate material. This introduces the benefit of separating the ChDR signal's propagation direction from the beam direction. A feature which becomes particularly advantageous in scenarios such as linear machines, where synchrotron radiation cannot be utilised, or large circular machines, where synchrotron radiation must propagate for a significant distance before achieving enough separation from the beam trajectory. In such contexts, ChDR offers an efficient means to extract a beam-generated signal. Moreover, ChDR can also be extracted in the vertical plane, while synchrotron radiation is emitted only in the plane of deflection. This brings the flexibility of installing a device based on ChDR in a location where background signals and exposure to radiation can be minimised.

2

Beam-Generated Radiation

This chapter provides an overview of beam-generated signals induced from the electromagnetic field of charged particles. Initially, the electromagnetic field of a relativistic charged particle, along with that of a bunch of relativistic charged particles, is introduced. Subsequently, both transition radiation and diffraction radiation are discussed. As elaborated in chapter 6, transition radiation finds application in the calibration process. Most of this chapter is dedicated to Cherenkov radiation (ChR) and Cherenkov diffraction radiation (ChDR) and the conditions for their generation. Following this, two analytical models of ChDR are presented, accompanied by an investigation of their spectral energy distribution and its key characteristics. Finally, the concept of coherent and incoherent emission of radiation, linked to the bunch form factor, is discussed.

2.1 Electromagnetic Field of a Relativistic Charged Particle

The following overview of the behaviour of the fields of relativistic charged particles follows the outline of a lecture by G. Stupakov and P. Baxevanis [51]. It is well-known that the electromagnetic field of a relativistic charge has certain characteristics when viewed from an observer in the laboratory frame. When dealing with radiation stemming from the electromagnetic field of a particle, it is, therefore, essential to consider the relativistic effects on its field. For this matter, we introduce two convenient variables γ and β to describe relativistic behaviour, defined as [52]:

$$\gamma = \frac{1}{\sqrt{1-\beta^2}} \qquad \text{with} \qquad \beta = v/c\,.$$

The variable γ is known as the Lorentz factor, and v denotes the constant velocity between two inertial systems that move relative to each other. The speed of light in a vacuum is given as c. At sufficient high particle energies, the particles attain the limit speed c, and their energy increase does not contribute to an increase in their velocity but to an increase in their mass. Therefore, we can neglect acceleration for a particle travelling along a straight trajectory and only consider a constant velocity. If we consider the electric and magnetic fields in two inertial systems which move with a constant velocity $|\vec{v}| = v < c$ with respect to each other, the transformation equations of the field are given as follows [52]:

$$\vec{E}_\parallel = \vec{E}'_\parallel \qquad\qquad \vec{E}'_\parallel = \vec{E}_\parallel$$
$$\vec{E}_\perp = \gamma\left(\vec{E}'_\perp - \vec{v}\times\vec{B}'\right) \qquad\qquad \vec{E}'_\perp = \gamma\left(\vec{E}_\perp + \vec{v}\times\vec{B}\right)$$

$$\vec{B}_\parallel = \vec{B}'_\parallel \qquad\qquad \vec{B}'_\parallel = \vec{B}_\parallel$$
$$\vec{B}_\perp = \gamma\left(\vec{B}'_\perp + \frac{\vec{v}\times\vec{E}'}{c^2}\right) \qquad\qquad \vec{B}'_\perp = \gamma\left(\vec{B}_\perp - \frac{\vec{v}\times\vec{E}}{c^2}\right)$$

The primed variables denote the electric and magnetic field vectors of the reference frame at which the particle is at rest. Parallel and perpendicular indices refer to the relative direction with respect to the direction of the velocity $\vec{v}$. If we assume the direction of $\vec{v}$ to be parallel to the z-axis, we obtain $\vec{E}_\parallel = E'_z$ and $\vec{E}_\perp = (E_x, E_y)$.

Despite the transformation of the fields, we also need to consider the Lorentz transformation between the two inertial coordinate systems. For the transformation of the coordinate systems, the choice of $\vec{v} \parallel z$ yields [52]:

$$\begin{aligned} x &= x' & \qquad x' &= x \\ y &= y' & \qquad y' &= y \\ z &= \gamma\,(z' + vt') & \qquad z' &= \gamma\,(z - vt) \\ t &= \gamma\left(t' + \frac{vz'}{c^2}\right) & \qquad t' &= \gamma\left(t - \frac{vz}{c^2}\right) \end{aligned}$$

A time period between two events in the rest frame of the particle $\Delta t'$ will be seen as a time dilation for an observer measuring the time period $\Delta t = \gamma \Delta t'$. For objects in the rest frame of the moving system of length l'_z, the observer in the laboratory will measure the same length as $l_z = l'_z/\gamma$, known as length contraction.

With this set of tools, we now look at the electric field of a particle at rest. We obtain a static field, which is also known as the Coulomb field of a single charge q [52]:

$$\vec{E}' = \frac{q}{4\pi\varepsilon_0}\,\frac{\vec{r'}}{r'^3} \tag{2.1}$$

This equation is valid for the inertial system in which the particle is at rest. However, we are interested in how the fields are being modified for an observer for whom the particle moves with constant velocity $v \sim c$. To transform this expression to the laboratory frame, we have to use the Lorentz transformation for the coordinates and time, as well as the transformation for the fields. We obtain

$$r' = \sqrt{x^2 + y^2 + \gamma^2 (z - vt)^2} \quad \text{and}$$

$$E_x = \gamma E'_x, \quad E_y = \gamma E'_y, \quad E_z = E'_z.$$

Substituting these results into equation 2.1 and combining the result in a single vector, we obtain:

$$\vec{E} = \frac{q}{4\pi\varepsilon_0}\,\frac{\vec{r}}{\gamma^2\left((z - vt)^2 + \dfrac{x^2 + y^2}{\gamma^2}\right)^{3/2}}\,, \tag{2.2}$$

with $\vec{r} = (x, y, z - vt)$. The fields parallel to the direction of motion become weak, whereas the fields perpendicular to the direction of motion become large compared to the rest frame of the particle [53]:

$$E_z = \frac{E'}{\gamma^2}, \quad E_{x,y} = \gamma E'$$

In the limit $\gamma \to \infty$, all fields would be confined in an infinitely thin plane perpendicular to the direction of motion. This situation is illustrated in fig. 2.1.

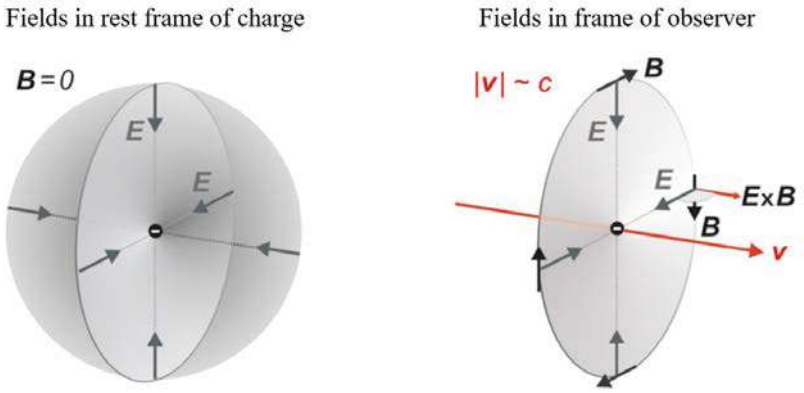

Figure 2.1: Left: Fields of an electron as viewed in the rest frame of the electron. Right: Fields of an electron with velocity $|v| \sim c$ [53].

2.2 Electromagnetic Field of a Relativistic Charged Particle Bunch

Let us consider a bunch of relativistic charged particles. We are interested in the field outside the bunch at a distance $\rho = \sqrt{x^2 + y^2}$ from the z-axis. For our needs, we assume the transverse bunch sizes $\sigma_{x,y}$ to be much smaller than the distance ρ. Neglecting the transverse bunch size, we can describe this situation by an ensemble of point charges distributed along the z-axis. From equation 2.2 we can find the radial component dE_ρ created by an infinitesimally small charge dq' at coordinate z':

$$dE_\rho(z, z', \rho) = \frac{1}{4\pi\varepsilon_0} \frac{\rho\, dq'}{\gamma^2 \left((z - z')^2 + \frac{\rho^2}{\gamma^2} \right)^{3/2}} \tag{2.3}$$

with z and ρ corresponding to the point of observation of the field. We now define a one-dimensional normalised longitudinal particle density distribution $S_{1D}(z)$ with $\int_{-\infty}^{+\infty} S_{1D}(z)\,dz = 1$. To obtain the field $E_\rho(z,\rho)$ at a certain location, we now integrate the field contributions in equation 2.3 from all the infinitesimally small charges in our previously defined particle density distribution.

$$E_\rho(z,\rho) = \frac{Q\rho}{4\pi\varepsilon_0\gamma^2} \int_{-\infty}^{+\infty} \frac{S_{1D}(z')\,dz'}{\left((z-z')^2 + \frac{\rho^2}{\gamma^2}\right)^{3/2}} \tag{2.4}$$

This equation describes the magnitude of the electric field at a certain location (z,ρ) with the assumption of $\rho \gg \sigma_{x,y}$.

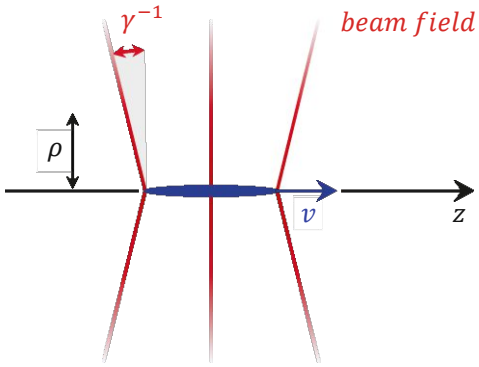

Figure 2.2: Illustration of a relativistic bunch of charged particles. The bunch travels in the z-direction with velocity v. The field lines approach the plane perpendicular to the direction of propagation for $\gamma \to \infty$.

However, it is also beneficial to check the behaviour of this equation for two extreme cases. Considering a distance $\sigma_z\gamma \gg \rho$, we have a closer look at how the function $\left((z-z')^2 + \frac{\rho^2}{\gamma^2}\right)^{-3/2}$ behaves. This function peaks at $z = z'$ and has a width of $\Delta z \sim \rho/\gamma$. For the condition of being close to the bunch, we can replace the function with the Dirac delta function $\delta(z-z')$. However, we still need to adapt the Dirac delta function to the integral over dz', which yields:

$$\int_{-\infty}^{+\infty} \left((z-z')^2 + \frac{\rho^2}{\gamma^2}\right)^{-3/2} dz' = \frac{2\gamma^2}{\rho^2}$$

We obtain the adapted delta function $\frac{2\gamma^2}{\rho^2}\,\delta(z-z')$. Inserting this approximation back into equation 2.4, the resulting field in the transverse direction can then be expressed as [54]:

$$E_\rho(z,\rho) = \frac{1}{4\pi\varepsilon_0}\frac{2\,Q\,S_{1\mathrm{D}}(z)}{\rho} \tag{2.5}$$

This result is equivalent to what one would obtain for the limit $\gamma \to \infty$. This can also be interpreted as neglecting the contribution from the $1/\gamma$ opening angle, which is small compared to the bunch length for short distances ρ and high values of γ.

On the contrary, if we deal with large distances from the beam $\sigma_z\gamma \ll \rho$, we can replace the particle distribution function itself with the Dirac delta function $\delta(z)$. Using equation 2.4, the resulting field in the transverse direction can then be directly expressed as:

$$E_\rho(z,\rho) = \frac{Q\rho}{4\pi\varepsilon_0}\frac{\gamma}{\left(z^2\gamma^2+\rho^2\right)^{3/2}} \tag{2.6}$$

This result is equivalent to the field of a point charge with a total charge Q.

For beam instrumentation purposes, one is most often confronted by the case described in equation 2.5, which has the obvious benefit of the electric field being a direct replica of the longitudinal particle bunch distribution $Q \cdot S_{1\mathrm{D}}$. However, for larger distances and low values of γ, one has to consider the broadening of the electric field compared to $S_{1\mathrm{D}}$ and therefore utilise equation 2.4. Often, we deal with bunches which have a Gaussian longitudinal particle density distribution, therefore:

$$Q \cdot S_{1\mathrm{D}}(z) = \frac{Q}{\sqrt{2\pi}\,\sigma_z}\exp\left(-\frac{z^2}{2\sigma_z^2}\right) \tag{2.7}$$

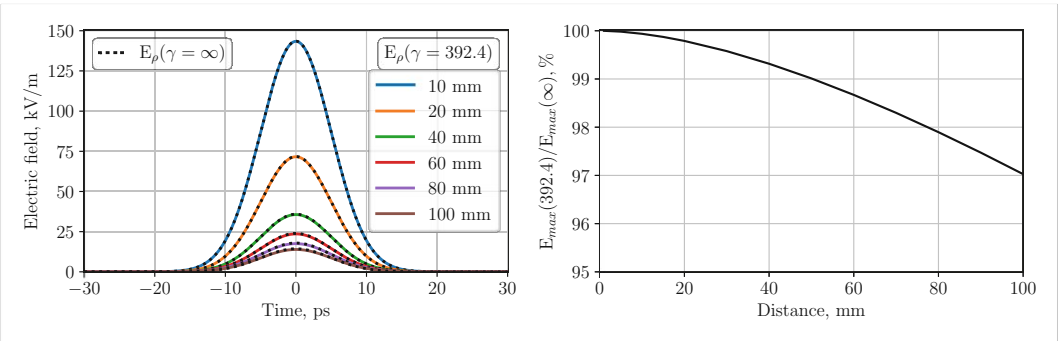

Figure 2.3: On the left, the transverse electric field of a particle bunch is given for different transverse distances. The coloured lines are calculated for a 5 ps bunch ($1\,\sigma$), a charge of 300 pC and $\gamma = 392.4$. The dotted line represents $\gamma = \infty$ for each distance. The peak electric field strength for $\gamma = 392.4$ relative to $\gamma = \infty$ is shown on the right.

2.3 Transition Radiation

Transition radiation refers to the radiation emitted at the boundary surface between two media of different permittivity as a charged particle passes through the boundary rapidly. The respective fields of the charged particle differ from each other within the two different media. As the particle transitions from one medium to the other, the rearrangement of fields leads to the emission of transition radiation. In fig. 2.4, this is illustrated for a thin layer of permittivity ε_1 surrounded by vacuum with a defined permittivity of $\varepsilon_0 = 1/(\mu_0 c^2)$, with the vacuum permeability μ_0. In the case presented, the layer is positioned normal to the particle trajectory. Transition radiation is then emitted in the forward and backward directions, centred around the particle trajectory.

The spectral and angular energy distribution is well known for the far field transition radiation in the backward direction and is described by the Ginzburg-Frank formula for a particle of charge q [55]:

$$\frac{d^2W}{d\omega d\Omega} = \frac{q^2}{4\pi^3\varepsilon_0 c}\frac{\beta^2\sin^2(\theta)}{(1-\beta^2\cos^2(\theta))^2}\,, \tag{2.8}$$

where $\beta = v/c$ is the normalised velocity of the particle with charge q, ε_0 the vacuum permittivity, ω the angular frequency and θ is the angle against the backward direction. This formula holds for a screen of infinite extension with perfect reflectivity; therefore, $\varepsilon_1 = \infty$. Moreover, equation 2.8 is only valid for angular frequencies much smaller than the plasma frequency of the material, $\omega \ll \omega_p$. Under such conditions, the spectral energy is constant. As described in fig. 2.4, the

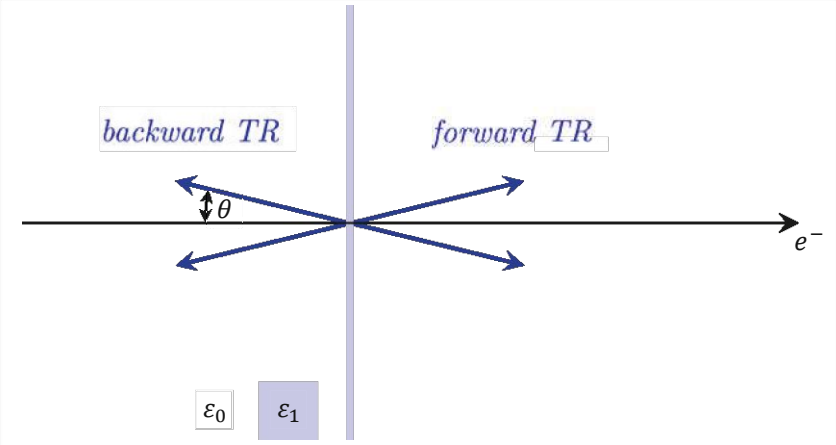

Figure 2.4: Schematic of the generation of transition radiation (TR). A charged particle traverses a medium with permittivity $\varepsilon_1 \neq \varepsilon_0$, generating backward and forward transition radiation. The maximum of the direction of emission lies on a cone with an opening angle of $2\theta \simeq 2\gamma^{-1}$.

angular distribution in the far field has its maximum at the angle $\theta \simeq \gamma^{-1}$ with respect to the particle trajectory.

By constraining the transverse dimension of the boundary, the Ginzburg-Frank equation 2.8 needs to be generalised. The case for a disk of radius a is shown in fig. 2.5. The distance between the disk and the plane of detection is denoted L, and the angle with respect to the beam trajectory is denoted θ. For a metallic disk normal with respect to the direction of the beam and a transverse dimension of radius a, the spectral and angular energy distribution reads [56, 57]:

$$\frac{d^2W^{(1)}}{d\omega d\Omega} = \frac{q^2\omega^4}{4\pi^3\varepsilon_0 c^5\beta^4\gamma^2}\left|\int_0^a J_1\left(\frac{\omega\rho\sin\theta}{c}\right)K_1\left(\frac{\omega\rho}{c\beta\gamma}\right)\rho\, d\rho\right|^2 \tag{2.9}$$

which can be analytically integrated over the disk radius ρ and yields

$$\frac{d^2W^{(1)}}{d\omega d\Omega} = \frac{d^2W}{d\omega d\Omega}\left(1 - T(\gamma, \omega a, \theta)\right)^2, \tag{2.10}$$

with the correction factor

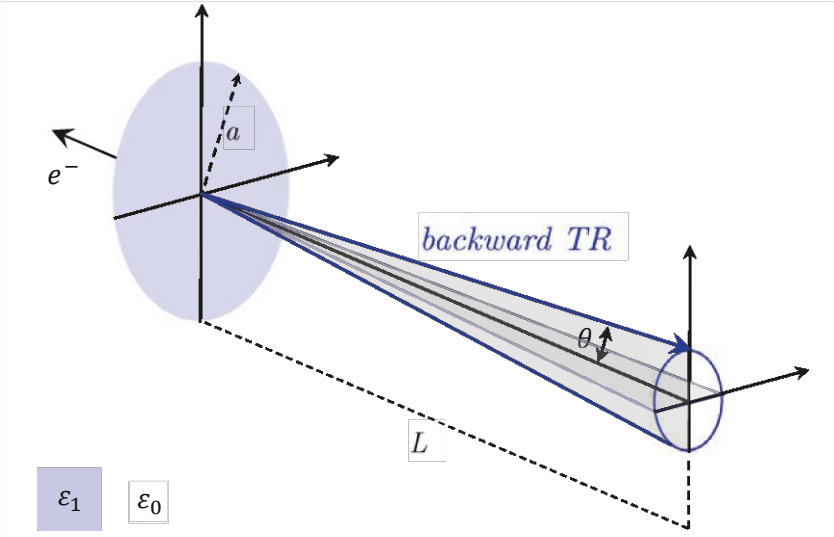

Figure 2.5: Backward transition radiation for a disk with radius a. The distance between the disk and the plane of detection is denoted L, and the angle with respect to the beam trajectory is denoted θ. If conditions $a > r_{\text{eff}}$ and $L > \gamma r_{\text{eff}}$ are fulfilled, the Ginzburg-Frank formula is valid and $\theta \simeq \gamma^{-1}$.

$$T(\gamma, \omega a, \theta) = \frac{\omega a}{c\beta\gamma} J_0\left(\frac{\omega a \sin\theta}{c}\right) K_1\left(\frac{\omega a}{c\beta\gamma}\right) + \frac{\omega a}{c\beta^2\gamma^2 \sin\theta} J_1\left(\frac{\omega a \sin\theta}{c}\right) K_0\left(\frac{\omega a}{c\beta\gamma}\right),$$

with Bessel functions J_α and the modified Bessel functions K_α. The generalised equation 2.10 is valid for an observation distance L much greater than the transverse size of the disk.

For smaller observation distances L, it was shown in [56] that the spectral and angular energy distribution is equivalent to equation 2.9 except for an additional phase factor:

$$\frac{d^2W^{(2)}}{d\omega d\Omega} = \frac{q^2\omega^4}{4\pi^3\varepsilon_0 c^5 \beta^4\gamma^2} \left| \int_0^a J_1\left(\frac{\omega\rho\sin\theta}{c}\right) K_1\left(\frac{\omega\rho}{c\beta\gamma}\right) \exp\left(\frac{i\omega\rho^2}{c2L}\right) \rho\, d\rho \right|^2 \quad (2.11)$$

The emission of transition radiation is only substantial up to a transverse distance $\rho \simeq \gamma\lambda/(2\pi)$ [52]. This distance is often denoted as an effective radius in literature [58, 59]:

$$r_{\text{eff}} = \frac{\gamma\lambda}{2\pi} \tag{2.12}$$

The Ginzburg-Frank formula requires the boundary to be infinite. However, a substantial contribution to transition radiation is only present for values of ρ up to r_{eff}. The radius of the disk a needs to be at least of the order r_{eff} to obtain the Ginzburg-Frank angular distribution:

$$a > r_{\text{eff}} = \frac{\gamma\lambda}{2\pi} \tag{2.13}$$

The second condition to be met for the Ginzburg-Frank formula to be valid is the far-field condition. The far-field condition is met for distances $L > (\gamma^2\lambda)/(2\pi)$. Using the effective radius r_{eff} we can write this as:

$$L > \gamma\, r_{\text{eff}} = \frac{\gamma^2\lambda}{2\pi} \tag{2.14}$$

In case both conditions 2.13 and 2.14 are met, the angular distribution will satisfy equation 2.8. If one of both conditions is not met, the angular distribution will vary greatly from the Ginzburg-Frank formula, with peak intensities not centred at angles $\theta \simeq \gamma^{-1}$, but shifted to higher angles [56]. Due to the symmetry of the particle field, there still will not be any contributions at $\theta = 0$.

An orientation of the layer at 90° with respect to the particle trajectory is usually not used for beam diagnostic purposes, as the emitted radiation is then concentrated along the particle trajectory for high particle energies [60]. The particle beam's presence makes it difficult to perform a measurement at this location. The most common orientation of transition screens for beam diagnostic purposes is at 45° with respect to the particle trajectory, as illustrated in fig. 2.6. The backward transition radiation follows the law of reflection, and consequently, the transition radiation cone is centred around 90°. In this configuration, the high directivity of transition radiation at high particle energies is a valuable benefit, as the separation from the particle trajectory eases its utilisation for beam diagnostic purposes. Often, the visible part of the frequency spectrum ($\approx$ 400 to 800 THz) is utilised to obtain information on the particle beam transverse size. For the beam parameters at the CLEAR facility with $\gamma = 392.4$ and an observation wavelength in the visible spectrum $\lambda \sim 500\,\text{nm}$, the effective radius $r_{\text{eff}} \sim 30\,\mu\text{m}$, is much smaller than

typical screen dimensions. The far-field condition $\gamma\, r_{\text{eff}} \sim 1.2\,\text{cm}$ is easily met for the given value of γ. The visible spectrum is still emitted incoherently for bunch lengths of several femtoseconds. Transmission radiation is also frequently used to generate THz radiation. For bunch lengths in the femtosecond range, coherent transmission radiation is emitted up to the low THz regime [56, 61, 62]. The use of transition radiation at the lower end of the frequency spectrum is also possible. For example, the bunch form factor was reconstructed with a modulated particle beam using transition radiation in the gigahertz range [63]. For the beam parameters at the CLEAR facility with $\gamma = 392.4$ and an observation frequency of 100 GHz, which corresponds to a wavelength of 3 mm, the effective radius becomes $r_{\text{eff}} \sim 19\,\text{cm}$ and the far field condition is only met for distances $L \gtrsim 75\,\text{m}$. These conditions are not easily met, and therefore, the Ginzburg-Frank formula 2.8 does typically not apply for low frequencies in the gigahertz range as typical radiator dimensions ($\sim$cm) and typical detection distances ($\sim$m) have a substantial influence on the spectral and angular energy distribution.

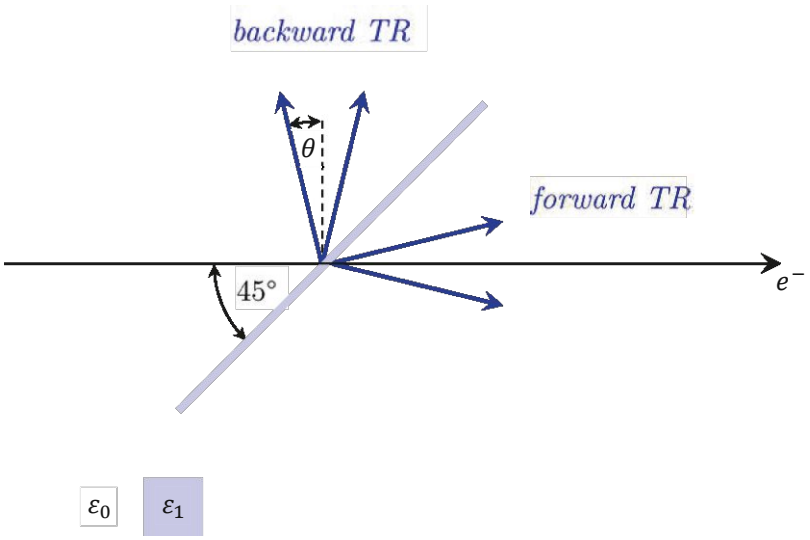

Figure 2.6: Schematic of the generation of TR for a transition screen tilted by 45° with respect to the particle trajectory as typically positioned for beam diagnostic purposes.

2.4 Diffraction Radiation

Diffraction radiation is based on the same principle as transition radiation. However, instead of the charged particle traversing a material boundary with $\varepsilon_1 \neq \varepsilon_0$ as shown in fig. 2.6, the material is only present at a certain distance from the particle

trajectory, as illustrated in fig. 2.7. Therefore, not the entire field of the particle can contribute to generating radiation, but only the fraction which extends far enough to reach the material. Following the introduction of the effective radius r_{eff} in the previous section, it is evident that for diffraction radiation to be emitted, the distance to the diffraction radiation screen $d/2$ needs to fulfil the condition [58]:

$$d/2 < r_{\text{eff}} = \frac{\gamma\lambda}{2\pi} \tag{2.15}$$

Diffraction radiation has similar properties as transition radiation. As illustrated in fig. 2.7 it also emits radiation in the forward and backward direction for a disk positioned around the particle trajectory. For the disk rotated at 45° with respect to the particle trajectory, the backward diffraction radiation is directed in specular reflection with respect to the disk. The diffraction radiation emission is then centred around 90° with respect to the particle trajectory. To fulfill the condition 2.15 in the visible spectrum (e.g. 500 nm) and at a value of $\gamma = 2000$ (e^- of $\approx 1\,\text{GeV}$), the parameter d must be in the order of $300\,\mu\text{m}$. For mechanical reasons, when performing measurements in the visible spectrum, the diffraction radiation screen is typically manufactured with a slit [64]. This then breaks the symmetry in θ as present for transition radiation. The main advantage compared to transition radiation for beam diagnostic purposes is the non-invasive nature of diffraction radiation. Several experiments have demonstrated a transverse beam size measurement with diffraction radiation in the micrometre range despite being a non-invasive method [65, 66].

However, the utilisation of DR for beam diagnostic purposes proposes several challenges. As demonstrated above, the maximum slit size d, even at high values of $\gamma = 2000$, is in the order of hundreds of μm. To align the slit with the beam is therefore challenging, and to maintain a non-invasive measurement, the transverse beam size $\sigma_{x,y}$ needs to be much smaller than the slit size d. The light yield of DR is also greatly reduced compared to TR, which makes it susceptible to background radiation. One major source of background radiation is synchrotron radiation, which, when reflected off the DR screen, is almost indistinguishable from the DR signal.

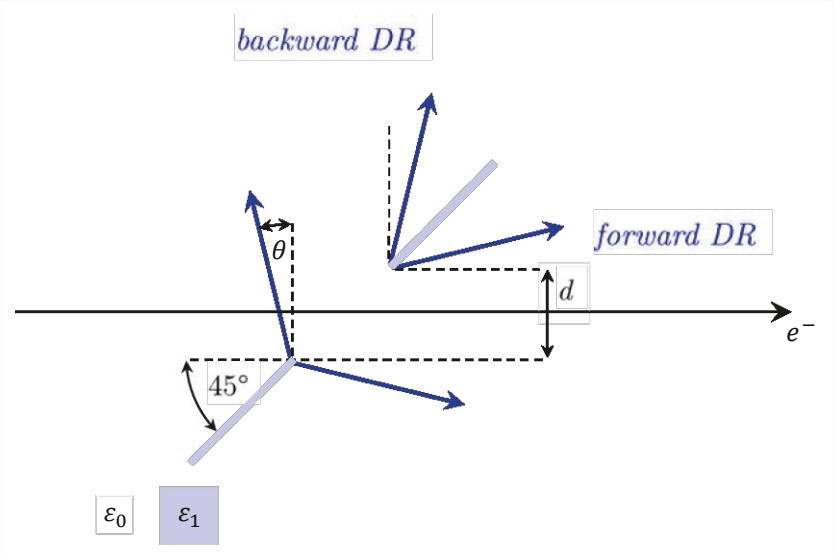

Figure 2.7: Schematic of the generation of diffraction radiation (DR). A charged particle passes near a medium with permittivity $\varepsilon_1 \neq \varepsilon_0$, generating backward and forward DR. The maximum of the direction of emission respects the same angle of γ^{-1} as present in TR.

2.5 Cherenkov Radiation

ChR is also produced in a stationary environment, with the particle being surrounded by a homogeneous dielectric material of a constant permittivity ε_1. This is in contrast to the generation of transition radiation or diffraction radiation, where a rapid change of the permittivity in the surrounding material $\varepsilon_0 \neq \varepsilon_1$ is required for radiation to be emitted. An illustration of ChR is shown in fig. 2.8. For a charged particle travelling with a velocity v through a material with refractive index n_1, ChR is emitted if the particle's velocity is greater than the phase velocity of electromagnetic waves in the material it is surrounded by. In other words, the particle needs to travel faster than the speed of light in the material. This is not contradictory to the theory of relativity, which proclaims the speed of light in vacuum c is a universal physical constant which can not be exceeded. However, the speed of light in any material is slowed down according to the material's refractive index to c/n_1. In fig. 2.8, it is illustrated that for a given time t, the charged particle travels a distance of $v \cdot t$, whereas the light in the medium only travels a distance of $c \cdot t/n_1$. This geometric observation already gives rise to the definition of the Cherenkov angle θ_{Ch}, which describes the direction of emission of ChR. We obtain:

$$\cos(\theta_{Ch}) = \frac{c}{v\,n_1} = \frac{1}{\beta\,n_1}, \tag{2.16}$$

with the relative particle velocity $\beta = v/c$. For any ChR to be emitted, this angle needs to be real, which leads to the Cherenkov condition:

$$\beta > \frac{1}{n_1} \tag{2.17}$$

As $\beta \leq 1$ by definition, ChR is only emitted for a refractive index $n_1 > 1$.

To give an illustrative example, we calculate the energy threshold for electrons to emit ChR in the visible spectrum in water. The refractive index of water for blue light of a wavelength of 450 nm is $n \approx 1.34$. The Cherenkov threshold for the kinetic energy of electrons is then 257 keV.

Pavel Alekseyevich Cherenkov observed blue light emitted in water through the Compton electrons liberated through the scattering of γ-rays the water was exposed to. This happened in 1934 when he was working under the supervision of Sergei I. Vavilov [67]. In literature, the radiation produced is, therefore, also referred to as Vavilov-Cherenkov radiation. After its discovery by Pavel A. Cherenkov, his colleagues Igor Y. Tamm and Ilya M. Frank interpreted and described the emission mechanism theoretically in 1937. Cherenkov, Tamm, and Frank received the Nobel Prize in Physics in 1958 for discovering and interpreting the Cherenkov effect [68].

The theory developed by Frank and Tamm explains the radiation of fast electrons passing through matter [69]. For the spectral energy distribution of ChR, they derived the formula:

$$\frac{d^2W}{dx\,d\omega} = \frac{q^2}{4\pi}\,\mu(\omega)\,\omega\left(1 - \frac{1}{\beta^2\,n^2(\omega)}\right), \tag{2.18}$$

where q denotes the particle charge, μ is the magnetic permeability of the material, $\beta = v/c$ the normalised velocity of the particle and n is the refractive index of the surrounding matter. The formula is given per unit length dx the particle travels through the matter. Equation 2.18 is referred to as the Frank-Tamm formula and is suitable for constant particle velocities. This is a valid approximation for particle energies that are much larger than the energy loss through ChR. Interestingly, according to the Frank-Tamm formula, the energy loss increases linearly with the observation frequency ω. The higher the frequencies, the greater the intensity of the emitted light. This characteristic also reflects the observation of ChR in the visible range. The shortest wavelengths observable for the human eye are of blue/violet colour, giving ChR a blueish appearance.

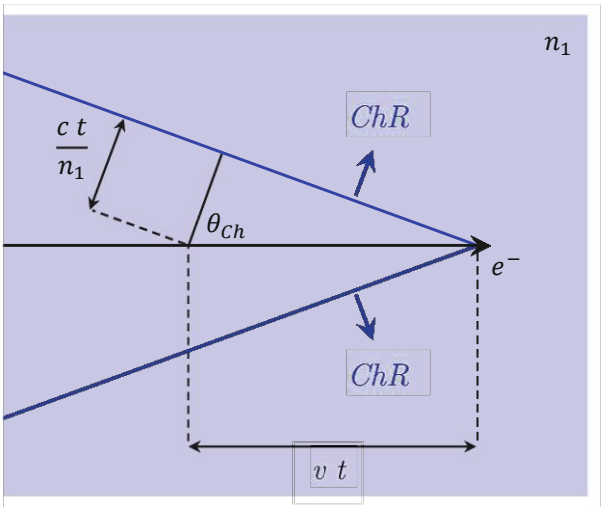

Figure 2.8: Schematic of the generation of Cherenkov radiation (ChR). A charged particle traverses a medium with refractive index n_1. ChR is emitted if the Cherenkov condition $v > c/n_1$ is fulfilled, stating that the particle's velocity needs to be greater than the speed of light in the dielectric material with refractive index n_1. The direction of emission is defined by the Cherenkov angle $\theta_{Ch} = \arccos(1/(\beta n_1))$.

2.6 Cherenkov Diffraction Radiation

Like diffraction radiation being equivalent to transition radiation except for the absence of matter in close vicinity to the particle trajectory, ChDR describes the radiation emitted by a particle travelling close to matter but not directly through it. A schematic of the generation principle of ChDR is illustrated in fig. 2.9.

In the scope of this thesis, two different analytical models are introduced to describe ChDR. Both models describe a flat geometry, with the surface of the dielectric material being a flat plane. In the transverse directions (both in width w and depth d), the dielectric material expands to infinity. We now investigate two different models, one with an infinite length l of the material and one with a finite length l. The stationary model will describe the case $l = \infty$, and the non-stationary model will describe the case $l < \infty$. It has to be noted, that the flat geometry was chosen, as it resembles the radiator geometry realised in this thesis better. Several analytical models also describe a stationary cylindrical geometry, which was investigated in detail by K. Łasocha [70]. It was shown that the spectral energy distribution of the stationary cylindrical and flat models show the same characteristics. Therefore, the cylindrical model's characteristics are qualitatively represented by the stationary flat model in this thesis.

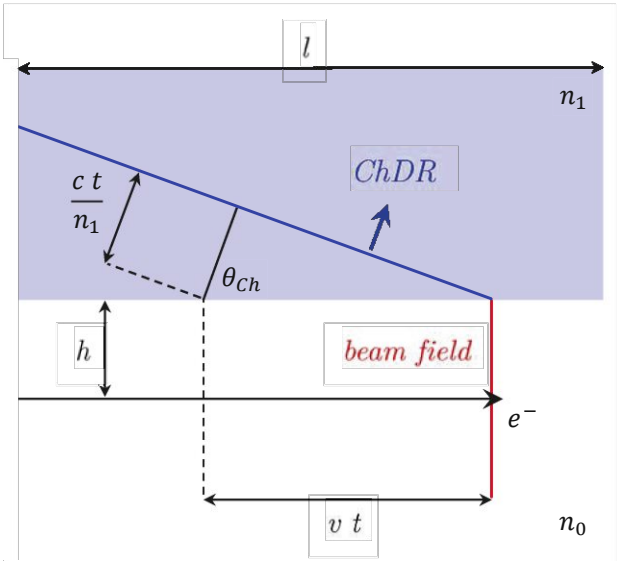

Figure 2.9: Schematic of the generation of Cherenkov diffraction radiation (ChDR). A charged particle passes close to a medium with refractive index n_1. ChDR is emitted if the Cherenkov condition $v > c/n_1$ is fulfilled, stating that the particle's velocity needs to be greater than the speed of light in the dielectric material with refractive index n_1. The direction of emission is defined by the Cherenkov angle $\theta_{Ch} = \arccos(1/(\beta n_1))$.

2.6.1 Stationary Model

As the stationary model, we refer to a geometry which separates an infinitely extending space into two volumes separated by a plane, as illustrated in fig. 2.10. One volume is filled with a dielectric ($l = w = d = \infty$) of refractive index n_1 while the other volume is considered vacuum and therefore $n_0 = 1$. A charged particle travels parallel to the separating plane at a certain distance h to the dielectric. Several authors investigated the geometry of an infinitely extending dielectric with a plane surface [71, 72]. For the materials considered in this thesis, we assume $\mu_r = 1$ and therefore $\mu = \mu_0$. For this simplified case, the spectral energy distribution according to R. Ulrich is given as [70]:

$$\frac{d^2W}{dx\,d\omega} = \frac{q^2}{4\pi}\,\mu_0\omega\,\frac{\varepsilon\beta^2 - 1}{\varepsilon - 1}\int_{-\pi/2}^{\pi/2} T(\phi, h, \varepsilon, \beta)\,d\phi \tag{2.19}$$

with

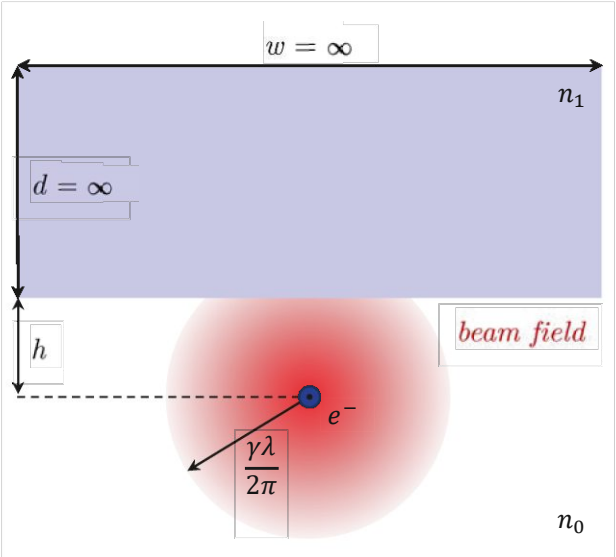

Figure 2.10: Schematic of the geometry used for the analytical models. The dielectric material's transverse dimensions w and d are infinite for both models.

$$T(\phi, h, \varepsilon, \beta) = \frac{(\varepsilon+1)(\varepsilon\beta^2-1)\sin^2\phi + \varepsilon(1-\beta^2)}{(\varepsilon+1)(\varepsilon\beta^2-1)\cos^2\phi - \varepsilon^2\beta^2}\cos^2\phi$$
$$\times \exp\left(-\frac{2h\omega}{v}\sqrt{(\varepsilon\beta^2-1)\sin^2\phi + 1 - \beta^2}\right).$$

In fig. 2.12, the spectral energy distribution is plotted as a function of frequency. The dashed lines correspond to equation 2.19 for a single electron for various values of γ. The calculation was performed for a permittivity $\varepsilon_r = 9$ and a distance between electron and dielectric of $h = 40\,\text{mm}$. The spectrum is divided into three different regimes. First, the radiated energy rises proportional to ω, then it falls proportional to ω^{-2}, and lastly, it falls rapidly for even higher frequencies. The separation between the first and second part of the spectrum scales with $1/h$, whereas the separation between the second and the third part of the spectrum scales with γ/h [70, 73]. For wavelengths up until approximately $2\pi \cdot h \approx 250\,\text{mm}$, which corresponds to a frequency of $f = 1.2\,\text{GHz}$, the energy spectrum increases proportionally to the frequency, as in the case of ChR described with equation 2.18. For shorter wavelengths, the radiated energy decreases significantly. However, the second part of the spectrum can be increased to shorter wavelengths by increasing the particle energy. The rapid fall-off of the radiated energy in the third part of

the spectrum corresponds to the effective radius of the particle field $r_{\text{eff}} = \gamma\lambda/(2\pi)$. The distance to the dielectric must be reduced to increase the emitted radiation in the visible spectrum, whereas the particle energy needs to be increased.

2.6.2 Non-stationary Model

The non-stationary model is the same in geometry as the stationary model, except that it is limited in length $l < \infty$. Its transverse dimensions also extend to infinity, as illustrated in fig. 2.10. The non-stationary model presented here is based on the polarisation current approach (PCA), which assumes that the electron shells of the dielectric material are polarised once exposed to the Coulomb field of the charged particle passing by [74]. In return, radiation is emitted from those polarised electron shells, with the magnetic field of the polarised radiation described in its general form:

$$\vec{H}^{pol}(\vec{r},\omega) = \nabla \times \frac{1}{c}\int_{V_T} \vec{j}^{pol}(\vec{r'},\omega)\,\frac{\exp\left(i\sqrt{\varepsilon}\,\frac{\omega}{c}|\vec{r}-\vec{r'}|\right)}{|\vec{r}-\vec{r'}|}\,d^3\vec{r'}, \tag{2.20}$$

with the induced polarisation current density $\vec{j}^{pol}(\vec{r'},\omega) = \sigma(\omega)E_q(\vec{r'},\omega)$, the dielectric volume V_T, the conductivity of the medium $\sigma(\omega) = (\varepsilon-1)\,\omega/(4\pi i)$ and the Fourier transformed Coulomb field of the particle $E_q(\vec{r'},\omega)$. Considering the geometry as presented in fig. 2.11 the magnetic field within the medium according to [74] is then expressed as:

$$\vec{H}^{pol}(\vec{r},\omega) = -\frac{q\beta\gamma}{4\pi c}\;\frac{\exp\left(i\sqrt{\varepsilon}\,\frac{\omega}{c}r\right)}{r}\;\frac{\sqrt{\varepsilon}\,(\varepsilon-1)}{\sqrt{1+\varepsilon(\beta\gamma n_x)^2}}\;\times$$
$$\times\;\frac{\vec{\xi}\,\exp\left(-h\frac{\omega}{\beta\gamma c}\sqrt{1+\varepsilon(\beta\gamma n_x)^2}\right)}{\sqrt{1+\varepsilon(\beta\gamma n_x)^2}+i\beta\gamma\sqrt{\varepsilon}\,n_y}\;\frac{\exp\left(i\,l\,\frac{\omega}{c\beta}\left(1-\sqrt{\varepsilon}\,n_z\beta\right)\right)-1}{1-\sqrt{\varepsilon}\,n_z\beta},$$

with the vector

$$\vec{\xi} = \begin{pmatrix} \gamma^{-1}n_y - in_z\sqrt{1+\varepsilon(\beta\gamma n_x)^2} \\ n_x\left(\sqrt{\varepsilon}\,\beta\gamma n_z - \gamma^{-1}\right) \\ n_x\left(i\sqrt{1+\varepsilon(\beta\gamma n_x)^2} - \sqrt{\varepsilon}\,\beta\gamma n_y\right) \end{pmatrix}$$

and the unity vector in the direction of $\vec{r}$

$$\vec{n} = \begin{pmatrix} n_x \\ n_y \\ n_z \end{pmatrix} = \begin{pmatrix} \sin\theta \sin\varphi \\ \sin\theta \cos\varphi \\ \cos\theta \end{pmatrix}.$$

The spectral and angular energy distribution within the medium is then obtained as:

$$\frac{d^2W}{d\omega d\Omega} = \frac{c\, r^2}{\left|\sqrt{\varepsilon}\right|^2} \left|\vec{H}^{pol}(\vec{r},\omega)\right|^2 \tag{2.21}$$

Two different contributions are present in the angular distribution in θ. One concentrated at the Cherenkov angle corresponding to the ChDR, and the second concentrated around $\theta \simeq 0$ as expected for diffraction radiation of high energy charged particles.

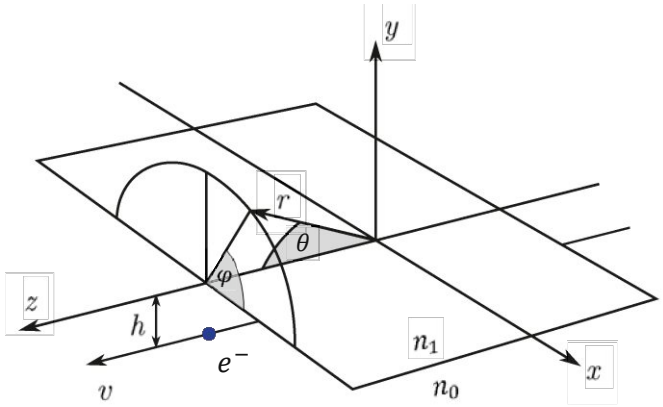

Figure 2.11: Schematic of the geometry and variables used in the non-stationary model. The space is divided into two halves filled with a vacuum (n_0) and a dielectric (n_1), as presented in fig. 2.10. The extension in the longitudinal direction z is restricted to a finite distance.

To exclude the diffraction radiation part of the radiated spectrum as described in equation 2.21, the angular distribution is only considered for $\theta \simeq \theta_{Ch}$. The resulting spectral energy distribution is shown in fig. 2.12 in solid lines for various particle energies. As for the stationary model, the energy spectrum is divided into three different parts. The turning points between the three different parts coincide with the one of the stationary model and scale as $1/h$ and γ/h, respectively. However, the second part of the spectrum is constant with respect to ω.

This difference between the two models was investigated in detail in [70] and would lead to a substantially different radiation yield for different key parameters of an experimental setup for any frequencies above $\simeq c/h$. For an impact parameter of $h = 40\,\mathrm{mm}$, as the design impact parameter in this thesis, a large discrepancy between the two models is present for $f > 7.5\,\mathrm{GHz}$. The discrepancy between the two analytical models still requires further experimental investigation and is of fundamental importance, especially for high particle energies.

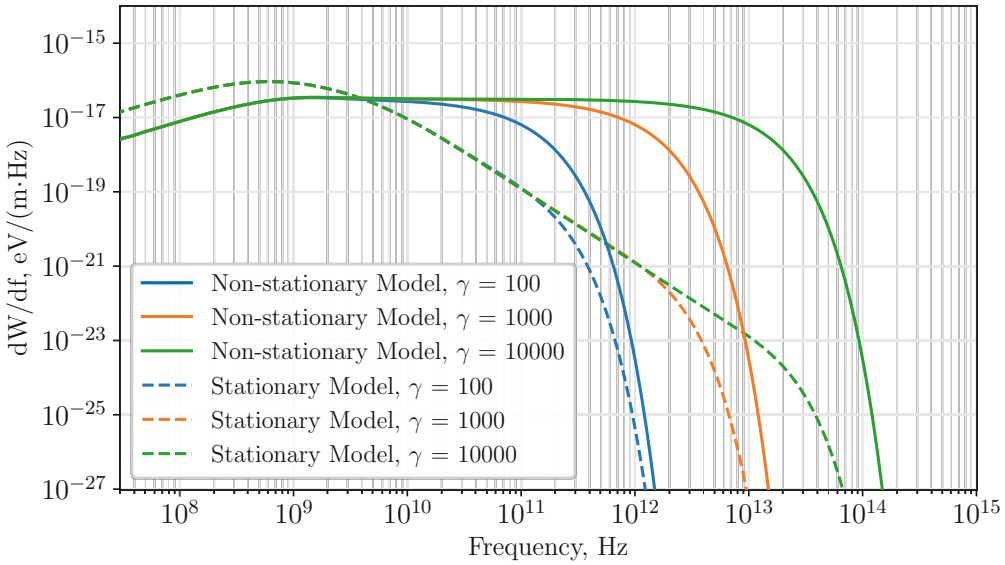

Figure 2.12: Spectral energy distribution for the non-stationary and stationary model for various particle energies. All spectra are plotted for h = 40 mm and $\varepsilon = 9$. The spectrum is divided into three regions, with $c/(2\pi h) < f < \gamma c/(2\pi h)$ denoting the second part of the spectrum. The dependence on frequency for the second part of the spectrum is constant for the non-stationary model and $\propto \omega^{-2}$ for the stationary model. For the first region ($f < c/(2\pi h)$), it increases like ChR $\propto \omega$, for the third region ($f > \gamma c/(2\pi h)$), there is a rapid decline, which can be explained by the effective radius r_{eff} of the Coulomb field of the particle.

2.7 Coherent and Incoherent Radiation

The equations presented for transition radiation, Cherenkov radiation and stationary and non-stationary ChDR all refer to the spectral energy distribution of a single charged particle. However, in particle accelerators, one usually deals with an ensemble of particles forming a particle bunch. As already discussed in section 2.2, where we introduced the electromagnetic field of a relativistic charged particle bunch, we describe the longitudinal distribution of the bunch with a one-dimensional normalised particle density distribution of Gaussian shape $S_{1\mathrm{D}}(z)$, which in the time domain reads as:

$$S_{1\mathrm{D}}(t) = \frac{1}{\sqrt{2\pi}\,\sigma} \exp\left(-\frac{t^2}{2\sigma^2}\right), \tag{2.22}$$

with $\int_{-\infty}^{+\infty} S_{1\mathrm{D}}(t)\,dt = 1$. The electric field at the location of measurement $\vec{r}$ of each particle j of a particle bunch of N particles will have a certain time delay with respect to the electric field of the reference particle due to the spatial offset amongst the particles in the longitudinal direction. The discrete nature of the particle bunch, which leads to this time delay between the particles, gives rise to the coherent and incoherent emission of radiation. To describe this behaviour, we follow the approach as presented in [75].

The total electric field in the time domain observed at a position $\vec{r}$ of the ensemble of N particles in the bunch is described by the sum of the electric field of all single particles j within the bunch under consideration of their temporal offset:

$$\vec{E}(\vec{r}, t) = \sum_{j=1}^{N} \vec{E}_1(\vec{r}, t + \Delta t_j) \tag{2.23}$$

This superposition of fields assumes that all single particles cause the same electric field E_1 at the location of observation $\vec{r}$, except for a temporal offset. For ChDR, this is a valid approximation for transverse bunch sizes, which are small compared to the longitudinal bunch size and the impact parameter h. The Fourier transform of the total electric field yields:

$$\begin{aligned}\vec{E}(\vec{r},\omega) &= \sum_{j=1}^{N}\int_{-\infty}^{\infty}\vec{E}_1(\vec{r},t+\Delta t_j)\,e^{-i\omega t}dt \\ &= \sum_{j=1}^{N}\int_{-\infty}^{\infty}\vec{E}_1(\vec{r},t)\,e^{-i\omega(t-\Delta t_j)}dt = \sum_{j=1}^{N}e^{i\omega\Delta t_j}\int_{-\infty}^{\infty}\vec{E}_1(\vec{r},t)\,e^{-i\omega t}dt \\ &= \vec{E}_1(\vec{r},\omega)\ \sum_{j=1}^{N}e^{i\omega\Delta t_j}\end{aligned} \tag{2.24}$$

This result we insert into the equation for the spectral energy distribution in the far field as given in the appendix of [75]. The factor two stems from the fact that $\vec{E}(t)$ is real and using $\vec{E}^*(-\omega)=\vec{E}(\omega)$ we limit the integration to positive values of ω:

$$\begin{aligned}\frac{dW}{d\omega} &= 2\varepsilon_0 c\left\langle\left|\vec{E}(\vec{r},\omega)\right|^2\right\rangle \\ &= 2\varepsilon_0 c\left\langle\left|\vec{E}_1(\vec{r},\omega)\ \sum_{j=1}^{N}e^{i\omega\Delta t_j}\right|^2\right\rangle \\ &= \left(\frac{dW}{d\omega}\right)_1\ \left\langle\left|\sum_{j=1}^{N}e^{i\omega\Delta t_j}\right|^2\right\rangle\end{aligned} \tag{2.25}$$

Here $\left(\frac{dW}{d\omega}\right)_1$ denotes the spectral energy distribution of a single particle, ε_0 is the vacuum permittivity and $\left\langle\cdot\right\rangle$ denotes the ensemble average of the particle bunch. The second term of the equation can be rewritten as [70]:

$$\begin{aligned}\left\langle\left|\sum_{j=1}^{N}e^{i\omega\Delta t_j}\right|^2\right\rangle &= \left\langle\left(\sum_{j=1}^{N}e^{i\omega\Delta t_j}\right)\left(\sum_{j=1}^{N}e^{-i\omega\Delta t_j}\right)\right\rangle \\ &= \left\langle\sum_{j=1}^{N}e^{i\omega(\Delta t_j-\Delta t_j)}+\sum_{\substack{j,j'=1\\ j\neq j'}}^{N}e^{i\omega\Delta t_j}\left(e^{i\omega\Delta t_{j'}}\right)^*\right\rangle \\ &= N+N(N-1)\left\langle e^{i\omega\Delta t_j}\right\rangle^2,\end{aligned} \tag{2.26}$$

with the factor $\left\langle e^{i\omega\Delta t_j} \right\rangle^2$ being referred to as the bunch form factor $F(\omega)$. It is defined as the squared absolute value of the Fourier transform of the particle density distribution in the time domain [76]. For the one-dimensional case, we obtain the following:

$$F_{1\mathrm{D}}(\omega) \coloneqq \left| \int_{-\infty}^{\infty} S_{1\mathrm{D}}(t)\, e^{-i\omega t} dt \right|^2, \tag{2.27}$$

with the Gaussian particle density distribution $S_{1\mathrm{D}}(t)$ as given in equation 2.22. The final result for the total spectral energy distribution of a one-dimensional particle bunch is then given as:

$$\frac{dW}{d\omega} = \left(\frac{dW}{d\omega}\right)_1 \cdot \Big(N + N\big(N-1\big)\, F_{1\mathrm{D}}(\omega)\Big), \tag{2.28}$$

with the spectral energy distribution of a single particle $\left(\frac{dW}{d\omega}\right)_1$, the number of particles within the bunch N and the bunch form factor $F_{1\mathrm{D}}$. The energy spectrum is divided into two parts. The first part, proportional to the number of particles N, is called the incoherent part of the spectrum. The second part, proportional to $\sim N^2$ for $N \gg 1$, is called the coherent part of the spectrum. The bunch form factor describes whether a frequency is emitted incoherently or coherently. For frequencies which correspond to wavelengths longer than the bunch length, all particles within the bunch can be considered in phase, which leads to coherent emission of radiation. For frequencies which correspond to wavelengths shorter than the bunch length, all particles within the bunch emit radiation independently, leading to incoherent emission of radiation.

3

Numerical Simulations of Coherent Cherenkov Diffraction Radiation

This chapter presents the numerical simulations conducted to investigate the expected properties of coherent Cherenkov diffraction radiation (CChDR) in a realistic experimental configuration. We introduce the simulation setup and describe the radiator geometry. The electric field properties of a particle bunch in a vacuum will serve as a simulation benchmark. We illustrate the general propagation of CChDR within the radiator and discuss the associated electric field's polarisation. Additionally, we examine the expected time signals for point probes and area-integrated signals. We analyse the cutoff frequency resulting from the radiator geometry and identify the anticipated resonating frequencies. Finally, we explore the dependence of the peak amplitude of the CChDR signal on the impact parameter.

3.1 Simulation Environment

To simulate the effects of a charged particle beam on dielectric media, the Computer Simulation Technology Studio Suite 2022 (CST Studio Suite® 2022) was used as the simulation environment. CST Studio Suite is an electromagnetic and multi-physics simulation environment, which includes the CST Particle Studio®. CST Particle Studio® provides several different electromagnetic simulation solvers, with an overview provided in table 3.1. The only two options suitable to describe ChDR are the Particle-in-Cell solver and the Wakefield solver. Of these two solvers, the wakefield solver was chosen as we are interested in the effect of the electromagnetic field of a beam on a dielectric interface rather than the particle trajectories and space charge effects within the bunch. Moreover, the simulation work on ChDR performed by E. Senes [77] demonstrated that the Particle-in-Cell solver generates significantly distorted electromagnetic fields at the entry boundary. In contrast, the wakefield solver provides a more realistic representation of the electromagnetic field at the entry boundary and throughout the entire structure.

Solver	**Application**
Particle-in-Cell	Particle trajectory, electromagnetic fields and space charge
Electrostatic Particle-in-Cell	Space charge dynamics
Particle Tracking	Particle trajectory in static fields and space charge
Wakefield	Electromagnetic fields without particle-fields interaction

Table 3.1: Overview of CST Particle Studio® Solvers [78].

3.1.1 Wakefield Solver

The wakefield solver calculates the wake potentials of a given structure using the electromagnetic fields of a test bunch. For this purpose, a bunch of charged particles, represented by a line current, travels through the predefined geometry. The charged particles carry an electromagnetic field that interacts with the surrounding structure. The fields are calculated with a time domain solver, and the wake potentials $\vec{W}$ are calculated from the fields.

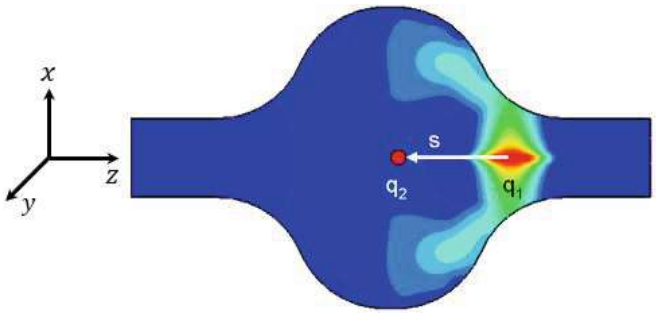

Figure 3.1: Illustration depicting the wakefields generated by a Gaussian bunch with charge q_1 travelling in the +z direction. The witness charge q_2 is positioned at a distance s from q_1 and follows the same trajectory [78].

$$\vec{W}(x,y,s) = \frac{1}{q_1}\int_{-\infty}^{+\infty}\left[\vec{E}(x,y,z,t) + c\,\vec{e_z}\times\vec{B}(x,y,z,t)\right]_{t=(s+z)/c} dz \tag{3.1}$$

The wake potential describes the accumulated force acting on a witness charge q_2, which is exposed to the wakes generated by a test charge q_1 travelling in the direction $\vec{e_z}$ [79]. The change in momentum of the witness charge q_2 following the same path as the test charge q_1 is given as $\Delta\vec{p} = q_1 q_2 \vec{W}(s)$. The integration path can be chosen independently from the beam path in the simulation environment.

The wake potential is also used to obtain the impedance corresponding to the wake potential's Fourier transform. The longitudinal impedance is given as [79]:

$$\vec{Z}_{\parallel}(x,y,\omega) = \frac{1}{c}\int_{-\infty}^{+\infty}\vec{W}_{\parallel}(x,y,s)\exp\left(-i\frac{\omega}{c}s\right)ds$$

$$\vec{Z}_{\parallel}(x,y,\omega) = \frac{1}{q_1 c}\int_{-\infty}^{+\infty}\int_{-\infty}^{+\infty} E_z(x,y,z,(s+z)/c)\,\exp\left(-i\frac{\omega}{c}s\right)dzds \tag{3.2}$$

as $\vec{e_z}\cdot(\vec{e_z}\times\vec{B}) = 0$. Wake potential and impedance both describe the coupling between the beam and its environment, whereas the wake potential is the time representation, and the impedance is the frequency representation of this coupling. In the wakefield solver, the calculated impedance is always normalised by the Fourier transformed charge distribution function $S_{1\mathrm{D}}(s)$.

Also, the wake loss factor is calculated within the wakefield solver and for the longitudinal wake component, it is given as [79]:

$$k_{\parallel} = -\int_{-\infty}^{+\infty} \vec{W}_{\parallel}(s) S_{1\mathrm{D}}(s)\, ds \tag{3.3}$$

The wake loss factor is used to calculate the energy lost $\Delta W = q_1^2\, k_{\parallel}$ of a bunch travelling through a given structure.

3.2 Radiator Geometry

As we are interested in analysing the general characteristics of ChDR, the radiator geometry should also reflect this approach. Ideally, one would have a radiator of infinite length and the possibility of probing the generated signal within the radiator itself. However, this is obviously impossible to implement, and we must consider restrictions on the radiator design. These restrictions mainly arise from implementing the final device into a real beam line. An overview of the requirements is presented in section 4.3.1, where the mechanical design of the radiator is introduced. For simulation purposes, the mechanical design is simplified as much as possible without changing the key parameters of the radiator geometry.

The schematic representation of the geometric configuration is depicted in fig. 3.2. The vacuum chamber has a circular cross-section with a diameter $D = 80\,\mathrm{mm}$. To provide sufficient space beyond the exit surface of the radiator for the ChDR to propagate, the vacuum chamber has a length $l = 100\,\mathrm{mm}$. The radiator has a cylindrical shape with a diameter $d = 36\,\mathrm{mm}$ and is constructed from alumina ($97.6\%\,Al_2O_3$). The relative permittivity of the utilised alumina is specified as $\varepsilon_r \approx 9.02\,(1.0 - 8.5\,\mathrm{GHz},\, 25^\circ\,\mathrm{C})$ [80]. The Cherenkov angle for ultra-relativistic particles is then given as $\theta_{Ch} = \arccos\left(\varepsilon_r^{-1/2}\right) = 70.55^\circ$. Consequently, the radiator is inserted into the metal body at an angle of 70.55° for the Cherenkov wavefront travelling within the alumina radiator being aligned with the exit surface of the radiator. This orientation minimises refraction of the wavefront upon exiting the radiator, preserving the original direction of propagation. Components shaded in dark grey in fig. 3.2 consist of aluminium or steel and are treated as perfect electrical conductors (PEC) for simulation purposes. This implies that they are modelled as materials with infinite electrical conductivity or, equivalently, no electrical resistivity.

In fig. 3.3, the concave surface of the radiator being exposed to the electromagnetic field of an electron e^- is shown. The radiator is machined to align seamlessly with the inner diameter of the vacuum chamber $D = 80\,\mathrm{mm}$. The distance between the electron and the radiator surface, also introduced as the impact parameter, is denoted h.

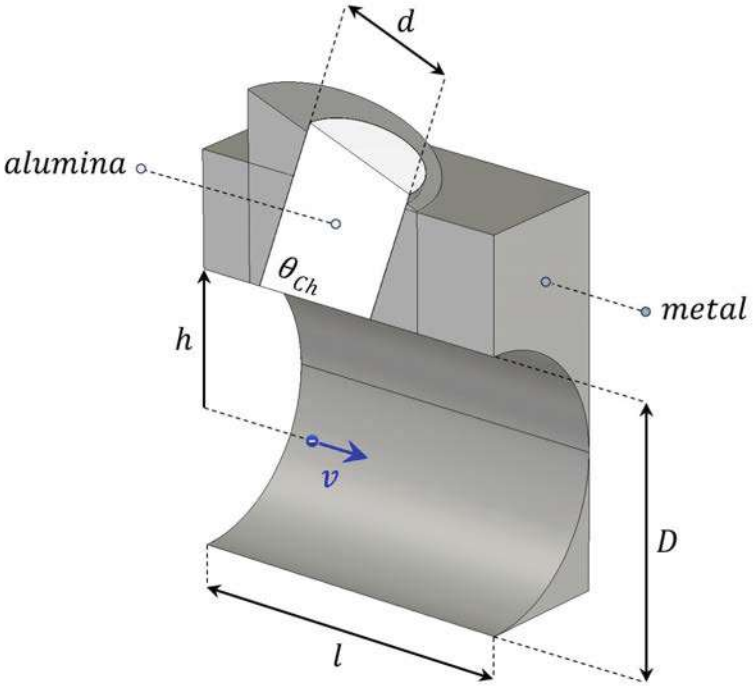

Figure 3.2: Half-plane view of the 3D model utilised for simulation purposes. The alumina radiator with a diameter of $d = 36\,\text{mm}$ is inserted at the corresponding Cherenkov angle $\theta_{Ch} = 70.55°$ into a metal body with a vacuum chamber diameter of $D = 80\,\text{mm}$.

3.3 Simulation Parameters

The simulation parameters are tailored to match the beam parameters of the CERN Linear Electron Accelerator for Research (CLEAR), which are described in more detail in section 4.1. When configuring the wakefield solver, only a subset of the beam parameters can be implemented. The longitudinal bunch shape is restricted to be Gaussian distribution. The normalised velocity β, the bunch charge and the bunch length can be adjusted. For all the presented simulations, the same bunch properties are used. The kinetic energy of the electrons at CLEAR typically amounts to 200 MeV. Taking into account the rest mass of an electron, approximately 511 keV, this results in a Lorentz factor of $\gamma \approx 392.4$. The normalised velocity is then given as $\beta = \sqrt{1 - 1/\gamma^2}$. The bunch charge is set to -300 pC, a value readily achievable at CLEAR for single-bunch operation. The bunch length is defined as $\sigma_z = 5\,\text{ps}$.

As illustrated in fig. 3.4, the power spectrum of a Gaussian bunch with a standard deviation of $\sigma = 5\,\text{ps}$ extends to approximately 100 GHz, which corresponds to a

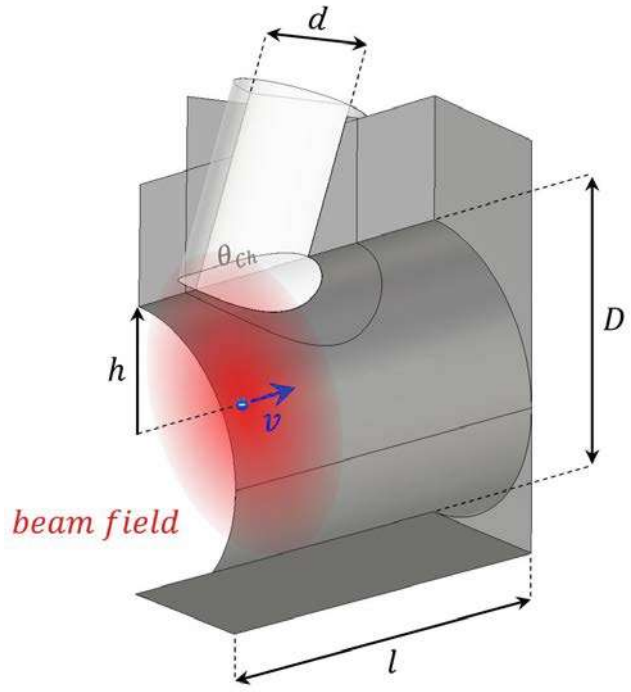

Figure 3.3: Half-plane view of the 3D model with one half of the radiator being transparent. The concave surface of the radiator exposed to the beam field is shown, with the same curvature as the vacuum chamber ($D = 80\,\text{mm}$). The distance between the electron e^- and the radiator surface is denoted as h.

wavelength in vacuum of approximately 3 mm. To sample this wavelength with sufficient resolution, the chosen meshing has a resolution of at least 10 cells per wavelength, resulting in a mesh size of 0.3 mm. The overall dimensions of the simulation setup are $80 \times 100 \times 160$ mm (width × length × height). This would lead to 0.47×10^8 mesh cells. However, given the need for a finer meshing within the dielectric material ($\varepsilon_r \approx 9.0$), the total number of mesh cells increases to 3.12×10^8. The chosen bunch length of 5 ps leans towards the longer end of the typical range of 3 to 5 ps at the CLEAR facility. It was chosen to minimise the computation time and output file sizes. Reducing the bunch length from 5 to 3 ps, the number of mesh cells would need to be at least $(3/5)^{-3} \approx 4.6$ times higher. Given that file sizes already approach approximately 150 GB for a bunch length of 5 ps, further shortening of the bunch length has been dismissed.

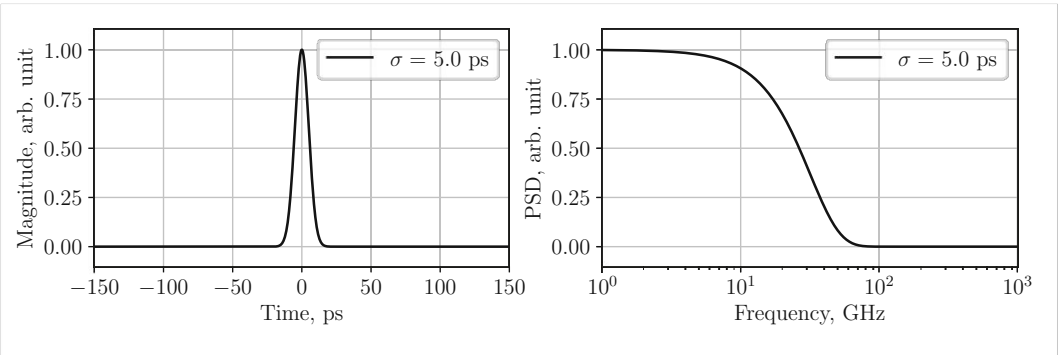

Figure 3.4: The charge distribution for a Gaussian bunch with $\sigma = 5\,\text{ps}$ is depicted on the left. On the right side, its corresponding power spectrum is presented.

Solver		Wakefield
Bandwidth		100 GHz
Cells / wavelength		10
Largest cell size		0.3 mm
Smallest cell size		0.1 mm
Bunch charge		300 pC
Bunch length	σ	5 ps
Lorentz factor	γ	392.4
Impact parameter	h	10-50 mm
Relative permittivity (Al_2O_3)	ε_r	9.0

Table 3.2: CST Particle Studio® simulation parameters.

3.4 Field in Vacuum

Before using the simulation environment to characterise ChDR, it is necessary to benchmark the calculated electromagnetic field under well-defined conditions. The electric field, expressed as a function of longitudinal position and transverse offset, has been analytically derived in equation 2.4 (see section 2.2). As the transverse electric field produced by an ultra-relativistic charge moving at the centre of a cylindrical, perfectly conducting pipe is the same as the one in free space, the geometry detailed in section 3.2 is suitable for comparing the simulated fields with the analytical formula for the transverse electric field mentioned earlier [54].

3.4.1 Comparison to Analytical Results

Utilising the results derived in section 2.2 for the transverse electric field, we assess whether the specified beam parameters would justify the estimation of the beam field in the limit case of $\gamma = \infty$. Equation 2.5 can be interpreted as an approximation for high particle energies $\gamma \to \infty$, or equivalently, as an approximation for short distances $h \to 0$. Consequently, we must evaluate the bunch parameters concerning a specific transverse distance from the beam. Throughout this study, the impact parameters are consistently in the order of several cm, which we consider as a reference.

In fig. 2.3, the transverse electric field is depicted for various impact parameters ranging from 10 to 100 mm at $\gamma = 392.4$. The dotted line in the figure represents the case of $\gamma = \infty$ for each impact parameter. On the right-hand side of fig. 2.3, the peak electric field strength for $\gamma = 392.4$ is plotted relative to that for $\gamma = \infty$. At a transverse distance of 40 mm from the beam, the deviation from the ultra-relativistic case is less than 1%. Hence, we are typically close enough to justify the approximation $\gamma = \infty$. According to equation 2.5, the electric field distribution is then a replica of the bunch charge distribution S_z.

In fig. 3.5 the results obtained from the CST simulation are plotted against the analytical expectation using equation 2.4 from section 2.2 assuming $\gamma = 392.4$. The deviations from the analytical expectations are minimal, prompting a closer examination of the differences in the peak electric field strength. On the right-hand side of fig. 3.5 the blue curve corresponds to $\gamma = 392.4$ for the analytical expectation. Notably, the blue curve slightly exceeds 100%, indicating that CST tends to overestimate the peak electric field strength. The black curve compares the CST results to the analytical expectation for $\gamma = \infty$. In this scenario, CST slightly underestimates the peak electric field strength. However, it has been demonstrated that the employed meshing considering frequencies up to 100 GHz, the deviation from CST simulations typically remains below 0.5% compared to analytical values.

3.5 Propagation at the Cherenkov Angle

A Gaussian bunch ($\sigma = 5\,\text{ps}, Q = 300\,\text{pC}, \gamma = 392.4$) propagates through the structure as outlined in section 3.2. The temporal evolution of the electric fields is depicted in fig. 3.6 at various points in time. Notably, the generation of ChDR at the surface of the dielectric and its propagation within the radiator at the Cherenkov angle θ_{Ch} is clearly apparent. The beam's electric field is saturated within the presented scale, which is optimised for ChDR in the order of 10 kV/m. Additionally, the generation of diffraction radiation (DR) at the location of edges in the structure is prominently visible. A considerable portion of DR also propagates

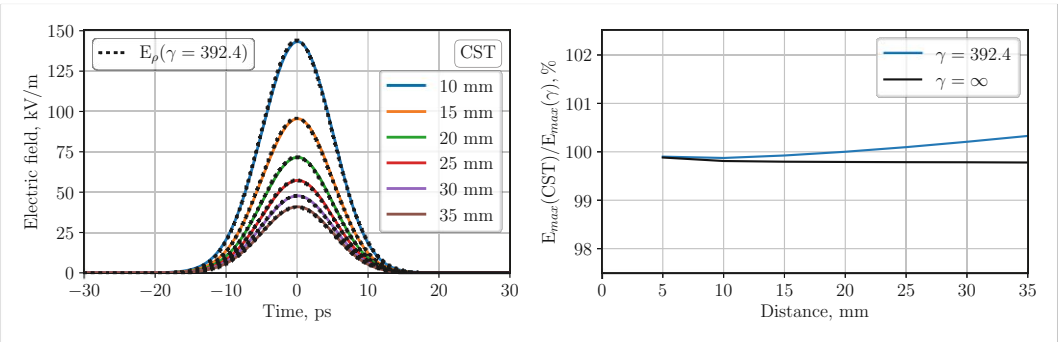

Figure 3.5: On the left, the transverse electric field of a particle bunch is given for different transverse distances. The coloured lines are simulated for a 5 ps bunch ($1\,\sigma$), a charge of 300 pC and $\gamma = 392.4$. The dotted line represents $\gamma = 392.4$ for each distance. On the right, the peak electric field strength from the simulation is compared to the analytical expectation for $\gamma = 392.4$ and $\gamma = \infty$.

within the radiator behind the ChDR, as illustrated in the time frame at 480 ps. The propagation velocity is slowed down within the radiator due to its refractive index $n = 3.0$. This view of the electric field's propagation is beneficial to show the propagation angle. However, it simplifies the problem to a 2D plane. As ChDR is produced on the whole surface exposed to the beam field, conducting a thorough investigation of the whole 3D structure is essential, rather than confining the analysis to a 2D plane within the structure.

3.6 3D Propagation within the Radiator

The electric fields resulting from DR at the time frame 230 ps in fig. 3.6 show that DR is generated at the first metal-radiator interface the beam field is exposed to. The circular wavefront expansion from this point source is clearly evident. However, the generation mechanism of the DR shown in time frame 480 ps is less apparent. To better understand this DR contribution, a closer examination of the 3D structure of the radiator proves beneficial. In fig. 3.7, both a longitudinal and a transverse cut through the radiator are presented.

The longitudinal cut provides a detailed view of the previous time frame at 480 ps, showing that DR is emitted from the two metal radiator edges on that plane (indicated by red points). However, this does not properly reflect the total generation, as DR is emitted from all points where the inner surface of the vacuum chamber exhibits a refractive index discontinuity. This is clearly visible in the transverse plane, cut normal to the Cherenkov angle $[0, -cos(\theta_{Ch}), sin(\theta_{Ch})]$. The two edges

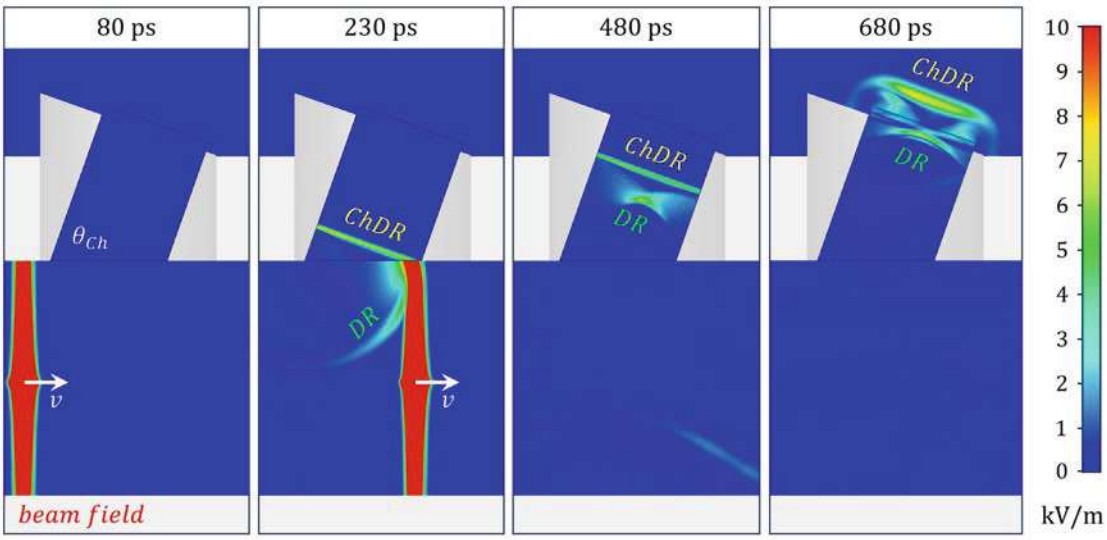

Figure 3.6: A Gaussian bunch ($\sigma = 5\,\text{ps}, Q = 300\,\text{pC}, \gamma = 392.4$) propagates through the predefined structure from left to right. Four different time frames are displayed. The mechanism of ChDR production is visible (230 ps) as well as diffraction radiation (DR) later in time (480 ps). The ChDR wavefront is also clearly visible after being refracted from the radiator (680 ps).

(indicated by orange points) radially emit DR, emphasised by the two white dashed lines. The contribution from DR in the transverse direction is more prominent than that from the longitudinal direction.

Furthermore, a closer examination of the two cuts through the radiator provides a clear understanding of the shape of the emitted ChDR wavefront. In the longitudinal view at the top right in fig. 3.7, the ChDR wavefront appears straight, aligning with the straight surface of the radiator in this longitudinal cut (indicated by the red line). In the transverse view at the bottom right in fig. 3.7, the ChDR wavefront is curved, corresponding to the curved surface of the radiator in the transverse cut (depicted by the orange line). Notably, the curved wavefront adheres to the symmetry of the generation of ChR, representing a segment of the Cherenkov cone, as indicated by the black dashed line.

It is essential to note that in an optimal ChDR radiator design, the contribution from DR would be minimised. Nevertheless, the design presented follows the approach of creating a radiator with a simplified geometry to facilitate mechanical production. Additionally, the different polarisation properties of the two types of radiation (ChDR and DR) facilitate their distinction, as demonstrated in section 3.8.

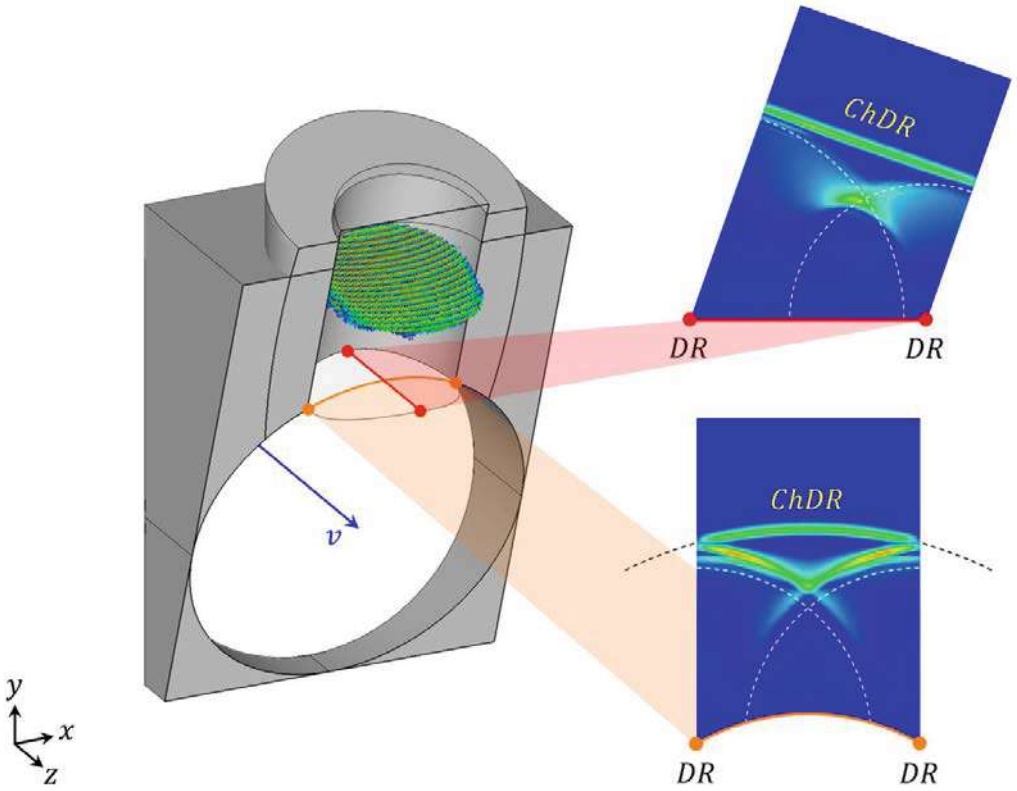

Figure 3.7: 3D distribution of the electric field within the radiator at the time frame of 480 ps. The longitudinal cut through the radiator is displayed in the top right, while the transverse cut at the Cherenkov angle is shown in the bottom right. The metal radiator edges are highlighted by red and orange points, representing only four distinct points of the radiator edge exposed to the beam field.

3.7 2D Field Distribution

The design of the radiator is such that the electromagnetic field needs to be measured after it has been refracted from the radiator. Consequently, our interest lies in understanding how the radiation traverses through the radiator and refracts out at its exit surface. In fig. 3.8 the electric field is depicted at a distance of 10 mm from the radiator exit. The 2D plane is oriented at the Cherenkov angle and is, therefore, co-planar with the radiator exit surface. In the first time frame, the peak of the ChDR pulse is shown and exhibits an even distribution over a large portion of the surface area. After 5 ps, the fields no longer exhibit a uniform distribution, given the curved nature of the ChDR wavefront, as illustrated in fig. 3.7. When integrating the ChDR signal over a 2D surface, this wavefront curvature broadens

the ChDR pulse in time. In section 3.9, where the temporal characteristics of the fields are discussed, this behaviour is presented in more detail. The third time frame in fig. 3.8 presents a segment of DR occurring 42 ps after the peak of ChDR. The different contributions from DR at the radiator edge exposed to the beam field constructively interfere at the centre of the radiator.

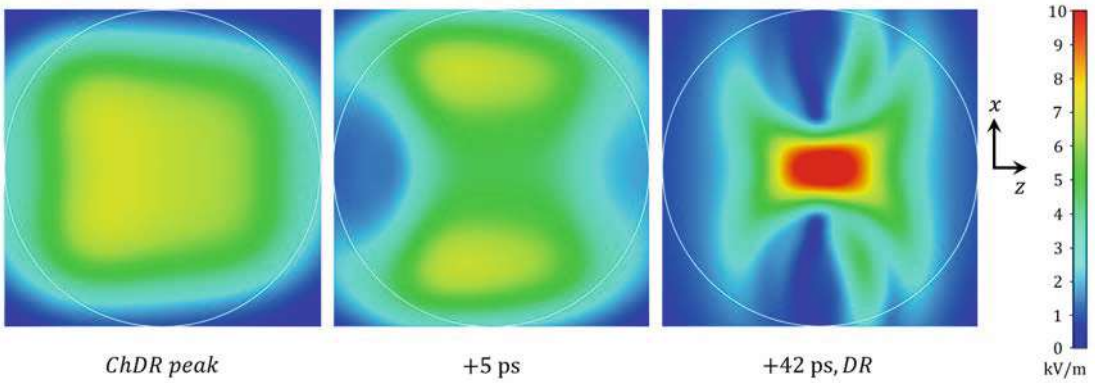

Figure 3.8: 2D distribution of the electric field 10 mm outside the radiator (cf. A_3 in fig. 3.11). The beam is travelling from left to right. The first frame shows the peak of the ChDR pulse. 5 ps later, the ChDR pulse intensity is higher on the sides due to the curved nature of the wavefront. 42 ps after the ChDR, a snapshot of DR is shown, with the constructive interference in the centre of the radiator being visible.

3.8 Polarisation

For the particle bunch travelling in the z-direction and the radiator mounted in the y-direction (cf. fig. 3.7), the polarisation of the beam's electric field is approximately $(x, y, z) = (0, -1, 0)$ in close proximity to the radiator surface. This approximation improves as we approach the yz-plane due to the radial symmetry of the beam field. The polarisation of ChDR within the radiator stems from the polarisation of the beam's electric field and is angled according to the Cherenkov angle. The polarisation vectors 10 mm outside of the radiator exit surface are illustrated in fig. 3.9. For ChDR, the electric field vectors are oriented in the same direction, specifically $\vec{e}_{Ch}$=$[0, -cos(\theta_{Ch}), sin(\theta_{Ch})]$. In the case of DR, the polarisation is not as uniformly aligned as it originates from the interference of various different sources. Notably, it is predominantly oriented in the opposite direction compared to ChDR, namely $[0, cos(\theta_{Ch}), -sin(\theta_{Ch})]$. The qualitative representation of these diverse polarisations will be investigated in more detail by examining the time traces of the electric fields.

In fig. 3.10, the electric fields from the 2D distributions are presented at various points in time. The blue curve represents the average electric field amplitude. The orange curve denotes the absolute value of the average electric field vector. Both curves are normalised for the surface area A. The blue curve is expected to exhibit a higher amplitude, as the orange curve cancels out all contributions which are directed in opposite directions. This discrepancy is primarily attributed to polarisation components in the x direction, given that the yz-plane is a symmetry plane of the simulation setup. Consequently, the difference between the two curves indicates the degree of polarisation across the entire surface area.

As shown in fig. 3.10, the difference between the blue and orange curves is negligible for the ChDR pulse. This observation aligns with the qualitative finding from fig. 3.9 that ChDR is highly linearly polarised across the entire area. Conversely, the situation differs for DR, which exhibits substantial contributions from electric fields in the x direction. This indicates varied orientations of polarisation distributed across the entire area, as illustrated in fig. 3.9.

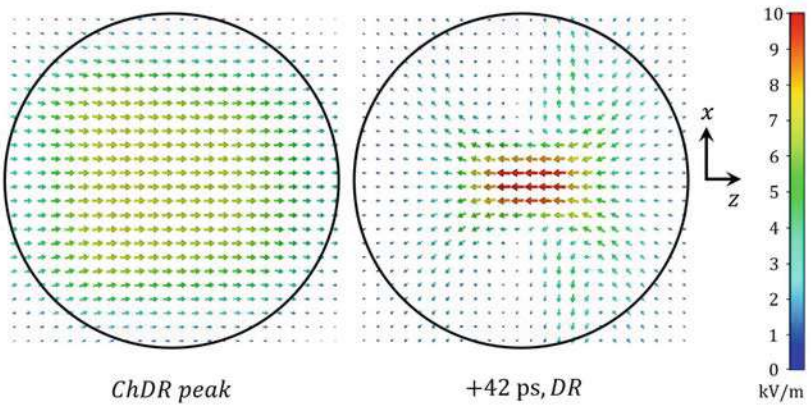

Figure 3.9: 2D distribution of the electric field vectors 10 mm outside the radiator (cf. A_3 in fig. 3.11). The beam is travelling from left to right. On the left, the peak of the ChDR pulse is shown with the electric field mainly oriented at $\vec{e}_{Ch}$=$[0, -cos(\theta_{Ch}), sin(\theta_{Ch})]$. A fraction of the DR signal 42 ps after the ChDR shows predominantly an opposite polarisation.

3.9 Time Domain

To gain a comprehensive understanding of the temporal structure of the ChDR pulse as it propagates within and is emitted from the radiator, time signals are sampled at various locations within the 3D structure. An overview of these different locations is presented in fig. 3.11. The electric field is sampled at distinct single

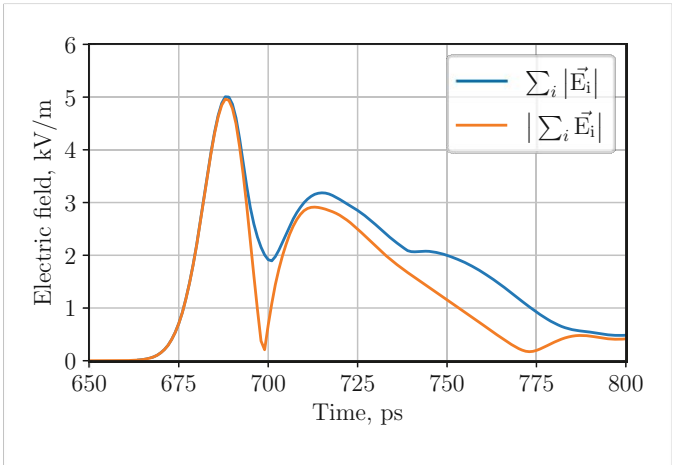

Figure 3.10: For the area in fig. 3.9, these two curves depict the electric field for two cases. The average amplitude of the electric field is shown in blue. The absolute value of the average electric field vector is presented in orange. For the ChDR pulse at 687 ps, the difference is negligible, indicating that it is highly linearly polarised across the entire area.

points denoted P_1 to P_4 and within four areas denoted A_1 to A_4, each with a diameter of 36 mm. The areas are positioned at the Cherenkov angle, parallel to the Cherenkov wavefront.

In fig. 3.11, the vector $\vec{e}_{Ch}$=$[0, -cos(\theta_{Ch}), sin(\theta_{Ch})]$ is depicted in blue, representing the predominant orientation of the electric field vectors of ChR, as identified in section 3.8. Points and areas labelled 1 and 2 are situated within the radiator, whereas points and areas labelled 3 and 4 are positioned after the exit surface of the radiator in a vacuum. Notably, area A_3 corresponds to the location of the 2D plots shown in sections 3.7 and 3.8.

3.9.1 Electric Field Amplitude

Point Sampling

In the initial analysis, we focus on the electric field amplitude at various locations. In fig. 3.12 the electric field amplitude is plotted for the four points P_1 to P_4, whereas P_1 and P_2 are placed within the dielectric with $\varepsilon_r = 9.0$ and P_3 and P_4 are placed in vacuum. The first pulse in each trace corresponds to the ChDR pulse, and each ChDR pulse is highlighted for clarity. While the ChDR pulse maintains its Gaussian shape throughout propagation, the electric fields from DR, occurring after the ChDR pulse, constantly change shape. This transformation results from the interference of field contributions from various edges. This interference is most

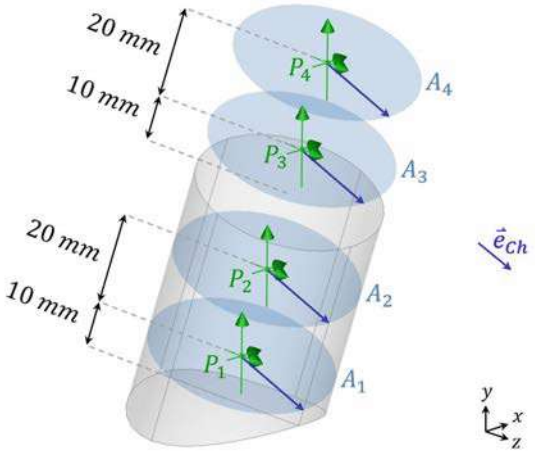

Figure 3.11: Overview of the location of probes (P_1 to P_4) and areas (A_1 to A_4) where the electric field is sampled in time. The surfaces are aligned to the Cherenkov angle. The vector $\vec{e}_{Ch}$=$[0, -cos(\theta_{Ch}), sin(\theta_{Ch})]$ denotes the prominent polarisation orientation of ChDR (cf. fig. 3.9).

prominent in the centre of the radiator, as shown in fig. 3.9. With the probes located in the radiator's centre, this effect is particularly evident when comparing the blue and orange curves. The blue curve is sampled at a location where the fields from DR do not yet interfere. The distances $|\overrightarrow{P_1P_2}|$ and $|\overrightarrow{P_3P_4}|$ are 20 mm each. The green and red peaks (P_3 and P_4) from ChDR are separated by 67 ps, while the propagation within the radiator is slowed down by $n = 3$ to a total of 201 ps between the blue and orange peaks (P_1 and P_2) from ChDR.

Area Sampling

In fig. 3.13 the average electric field amplitude is depicted for four areas A_1 to A_4, whereas A_1 and A_2 are situated within the dielectric and A_3 and A_4 are placed in vacuum. The three components must be calculated within a volume enclosing the area of interest to compute the electric field amplitude. Storing the vector field of a densely meshed volume for numerous points in time is memory intensive. Consequently, the areas of interest were confined to the diameter of the radiator and the fields were sampled for a maximum time of 200 ps with a temporal resolution of 1 ps. The three different field components were then integrated over the respective surface for each point in time. The obtained results are normalised to the surface area, providing an average electric field amplitude for each area.

This average indicates that the ChDR is evenly distributed over the different areas,

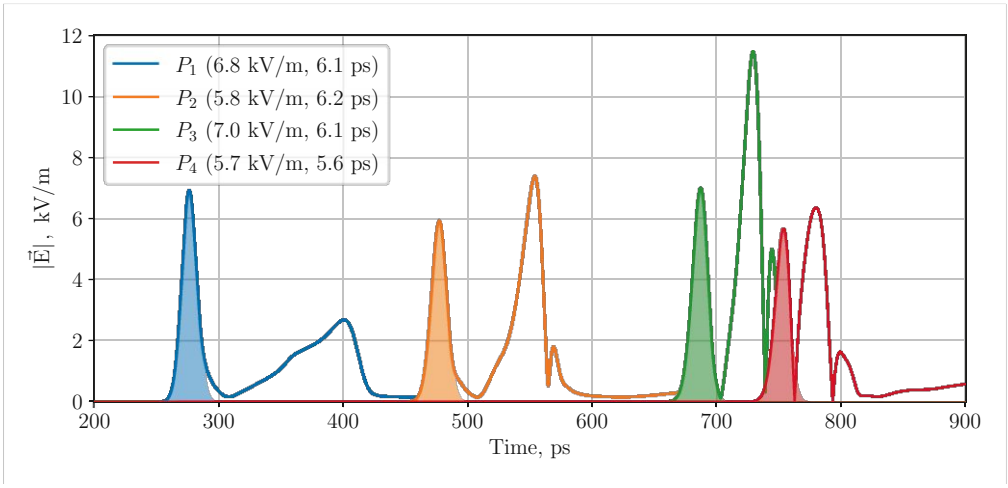

Figure 3.12: The electric field amplitude sampled at point probes P_1 to P_4. The ChDR pulse is fitted with a Gaussian function for every trace. The peak electric field strength and the standard deviation of the Gaussian function are provided in parentheses.

maintaining a Gaussian shape. In contrast, the contributions from DR average out over the different areas and become smaller in amplitude than ChDR at each given location. Nonetheless, the peak electric field strength of ChDR decreases by approximately 30% when averaged over the surface. This reduction is attributed to the fact that ChDR is less pronounced close to the borders of the radiator (cf. fig. 3.9) and due to the curved nature of the ChDR wavefront, which elongates the ChDR signal in time when integrated over a surface.

3.9.2 Parallel Electric Field Component

Point Sampling

The measurement devices utilised in this work are sensitive to one component of the electric field vector rather than the electric field amplitude. In section 3.8, the vector $\vec{e}_{Ch} = [0, -cos(\theta_{Ch}), sin(\theta_{Ch})]$ was identified as denoting the predominant orientation of the electric field of ChDR. This direction corresponds to where the electric field of ChDR is the strongest and is the preferred orientation for measurements. To facilitate a comparison between experimental data and simulations, we therefore focus on the electric field component parallel to this vector $\vec{e}_{Ch}$.

In fig. 3.14, the product of the electric field vector and the vector $\vec{e}_{Ch}$ is depicted for the same points P_1 to P_4 as in fig. 3.12. These time traces represent what one would expect when sampling the electric field with a device sensitive to the

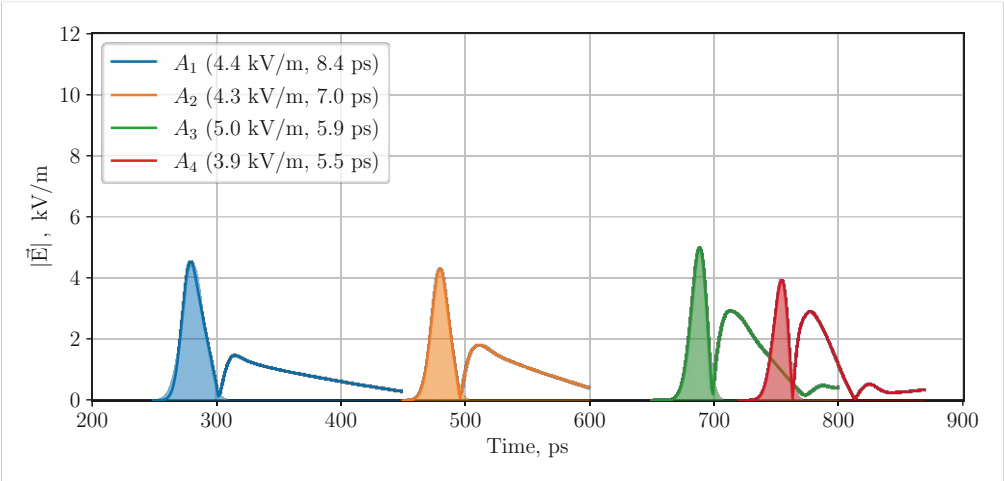

Figure 3.13: The average electric field amplitude is sampled at areas A_1 to A_4. The ChDR pulse is fitted with a Gaussian function for every trace. The peak electric field strength and the standard deviation of the Gaussian function are provided in parentheses.

orientation of the electric field vector in different locations. Comparing this plot to the results obtained in fig. 3.12, two key characteristics emerge. The amplitudes of the ChDR pulse at the various locations in fig. 3.12 match with the amplitudes of the polarisation-dependent amplitudes of the ChDR pulse at the various locations in fig. 3.14. This indicates that the electric field vector is highly aligned with the vector $\vec{e}_{Ch}$. Secondly, the electric field vectors of ChDR and DR are indeed directed in opposite directions, as demonstrated in fig. 3.9. When measuring the electric field of ChDR, this difference in the behaviour of the electric field vector provides a straightforward means of distinguishing the ChDR signal from the DR signal.

Area Sampling

In fig. 3.15, the product of the average electric field vector and the vector $\vec{e}_{Ch}$ is depicted for the same areas A_1 to A_4 as in fig. 3.13. It is important to note that the amplitudes of the ChDR pulse at the various locations in fig. 3.13 match with the amplitudes of the polarisation-dependent amplitudes of the ChDR pulse at the various locations in fig. 3.15. This indicates that the electric field is predominantly oriented in the direction of the vector $\vec{e}_{Ch}$. When comparing fig. 3.15 with fig. 3.14, it becomes evident that the ChDR pulse maintains its pulse-like shape even when averaged over the area, whereas the DR appearing afterwards averages out and is smaller in amplitude than the ChDR pulse.

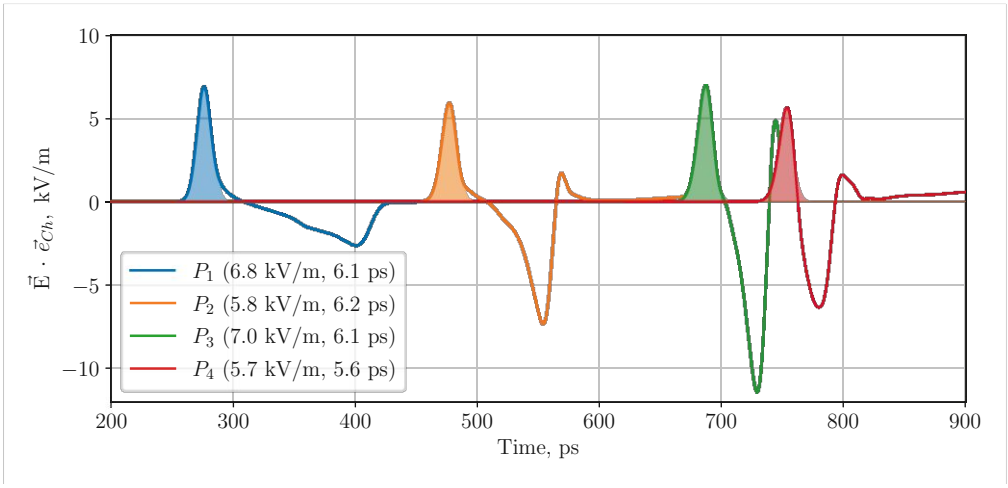

Figure 3.14: The electric field parallel to the field of ChDR ($\vec{e}_{Ch}$) is sampled at point probes P_1 to P_4. The ChDR pulse is fitted with a Gaussian function for every trace. The peak electric field strength and the standard deviation of the Gaussian function are provided in parentheses.

3.10 Frequency Domain

3.10.1 Cutoff Frequency

With the radiator being surrounded by a conductive material on its lateral surface, it can be regarded as a dielectric-loaded waveguide [77]. The cutoff frequency for transverse electrical modes of a circular waveguide is given as [52]:

$$f_{m,n} = \frac{v}{2\pi r} x_{m,n} \tag{3.4}$$

with the velocity $v = c/n = c/\sqrt{\varepsilon_r \mu_r}$ of the wave travelling in the medium filling the waveguide, the radius r of the waveguide and with $x_{m,n}$ being the n-th root of the Bessel function derivative $J'_m(x) = 0$. For the dominant TE_{11} mode we obtain the cutoff frequency:

$$f_{11} \approx \frac{v}{2\pi r}\, 1.841$$

Calculating the cutoff frequency for the given parameters $\varepsilon_r = 9.0$, $\mu_r = 1.0$ and $r = 18\,\mathrm{mm}$ we obtain a value $f_{11} = 1.63\,\mathrm{GHz}$. In fig. 3.16, the power spectrum of the electric field is plotted for two different probing locations. The blue curve represents the electric field at the location 10 mm before the radiator. In the logarithmic scale, the field's gradual decline is already noticeable at higher frequencies, a behaviour

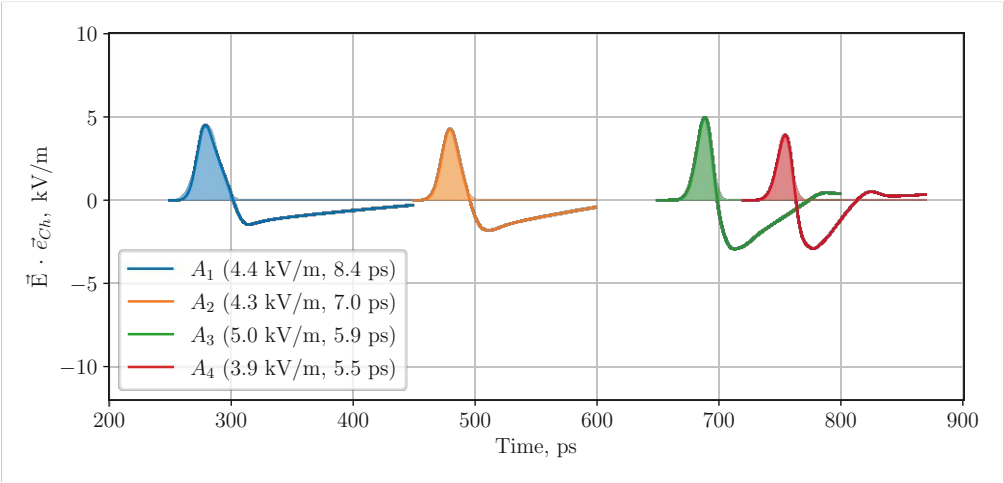

Figure 3.15: The average electric field parallel to the field of ChDR ($\vec{e}_{Ch}$) is sampled at areas A_1 to A_4. The ChDR pulse is fitted with a Gaussian function for every trace. The peak electric field strength and the standard deviation of the Gaussian function are provided in parentheses.

stemming from the coherency of the Gaussian particle distribution. The grey curve corresponds to the electric field at the location 10 mm after the radiator, denoted as P_3 in previous sections (cf. fig. 3.11). The dashed blue line represents to the previously calculated cutoff frequency for the dominant TE_{11} mode. The electric fields after the radiator are subject to this cutoff frequency. However, the cutoff is indistinct as equation 3.4 assumes a circular waveguide of infinite length. The radiator is, however, only about 32% longer than its width. Moreover, only a short time trace was used to avoid considering any reflections.

3.10.2 Reflections

Until now, we have only examined time signals of less than 1 ns in duration. To quantify the reflections within the radiator and comprehend their impact on the measurement, it is necessary to extend the time window of simulations. However, this is not easily feasible for areas as this would require several terabytes of memory. Therefore, only the signal behaviour for point probes is presented. In fig. 3.17, the electric field component parallel to the vector $\vec{e}_{Ch}$ is plotted for the probe location P_3. In the time domain, some ripples are visible even after 10 ns. These contributions within the radiator must be considered for bunches with a time spacing in the tens of nanoseconds.

We perform a Fourier transformation on the data to investigate the power spectrum of this time domain signal. Since the time trace is much longer, the Fourier

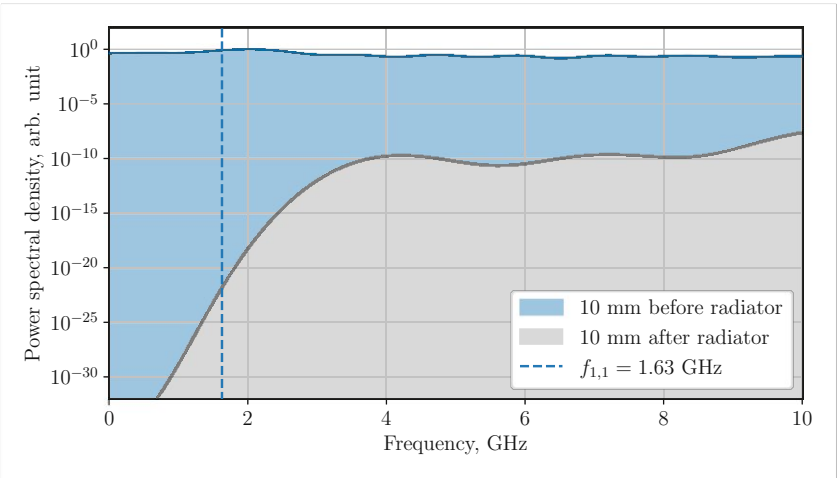

Figure 3.16: Power spectrum of the electric field at two different probing locations. The black curve corresponds to the electric field at the centre location 10 mm before the radiator, and the blue curve to the electric field at the centre location 10 mm after the radiator. The transmission through the radiator is affected by the cutoff frequency of the TE_{11} mode at $f_{11} = 1.63$ GHz.

transform's resolution improves accordingly. Therefore, the grey curve in fig. 3.18 has a much higher resolution than the grey curve shown in fig. 3.16. Comparing these two grey curves, the most notable change is the appearance of some resonant frequencies, which stem from the multiple reflections within the radiator. These resonances are not present in fig. 3.16 as the time traces are not long enough to take them into consideration. The three strongest resonant peaks appear at the frequencies 1.75 GHz, 2.15 GHz and 2.76 GHz. Also, the cutoff frequency at 1.63 GHz is evident in this plot. In table 3.3, these notable frequencies and their corresponding wavelengths are provided. The strongest frequency corresponds to a wavelength of 46.5 mm in the radiator, with the central axis length of the radiator being 47.6 mm. The second strongest frequency corresponds to a wavelength of 36.2 mm, with the diameter of the radiator being 36.0 mm. The third strongest frequency corresponds to 57.1 mm, with the average diagonal dimension of the radiator being approximately 59.7 mm.

3.11 Impact Parameter

The impact parameter refers to the distance between the inner surface of the radiator and the beam and is denoted h in this work, as introduced in fig. 3.2 and 3.3. Since the shape and material of the radiator cannot be adjusted during experiments, the

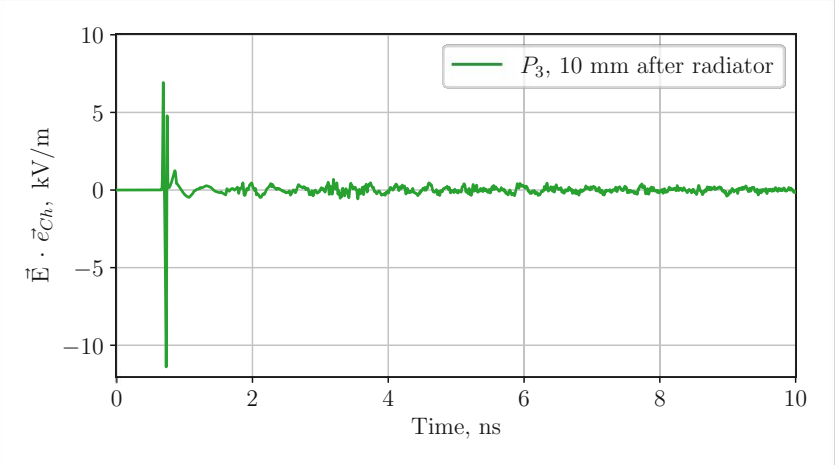

Figure 3.17: The electric field parallel to ChDR is illustrated at a distance of 10 mm from the radiator surface, corresponding to point P_3 as indicated in fig. 3.11. Even after 10 ns, some ripples are noticeable in the time signal. It is important to note that this plot covers a time span roughly ten times longer than the ones previously displayed.

f, GHz	$\lambda(\varepsilon_\mathbf{r} = \mathbf{1})$**, mm**	$\lambda(\varepsilon_\mathbf{r} = \mathbf{9})$**, mm**
1.63	183.9	61.3
1.75	171.3	57.1
2.15	139.4	46.5
2.76	108.6	36.2

Table 3.3: Notable frequencies of the radiator signal and their corresponding wavelengths in vacuum, as well as, alumina with $\varepsilon_r = 9$.

impact parameter becomes the sole variable for modifying the ChDR signal without altering any beam parameters. This ensures stable measurement conditions and makes the variation of the impact parameter a suitable method for characterising the ChDR signal originating from the radiator.

In fig. 3.19, the peak electric field strength of the ChDR signal is plotted as a function of the impact parameter. The electric field is sampled at probe location P_3. The impact parameter in all the previous figures was $h = 40$ mm, where a peak electric field strength of 7.0 kV/m was obtained (cf. fig. 3.14). By decreasing the distance between the beam and the radiator surface to 10 mm, the obtained ChDR signal reaches electric field strengths above 40 kV/m. The beam field decreases proportionally to $1/r$, with r being the radial distance from the beam. The blue fitting function compares the obtained results to this $1/r = 1/h$ behaviour.

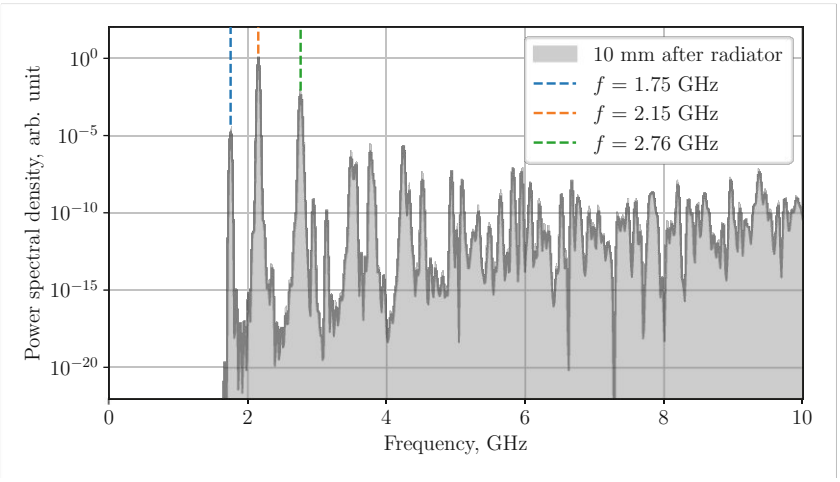

Figure 3.18: Power spectrum of the electric field component parallel to $\vec{e}_{Ch}$ at a distance of 10 mm from the radiator surface, corresponding to point P_3 as indicated in fig. 3.11. The spectrum is normalised to its maximum value at $f = 2.15$ GHz, and dashed lines are used to highlight the three most prominent resonant frequencies. Also note the low cutoff frequency, as previously illustrated in fig. 3.16.

This is a coarse estimation only, stemming from the fact that the beam field at the location exposed to the radiator surface produces the ChDR signal. The underestimation might come from the fact that the particle bunch does break the symmetry of the vacuum chamber once it is displaced. This will influence the electric field lines accordingly. Also, the presence of the radiator itself might lead to a distortion of the electric field lines. The actual reason is unknown, and why the simulation environment seems to underestimate the peak electric field strength still requires some further studies.

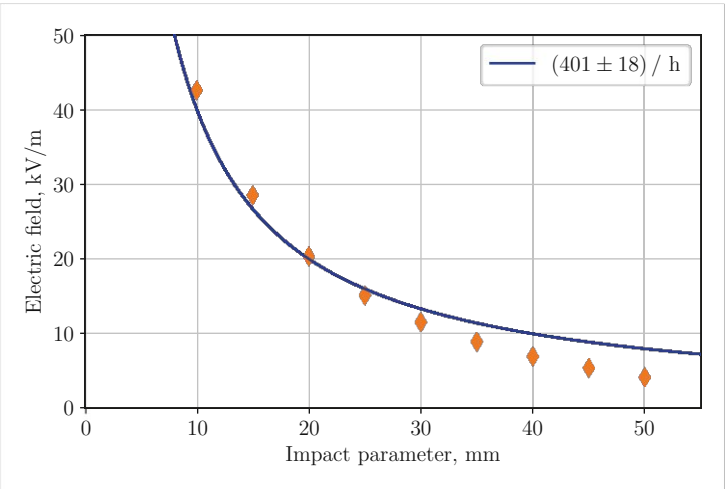

Figure 3.19: Peak electric field strength of ChDR as a function of the impact parameter. The electric field is sampled at a distance of 10 mm from the radiator surface, corresponding to point P_3 as indicated in fig. 3.11. A 1/h behaviour would be expected for a decreasing beam field (cf. equation 2.5).

3.12 Findings from Numerical Simulations

The numerical simulations of a realistic experimental configuration elucidate various key results:

- ChDR and DR coexist due to the limited radiator surface.
- ChDR and DR differ in their time structure, with ChDR exiting the radiator first.
- The wavefront of ChDR is preserved, and ChDR is highly linearly polarised.
- The wavefront of DR continuously changes as it interferes with itself. DR is not linearly polarised and predominantly exhibits the opposite polarity of ChDR.

With a radiator surface, which is limited in size, there will always be contributions from DR. However, two main differences allow us to distinguish both from each other in an experimental campaign: their difference in arrival time and their opposite polarity.

4

Experimental Methods

This chapter introduces the accelerator facility and the beam parameters used for the experiments with particle beams. It also shows the mechanical design of the ChDR radiator and its integration into the accelerator complex. The larger part of this chapter discusses the two different electro-optical detection techniques used. The first system is based on an electro-optical crystal directly exposed to electromagnetic fields and read out using a continuous wave laser. The second system uses an electro-optical Mach-Zehnder interferometer and a spectral decoding scheme utilising chirped laser pulses.

4.1 CLEAR Facility

This work's experiments with particle beams were conducted at the CERN Linear Electron Accelerator for Research (CLEAR). The CLEAR facility [81] was established after the successful completion of the experiments in the CLIC Test Facility (CTF3), which tested the feasibility of the central concepts of the Compact Linear Collider (CLIC). The CTF3 probe beam injector, CALIFES, was proposed to be reused after the CTF3 operation ended in 2016. Originating from this proposal, the CLEAR facility was established in 2017, and CALIFES provided electron beams for this new stand-alone user facility. Amongst others, one of the aims of the CLEAR facility is to provide a test bench for beam instrumentation for the consolidation and upgrade of the CERN accelerator complex and future accelerators. Located at the Meyrin site at CERN, CLEAR provides a flexible user beamline, which can be easily adapted for different experimental needs. The layout of CLEAR is shown in fig. 4.1 and is divided into two parts. The top part in fig. 4.1 shows the gun, accelerating structures and a deflecting cavity. This part previously made up the CALIFES injector. The bottom part of fig. 4.1 shows the user beamline dedicated to several experiments. There is currently a section for diagnostic tests, the ChDR test stand and the plasma test stand, whereas these sections are constantly evolving and used to host different experimental setups. In between those sections, several diagnostic devices for beam operation, a few triplets and a dipole are installed. After the dipole, the vacuum chamber ends, and the beam exits the vacuum chamber. Here, it can be used for different experimental campaigns in the in-air test stand. Compared to the vacuum line, the in-air test stand brings the flexibility of easily installing and modifying an experimental setup, avoiding the need for vacuum-compatible installations.

4.2 Beam Parameters

An overview of the beam parameters at CLEAR is given in table 4.1. Even though the particle energy varies from 60 to 220 MeV, high energies are needed for the beam field to replicate the longitudinal bunch distribution as shown in equation 2.5. Therefore, a beam energy of around 200 MeV was targeted during experiments, corresponding to the standard beam energy at CLEAR. The single bunch charge should be as high as possible to increase the charge density and signal strength. However, the two experimental setups in this work have different requirements concerning the upper threshold of the charge. Therefore, the bunch charge had to be reduced to only a few tens of pC for the tests performed in chapter 6. The bunch length is measured using the deflecting cavity after the accelerating structures, as shown in fig. 4.1. The number of bunches per train was always reduced to a single

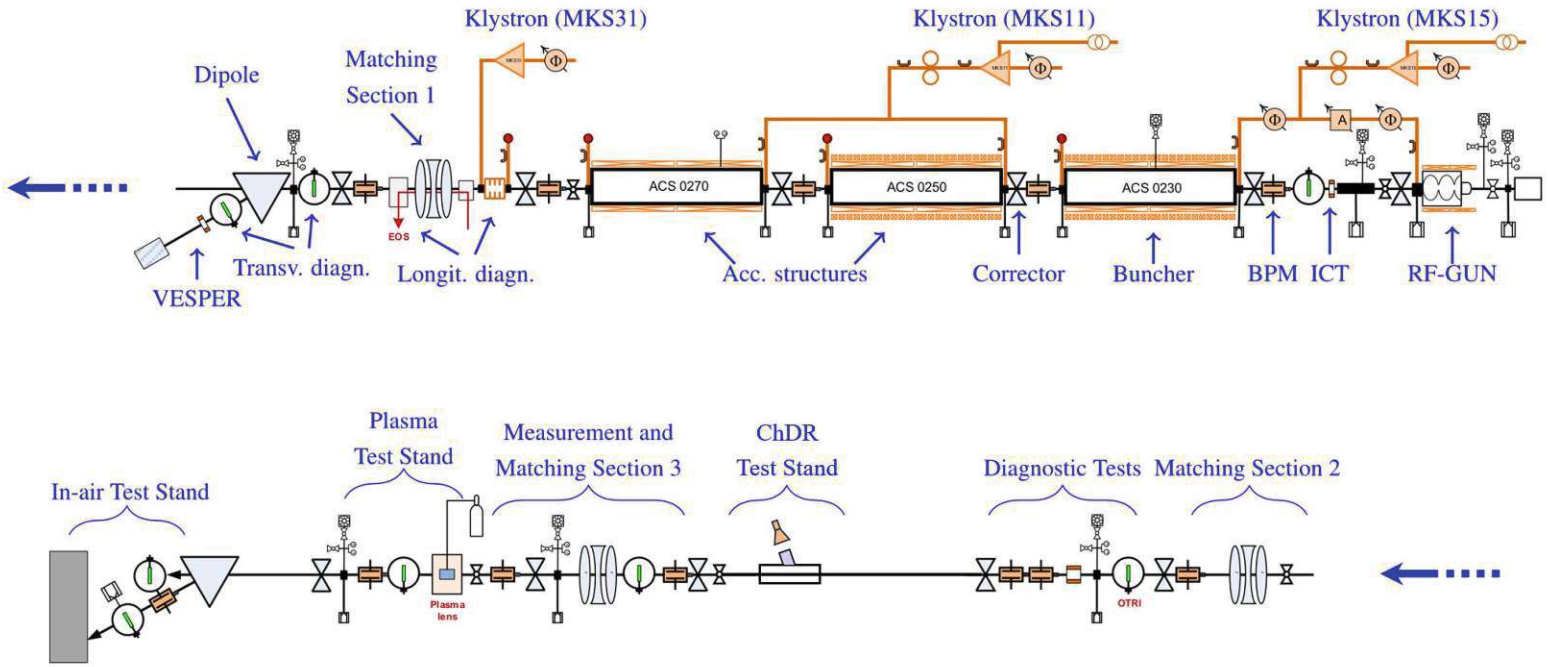

Figure 4.1: Overview of the CLEAR layout. The beam travels from right to left. On top, the electron gun and the accelerating structures are shown, and on the bottom is the user beamline. The original graph was taken from [81] and modified to represent the current layout.

bunch, as both acquisition systems in this work were optimised for measuring the single pulse response of the ChDR radiator. The repetition rate was set to 10 Hz as a standard value, which allowed for a significant decrease in the time needed for data taking. As bunch charges are low, the 10 Hz operation delivers doses comparable to the ones obtained during standard operation at 0.8 Hz. The 10 Hz operation typically requires an intervention on the CLEAR photo-injector laser to ensure its stability. It also must be noted that the standard repetition rate is 0.8 Hz, and many diagnostic devices are unavailable during 10 Hz operation. For reading the BPMs, beam TVs and bunch length measurements with the deflector, the repetition rate was decreased to 0.8 Hz.

Beam Parameter	**Range**	**Unit**
Energy	60 to 220	MeV
Bunch charge	0.01 to 1.5	nC
Bunch length	0.15 to 1.5	mm
Bunch length	0.5 to 5	ps
Energy spread rms $\Delta p/p_0$	$< 0.2\%$	
Repetition rate	0.8 to 10	Hz
Number of micro-bunches/train	1 to 150	
Intra-bunch train spacing	1.5 / 3.0	GHz
Intra-bunch train spacing	667 / 333	ps
RF frequency	3	GHz

Table 4.1: Overview of beam parameters at CLEAR [81, 82]

4.3 Cherenkov Diffraction Radiator

4.3.1 Mechanical Design

The ChDR radiator is the first prototype to study the basic properties of ChDR, focusing on the time domain signal, whereas it can not be considered to be optimised for diagnostic purposes. The mechanical design of the radiator is driven mainly by its vacuum compatibility and simplification of the essential parameters. The first restriction comes from the vacuum chamber aperture. The aperture should be of the order of the ones expected for FCC-ee. The parameters of the FCC-ee vacuum chamber are not finalised, but the diameter is expected to be around $\varnothing\,70\,\mathrm{mm}$. To make the radiator design compatible with an existing machine and hence increase the possible number of use cases of the radiator, a vacuum chamber aperture of $\varnothing\,80\,\mathrm{mm}$ was chosen, corresponding to the LHC's vacuum chamber aperture. To facilitate a versatile radiator installation, it is essential to ensure the

possibility of mounting and dismounting the radiators. The largest standard flange fitting an 80 mm chamber and leaving some margin for mechanical robustness is the DN 63 type, which has an inner diameter of ⌀ 63 mm. As the ChDR wavefront propagates at the Cherenkov angle and this propagation needs to be restricted to the dimensions of the vacuum flange, the Cherenkov angle should be reasonably high. Moreover, the dielectric material of the radiator needs to be brazed to the flange to be vacuum-tight. For this reason, a metallic coating is typically applied to the dielectric.

Requirement	**Implementation**
Large vacuum chamber aperture	⌀ 80 mm
Standard vacuum flange fitting the aperture	DN 63
Ease of radiator implementation	circular radiator cross-section
Large θ_{Ch}	high rel. permittivity
Large radiator surface	⌀ 36 mm
Vacuum tight radiator	suitable for brazing

Table 4.2: Overview of requirements on the mechanical design of the radiator.

Considering these restrictions, alumina was chosen as a dielectric material for the radiator. The properties of the alumina used to manufacture the radiator are summarised in table 4.3. Alumina is known for its high relative permittivity, and as typical for ceramics, it is hard, has a small thermal expansion coefficient and sustains high temperatures. Alumina is a dense vacuum-tight material that allows for high-temperature brazing after being metallised. For this reason, the outside at the top end of the radiator is coated with 10 to 35 μm of Molybdenum-Manganese followed by 2 to 5 μm of Nickel. The relative permittivity of alumina at 25°C is $\varepsilon_r \approx 9.0$ in the low gigahertz range. For ultra-relativistic particles, one obtains a large Cherenkov angle $\theta_{Ch} = arccos(1/\sqrt{9.02}) = 70.55°$. This high Cherenkov angle allows for maximising the radiator surface exposed to the beam while, at the same time, fitting within the given inner diameter of the flange of ⌀ 63 mm.

Figure 4.3 shows the finished assembly of one radiator. On top the radiator assembly is shown as seen from the outside. Note the copper-coloured brazing around the radiator to join it permanently with the transition piece and make the assembly vacuum-tight. On the bottom, the inside of the radiator assembly is shown. The curvature resembles the one from the vacuum chamber with a diameter of 80 mm. The half-view representations of the outside and the inside radiator assembly are shown on the right in fig. 4.3 respectively. Note the maximisation of the radiator surface exposed to the beam, while still maintaining a cylindrical

Figure 4.2: Exploding view of the radiator assembly. The design is based on a commercial DN 63 Flange, with an inner diameter of 63 mm. The cylindrical radiator is optimised for a large surface area and has a diameter of 36 mm. The radiator is coated and brazed to the transition piece.

shape of the radiator, inserting it at the Cherenkov angle and fitting it within the flange diameter restricted to 63 mm.

4.3.2 Beam Line Integration

The radiator assembly is built for a vacuum chamber diameter of 80 mm. However, the standard vacuum chamber aperture at CLEAR is only 40 mm in diameter. It is, therefore, necessary to have a transition from 40 mm to 80 mm. Moreover, characterising the behaviour of ChDR with respect to the impact parameter is the only scan where the beam properties do not need to be changed. To be able to adapt the impact parameter, the whole ChDR setup must be moveable in the transverse direction with respect to the beam trajectory. In fig. 4.4, a schematic of the ChDR section is shown. The beam enters on the top left, coming from a vacuum chamber with a diameter of 40 mm. Afterwards, there is a short transition to 60 mm, followed by a shielded bellow with the same diameter. It follows a straight section, allowing the installation of a different radiator design manufactured for a 60 mm vacuum chamber. Then, there is a short transition from 60 mm to 80 mm. Here, the main vacuum chamber of the assembly begins, and the radiator assembly can be mounted on either side of the horizontal plane. After the radiators, the

Property	Value
Chemical formula	Al_2O_3
Purity	97.6%
Colour	white
Rockwell hardness, 45N	75
Thermal expansion coefficient @ 25-200°C	6.9×10^{-6}
Maximum no-load temperature	1650°C
Coating	Mo-Mn + Ni
Relative permittivity @ 25°C	9.00 @ 1.0 GHz
	9.04 @ 8.5 GHz

Table 4.3: Properties of the alumina used to manufacture the radiator [80].

diameter decreases again to 60 mm, followed by a second shielded bellow of the same diameter. The last transition is from 60 mm down to the nominal diameter of 40 mm from the CLEAR beam line. The two bellows allow for a horizontal movement of the whole setup in between the two bellows. The shaded section in the background in fig. 4.4 illustrates this possibility of introducing a horizontal offset with respect to the beam. The total range for the horizontal offset is ±8.5 mm. For all experimental configurations, except impact scans, the ChDR setup was placed in the central position to avoid unnecessary bending of the shields in the bellows and reduce wakefields in the transitions.

4.3.3 In-air Setup

For measurements performed in the in-air test stand, the radiator assembly was just mounted on an in-air chamber with an inner diameter of 80 mm. After exiting the vacuum chamber at the end of the beamline, the beam already travels for approximately 50 cm in air until it reaches the in-air chamber. The in-air chamber has a length of 200 mm, whereas the radiator was mounted 60 mm before the end of the chamber. The in-air chamber was mounted on a translation stage, which allowed the whole chamber to be moved with respect to the beam in the transverse horizontal direction. Compared to the vacuum setup, the only advantage of the in-air setup is its larger range for a horizontal offset, as there is no restriction from any bellows. Impact parameters as small as 10 mm were investigated, corresponding to an offset of the nominal center of 30 mm.

Figure 4.3: The finished assembly of a ChDR radiator. On top, the outside of the radiator assembly is shown, with the brazing between the radiator and transition piece visible. On the bottom, the inside of the radiator assembly is shown, resembling the curved vacuum chamber aperture.

4.4 Choosing Suitable Detection Techniques

As the radiation we are interested in has a bandwidth of at least several tens of gigahertz, the acquisition system must have a bandwidth in this order of magnitude. The transmission of electrical signals of such high bandwidths is only feasible for short distances, as the high-frequency components in an RF cable attenuate substantially only after a few meters of cable. However, the signal is generated inside the accelerator hall, where radiation levels are problematic for electronic devices. To deliver the signal outside of the accelerator hall, cables of at least ten meters would be needed. The transmission line would, therefore, act as a low-pass filter, attenuating all the high-frequency components in the signal.

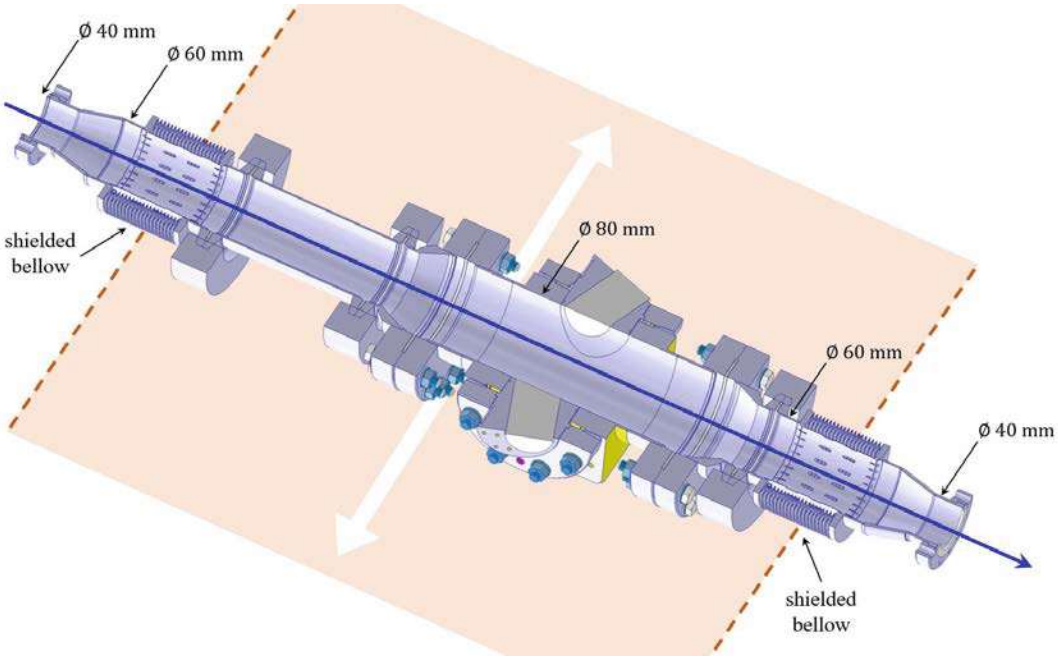

Figure 4.4: Schematic of the beamline integration of the ChDR setup into the CLEAR vacuum line. The whole setup between the two bellows can be moved in the transverse direction with respect to the beam. The total range for the horizontal offset is ±8.5 mm.

To avoid long transmission distances of RF signals, electro-optical techniques were chosen, which are based on the modulation of different laser light properties to encode the signals. The modulation of the polarisation state, as well as the modulation of the intensity, is used. The encoding occurs close to the signal source, ensuring that the high-frequency components are captured accordingly. The modulated laser light is then transmitted through optical fibres, allowing for signal transmission over longer distances. Beyond enabling the transmission of high-frequency signals over long distances, this method offers several advantages for accelerator applications. Notably, it avoids the need for electronic devices within the accelerator hall, enhancing the robustness of the setup against radiation and minimising interventions in the accelerator hall. Furthermore, the signals transmitted through the fibres are not prone to electromagnetic interference.

4.5 Electro-optical Probes

The electro-optical probe used for the experiment was of the type eoProbe^{TM} EL5 – air. It measures the electric field vector in the longitudinal direction with respect to the probe orientation. The sensing crystal is made out of BSO ($Bi_{12}SiO_{20}$) and is 5 mm long. The probe is fully dielectric, with the probe being housed in a quartz cylinder with a spherical tip. The probe is based on the Pockels effect, which describes the linear change of the refractive index of a medium when exposed to an electric field. In the BSO crystal, an external electric field introduces a birefringence. A continuous wave laser is sent through the crystal, and the laser light is exposed to the birefringence of the crystal. The laser light is experiencing a change in polarisation state as it travels through the crystal. As the polarisation state is known before entering the crystal, the changed polarisation state after travelling through the crystal carries information on the electric field strength the crystal was exposed to. By sending the laser light of altered polarisation through polarisers, the different polarisation components can be directly analysed using fast photodiodes. Electric field vectors of up to 10 MV/m can be measured using this principle. Table 4.4 summarises the probe's most important parameters. It has a broadband response with a low cutoff of 10 Hz and a high cutoff of at least 10 GHz. The rejection of orthogonal electric field components is at least 50 dB, making it very suitable for performing polarisation measurements. The damage threshold of 10 MV_{RMS}/m is much higher than the electric field strengths expected during the measurement. Even at distances to the particle beam of only 10 mm, the peak electric field strength is below 0.15 MV/m, and this field is only present for a few ps in time. Moreover, the electro-optical probes are calibrated for a known electric field and using the antenna factor, the actual electric field strength at the probe's location is calculated.

4.5.1 Electro-optical Probing Setup

The electro-optical probe was placed just at the exit of the radiator surface, as shown in fig. 4.6. The probe was mounted on several motorised stages to allow for remote manipulation of the probe location. The setup for manipulating the probe consisted of four motors. Three of the motors were used for a 3D stage, which allowed the change in the distance between the radiator exit surface and the probe itself and the manipulation of the probe in a 2D plane parallel to the radiator exit surface. The distance between the probe and the exit surface of the radiator was set to approximately 10 mm for all experiments. The motorised translation stages used to scan the exit surface had a travel range of ±25 mm [84]. Their precision in position is in the order of $\leq 10\,\mu$m, which is negligible compared to the spatial resolution of the electro-optical probe of the order of ≤ 1 mm. Moreover, the probe

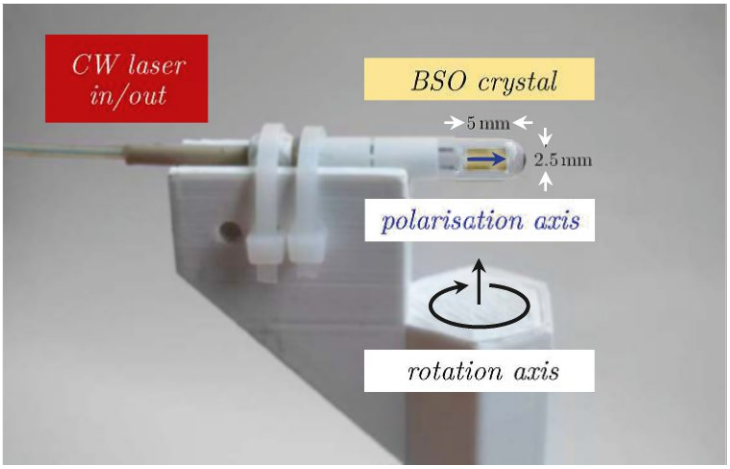

Figure 4.5: The eoProbe™ EL5-air with the 5 mm long $Bi_{12}SiO_{20}$ (*BSO*) sensing crystal visible in the transparent capsule. The polarisation axis, which determines the component of the electric field vector being sensed, is denoted with a blue arrow.

Probe Parameter	**Value**	**Unit**
Low frequency cutoff	10	Hz
High frequency cutoff	$\geq$ 10	GHz
Orthogonal electric field rejection	$\geq$ 50	dB
Damage threshold	10	MV_{RMS}/m
Antenna factor	111	dB/m
Temperature range	10 to 50	°C
Probe length	$\leq$ 36	mm
Probe diameter	5.5	mm
Active crystal length	4.8 to 5.2	mm
Active crystal diameter	$\leq$ 1	mm

Table 4.4: Characteristics of the eoProbe™ EL5-air [83].

was mounted on a rotational stage, which allowed for a rotation of 90° to measure the different polarisation components of the radiation. The fibres of the probe were connected to extension fibres of 20 m in length. This extension was needed to transmit the obtained signal from the accelerator hall. It was then measured in a radiation-protected environment close to the beam line.

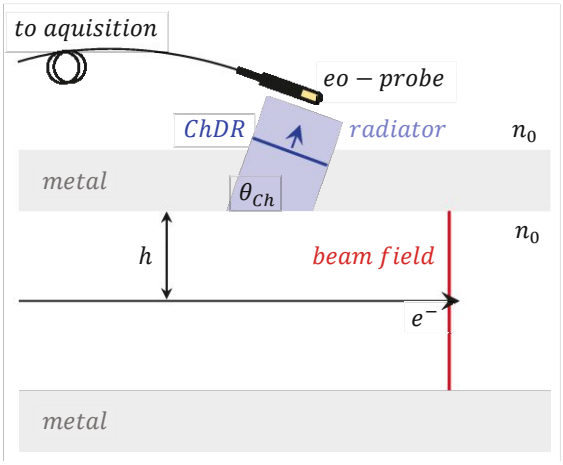

Figure 4.6: Schematic of the experimental setup with an electro-optical probe. The distance between the probe and the exit surface of the radiator is approximately 10 mm. The probe is shown in its nominal position with the sensing crystal in the centre of the radiator surface and the probe oriented parallel to the electric field vector from ChDR.

4.5.2 Data Acquisition

The signal carried by the continuous wave laser was converted to an electrical signal using fast photodiodes connected to a high-bandwidth oscilloscope. The oscilloscope was set to a high-frequency cutoff of 10 GHz to match the bandwidth of the electro-optical probe. The signal was acquired at a sampling rate of 256 GSa/s at a 10-bit resolution [85]. The measured voltage on the oscilloscope is subject to several corrections before one obtains the final signal. During the measurement, the laser system's insertion loss L_{system} was recorded with a benchtop multimeter [86] at a repetition rate of 1 Hz. The antenna factor from the calibration AF_{calib} must be normalised to the insertion loss L_{system} obtained during the measurement. The antenna factor converts the measured voltage to electric field strength, and for the antenna factor of the whole system AF_{system}, we then obtain:

$$AF_{system} = AF_{calib} \times \frac{L_{calib}}{L_{system}} \tag{4.1}$$

whereas $L_{calib} = 1.06\,\mathrm{V}$ is the insertion loss factor from the calibration. The measured voltage on the oscilloscope is then converted to the actual electric field strength at the probe's location according to

$$\vec{E}_{\parallel} = AF_{system} \times V \tag{4.2}$$

with $\vec{E}_{\parallel}$ being the electric field vector parallel to the longitudinal axis of the probe (cf. fig. 4.5) and V being the voltage recorded at the oscilloscope. If we consider a bunch of 5 ps ($1\,\sigma$), the bandwidth limitation of 10 GHz will only be able to capture a fraction of the power spectrum as already shown in fig. 3.4. The strength of the measured electric field vector will, therefore, be lower than the strength of the actual electric field vector at the probe location. We will correct this underestimation using the direct beam field to calibrate the probes for short bunches. This will be shown in detail in section 5.1.

4.6 Electro-optical Spectral Decoding with Mach-Zehnder Modulators

The electro-optical probes introduced in section 4.5 are especially suitable for measuring the electric field vector in absolute numbers. However, they have two disadvantages which we would like to overcome. The first one is their rather low sensitivity, as the small crystal only interacts with a small portion of the ChDR signal. The second disadvantage is the probe's bandwidth, which is limited to 10 GHz. An electro-optical spectral decoding setup based on an intensity modulator was developed to improve the signal strength and bandwidth.

In fig. 4.7, a schematic of the experimental setup is shown, which provides an overview of the different components of the detection line. The following sections will introduce the different parts in the order they are used. Before describing them in detail, it is beneficial to describe the main principle using this overview. A femtosecond laser provides laser pulses with a spectral bandwidth of approximately 7 nm. In the delay stage, the pulses are aligned temporally with the signal to be measured later in the detection line. They pass through a pair of gratings, where they are pre-stretched to several picoseconds. Afterwards, a Pockels cell is used as a pulse picker to select one pulse for each particle bunch. The laser pulse is then coupled into fibre and passes through a circulator to reach a chirped fibre Bragg grating (CFBG), where the pulse is stretched to several hundreds of ps. The chirped laser pulse travels in fibre to the intensity modulator. The intensity modulator is fed by the ChDR signal collected by a broadband horn antenna. The chirped laser pulse, modulated by the input signal, travels in fibre to the spectrometer. The signal is amplified and read out using an intensified camera. The profile of the image is background-subtracted to obtain the bunch profile.

4.6.1 Laser Setup

Femtosecond Laser

The pulsed laser used for the experiments is a femtosecond laser from Toptica. The characteristics of the FemtoFiber pro NIR laser are summarised in table 4.5. It is an Erbium-doped fibre laser pumped at a fundamental wavelength of 1560 nm. It utilises second-harmonic generation in a periodically poled Lithium niobate crystal to provide a wavelength of 780 nm. The average output power at 780 nm is between 140 to 200 mW. Considering the repetition rate of 75 MHz, the pulse energy should reach 1.9 to 2.7 nJ, even though during experiments, the pulse energy at the laser output was typically lower in the order of 0.9 to 1.2 nJ. The repetition rate of the laser needs to be a subharmonic of the 3 GHz radiofrequency of the

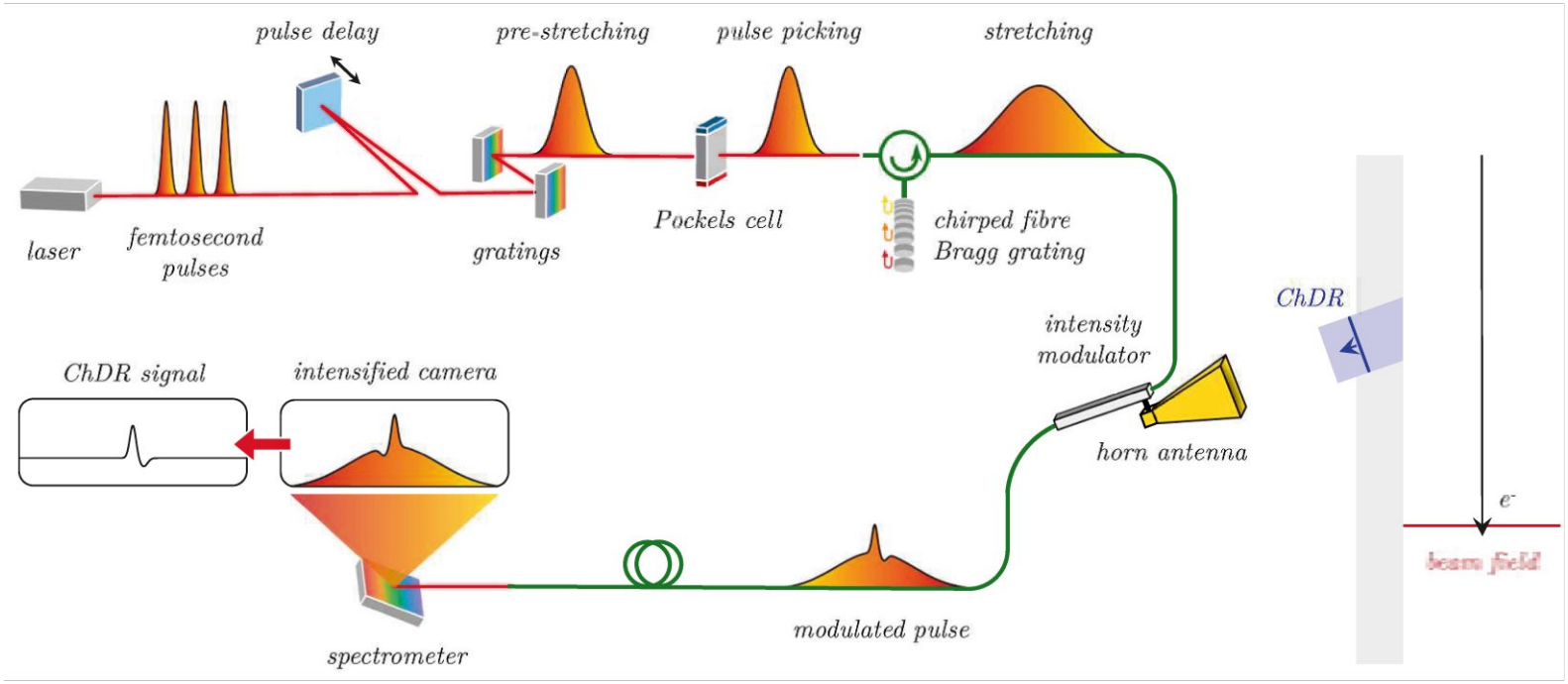

Figure 4.7: Schematic of the experimental setup based on electro-optical spectral decoding with a Mach-Zehnder intensity modulator and stretching to long laser pulses with a chirped fibre Bragg grating.

CLEAR accelerating structures. The standard repetition rate of the laser is 80 MHz. Therefore, adapting it to 75 MHz, the 40$^{\text{th}}$ subharmonic of the 3 GHz RF signal was a natural choice. The spacing between the laser pulses is then 13.3 ns, which is by a factor of 20 longer than the intra-bunch train spacing of 667 ps in the CLEAR facility. The whole EOSD detection system is, therefore, optimised for single-bunch acquisition. The laser pulses need to be temporally synchronised to the particle bunches. The synchronisation uses a laser repetition rate control (LRC) unit from Toptica. The LRC is fed by a sinusoidal 75 MHz reference signal from the CLEAR facility. The monitoring signal from the laser unit is compared to this reference signal by analysing the phase difference. A proportional-integral-derivative (PID) controller then actively changes the length of the oscillator's free-beam section, which changes the repetition rate of the laser pulses. The length of the free-beam section is set coarsely by a stepper motor, and the fine adjustments are done using a Piezo motor. Once the phase-locked loop is closed, the jitter between the pulses and beams should typically be of the order of several hundred fs. However, the locking achieved during experiments was typically around 5.0 ps (1 σ).

Laser Parameter	**Specification**	**Unit**
Laser type	Erbium-doped fibre	
Center wavelength	780	nm
Average output power	140 to 200	mW
Peak power	< 50	kW
Pulse duration	< 120	fs
Customised repetition rate	75	MHz
Pulse spacing	13.3	ns
Beam diameter	1.2	mm
Linear polarisation	$> 95\%$	

Table 4.5: Parameters of the femtosecond laser (FemtoFiber pro NIR from Toptica).

Free Space Setup

The free space setup is shown in detail in fig. 4.8 and 4.10. The laser pulses are separated by 13.3 ns (repetition rate of 75 MHz). They are sent to a delay stage with a maximum translation range of 15 cm. As the laser pulses propagate through the delay stage back and forth, the maximum change in optical path length is 30 cm, which equals a temporal delay of 1 ns. This covers the intra-bunch train spacing of the CLEAR facility of 0.667 ns, to ensure that temporal alignment is achievable. After the delay stage, the pulses are sent on a grating stretcher, passing

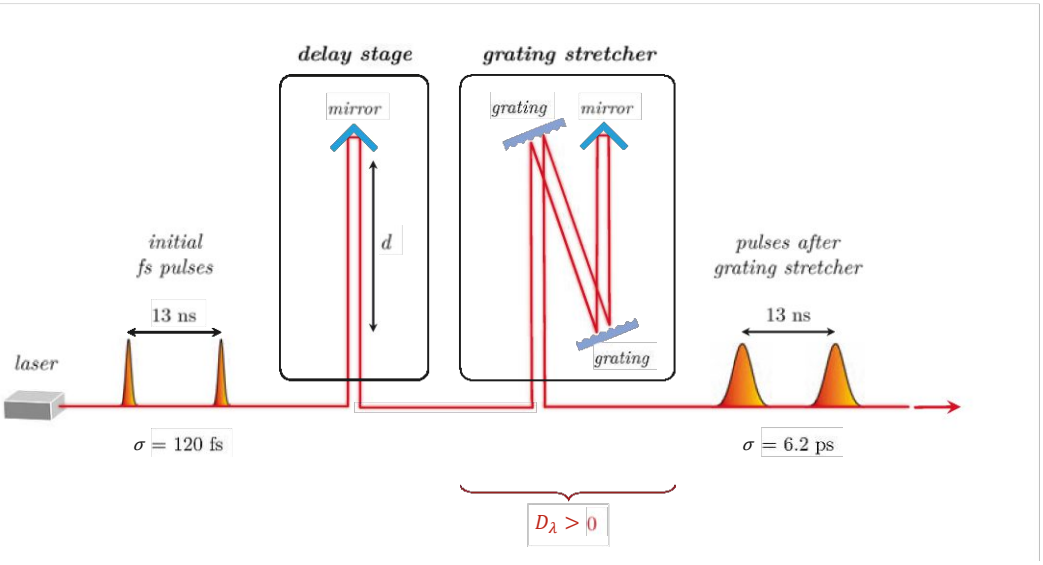

Figure 4.8: Illustration of the free space setup of the laser system. The femtosecond pulses are separated by 13 ns. They are sent via a delay stage, introducing a maximum delay of 1 ns ($d \leq 15$ cm), to the grating stretcher, where each grating is passed twice. The femtosecond pulses are stretched to pulse lengths with a standard deviation of $\sigma = 6.2$ ps.

each grating twice. Figure 4.9 shows the spectrum of the laser pulses. The spectra were measured with a commercial spectrometer [87] with a typical spectral accuracy < 0.6 nm and a resolution of 6 px/nm. The black curve shows the spectrum before the gratings, where a Gaussian fit yields a standard deviation of $\sigma = 3.0$ nm. The FWHM is, therefore, approximately 7.0 nm. The spectrum remains unchanged in the blue curve, which is measured after the pulses have passed the grating stretcher.

After the stretching to several ps, the pulses are sent to the pulse picker to reduce the repetition rate of the laser pulses. The pulse picker comprises a half-waveplate, a Pockels cell [88] and a polariser. The Pockels cell manipulates the polarisation state of the incoming laser light, effectively rotating the polarisation plane by 90°. It houses a DKDP crystal (deuterated potassium dihydrogen phosphate, KD_2PO_4), which covers a wavelength range from 300 to 1200 nm. However, the crystal and the transmission windows have an anti-reflective coating for a wavelength range of 760 to 790 nm. The halfwave voltage in AC operation is approximately 7.5 kV at 1064 nm. The extinction ratio is more than 1000:1, and the insertion loss is below 2%. The optical rise time of the crystal is below 1 ns, and the operation is therefore limited by the rise time of the high-voltage driver, which has a rise time below 3 ns. This rise time is fast enough to pick one pulse from the pulse train with a pulse separation of 13.3 ns. All the pulses are then sent to a Glan-Taylor calcite

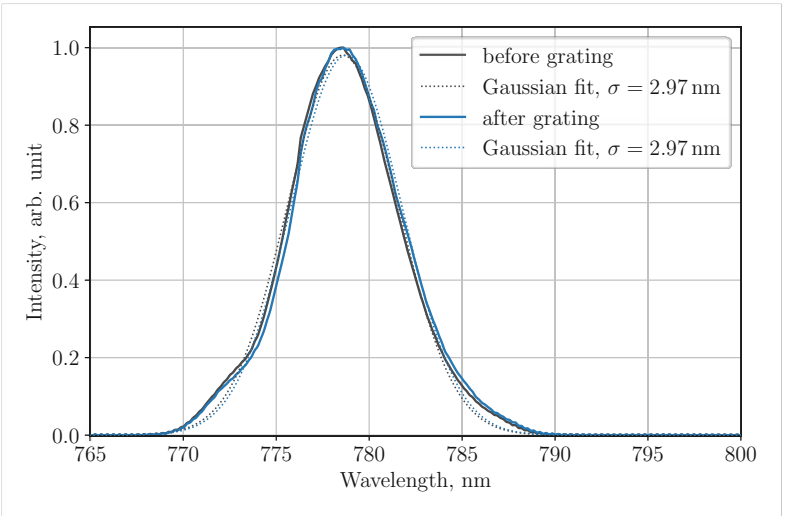

Figure 4.9: The black curve shows the laser spectrum before entering the grating stretcher. The blue curve shows the spectrum after the pulses passed through the grating stretcher. The spectrum shows no significant difference after the pulse is stretched. The spectral bandwidth has a FWHM of approximately 7.0 nm.

polariser with an anti-reflective coating for a wavelength range of 760 to 790 nm. By only changing the polarisation of one pulse to fit the through-polarisation of the polariser, only one pulse is transmitted, leading to the desired pulse picking. The high-voltage driver limits the pulse-picking repetition rate, with a maximum performance of 100 Hz. The repetition rate during experiments was fixed to 10 Hz to match the repetition rate of CLEAR. The pulses are, therefore, separated by 100 ms after passing the pulse picking setup.

The half-waveplate before the Pockels cell changes the polarisation angle of the incoming linear polarised laser light. This allows for optimising the laser light transmission through the pulse picker setup. Moreover, it allows the rotation of the polarisation plane by 90° with respect to the nominal pulse-picking position. In this way, all the pulses, except those usually picked, are transmitted through the pulse-picking setup, increasing the average transmitted intensity by more than 10^7. The higher intensity is needed for alignment procedures and transmission optimisation.

The pulse picker is the last optical element in the free space setup. After the pulse picking, the laser light is coupled into an optical fibre using a collimator [89]. The collimator has an effective focal length of 4.6 mm, an input mode field diameter of 5.0 μm and an output waist diameter of 1.0 mm. The aperture diameter is 4.9 mm, with a numerical aperture of 0.53 and an anti-reflective coating for a wavelength

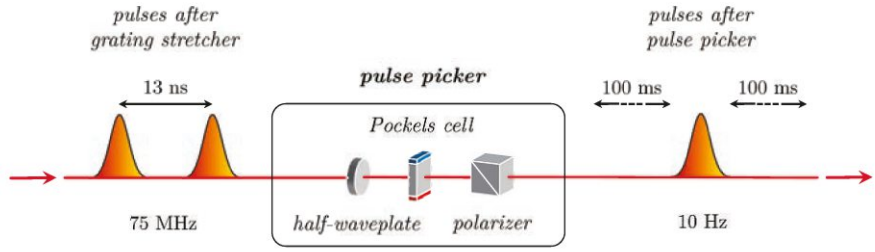

Figure 4.10: The pulses stretched by the grating stretcher are still separated by the initial 13 ns. In the pulse picker, one laser pulse is picked according to the repetition frequency of the particle bunches. Most often, 10 Hz is used, which leads to a temporal separation between the laser pulses of 100 ms.

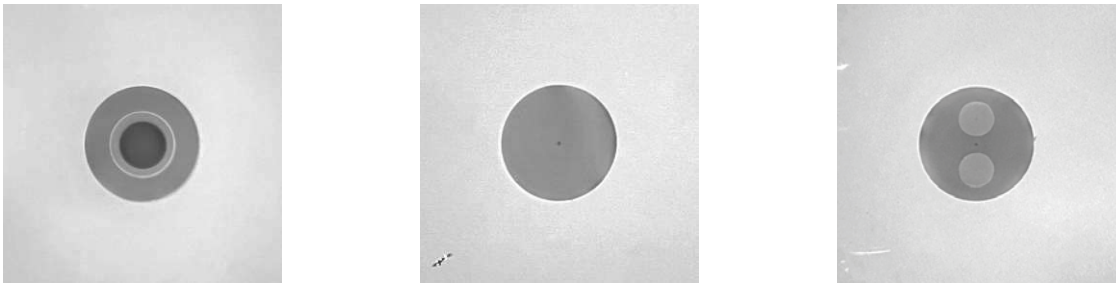

(a) **(b)** **(c)**

Figure 4.11: Overview of various cross-sections of fibres: (a) multi-mode fibre, (b) single-mode fibre, and (c) polarisation maintaining fibre. The darkest circle shows the fibre's core, which has a diameter of 50 μm for the multi-mode fibre and $\leq 5.0\,\mu$m for the other two fibres. In (c), the two PANDA stress rods above and below the core can be seen. The cladding diameter is the same for all three fibre types with approximately 125 μm.

range of 600 to 1050 nm. The single-mode patch fibre is a Thorlabs 780-HP with a core diameter of 4.4 μm and a mode field diameter of $5.0 \pm 0.5\,\mu$m at 850 nm. The collimator focal length was chosen for the diffraction-limited laser spot size being smaller than the mode field diameter of the fibre. The single-mode patch fibre has FC/PC connectors, allowing for switching between both stretching setups.

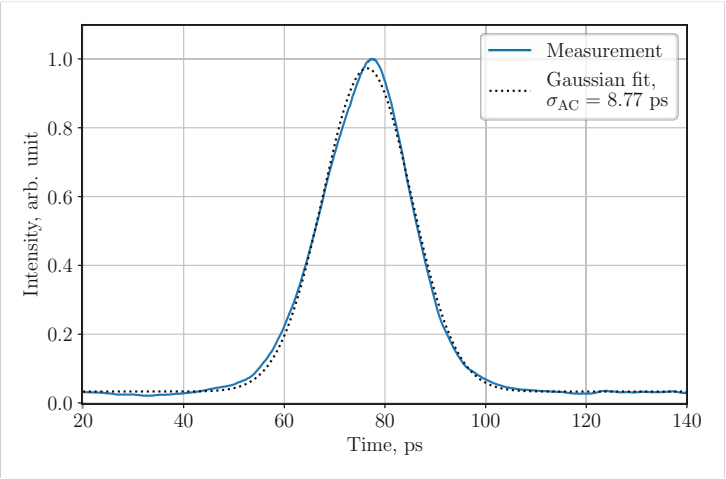

Figure 4.12: Autocorrelator measurement of the laser pulse length after the grating stretcher. The measured standard deviation of the Gaussian fit σ_{AC} needs to be deconvoluted. The final pulse length is given as $\sigma_{real} = \sigma_{AC}/\sqrt{2} = 6.20\,\text{ps}$.

4.6.2 Pulse Stretching

The pulse length after the grating stretcher was measured using an autocorrelator [90]. The incoming pulse is split into two pulses, whereas one of the pulses is linearly delayed in time with respect to the other. Both pulses are then overlapped in a nonlinear crystal in such a way that they produce a second harmonic signal. Only the second harmonic signal is read out using a photomultiplier tube. The pulses must be aligned in time for the second harmonic signal to be measured. Therefore, by delaying one pulse with respect to its replica pulse in time, we obtain a signal corresponding to the convolution of two pulses. The measured pulse length, as well as its Gaussian fit, is shown in fig. 4.12. Assuming a Gaussian profile of the pulses, the measured value σ_{AC} must be corrected for the convolution of the two identical pulses. With $\sigma_{AC} = \sqrt{2}\sigma_{real}$, we obtain a pulse length $\sigma_{real} = 6.20\,\text{ps}$. This pulse length is in the order of magnitude of the electron bunches at CLEAR. It is, therefore, necessary to stretch the laser pulses further, increasing our time window for scanning. In the framework of this work, two different approaches were used to achieve stretching of the laser pulses. The first one uses a chirped fibre Bragg grating for longer stretching. The second one uses the dispersion present in the transmission fibre.

Pulse Stretching with Chirped Fibre Bragg Grating

The pulse stretching setup using the chirped fibre Bragg Grating (CFBG) is shown in fig. 4.13. The pulses in the fibre are transmitted to a high-power 3-port optical circulator. The three ports of the circulator are all pig-tailed with a 1-meter-long 780-HP single-mode fibre and are FC/UPC connectorised. The maximum peak power is 20 kW, and the maximum average power is 300 mW. The center wavelength is 780 nm with an operating wavelength range from 775 to 785 nm. The pulses are transmitted from port one to port two and sent towards the CFBG. The parameters of the CFBG are summarised in table 4.6. Its center wavelength is 780 nm with an operating wavelength range from 770 to 790 nm. A fibre Bragg grating contains a periodic modulation of the refractive index of the fibre core, which causes the grating to act like a mirror. The reflected Bragg wavelength λ_B depends on the period between two high-index sections Λ as well as the average effective refractive index n_{eff}. We obtain $\lambda_B = 2\, n_{\text{eff}}\, \Lambda$. The periodicity of the grating, therefore, tunes the reflected wavelength. This behaviour is utilised in a CFBG, for which the periodicity is linearly changed along the fibre. In the used CFBG, short wavelengths are reflected first, so the period Λ is short at the beginning of the grating and gets longer towards its end. This behaviour is also illustrated in fig. 4.13. Different wavelengths are reflected at different positions in the fibre, leading to an optical path length difference between the different wavelengths in the laser pulse. The result is a long chirped laser pulse as it is required for the electro-optical spectral decoding scheme. The CFBG used stretches to approximately 60 ps/nm. It was custom-made for this application and provided the highest stretching value available, considering the given wavelength and bandwidth. To achieve a similar stretching in a 780-HP fibre, it would need to be approximately 470 m long. It also has to be noted that the dispersion parameter D_λ in an optical fibre is negative, whereas the dispersion parameter of the CFBG has a positive value. Therefore, the pulse stretched in the CFBG is compressed in the transmission fibre afterwards.

With a measured bandwidth of $\sigma = 3.0$ nm of the laser pulse, we would expect the stretched pulse to have a pulse length $\sigma_{\text{CFBG}} \approx 180$ ps. This is longer than the range of the autocorrelator introduced in this section, which covers a maximum time window of 75 ps. The pulse length was therefore measured with a streak camera [91]. In fig. 4.14, the measured pulse length is shown for two cases. The blue curve corresponds to the pulse length measured directly after the CFBG plus 13.5 m of 780-HP fibre. The pulse length $\sigma_{\text{direct}} = 152.8 \pm 0.6$ ps is averaged over several hundred shots and must be corrected for the timing jitter $\sigma_{\text{jitter}} = 28.1$ ps as well as the broadening from the slit width $\sigma_{\text{slit}} = 27.5$ ps of the streak camera. The corrected value is then $\sigma_{\text{direct}} = 147.6 \pm 0.6$ ps. Moreover, the laser pulse is transported to the streak camera in fibre. So, until the pulse reaches the streak camera, it is already compressed in the transmission fibre. Correcting for the compression in

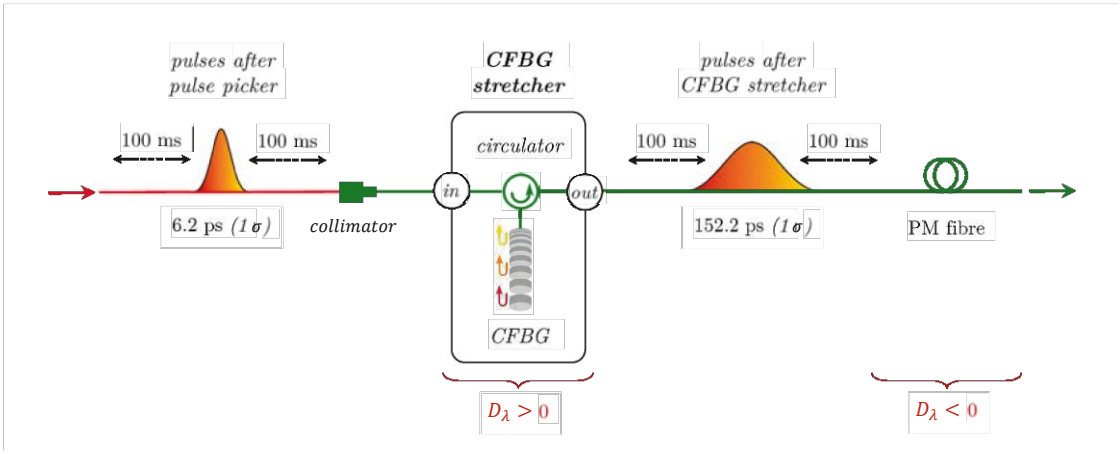

Figure 4.13: Illustration of the pulse stretcher with a chirped fibre Bragg grating. The chirping in the gratings and the CFBG leads to anomalous dispersion, so $D_\lambda > 0$. The pulses have a final length after the CFBG stretcher of $\sigma_{\text{CFBG}} = 152.2 \pm 0.6\,\text{ps}$ and are then compressed further down along the transmission line due to the normal dispersion, so $D_\lambda < 0$, in the transmission fibres.

Stretcher Parameter	Specification	Unit
Center wavelength	780 ± 1	nm
Reflectivity over 80% of FWHM	$\geq 70\%$	
Reflection bandwidth	20 ± 2	nm
Dispersion parameter$^{(1)}$	≈ 60	ps/nm
Pigtail input	≥ 1.5	m
Connector type	FC/UPC	
Fibre type	Nufern 780-HP	

Table 4.6: Parameters of the chirped fibre Bragg grating (CFBG) used to stretch the laser pulses to a few hundred of ps. Costume-made phase mask and production from TeraXion. $^{(1)}D_\lambda$ of CFBG, normalised for length.

the transmission fibre, we obtain a standard deviation of $\sigma_{\text{CFBG}} = 152.2 \pm 0.6\,\text{ps}$ after the CFBG. To calculate the dispersion parameter of the CFBG, we need to consider the pulse length at the input to the grating. With the autocorrelator measurement of 6.2 ps and considering the 4.5 m of fibre until the CFBG, we obtain a pulse length at the input to the grating of 4.7 ps. Finally, for the stretching in the CFBG, we obtain $147.5 \pm 0.6\,\text{ps}$. With the slightly narrower bandwidth of the laser spectrum of $\sigma_{\text{laser}} = 2.67\,\text{nm}$, the dispersion parameter of the stretcher is $55.3 \pm 0.2\,\text{ps/nm}$, compared to the 60 ps/nm as stated by the manufacturer.

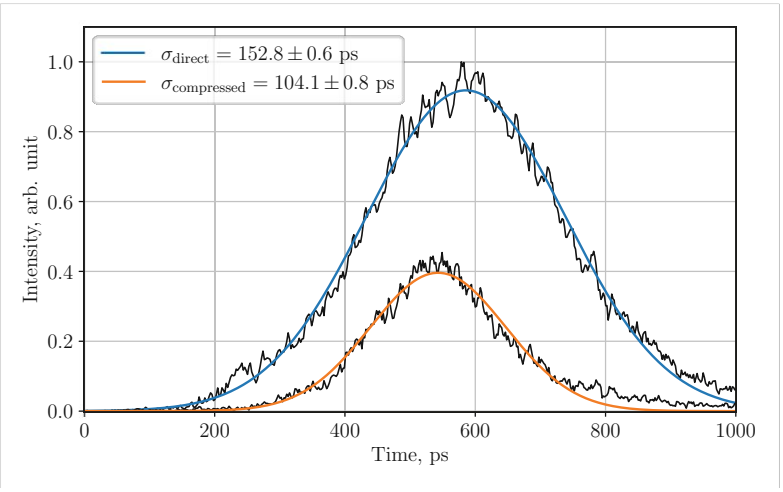

Figure 4.14: Laser pulse length at different locations after the chirped fibre Bragg grating (CFBG). The blue curve is obtained 13.5 m after the CFBG and used to calculate the dispersion parameter of the CFBG. The orange curve is obtained after adding another 139 m of fibre and used to calculate the dispersion parameter of the fibre.

Since the CFBG has anomalous dispersion, which is opposite from the normal dispersion of the glass core in the optical fibre, the stretched pulse is compressed until it reaches the modulator in the accelerator hall. We, therefore, need to check the dispersion in the fibres going down to the accelerator hall. As these long transmission fibres between the laboratory and the accelerator hall are permanently installed at the CLEAR facility, they are subject to irradiation throughout the operation of CLEAR. Therefore, the selection of the fibres aimed for a high radiation tolerance. The natural choice, with all the other components being optimised for the centre wavelength of the laser at 780 nm, would be a polarisation-maintaining 780-HP fibre. However, the only available radiation-hard fibre was a 630-HP type with an operating wavelength of up to 780 nm. The preference was given to the radiation hardness of the fibres, which led to the selection of the Nufern $PM-S630-HP$. The specifications of this fibre are given in table 4.7. It has a pure silica core to increase resistance against radiation-induced damage. Unfortunately, the dispersion parameter is not given for these fibres, so it has been measured using the streak camera. The result is plotted together with the measurement of the CFBG in fig. 4.14. The blue curve corresponds to the pulse length after the CFBG and before the long transmission line. The orange curve corresponds to the compressed pulse length measured after the blue curve plus approximately 133 m of PM-S630-HP fibre and 6 m of PM-780-HP fibre. The pulse length of the compressed pulse $\sigma_{\text{compressed}} = 104.1 \pm 0.8$ ps is averaged over several hundred shots

and must be corrected for the timing jitter $\sigma_{\text{jitter}} = 28.1\,\text{ps}$ as well as the broadening from the slit width $\sigma_{\text{slit}} = 27.5\,\text{ps}$ of the streak camera. The corrected value is $\sigma_{\text{compressed}} = 96.4 \pm 0.7\,\text{ps}$. The compression from the fibre introduces the difference between the two pulse widths and allows us to calculate the dispersion in the fibre. Correcting for the dispersion in the 6 m of PM-780-HP fibre, we obtain a total pulse length difference $\sigma_\Delta = 49.2 \pm 0.9\,\text{ps}$ for the stretching in the S630-HP fibre. With a difference in fibre length of $133 \pm 1\,\text{m}$ between the two measurements and a bandwidth of the laser spectrum of $\sigma_{\text{laser}} = 2.67\,\text{nm}$ after the CFBG, we obtain a dispersion parameter of $D_\lambda = -138.6 \pm 2.8\,\text{ps/nm/km}$ for the PM-S630-HP fibres. The dispersion parameter of silica is $-116.3\,\text{ps/nm/km}$ at 780 nm, as shown in fig. 4.15. The obtained value of $-138.6\,\text{ps/nm/km}$ for the PM-S630-HP fibre is in between the dispersion parameter for the PM-780-HP fibre of $-127.2\,\text{ps/nm/km}$ and the 630-HP fibre of $-149.7\,\text{ps/nm/km}$.

Fibre Parameter	**Specification**	**Unit**
Fibre type	Nufern PM-S630-HP	nm
Operating wavelength	630 to 780	nm
Cutoff	580 ± 40	nm
Attenuation @ 630 nm	≤ 12	dB/km
Core diameter	3.5	μm
Birefringence	1.3×10^{-4}	
Operating temperature	-40 to 85	°C
Length	≈ 66.5	m
Connector type	FC/APC	
Typ. insertion loss	1	dB
Typ. reflection loss	70	dB

Table 4.7: Parameters of the fibres for transmitting the laser pulses between laboratory and accelerator hall.

Considering the obtained dispersion parameter for the CFBG and the transmission fibres, we estimate the laser pulse length at the location of the modulator in the accelerator hall. The laser pulses are compressed from $\sigma_{\text{CFBG}} = 152.2 \pm 0.6\,\text{ps}$ after the CFBG, down to a pulse length of $\sigma_{long} = 119.3 \pm 0.8\,\text{ps}$. We denote it as long stretching compared to the short stretching in the setup without CFBG. This pulse length determines the length of the time trace available for experimental measurements. It is therefore convenient to provide the $\text{FWHM}_{long} = 281.0 \pm 1.9\,\text{ps}$.

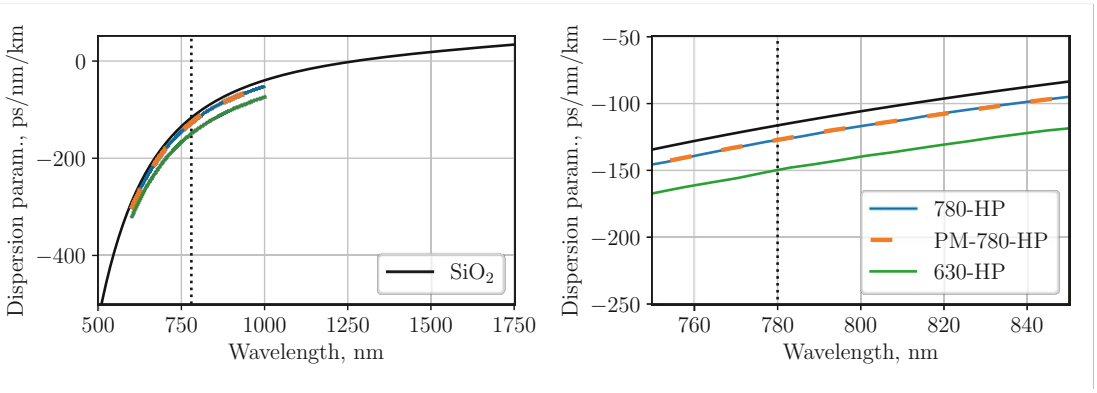

Figure 4.15: Dispersion parameter as a function of wavelength for various fibre types. The dispersion parameter of pure silica (SiO_2) is given in black. The dotted black line corresponds to 780 nm [92, 93].

Pulse Stretching with Transmission Fibre

For the pulse stretching with the transmission fibre, the CFBG is removed from the setup. This is illustrated in fig. 4.16. The anomalous dispersion $D_\lambda > 0$, which is introduced by the gratings, is overcompensated by the normal dispersion $D_\lambda < 0$ in the fibres. The resulting laser pulse at the modulator is chirped in the opposite direction compared to the setup with the CFBG. After coupling the laser pulse with the collimator, the combined fibre lengths up until the location of the modulator in the accelerator hall is approximately 89 m. Considering the dispersion in those fibres, we obtain a $\sigma_{short} = 25.9 \pm 0.5$ ps. This corresponds to a $\mathrm{FWHM}_{short} = 61.0 \pm 1.3$ ps. The ratio between the two pulse lengths is $\sigma_{long}/\sigma_{short} = 4.6 \pm 0.1$. Therefore, the time window available for measurements decreases by a factor of 4.6 when removing the CFBG. However, as the spectral content of the pulse remains the same, the time conversion on the spectrometer decreases by the same factor, improving the temporal resolution of the spectrometer by the same factor. Shortening the time window, therefore, comes with the benefit of increasing the temporal resolution of the measurement.

4.6.3 Electro-optical Mach-Zehnder Modulator

As the laser covers a certain optical bandwidth, the Mach-Zehnder intensity modulator must also be selected for these operating wavelengths. As already shown in fig. 4.9, the laser spectrum is given as 779 ± 3 nm. Another requirement for the modulator is a high electro-optical bandwidth to encode the signal on the laser pulse. Moreover, the sensitivity should be as high as possible to keep the required input voltage low, which is reflected in small values of V_π. In modulators based

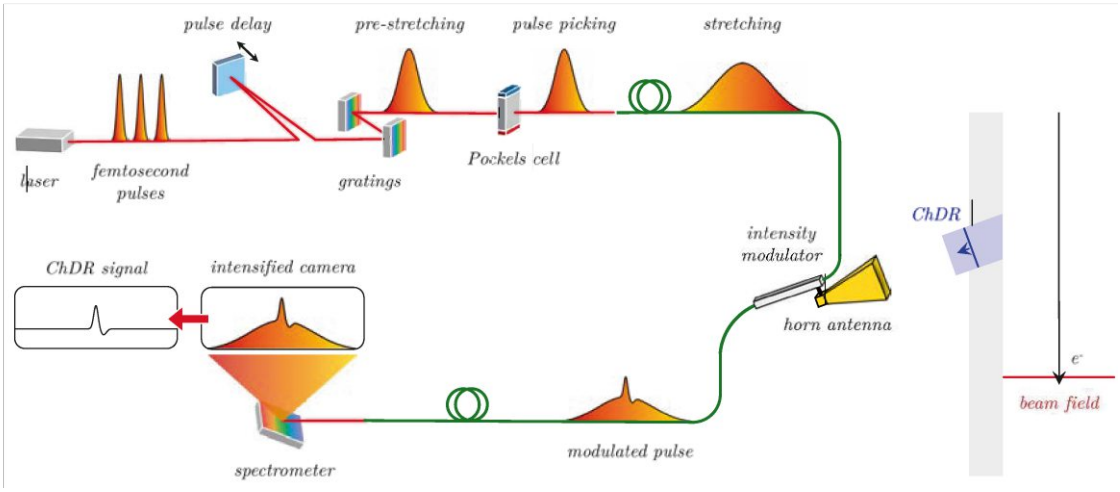

Figure 4.16: Schematic of the experimental setup based on electro-optical spectral decoding optimised for short bunches. The chirped fibre Bragg grating is removed, only using the dispersion in the transmission fibre for stretching. The chirping at the modulator is inversed compared to the long stretching shown in fig. 4.7.

on Lithium niobate ($LiNbO_3$), a low value of V_π is mainly achieved through its high effective electro-optic coefficient and small distances between the electrodes (cf. equation 4.5). An overview of the parameters of the modulator selected for the measurements presented in this thesis is shown in table 4.8. The operating wavelength ranges from 780 to 850 nm, which is not ideal considering that the spectrum of the laser pulses also covers wavelengths below 780 nm. However, the modulator was selected despite its optical cutoff at 780 nm, due to a lack of alternatives for a high electro-optical bandwidth of at least 25 GHz. In fig. 4.17 an illustration of the modulator and its working principle is shown. On the left, a Mach-Zehnder intensity modulator based on a $LiNbO_3$ crystal is shown. The optical waveguide is shown in red. The optical power is split into two arms and recombined after passing the different electrodes. The electrodes are shown in yellow and segmented into RF and DC electrodes. The RF electrodes accept an input signal with a maximum power of 28 dBm ($\approx$ 630 mW) and cover a bandwidth of at least 25 GHz. The RF signal is connected to a SMK 2.92 mm connector, a standardised microwave connector built for a maximum frequency of 40 GHz. The DC electrodes accept a bias voltage from -20 to 20 V. The bias voltage is used to choose the working point of the modulator. On the right side of fig. 4.17, a cross-section of the modulator is shown. The electrodes are on top of the $LiNbO_3$ crystal, whereas the electric field, shown in blue, penetrates the optical waveguides within the crystal.

The modulation of the light is based on the Pockels effect, which describes the

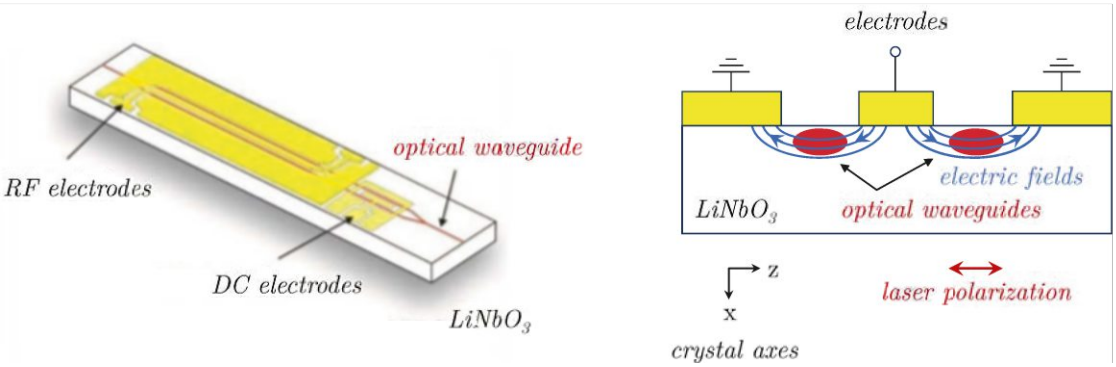

Figure 4.17: Illustration of a Mach-Zehnder intensity modulator with the RF and DC electrodes shown in yellow (adapted from [94]). On the right side, a transverse view of the modulator with the optical waveguides exposed to an electric field from the electrodes is shown (redrawn from [95]). Both illustrations show an x-cut design with the TE polarisation of the laser light in the z-direction.

linear change of the refractive index of a material exposed to an electric field. For an x-cut modulator design as illustrated in fig. 4.17, we are interested in light polarised in z-direction with an electric field applied in parallel. The change in refractive index in the z-axis is then given as [23]:

$$\Delta n_z = -\frac{1}{2}\, n_e^3\, r_{33}\, E_z \tag{4.3}$$

with the extraordinary refractive index $n_z = n_e$, the electro-optic coefficient r_{33} and the electric field component E_z. At a wavelength of 780 nm, the ordinary refractive index of $LiNbO_3$ is $n_{x,y} = n_o \approx 2.3$, and the extraordinary refractive index is $n_z = n_e \approx 2.2$. The electro-optic coefficient r_{33} for $LiNbO_3$ is given as $r_{33} = 30.8\,\mathrm{pm/V}$, which presents the highest electro-optic coefficient of any axis of the $LiNbO_3$ crystal [23]. This crystal orientation presents the largest change in refractive index and, therefore, increases sensitivity to external fields. Moreover, due to the symmetric modulation of the phase, which is ensured by the symmetric design of the x-cut configuration, the modulator has a zero-chirp parameter. Ideally, the output signal is then only modulated in intensity, minimising the frequency chirp within the modulated signal.

The transfer function of a Mach-Zehnder intensity modulator is given as [95]:

$$T(V) = \sin^2\left(\frac{\pi\,(V - V_0)}{2\,V_\pi}\right) \tag{4.4}$$

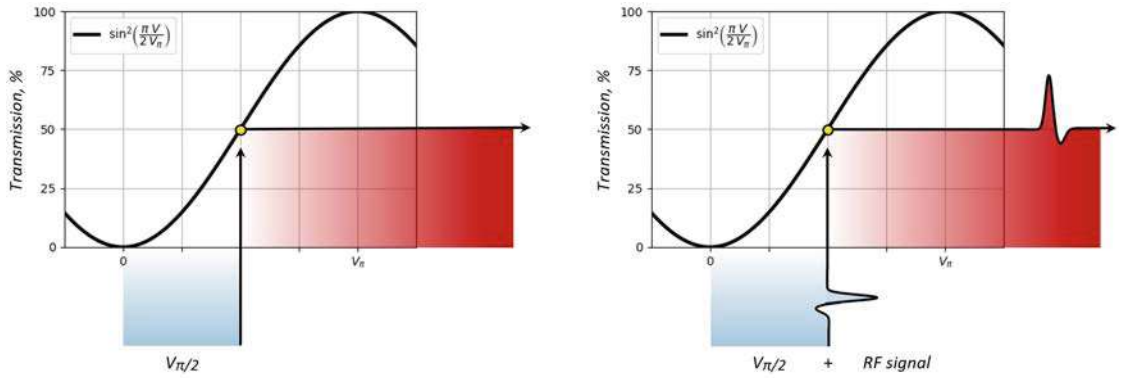

Figure 4.18: On the left, the working point for 50% light transmission is shown. This equals a $\pi/2$ phase shift between the two modulator arms and, therefore, is denoted the quadrature bias point. On the right, an RF signal is combined with the DC voltage, leading to a modulation of the transmitted light. As the modulator is operated at the quadrature bias point and the RF signal amplitude is smaller than V_π, we obtain a linear modulation of the input signal.

It is a function of the voltage V and is shifted by the bias voltage V_0 introduced by the DC electrodes. The periodicity of the function depends on V_π. It indicates the voltage necessary to introduce a phase shift of π between the modulator arms. The bias voltage V_0 corrects for any differences between the two modulator arms and, more importantly, allows for an adaptation of the working point during operation.

In fig. 4.18, the transfer function is shown, with an overlay of the input voltage in blue and the transmitted light intensity in red. In this example, we remove the bias voltage V_0 in equation 4.4 and introduce the bias as a DC background voltage on the RF input. So, instead of showing the effect of the bias voltage and the RF signal separately, we add them together for a more straightforward representation. The left plot in fig. 4.18 shows a DC background voltage of $V_{\pi/2}$. By introducing this phase shift of $\pi/2$ between the modulator arms, we have a constant light transmission of 50%. This point is referred to as the quadrature bias point. On the right plot in fig. 4.18, we add an RF signal to the DC background voltage. Combining both, we obtain a total light modulation, which resembles the input RF signal on top of a constant background light level. For the modulation of the light to be linear, we have chosen the quadrature bias point, as it is in the linear region of the transfer function. Moreover, the RF signal amplitude must be substantially smaller than V_π. If the signal amplitude is in the order of $V_{\pi/2}$, the modulation of the transmitted light would be subject to distortions. The value of $V_{\pi/2}$ is, therefore, a hard limit for the maximum amplitude of the input signal.

As V_0 only shifts the transfer function along the abscissa but does not influence its general shape, just the value of V_π is left to modify the transfer function. The value of V_π of a Mach-Zehnder intensity modulator is given as [95]:

$$V_\pi = \frac{\lambda}{n_{\text{eff}}^3 \, r_{\text{eff}}} \frac{d}{L \, \Gamma} \tag{4.5}$$

with the wavelength λ, the effective refractive index n_{eff}, the effective electro-optic coefficient r_{eff}, the gap between the electrodes d, the length of the modulating electrodes L and the dimensionless overlap integral of the electric field and the waveguides Γ. As for a fixed modulator design, all values are constant, except for the wavelength λ, we obtain $V_\pi \propto \lambda$. As the working principle of an intensity modulator is based on interference, it performs best with monochromatic light. Using it with broadband light will, therefore, affect its performance. According to the modulator parameters given in table 4.8, V_π DC varies by 0.6 V for a wavelength range of 70 nm. For the final system, the modulator will be used with chirped laser pulses of a bandwidth of 7 nm FWHM. A first rough estimation, therefore, yields that V_π would vary in the order of magnitude of ≈ 0.1 V for the different wavelengths in the spectrum. Compared to the smallest V_π DC voltage of 3.9 V this is less than 3%.

Modulator Characterisation

Before testing the modulator with laser pulses, it was characterised under controlled conditions in the laboratory using a continuous wave fibre-coupled laser source [96]. The laser had a polarisation-maintaining fibre-coupled output with a centre wavelength of 785 nm. After 10 m of PM-780-HP fibre, the modulator was connected. Another 10 m of PM-780-HP after the modulator, the transmitted light was measured using a photodiode [97]. The voltage output of the photodiode was monitored with a benchtop multimeter [86]. The bias voltage was changed using a waveform generator [98] connected to the DC electrodes of the modulator. The RF electrodes remained unconnected during these tests. The modulator was placed inside a climate chamber [99] to control the ambient temperature.

DC Bias Switching

Before measuring the transfer function, the behaviour of the transmitted laser power with respect to fast-switching DC voltages was analysed. A change in bias voltage introduces an electrically induced drift of the transfer function of the modulator. This is due to the electrical inhomogeneities of the different materials near the electrode. After changing the bias voltage, the electrical charges redistribute,

Modulator Parameter	Specification	Unit
Crystal	Lithium Niobate	
Crystal cut	X-Cut	
Operating wavelength	780 to 850	nm
Max. optical input power	14	dBm
Typ. insertion loss	4.5 to 5.5	dB
Fibre type	Corning PM 85-U25D	
Input/Output fibre length	1.0 / 1.5	m
Optical connector	FC/APC	
RF connector	Female SMK 2.92 mm	
Typ. electro-optical bandwidth	> 25	GHz
V_π RF	3.5 to 4.5	V
V_π DC	3.9 to 4.5	V
Impedance RF	50	Ω
Impedance DC	1	MΩ
Max. RF power	28	dBm
Bias voltage	-20 to 20	V
DC extinction ratio	22	dB
Operating temperature	0 to 70	°C

Table 4.8: Parameters of the intensity modulator NIR-MX800-LN from iXblue photonics.

changing the effective electric field and leading to a drift in the transmitted laser power until an equilibrium distribution is reached. Also, a change in optical power and ambient temperature leads to a drift of the bias voltage [100].

In fig. 4.19, the transmitted laser power is shown for three different input laser powers at an ambient temperature of 20°C. The laser power before and after the modulator is summarised in table 4.9. The bias voltage of $V_0 = -0.75\,\mathrm{V}$ was close to the maximum transmission power for all three input power levels. At maximum transmission, the laser light was therefore attenuated by approximately 10 dB with respect to the input light. After reaching a stable state at each power respectively, the bias voltage was changed from $V_0 = -0.75\,\mathrm{V}$ to the quadrature bias point at $V_0 = -2.50\,\mathrm{V}$. At this voltage, the transmission of the laser light is expected to be reduced to 50% with respect to the previous value. Figure 4.19 shows that the transmission drops significantly when the bias voltage changes and then slowly recovers over time to reach the expected value of approximately 50%. The time needed for the transmission power to relax by $1/e$ is approximately one hour on average. As a drift in the bias voltage would change the working point, it is helpful

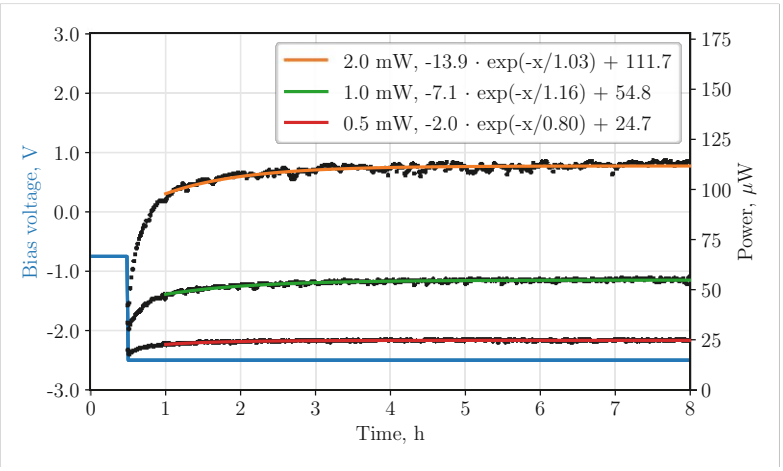

Figure 4.19: The relaxation of the transmission power when switching the bias voltage from a maximum in transmission ($V_{100} \approx -0.75\,\mathrm{V}$) to the quadrature bias point ($V_{50} \approx -2.50\,\mathrm{V}$) is shown. All data was recorded at an ambient temperature of 20°C. The time needed for the transmission power to relax by $1/e$ is approximately one hour on average.

to check the relaxed transmission power with respect to the maximal transmission. As shown in table 4.9, the ratio for the different input powers stays within a few percentage points around the targeted value of 50%.

Input power	**Temperature**	**Exit power**		
		$V_{100} \approx -0.75\,\mathrm{V}$	$V_{50} \approx -2.50\,\mathrm{V}$	Ratio
2.0 mW	20°C	207.5 μW	111.7 μW	54%
1.0 mW		105.5 μW	54.8 μW	52%
0.5 mW		52.9 μW	24.7 μW	47%
0.5 mW	10°C	56.3 μW	27.4 μW	49%

Table 4.9: Power levels before and after the modulator. $V_{100} = -0.75\,\mathrm{V}$ corresponds to the maximum of transmission, whereas $V_{50} = -2.50\,\mathrm{V}$ corresponds to the quadrature bias voltage, with 50% of transmission.

In fig. 4.20, the relaxation of the transmission power when switching the bias voltage is shown at different temperatures. At an ambient temperature of 10°C, it took approximately 1.3 hours for the transmission power to relax by $1/e$. Comparing the ratios in table 4.9 for an input power of 0.5 mW shows that the working point increased by two percentage points, indicating a negligible drift of the transfer function.

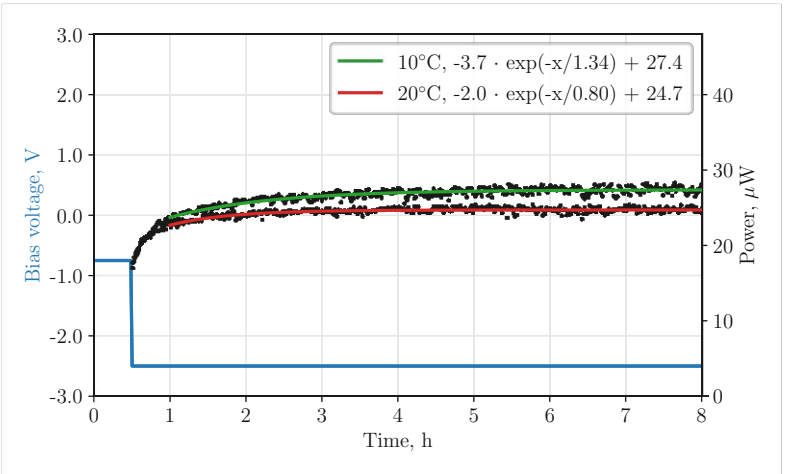

Figure 4.20: The relaxation of the transmission power when switching the bias voltage from a maximum in transmission ($V_{100} \approx -0.75\,\mathrm{V}$) to the quadrature bias point ($V_{50} \approx -2.50\,\mathrm{V}$) is shown. All data was recorded with an input power of 0.5 mW. The time needed for the transmission power to relax by $1/e$ varies from 0.8 to 1.3 hours.

Transfer Function

As shown in fig. 4.19 and fig. 4.20, a rapid bias voltage change introduces a drift in the transmitted laser power. A stable behaviour is only reached after several hours. However, scanning the transfer function is essential for finding the quadrature point during the experiment. To wait for the transmission power to be fully relaxed at each sampling point is impractical and not feasible during an experimental campaign with particle beams. As we are not interested in the actual values of V_0 and V_π of the transfer function, but rather in locating the quadrature point, we introduce an alternative procedure to locate the quadrature point V_{50}. This procedure is much faster as it does not require the relaxation of the bias voltage. However, it will not yield accurate values of V_0 and V_π.

Before the measurement, the modulator could stabilise at a bias voltage of $V_{50} \approx -2.5\,\mathrm{V}$. Then, the bias voltage was changed periodically, increasing and decreasing its value with respect to $-2.5\,\mathrm{V}$. The bias voltage pattern is shown in fig. 4.21 on the right, where the bias voltage was switched every 30 seconds. The left plot in fig. 4.21 shows the resulting transfer function for two different samples. The orange curve stems from sampling right after switching the bias voltage, as indicated by the orange points in the right plot. The green curve, on the other hand, stems from sampling 25 seconds after switching the bias voltage, as indicated by the green points in the right plot. As the transmitted laser power

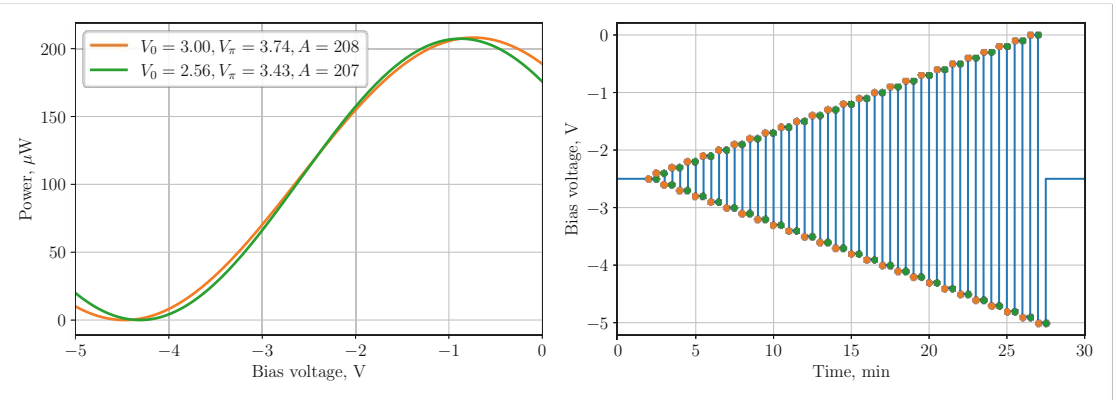

Figure 4.21: On the left, the transfer function is shown for two different sampling times. The orange curve corresponds to a sampling right after switching the bias voltage, the green curve corresponds to a sampling 25 seconds later. The transfer function's distortion stems from the modulator's relaxation time after switching the bias voltage. The voltage switching pattern is shown on the right, with the orange and green dots denoting the sampling time used to calculate the transfer functions in the left plot.

is still changing substantially after a few seconds of switching the laser power, the resulting transfer functions yield different values for V_0 and V_π as expected. However, the values around $V_{50} \approx -2.5\,\mathrm{V}$ are hardly affected by this procedure. The bias voltage is only changed by values $\ll V_\pi$ near the initial V_{50} working point. The change with respect to the initial electric field strength in the crystal is, therefore, small, reducing the electrically induced drift. The second benefit of this bias voltage pattern is that after performing the scan, the average applied voltage is approximately $-2.5\,\mathrm{V}$. In such a way, the relaxation of several hours to again reach a stable transmission is avoided. By following this procedure, we obtain two crucial values necessary for measurement. First, the modulator's V_{50} value must be set during measurements. And secondly, the maximum and minimum of the transmission curve. This procedure can be used for any bias point, and an accurate value is only obtained after the modulator has had sufficient time to stabilise at this working point. Finding the value of V_{50} for an auto-stabilised modulator setup is therefore an iterative process.

The transfer function was measured for different input power levels after switching the bias voltage as described above. The resulting transfer functions are shown in fig. 4.22. To obtain these curves, the transmitted laser power was averaged over a period of 25 seconds at each bias voltage. A full scan of the transfer function, therefore, took approximately 25 minutes. The obtained value for the quadrature point for the three different laser powers was $V_{50} \approx -2.58 \pm 0.02$.

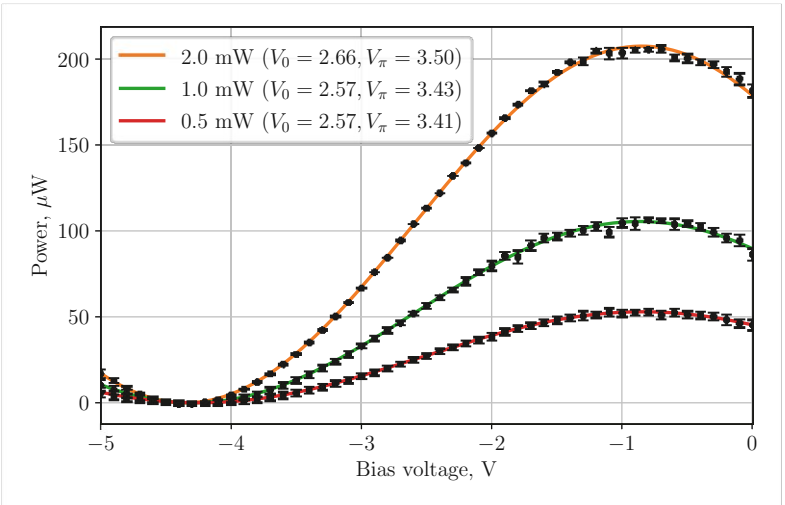

Figure 4.22: Transfer function of the modulator for various laser powers at an ambient temperature of 20°C and without any relaxation of the transmitted power after bias voltage switching, as introduced in fig. 4.21. The obtained average quadrature point is $V_{50} \approx -2.58 \pm 0.02$.

The transfer function was also measured at two different temperatures, as shown in fig. 4.23. Both curves were obtained with an input power of 0.5 mW. The obtained value for the quadrature point at 10°C and 20°C was $V_{50} \approx -2.55 \pm 0.01$ and sufficiently stable between the two measurements. Transmission power was found to be slightly higher at a lower temperature.

Radio Frequency Signal Input

As presented in table 4.8, the intensity modulator is equipped with an SMK 2.92 mm female connector, which is designed for frequencies up to 40 GHz. A broadband horn antenna [101] was chosen to detect and feed the electric fields into the modulator. The SMA female output of the antenna is connected to the modulator via an SMA to 2.92 mm adapter [102]. Priority was given to a flat and broadband frequency response, with the antenna having a low cutoff frequency of 6.5 GHz. This is substantially higher than the 1.6 GHz expected from the radiator diameter. Therefore, all signals detected by the system will be high-pass filtered with a low cutoff of 6.5 GHz. The high cutoff of the antenna is given as 18 GHz. However, the integrated setup is measured for its pulse response in section 6.2. The antenna has an aperture of 78 × 65.5 mm and is positioned 250 mm from the beam during the transition radiation measurement and 70 mm from the exit surface of the radiator during the ChDR measurement.

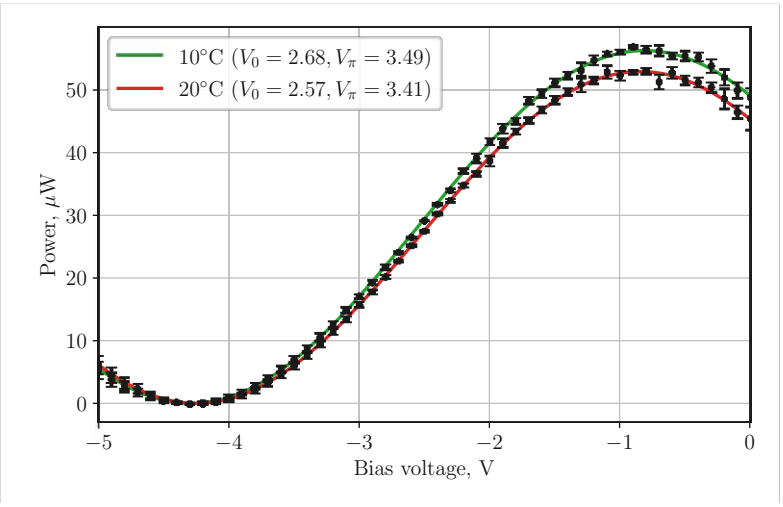

Figure 4.23: Transfer function of the modulator for different ambient temperatures at an input power of 0.5 mW and without any relaxation of the transmitted power after bias voltage switching, as introduced in fig. 4.21. The obtained average quadrature point is $V_{50} \approx -2.55 \pm 0.01$.

4.6.4 Intensified Spectrometer

The final element of the acquisition chain is the intensified spectrometer. The initial design of the in-house built spectrometer is described in [103] and has been subject to several modifications since then. An illustration of the updated setup is shown in fig. 4.24. The laser light is launched via a collimator, passes a beam expander with a slit for spatial filtering, and is then refracted at a planar grating. The dispersed laser light is amplified with an image intensifier and digitised with a digital camera. The expected performance of the spectrometer is discussed in the following paragraphs.

The laser light is launched into free space using a collimator with a collimated beam diameter of 7.5 mm [104]. The collimated light is expanded in transverse size to increase the system's spatial resolution. The beam expander consists of lenses L1 ($f_1 = 60$ mm) and L2 ($f_2 = 150$ mm), leading to a magnification of $f_2/f_1 = 2.5$. After passing two 2-inch mirrors M, the diameter of the laser spot at the grating location is $D \approx 18.75$ mm. The spatial resolution is approximated as $\Delta x \approx 1.22\, f\lambda/D$, with the focal length f of the objective lens, the wavelength λ, and the collimated beam's diameter D. Using the focal length f_3 and a wavelength of 780 nm, we obtain a value $\Delta x \approx 10\,\mu$m. This is smaller than the resolution of the intensifier [105], which is 32 Lp/mm $\approx 16\,\mu$m, hence providing the ideal resolution limit for perfectly collimated light in our system. Between the image intensifier and the digital camera, a relay lens [106] magnifies the spectrum by a

factor of two. Therefore, the limiting resolution of the intensifier imaged on the camera sensor is approximately 32 μm. The digital camera [107] has a resolution of 1200×1920 pixels with a pixel size of 5.86 μm and a pixel pitch in the horizontal plane of 5.90 μm. The limiting resolution of the intensified camera is given as $\Delta x \approx 5.4\,\mathrm{px}$. This represents the resolution limit of the system. To be as close as possible to this ideal resolution, a vertical slit [108] is located at the focal points of lenses L1 and L2. The slit was closed to approximately 10 μm, which increased resolution and decreased the light intensity substantially. However, using the image intensifier, the loss in light yield was partially compensated for. The limiting factor of the spectrometer resolution is the reduction in slit width, which translates into a minimisation of the angular spread of the light impacting the grating.

The linear dispersion to be expected from the spectrometer is estimated using the grating equation [109]:

$$m \cdot \lambda = d\,(\sin\alpha + \sin\beta) \tag{4.6}$$

with the groove spacing d, the diffraction order m, wavelength λ, angle of incidence α and angle of diffraction β. The angular dispersion is calculated by differentiating λ as defined in equation 4.6 with respect to β. One obtains $d\lambda/d\beta = d/m \cdot \cos\beta$. For small angles, we approximate $d\beta \approx dx/f$, and we obtain the linear dispersion:

$$\frac{d\lambda}{dx} \approx \frac{d \cdot \cos\beta}{m \cdot f} \tag{4.7}$$

with the focal length f of the objective lens. The planar holographic reflection grating has a groove density of $G = 1/d = 1200\,\mathrm{grooves/mm}$ [110]. With a design diffraction angle of $\beta = 45°$ (at m = 1 and $\lambda = 780\,\mathrm{nm}$) and a focal length of the objective lens L3 of $f_3 = 200\,\mathrm{mm}$, we obtain a linear dispersion of 2.95 nm/mm. Considering the magnification of the relay lens again by a factor of two, as well as the pixel pitch of 5.90 μm, we obtain a linear dispersion in pixels of $d\lambda/dx \approx 34.8 \times 10^{-3}\,\mathrm{nm/px}$.

The spectrometer was calibrated using a Krypton lamp [111]. The obtained spectrum is shown in fig. 4.25. On top, the obtained image is shown for an integration time of 5 ms. To plot the horizontal profile underneath, only a small fraction of 10 px in height, as indicated by the red lines, was used. The characteristic double peaks easily identify the corresponding wavelengths in the spectrum. Fitting each peak of the spectrum in fig. 4.25 with a Gaussian function and taking its respective mean position on the sensor, we obtain a relation between wavelength and pixel position of $d\lambda/dx = (35.5 \pm 0.1) \times 10^{-3}\,\mathrm{nm/px}$. This is to be compared to the

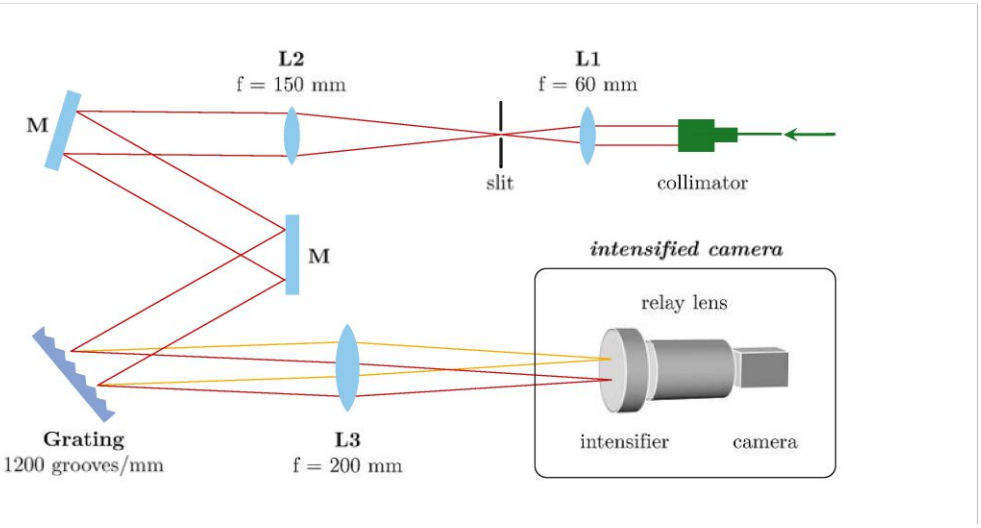

Figure 4.24: Illustration of the spectrometer with the intensified camera. The collimated light is expanded in transverse size with lenses L1 and L2 and spatially filtered with a vertical slit. After being diffracted at the grating, the angular spectrum is evaluated at the intensifier located in the focal plane of lens L3. The intensified image is magnified with a relay lens and acquired with a digital camera.

analytical estimation from equation 4.7, which yielded $d\lambda/dx \approx 34.8 \times 10^{-3}\,\mathrm{nm/px}$. The measured value, therefore, deviates by approximately 2% from expectation. It has to be noted that, more accurately, $d\lambda/dx$ has a negative value for our setup as wavelengths decrease with increasing pixel number. The linear dispersion is therefore given as $d\lambda/dx = (-35.5 \pm 0.1) \times 10^{-3}\,\mathrm{nm/px}$. Considering the bandwidth of the femtosecond laser with a FWHM of 7 nm, the laser pulse spectrum will cover approximately 200 px of the camera sensor with longer wavelengths being located towards the left and shorter wavelengths towards the right in the horizontal plane.

To measure the resolution of the spectrometer, the peak at 785.5 nm is used as it is the closest to the centre wavelength of the laser pulse. Also, it is close to the image sensor's centre, minimising distortions. On the left side of fig. 4.26, the spectral line at 785.5 nm is shown for different intensifier gains. The individual peaks were fitted with a Gaussian function, and their standard deviation is given in the legend. The plot on the right summarises the obtained standard deviations as a function of the intensifier gain. As the intensifier gain introduces noise to the system, the resolution worsens for higher gain values. During experiments, it is beneficial to keep gain values low. The resolution is provided in pixels in these plots, as later on, it is more convenient to apply the time-to-pixel conversion to these values. However, it is still interesting to convert these values to wavelength

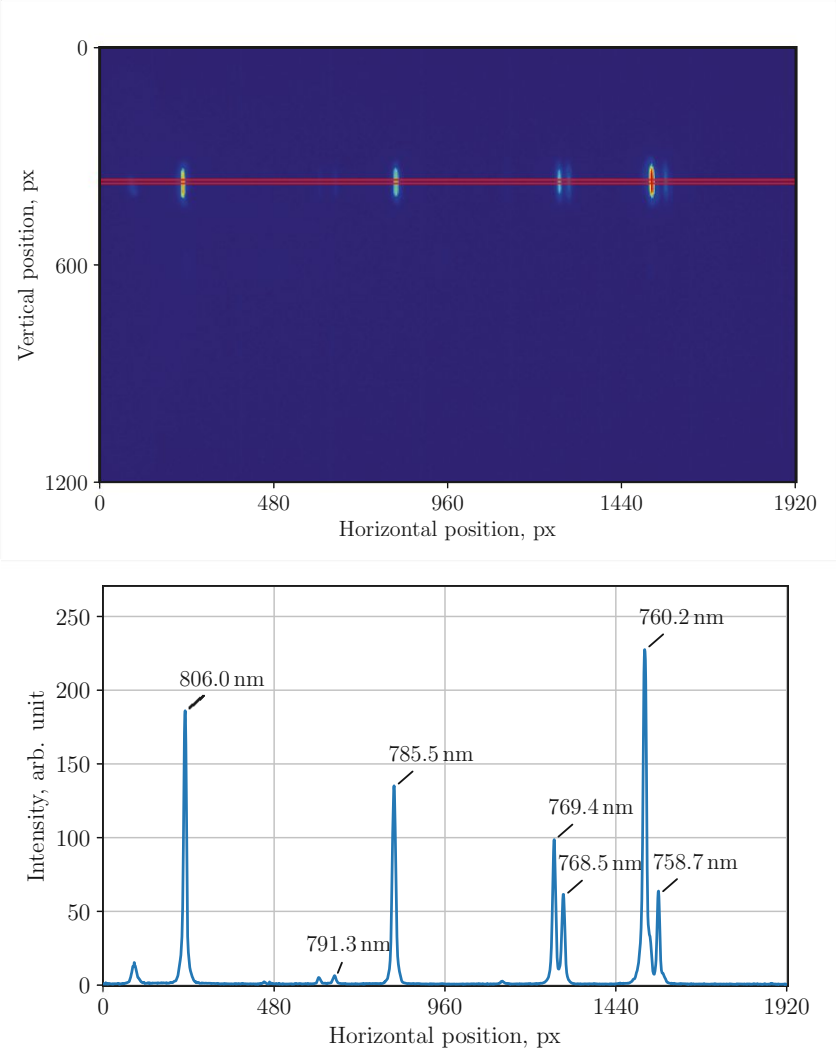

Figure 4.25: On top, the spectral lines of the calibration lamp are shown as captured by the camera. The sensor has an array size of 1200×1920 pixels. The red rectangle indicates the integration area. The lower graph shows the vertical profile of the pixels in the integration area. The wavelengths of the Krypton calibration lamp are indicated.

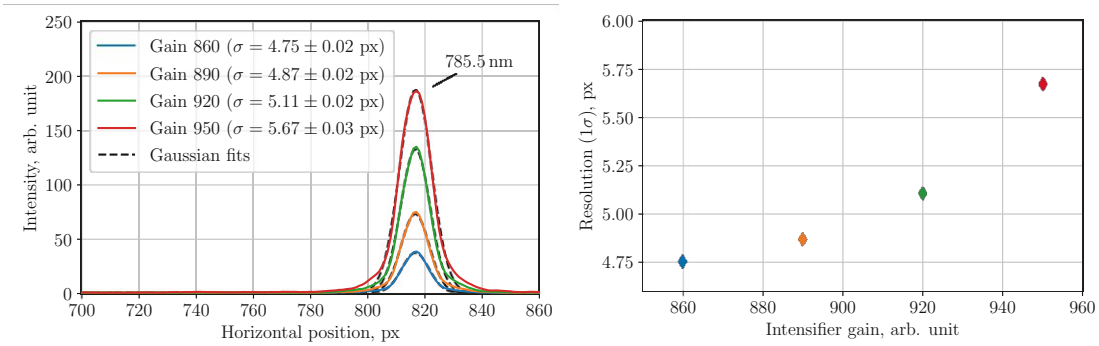

Figure 4.26: On the left, the 785.5 nm spectral line of Krypton is shown for different gains of the intensifier. Each peak is fitted with a Gaussian function to obtain the spectrometer's resolution. On the right, the standard deviation of the Gaussian fit is plotted as a function of the intensifier gain, showing an increased resolution for lower gain values. The standard deviations of 4.8 to 5.7 px correspond to spectral widths of 0.17 to 0.20 nm.

as well. For the resolution in pixels of $\sigma = 4.8$ to 5.7 px, using the linear dispersion value of $d\lambda/dx = -35.5 \times 10^{-3}$ nm/px, yields a spectral width ranging from $\sigma_\lambda = 0.17$ to 0.20 nm. The spectral width of the 785.5 nm spectral line of Krypton is less than 0.0001 nm and serves the purpose of a delta function for the resolution measurement [112].

The image intensifier [105] in the spectrometer serves mainly two purposes. First, it compensates for the decrease in light intensity introduced by the spatial filtering using the vertical slit. This allows us to obtain a resolution down to $\Delta x_{\mathrm{FWHM}} = 2\sqrt{2\ln(2)} \cdot \sigma_x = 2\sqrt{2\ln(2)} \cdot 4.75 = 11.2$ px compared to the ideal resolution of the intensifier of $\Delta x \approx 5.4$ px. Secondly, the image intensifier serves the purpose of gating the laser pulse to remove the contributions from the laser pulses, which the pulse picker does not entirely remove.

5

Experimental Characterisation using Electro-optical Probes

This chapter introduces the measurement results obtained with electro-optical probes as presented in section 4.5. The probes were calibrated with the direct beam field and afterwards used to measure different properties of CChDR. Its peak electric field strength as a function of bunch charge, its dependency on the distance between the beam and radiator surface, as well as the polarisation of the electric field were measured. Moreover, the time and frequency domain signals are analysed to study reflections within the radiator and obtain its cutoff frequency. Finally, the field distribution at the exit surface of the radiator is shown.

5.1 Calibration with the Direct Beam Field

The electro-optical probes used for the measurements presented in this chapter are capable of measuring the absolute value of the electric field strength. They are calibrated by the manufacturer for their given bandwidth of 10 GHz. However, as we measure bunches, which are a few picoseconds in duration, their power spectrum extends to much higher frequencies. To compensate for this underestimation of the signals, we perform a calibration with short signals of known intensity, namely the direct beam field. An overview of the results from the calibration of the probes, leading to a measurement of the absolute value of the electric field strength of CChDR, was presented before the writing of this thesis [113]. The data presented in this section expands these results in more detail. The general measurement setup for CChDR is introduced in section 4.5, and the setup used for the calibration measurement is illustrated in fig. 5.1. Instead of measuring the electric field at the exit surface of the radiator, the electro-optical probe is directly exposed to the beam field. The probe is located in the horizontal plane with respect to the beam trajectory. In the laboratory frame, the field lines are confined within a narrow cone with an opening angle $\sim 2/\gamma$, as illustrated in fig. 2.2. As the electric field distribution of a relativistic particle bunch can be described analytically using equation 2.4 from section 2.2, this setup is used to calibrate the probe. The electric field distribution equation depends on the distance to the beam r, its total charge, the Lorentz factor γ and the longitudinal bunch distribution. Assuming a Gaussian distribution, the longitudinal bunch distribution is characterised by its standard deviation σ. Despite the parameters given by theory, the insertion loss of the acquisition system must also be monitored during the measurement. All relevant properties, except bunch length, were monitored continuously during operation. The calibration was performed by keeping the beam conditions constant and only varying the distance by moving the probe in the transverse plane away from the beam trajectory.

Figure 5.2 shows a subset of the averaged acquired traces at different distances from the beam. Each trace is an average of 600 shots. A decrease in the signal amplitude is visible as the distance between the probe and the beam increases. These raw signals are obtained with a high-bandwidth oscilloscope (10 GHz, 256 GSa/s, 10-bit) [85] and need further processing to get an absolute electric field value.

First, the averaged time signals must be corrected for the charge fluctuation during acquisition. In fig. 5.3, the evolution of the bunch charge during acquisition is shown. Grey columns indicate the acquisition window of one minute at each distance. The acquisition at 50 different distances from the beam took approximately one hour. The black data points indicate each acquisition window's average and standard deviation. The standard deviation remains similar during operation. However,

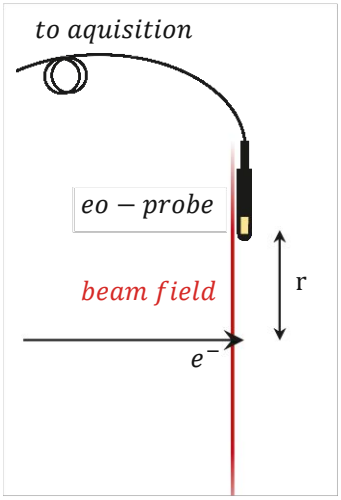

Figure 5.1: Illustration of the calibration setup for the electro-optical probe. The transverse beam field is measured at different distances r from the beam to calibrate the probe's response against analytical expectations.

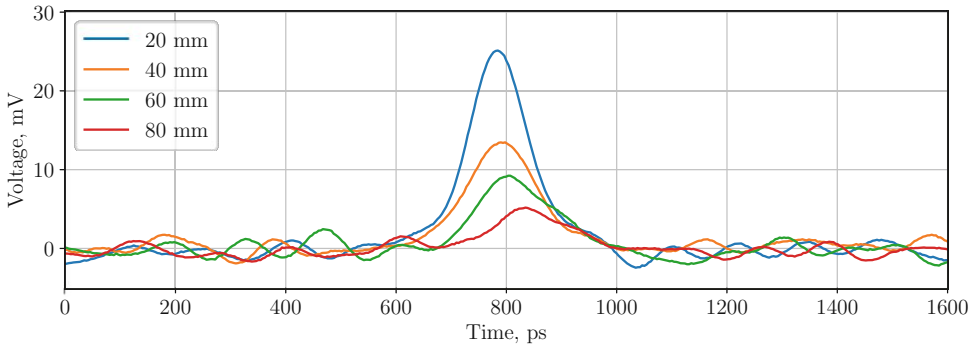

Figure 5.2: Averaged time traces of the direct beam field at different distances from the beam as measured with a high-bandwidth oscilloscope (10 GHz, 256 GSa/s, 10-bit). The traces are subject to charge fluctuations, bandwidth limitation, as well as insertion loss and timing jitter of the acquisition system.

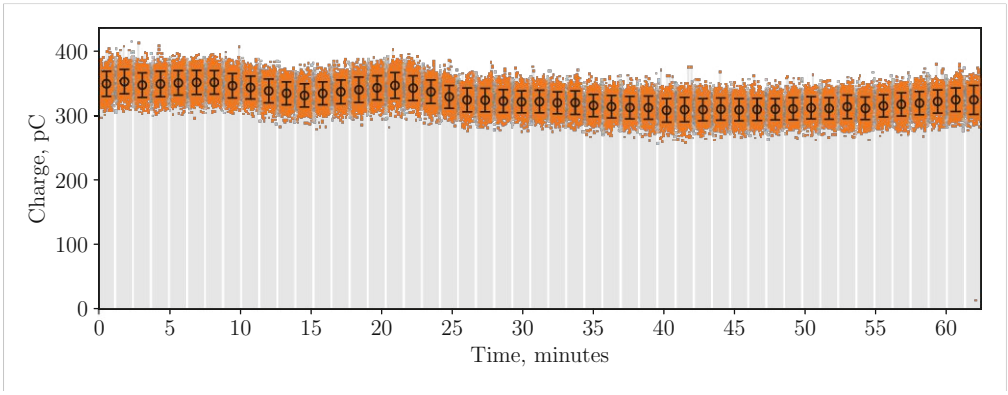

Figure 5.3: Evolution of the bunch charge during measurement of the direct beam field. Grey columns indicate the acquisition window for each time trace. The black data points indicate each acquisition window's average and standard deviation.

there is a non-negligible drift of the average bunch charge during the acquisition time. All traces are, therefore, normalised to a bunch charge of 300 pC. The normalisation is linear as the dependence of the electric field strength depends linearly on the bunch charge for coherent radiation.

First, the averaged time signals must be corrected for the insertion loss change during acquisition. In fig. 5.4, the evolution of the insertion loss during acquisition is shown. By monitoring the insertion loss of the system, we calculate the antenna factor of the probe according to equation 4.1 in section 4.5. Inserting the obtained antenna factor into equation 4.2 for each averaged time trace (cf. fig. 5.2), we convert the voltage amplitude in each time trace to the absolute value of the electric field strength.

Taking each curve's peak electric field strength as a function of the distance, we obtain the expected $1/r$ decay of the beam field. This is shown in fig. 5.5. The total distance range scanned was approximately 100 mm. Fitting the data points, we obtain $(203.1 \pm 6.3)/r$ [V/m].

As we converted the measured amplitudes, we finally compare them to the analytical expectations. The energy of the particles was measured to be 200 MeV during the experiment. Considering the high particle energies and the fact that the distance between the particle beam and the probe location is small, the approximation of an electric field of a charged particle with $\gamma = \infty$ is used. At this point, it is convenient to recall the analytical expectation of the electric field strength of a relativistic particle bunch shown in fig. 2.3. Considering a particle energy of 200 MeV ($\gamma = 392.4$) at a distance of 100 mm from the beam, the introduced

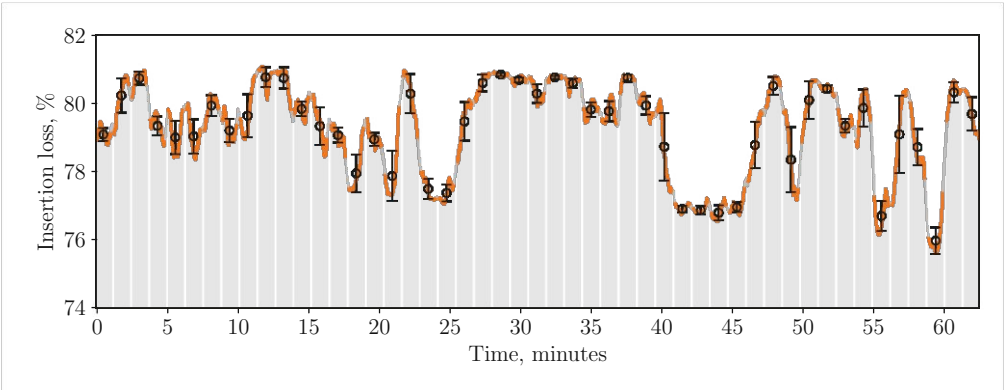

Figure 5.4: Evolution of the insertion loss during measurement of the direct beam field. Grey columns indicate the acquisition window for each time trace. The black data points indicate each acquisition window's average and standard deviation.

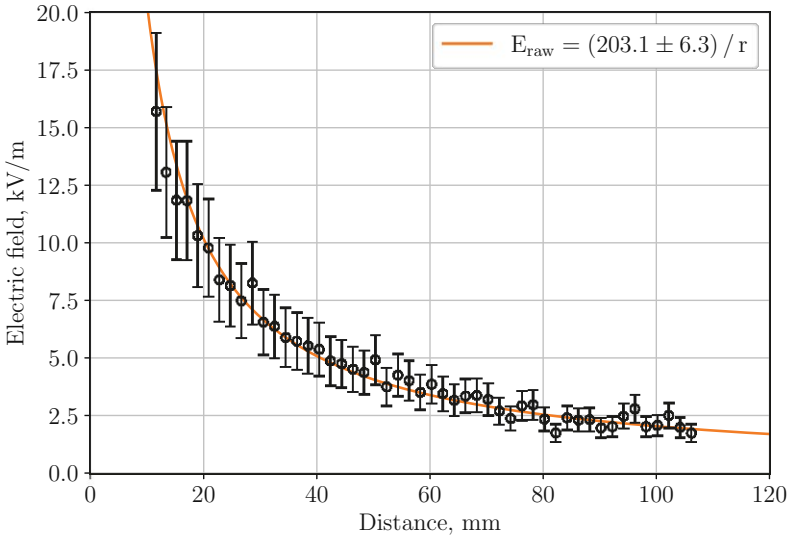

Figure 5.5: Peak electric field strength of the direct beam field as a function of distance. As measured with the probe, the raw data shows a 1/r decay as expected by theory. However, the absolute numbers are smaller due to the bandwidth limitation and timing jitter of the acquisition system.

approximation deviates by less than 3%, as shown in fig. 2.3. We, therefore, use equation 2.5, which yields the electric field strength for E(r, z, $\gamma = \infty$). The signals we measure are also subject to bandwidth limitation and timing jitter. As we are interested in the absolute value of the peak field, we take the maximum of each trace, corresponding to z = 0 in equation 2.5. The formula for the analytical expectation is then given as:

$$E_{max}(r, \gamma = \infty) = \frac{1}{2\sqrt{2}\,\pi^{3/2} c \varepsilon_0} \frac{Q}{\sigma} \frac{1}{r}\,, \tag{5.1}$$

with the speed of light in vacuum c, the vacuum permittivity ε_0 (it is assumed $\varepsilon_0 = \varepsilon_{air}$ in this frequency range) and the variables Q for the bunch charge, $\sigma = \sigma_z/c$ for the standard deviation of the bunch duration, and r the distance from the particle bunch. With $\sigma = 5\,\text{ps}$ and a bunch charge of 300 pC we obtain $E_{max} = 1435.2\,/\,r$ [V/m] for the peak electric field strength. The measured value of $203.1 \pm 6.3\,\text{V}$ shown in fig. 5.5 is smaller by a factor 7.1 ± 0.2 than the analytical expectation of 1435.2 V. This is a substantial difference and reflects the expected underestimation of the peak electric field strength due to the bandwidth limitation of the electro-optical probe, as well as the timing jitter of the acquisition system. However, even though this underestimation is expected, it is worth checking whether the combined effects justify its magnitude.

5.1.1 Bandwidth Limitation

As introduced in section 4.5, the electro-optical probes used for the measurement have a high-frequency cutoff $\geq 10\,\text{GHz}$. To have controlled conditions during the experiment and to reduce high-frequency noise, the acquisition bandwidth of the oscilloscope was limited to 10 GHz. Assuming a Gaussian longitudinal profile of the particle bunch with a standard deviation of $\sigma = 5\,\text{ps}$, we investigate the effect of a high-frequency cutoff on the amplitude of the measured signal. In fig. 5.6 the power spectrum and the corresponding time traces are shown for different cutoff frequencies. The black curves are equivalent to the data shown in fig. 3.4 and correspond to a Gaussian pulse with a standard deviation of $\sigma = 5\,\text{ps}$. The power spectra for various cutoff frequencies are obtained by applying a Butterworth low-pass filter of 5^{th} order. As the high-frequency components are missing in the time signal, the recovered amplitude must be smaller than the amplitude of the initial pulse. For the blue curve, corresponding to our case of $f_0 = 10\,\text{GHz}$, the amplitude of the time signal is reduced to approximately 1/4 of its initial value. Furthermore, the ringing of the time signal due to missing frequency components is evident. The ringing period is inversely proportional to the high cutoff frequency

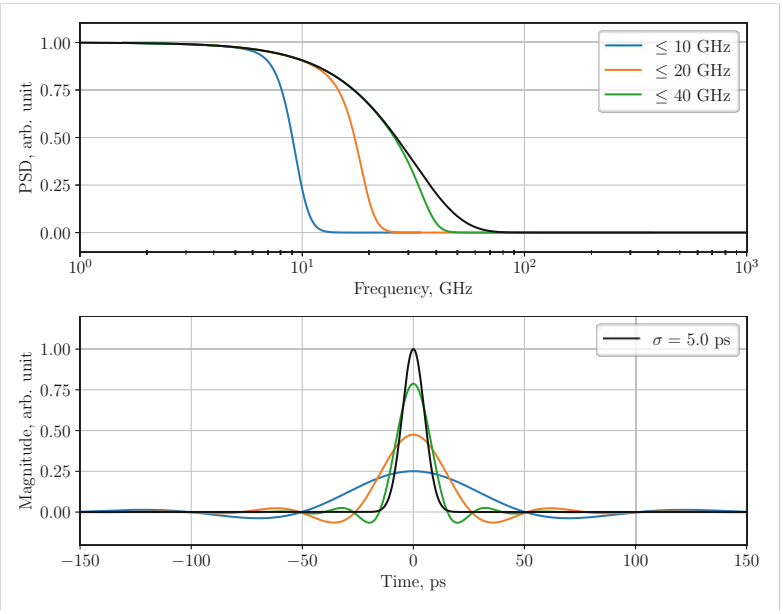

Figure 5.6: Power spectrum and time trace of a Gaussian pulse (σ = 5.0 ps) in black. The bandpass filtered time traces are shown for three different high cutoff frequencies. The amplitude of a 5 ps long pulse is reduced to approximately 1/4 with a 10 GHz high cutoff frequency.

f_0. For the three cutoff frequencies of 40 GHz, 20 GHz and 10 GHz, we obtain a ringing period of 25 ps, 50 ps and 100 ps.

5.1.2 Timing Jitter

As signal levels were low during the measurements, it was necessary to trigger on an external trigger and average the time traces. The average data presented in the calibration measurement was obtained over 600 shots (1 minute at 10 Hz). In fig. 5.7, the obtained averaged signal is depicted on the left. We use the oscilloscope's high sampling rate to estimate the timing jitter. With 256 GSa/s, the time resolution is approximately 4 ps. Each shot was recorded individually at a distance to the beam of approximately 12 mm where also single-shot signals were reasonably high. The individual traces were then aligned at the maximum of each trace and averaged to estimate the single pulse response. This aligned average is depicted in orange in fig. 5.7 on the right side. This jitter-corrected signal has a higher amplitude than the averaged signal in black. The timing jitter in the acquisition system leads to an amplitude of approximately 1/2 of the jitter-corrected signal amplitude. The combined effect of the bandwidth limitation and the timing jitter would then reduce the amplitude to approximately $1/4 \times 1/2 = 1/8$. All averaged results

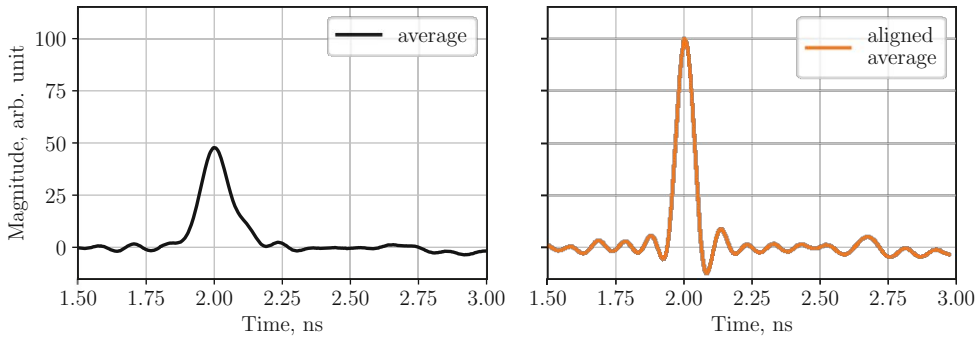

Figure 5.7: The average signal subject to timing jitter is depicted in black. The orange curve represents the aligned average and is obtained by aligning the maxima of single traces. This jitter-corrected curve shows that the averaged amplitude is approximately reduced by a factor of 1/2 due to the timing jitter present in the acquisition system.

would, therefore, need to be scaled up by a factor of 8 according to this rough estimation. Consequently, the obtained correction factor of 7.1 is close to what would be expected, considering the bandwidth limitation and timing jitter of the acquisition system.

The solidity of the jitter-corrected average is confirmed by two features visible in fig. 5.7. Firstly, the ringing period of the aligned average shows the expected periodicity of 100 ps due to the 10 GHz high-frequency cutoff. Secondly, there is a small contribution visible at 2.7 ns. This contribution can be attributed to a second bunch in the train, as it would appear 667 ps after the main peak. This contribution averages out entirely in the averaged signal, whereas it emerges from the noise floor in the aligned average. This contribution stems from a leakage of the CLEAR laser providing the laser pulses for the photocathode. It can be removed by changing the timing window of the pulse-picking setup. These observations show that the aligned averaging yields reasonable results due to the high sampling rate of the oscilloscope.

5.1.3 Bunch Length

During the measurements with electro-optical probes, the RF deflector for longitudinal bunch size measurements was unavailable due to issues with the klystron feeding the deflecting cavity. Without bunching the beam, the bunch length would typically range from 3 to 7 ps. The expected relative amplitude is shown in fig. 5.8 for low-pass filtered Gaussian pulses of different lengths. As already depicted in

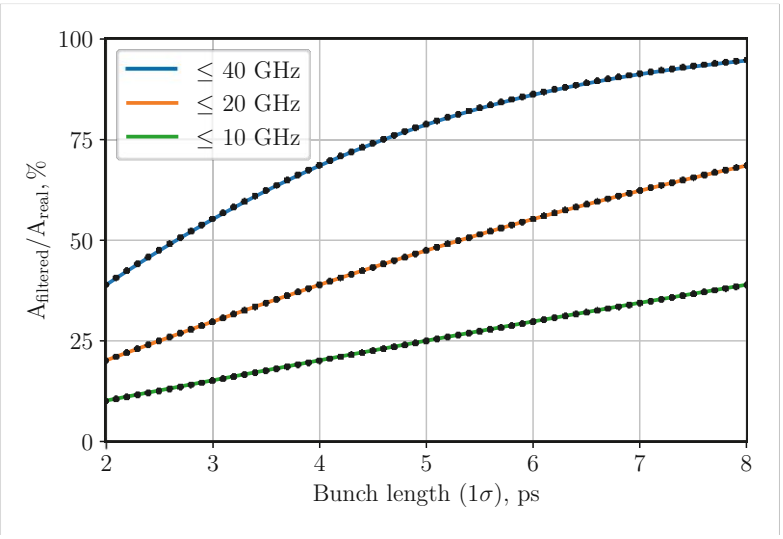

Figure 5.8: Relative amplitude of low-pass filtered Gaussian pulses. For a Gaussian pulse with $\sigma = 5\,\text{ps}$, the amplitude is reduced to approximately 1/4 when considering a 10 GHz cutoff frequency (cf. fig. 5.6).

fig. 5.6, the filtered amplitude reduces to approximately 1/4 for an initial pulse length of 5 ps and a 10 GHz high cutoff frequency. The green curve can be approximated by the linear function $y = 5 \cdot x$, with a negligible deviation less than 1.8% for bunch duration values $3\,\text{ps} \leq x \leq 7\,\text{ps}$. This linear dependence on the bunch duration cancels out with the $1/\sigma$ dependence in equation 5.1. It is, therefore, not possible to extract the real bunch duration from optimising the correction value. Consequently, all data was normalised for a bunch duration of 5 ps. This calibration remains valid for any bunch duration ranging from 3-7 ps, as long as the actual value of the bunch length remains constant throughout the measurement. Assuming one stable bunch length throughout the measurement is much more reliable than estimating a bunch length, which must also stay stable throughout the measurement. The accelerator complex was run under the same conditions for all experiments with electro-optical probes to justify the assumption of constant bunch duration.

However, if the bunch length drifted during the measurement, this would impact the estimated electric field strength according to the green curve in fig. 5.8. The electric field strength would scale inversely for small deviations of the real bunch length. It must be noted that a change in bunch length also impacts the convolution with the timing jitter. However, as the measured signals are low-pass filtered at 10 GHz the dependence of the standard deviation of the measured signal with respect to the initial bunch length is negligible.

5.2 Charge Dependency

The first measurements of CChDR using electro-optical probes concern its dependency on bunch charge as a sanity check. As the bandwidth of the acquisition system is only sensitive to the coherent part of the radiation spectrum, it is expected for the electric field strength to increase linearly with charge. This dependency was derived in section 2.7. Moreover, as the electromagnetic field of the beam is polarising the surface of the dielectric and consequently producing ChDR propagating within the dielectric, also equation 5.1 is a suitable reference for this dependence. At a constant distance r from the dielectric and a constant bunch duration σ, the polarising beam field scales linearly with the bunch charge Q. Furthermore, the linear dependence of CChDR has been demonstrated within specific frequency bands, a behaviour expected for any frequency band in the coherent part of the spectrum and consequently for a broadband acquisition, as presented in this work. Therefore, the linearity of the electric field amplitude is a strong indication of the coherent nature of a beam-generated signal, such as ChDR.

The probe was placed 10 mm away from the exit surface of the radiator, as introduced in fig. 4.6. It was located in the horizontal plane with respect to the beam trajectory and oriented in such a way as to be sensitive to the horizontal component of the electromagnetic field (more details on the polarisation of the field are presented in section 5.3). As signal levels were low, the beam was moved closer to the radiator surface. The distance between the beam and the radiator surface is approximately 20 mm. This offset from the standard impact parameter of 40 mm is achieved by steering the beam horizontally and moving the radiator setup in the horizontal plane, as illustrated in fig. 4.4.

In fig. 5.9, the bunch charge and the insertion loss during the acquisition are depicted. Throughout around 20 min, the bunch charge was reduced from approximately 410 to 60 pC. The attenuation of the bunch charge is achieved by changing the intensity of the CLEAR laser, providing the laser pulses for the photocathode. This attenuation needs to be performed manually in between acquisition windows. The grey columns in fig. 5.9 indicate the acquisition windows for each time trace. The black data points indicate each acquisition window's average and standard deviation. The averaging time was increased to 2 minutes, which resulted in 1200 traces for each data point. This was necessary to increase the signal-to-noise ratio, as signal levels were lower than during the calibration measurement using the direct beam field.

The obtained averaged time traces are depicted in fig. 5.10. For high bunch charges of around 400 pC, we obtain a positive CChDR pulse with its peak located at around 375 ps, followed by a negative pulse at around 500 ps. The absolute time

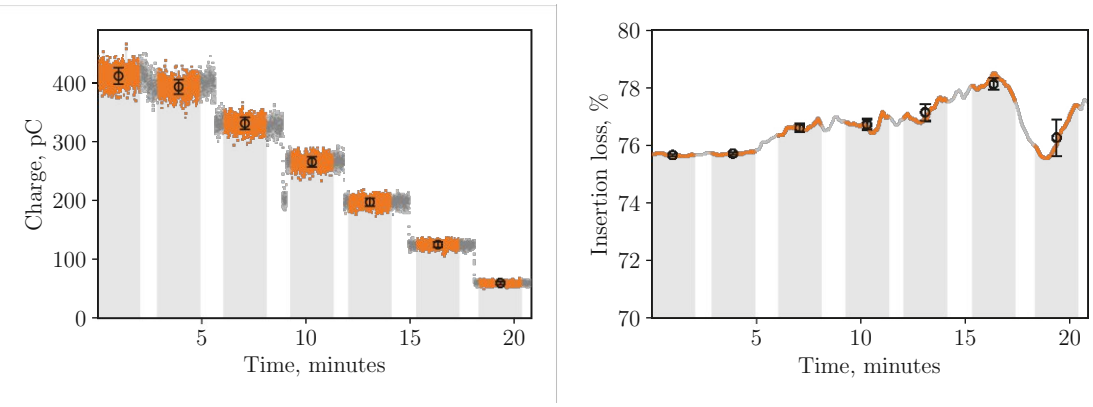

Figure 5.9: Bunch charge and insertion loss during the charge dependency measurement. The charge was varied from approximately 410 to 60 pC. Grey columns indicate the acquisition window for each time trace. The black data points indicate each acquisition window's average and standard deviation.

difference is of minor importance as time resolution is limited by the 10 GHz high-frequency cutoff. However, contrary to the time signals obtained for the direct beam field (cf. fig. 5.2), a negative pulse following the initial pulse indicates a physical electromagnetic field of negative polarity. The first pulse in the signal corresponding to the CChDR signal maintains a uniform shape throughout various bunch charges, with a decreasing signal amplitude for decreasing bunch charges. Also, the location of the peak in time stays rather constant. Contrary to that, the negative pulse following the CChDR signal does not stay uniform in shape, its maxima are not aligned in time, nor do they follow any obvious behaviour when altering the bunch charge. This negative pulse will be discussed in more detail in chapter 6, where the time resolution is high enough to draw more reliable conclusions.

To identify the dependence of the obtained signals with respect to bunch charge, the signals are processed as described in section 4.5. They are corrected for the insertion loss of the acquisition system (cf. fig. 5.9) and scaled according to the correction factor obtained during calibration (cf. section 5.1). It has to be noted that we assume the electromagnetic pulse duration to be constant for all presented measurements as introduced in section 5.1.3. Considering this calibration mechanism, the presented values of the electric field strength are considered an upper margin for the electric field strength of CChDR. The calibration only affects the magnitude of the electric field strength and not its relative change. The linear dependence is, therefore, not affected by this calibration. In fig. 5.11, the peak electric field strength of the CChDR pulse, as identified in fig. 5.10 is depicted as

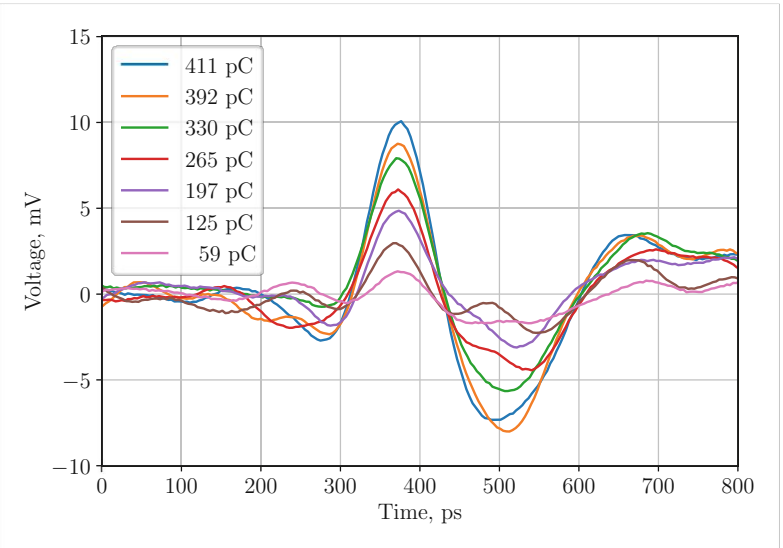

Figure 5.10: Averaged time traces of CChDR for different bunch charges as measured with a high-bandwidth oscilloscope (10 GHz, 256 GSa/s, 10-bit). The traces are subject to bandwidth limitation, as well as insertion loss and timing jitter of the acquisition system.

a function of bunch charge. The data points are shown in black, and the error bars indicate the standard deviation of the electric field strength and the bunch charge accordingly. Each data point is an average of 1200 single-shot acquisitions. A linear fitting function yields a slope of (79.6 ± 6.4) (V/m)/pC. Consequently, the linear dependence of the peak electric field strength of the CChDR signal is demonstrated.

5.3 Polarisation

After identifying the linear dependence of the peak electric field strength with respect to charge, we investigate the polarisation of the electric field. The polarisation of the electric field from CChDR is expected to resemble the radial polarisation of the beam field, a behaviour which was also presented with numerical simulations in section 3.8. As the electro-optical probe is positioned in the horizontal plane, the electric field is expected to be highly linearly polarised in the horizontal direction. In fig. 5.12, the orientation of the electro-optical probe is shown for the horizontal and vertical measurements. The dark blue arrow indicates the axis of the polarisation sensitivity of the electro-optical crystal. The exit surface of the radiator is shown underneath in light blue. The x- and y-coordinates are parallel with the exit surface of the radiator. The probe is located 10 mm from the exit surface within area A_3

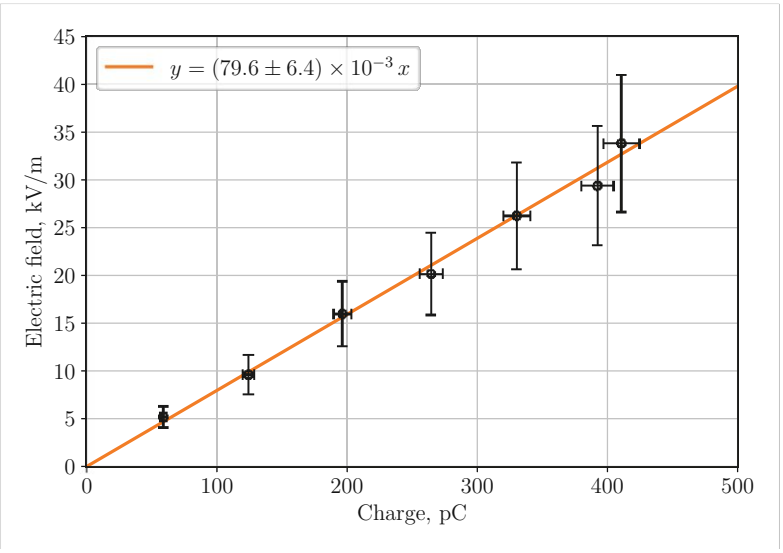

Figure 5.11: Charge dependency of the peak electric field strength of CChDR. Error bars indicate the standard deviation of the measurement and increase for higher charges due to larger fluctuations of the bunch charge (cf. fig. 5.9). The parameter for the linear fitting function in orange is provided in the legend.

as defined in fig. 3.11. The coordinate system in fig. 5.12 is therefore rotated by the Cherenkov-angle θ_{Ch} to be parallel with the exit surface of the radiator.

In fig. 5.13, the bunch charge and insertion loss are provided analogous to the previous measurements. The contribution from vertical polarisation is expected to be negligible compared to that from horizontal polarisation. To improve the signal-to-noise ratio, this measurement's acquisition window was extended to 4 minutes, corresponding to 2400 single shots. To obtain higher signal levels, this measurement was conducted using the in-air setup (cf. section 4.3.3) in the in-air test stand at the end of the CLEAR accelerator (cf. fig. 4.1). The bunch charge for each acquisition window was kept at approximately 400 pC and the impact parameter was reduced to 10 mm.

The average time traces are presented in fig. 5.14, and the signals are processed as described in section 4.5. They are normalised to a bunch charge of 300 pC, corrected for the insertion loss of the acquisition system (cf. fig. 5.13) and scaled according to the correction factor obtained during calibration (cf. section 5.1). The traces are recorded in the order as presented in the legend of fig. 5.14. The blue curves correspond to the first set of measurements. The horizontal component was measured, and right afterwards, the electro-optical probe was rotated by 90° as indicated in fig. 5.12. Afterwards, the probe was rotated back to its horizontal

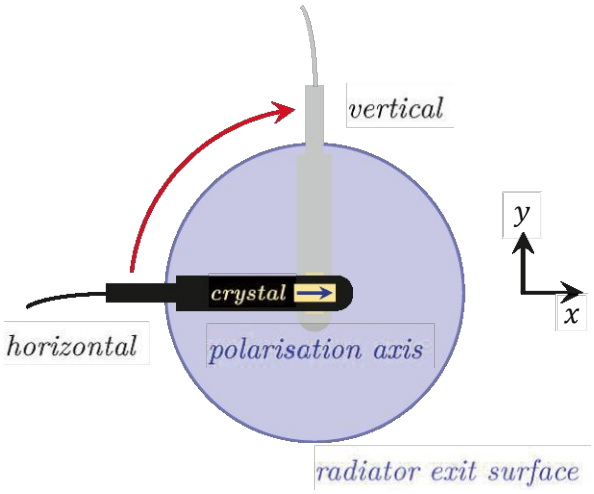

Figure 5.12: Orientation of the electro-optical probe for different polarisations. The probe is positioned parallel to the exit surface of the radiator at a distance of 10 mm (cf. P_3 in fig. 3.11). The dark blue arrow indicates the axis of polarisation sensitivity of the electro-optical crystal and is equivalent with $\vec{e}_{Ch}$ in fig. 3.11. For the beam travelling from left to right, the electric field from ChDR is expected to be aligned with $\vec{e}_{Ch}$.

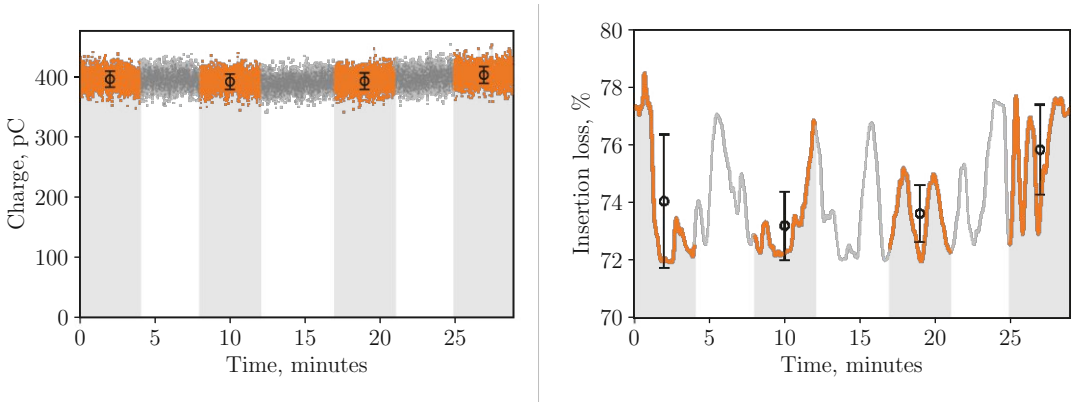

Figure 5.13: Bunch charge and insertion loss during the polarisation measurement. The charge was kept stable at 400 pC. Grey columns indicate the acquisition window for each time trace. The black data points indicate each acquisition window's average and standard deviation.

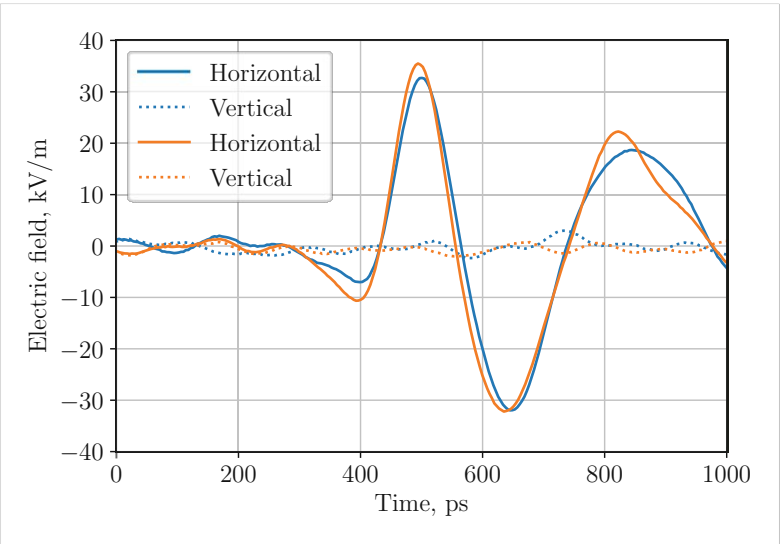

Figure 5.14: Averaged time traces for the horizontal and vertical polarisation components as illustrated in fig. 5.12. The legend reflects the order of measurements, switching back and forth between probe orientations.

position. Then, the second set of measurements was acquired and is depicted by the orange curves. As expected from simulations, the vertical component is below the noise floor of the measurement and is negligible compared to the horizontal component of the electric field. It is demonstrated that the polarisation of the CChDR propagating within the dielectric is maintained and resembles the polarisation of the beam field inducing the CChDR in the first place.

5.4 Impact Parameter

Similar to the procedure presented in section 5.1, the peak electric field strength was measured for different distances h between the radiator and the beam. Analogous to the calibration measurement, the distance is the only parameter that alters the strength of the beam field, which is not a property of the beam itself. Therefore, changing the impact parameter h leaves all the beam properties untouched, resulting in stable measurement conditions. To have an extensive range of the impact parameter, this measurement was conducted using the in-air setup (cf. section 4.3.3) in the in-air test stand at the end of the CLEAR accelerator (cf. fig. 4.1). To keep the beam position as controlled as possible, instead of steering the beam in the horizontal plane, the whole setup was moved horizontally with respect to the beam position. The radiator assembly, including the electro-optical probe, was moved to cover an impact parameter range of 10 to 50 mm.

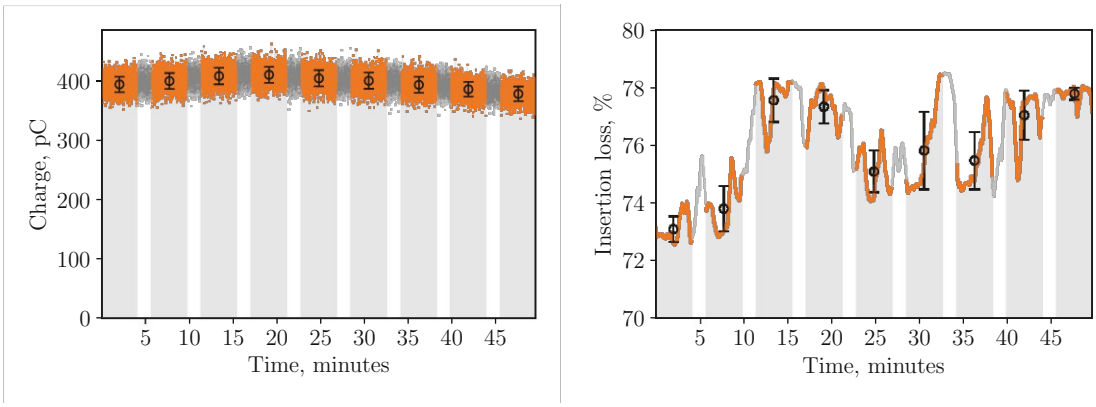

Figure 5.15: Bunch charge and insertion loss during the impact parameter scan. The charge was kept at approximately 400 pC. Grey columns indicate the acquisition window for each time trace. The black data points indicate each acquisition window's average and standard deviation.

The average time traces for various impact parameters are depicted in fig. 5.16. The acquisition window was extended to 4 minutes to improve the signal-to-noise ratio, corresponding to 2400 single shots. The bunch charge for each acquisition window was kept at approximately 400 pC to increase signal strength. The time traces are normalised to a bunch charge of 300 pC, corrected for the insertion loss of the acquisition system (cf. fig. 5.15) and scaled according to the correction factor obtained during calibration (cf. section 5.1).

In fig. 5.17, the peak electric field strength of the CChDR pulse is depicted as a function of the impact parameter h. The traces are corrected for charge fluctuations and insertion loss and calibrated as presented in section 5.1. The data points are shown in black, and the error bars indicate the standard deviation of the measurement. It has to be noted that we assume the electromagnetic pulse duration to be constant for all presented measurements as introduced in section 5.1.3. Considering this calibration mechanism, the presented values of the electric field strength are considered an upper margin for the electric field strength of CChDR. The calibration only affects the magnitude of the electric field strength and not its relative change. Therefore, this calibration does not affect the 1/h dependence of the fitting function. The obtained constant of (354 ± 25) V is lower than the expectation from the simulation of (401 ± 18) V. The impact parameter dependence measurement still yields an agreement of 88.3 ± 7.4 % compared to simulations. Notably, for all data points with $h \leq 40$ mm, the simulated expectation lies within $1\,\sigma$ of the standard error of the measurement.

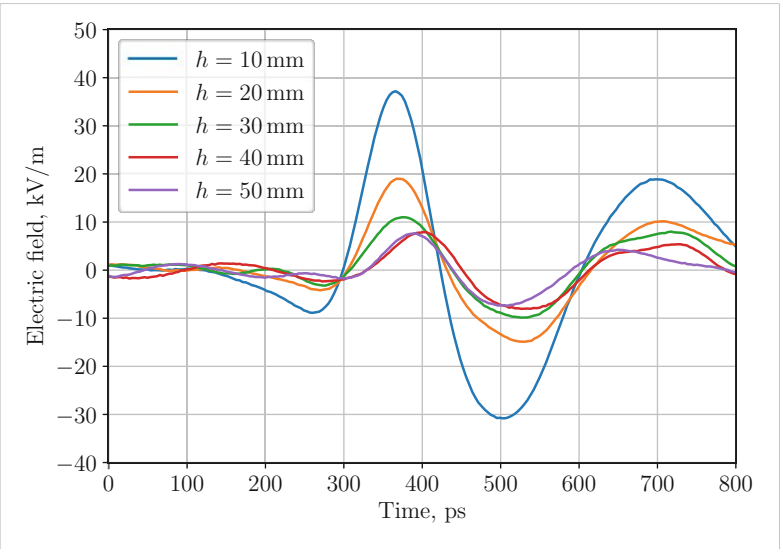

Figure 5.16: Several averaged time traces of the CChDR signal for various impact parameters h. Signal levels decrease for larger impact parameters. The traces are corrected for charge fluctuations and insertion loss and calibrated as presented in section 5.1.

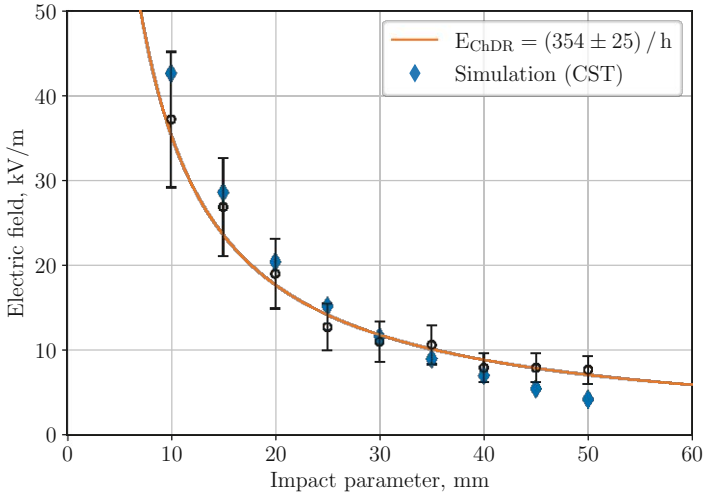

Figure 5.17: Peak electric field strength of CChDR as a function of the impact parameter h. A fitting function with a 1/h dependence is plotted in orange. The expected peak electric field strength from simulations is plotted in blue and taken from fig. 3.19.

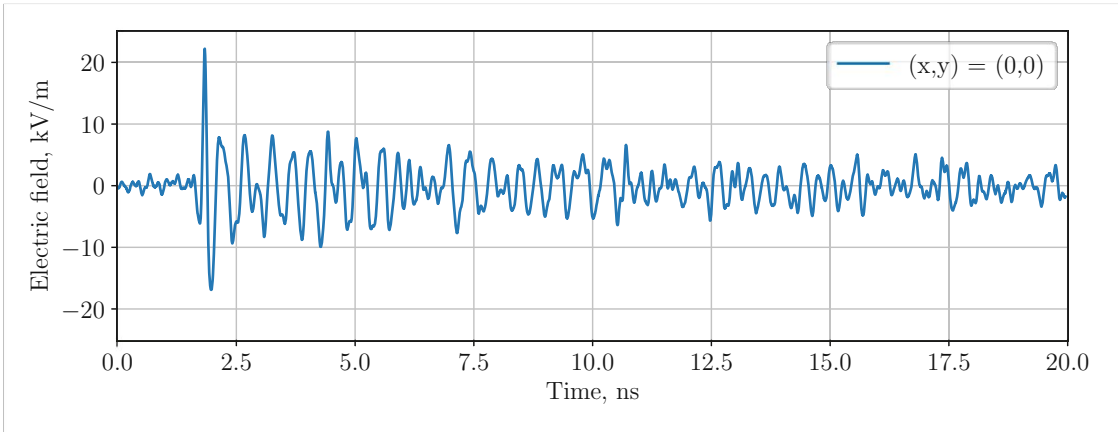

Figure 5.18: 20 ns long time trace at the exit surface of the radiator. The trace is acquired at the centre of the exit surface (x,y) = (0,0) at a distance of 10 mm from the exit surface. This point corresponds to P_3 as introduced in fig. 3.11.

5.5 Time Domain

So far, we have investigated the first peak of the signal, which we identified as the peak of the CChDR pulse. However, in section 3.10.2, we have seen that the radiation within the dielectric (ChDR and DR) is partially reflected inside the radiator, which leads to ripples in the time trace. A 20 ns long averaged time trace over 2400 single shots is depicted in fig. 5.18. The averaged trace was normalised to a bunch charge of 300 pC, corrected for insertion loss and calibrated according to the results from section 5.1. The electro-optical probe was located at the centre of the exit surface 10 mm from the radiator, as illustrated for the horizontal position in fig. 5.12. The distance between the beam and the radiator surface is approximately 20 mm. Even after tens of nanoseconds after the initial pulse, a significant contribution is visible in the time trace. These contributions would interfere with the signal generated by a second bunch if their bunch spacing is of the order of tens of nanoseconds, as foreseen for FCC-ee. The following sections identify the cause of these ripples in the frequency domain. They are caused by the radiator geometry, and a final radiator design would need to be optimised to reduce these contributions.

5.6 Frequency Domain

Except for the duration of the unintended signals following the initial CChDR pulse, the time trace presented in fig. 5.18 is challenging to analyse in the time

domain. For this reason, we investigate the frequency domain, which will turn out to be of high interest in understanding those signals.

5.6.1 Reflections

To investigate the frequency content of the time domain signal presented in fig. 5.18, we have a closer look at the power spectrum of the data. To improve the resolution of the spectrum, the time trace was extended in time with a Gaussian-distributed noise floor resembling the noise floor of the initial signal. As presented in section 3.10.2 for the power spectrum of long time traces, which also include the reflections within the radiator, we expect some resonant frequencies of the radiator to be prominent in the spectrum. They are shown in fig. 3.18 and the three most prominent frequencies were identified as 1.75 GHz, 2.15 GHz and 2.76 GHz in the simulation. In fig. 5.19, the measured power spectrum is shown alongside the simulated power spectrum. The three most prominent frequencies present in the measured spectrum are 1.72 GHz, 2.12 GHz and 2.70 GHz. They differ from the expected frequencies by approximately 2% each. In table 5.1, the prominent measured frequencies and their corresponding wavelengths are provided. The strongest frequency corresponds to a wavelength of 47.1 mm in the radiator, with the central axis length of the radiator being 47.6 mm. The second and third strongest frequencies correspond to a wavelength of 37.0 mm and 58.1 mm and can be related to the width and diagonal dimension of the radiator.

$\mathbf{f, GHz}$	$\lambda(\varepsilon_\mathbf{r} = \mathbf{1}), \mathbf{mm}$	$\lambda(\varepsilon_\mathbf{r} = \mathbf{9}), \mathbf{mm}$
1.72	174.3	58.1
2.12	141.4	47.1
2.70	111.0	37.0

Table 5.1: Notable frequencies of the radiator signal and their corresponding wavelengths in vacuum, as well as alumina with $\varepsilon_r = 9$.

5.6.2 Cutoff Frequency

As presented in section 3.10.2, the radiator can also be considered a circular dielectric-loaded waveguide. With a diameter of 36 mm and a relative permittivity of $\varepsilon_r = 3.0$, we obtained a cutoff frequency for the dominant $TE_{1,1}$ mode of $f_{1,1} = 1.63$ GHz. This cutoff is also visible in the power spectrum, as presented in fig. 5.19. The long time trace with its several internal reflections gives the impression of the radiation travelling through a much longer radiator. The longer the radiator,

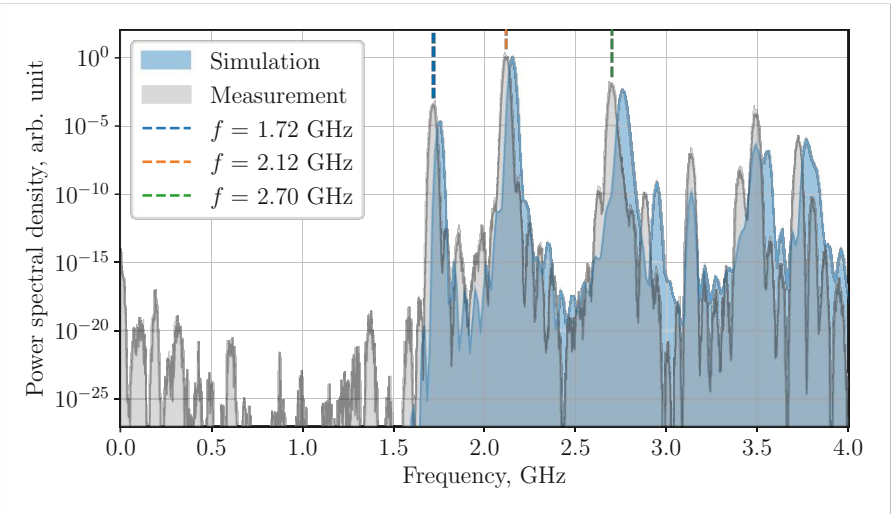

Figure 5.19: Power spectrum of the electric field component parallel to $\vec{e}_{Ch}$ at a distance of 10 mm from the radiator surface, corresponding to point P_3 as indicated in fig. 3.11. The spectrum is normalised to its maximum value at $f = 2.12$ GHz, and dashed lines are used to highlight the three most prominent resonant peaks. The simulated power spectrum is shown in light blue (cf. fig. 3.18).

the more prominent the low-cutoff frequency is expected to be. However, we are also interested in the cutoff of the initial pulses, which have not been reflected yet.

The time trace presented in fig. 5.18 is subject to timing jitter, which does affect the power spectrum. We, therefore, align the maxima of the single-shot traces in time, analogous as presented in fig. 5.7. The jitter-corrected trace is then cut in time 0.9 ns after the peak of the CChDR pulse, which does not allow any reflection of the initial signal to exit the radiator and contribute to the power spectrum. To improve the resolution of the spectrum, the time trace was extended in time with a Gaussian-distributed noise floor resembling the noise floor of the initial signal. In fig. 5.20, the power spectrum of this jitter-corrected pulse without any reflections present in the time trace is depicted. The low cutoff frequency at $f_{1,1} = 1.63$ GHz is visible in the power spectrum. For comparison, the power spectrum of the jitter-corrected pulse of the direct beam field is also presented.

5.7 Field Distribution

The CChDR wavefront is expected to be rather uniformly distributed when exiting the radiator. The simulations for the 2D field distribution were presented in sec-

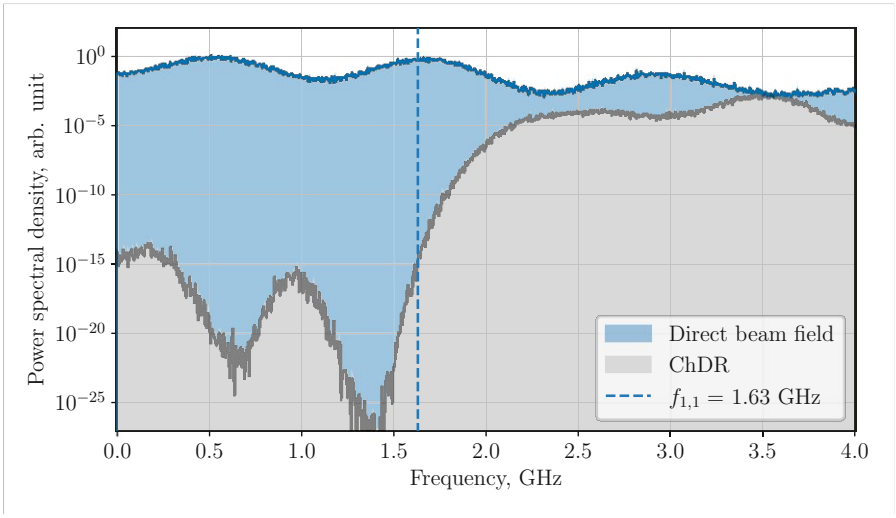

Figure 5.20: Power spectrum of the electric field of the jitter-corrected pulses. In light blue, the power spectrum of the direct beam field is depicted, indicating the probe's response. In grey, the power spectrum of the CChDR pulse, omitting any multiple reflections within the radiator, is shown. The dashed blue line represents the analytical low cutoff frequency of the TE_{11} mode of an infinite dielectric-loaded circular waveguide.

tion 3.7, and the fact that ChDR is a surface effect does anticipate this expectation. The probe was kept in the horizontal position to scan the field distribution at the exit surface, as depicted in fig. 5.12. The probe was then moved parallel to the exit surface at a distance of 10 mm from the surface, corresponding to the area A_3 as introduced in fig. 3.11. The centre of the area A_3 is defined as the zero point in that plane, (x,y) = (0,0). The vector $\vec{e}_{Ch} = [0, -cos(\theta_{Ch}), sin(\theta_{Ch})]$ as defined in section 3.8, corresponds to (x,y)=(1,0) in the new coordinate system for the 2D plane.

The probe was moved in steps of 5 mm in the horizontal direction (x-axis), corresponding to the probe's active crystal length. In the vertical direction (y-axis), the probe was moved in steps of 3 mm, as available measurement time did not allow for a step size of 1 mm, which would correspond to the probe's active crystal diameter. The measurement was started at point (x,y)=(-10,9) and continued in horizontal lines from left to right until point (x,y)=(10,-9). The acquisition window for each data point was 2 minutes, corresponding to 1200 single-shot traces. The measurement of all points took approximately 1 hour and 45 minutes. The bunch charge shifted significantly to higher values during this time, as shown in fig. 5.21. In fig. 5.23, the peak electric field strength of the CChDR pulse is depicted for the various scanned positions. The presented values are normalised to a bunch

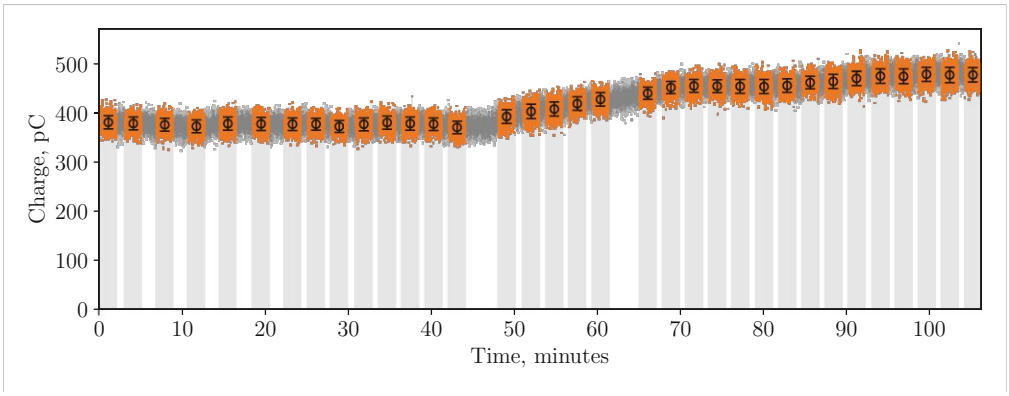

Figure 5.21: Evolution of bunch charge during the field distribution scan. Grey columns indicate the acquisition window for each time trace. The black data points indicate each acquisition window's average and standard deviation.

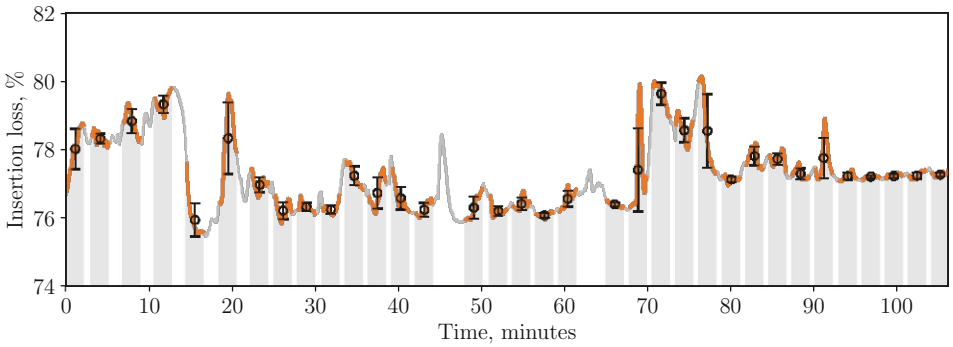

Figure 5.22: Evolution of insertion loss during the field distribution scan. Grey columns indicate the acquisition window for each time trace. The black data points indicate each acquisition window's average and standard deviation.

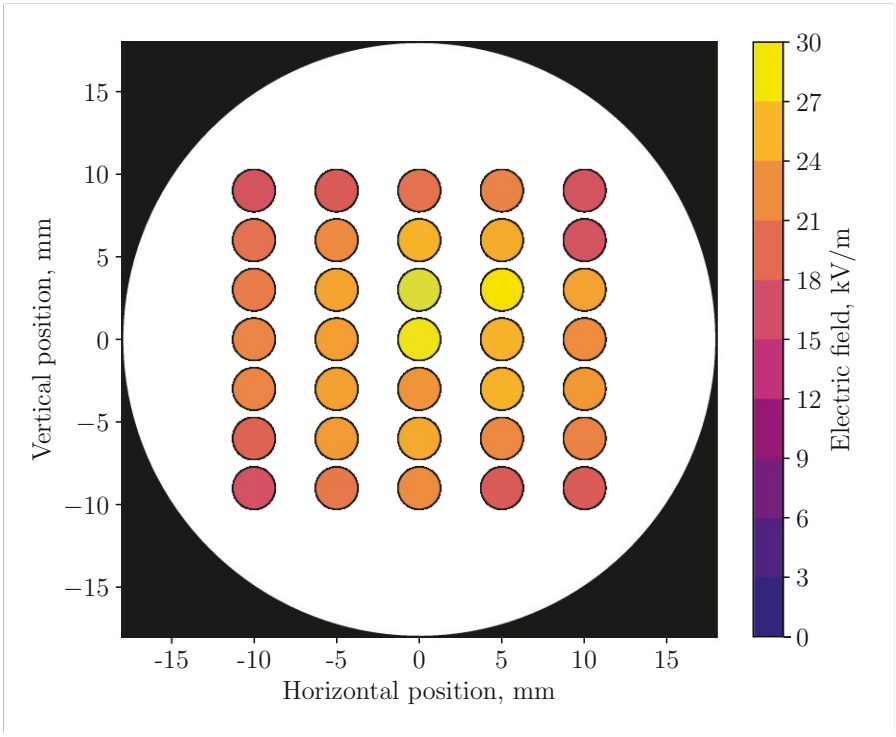

Figure 5.23: Peak electric field strength of the CChDR pulse at various locations after the exit surface. The area depicted corresponds to the area A_3 as defined in fig. 3.11.

charge of 300 pC (cf. fig. 5.21), corrected for the insertion loss of the acquisition system (cf. fig. 5.22) and scaled according to the correction factor obtained during calibration (cf. section 5.1). The surface distribution of the peak electric field strength shows a clustering of higher values in the very centre and a decay towards the radiator edges. This is also shown in fig. 5.24, where the horizontal and vertical profiles of the surface scan are presented. The data points indicate a trend for an axial symmetry of the signal amplitudes. The grid density and the amplitude resolution are too low to reliably reconstruct a 2D distribution. However, for beam diagnostic purposes, it is evident that the probe's location should be preferably centred close to the radiator's axis, whereas a small offset of a few millimetres does not have a significant impact on the signal amplitude.

To complement fig. 5.23, various time traces used to create this 2D grid are shown for several different points in fig. 5.25. On the left, the average time traces are shown for the outermost points of the central horizontal and central vertical lines. The peak signal of those traces was also used for some of the data points depicted in fig. 5.24. On the right, the average time traces for the outermost points in the

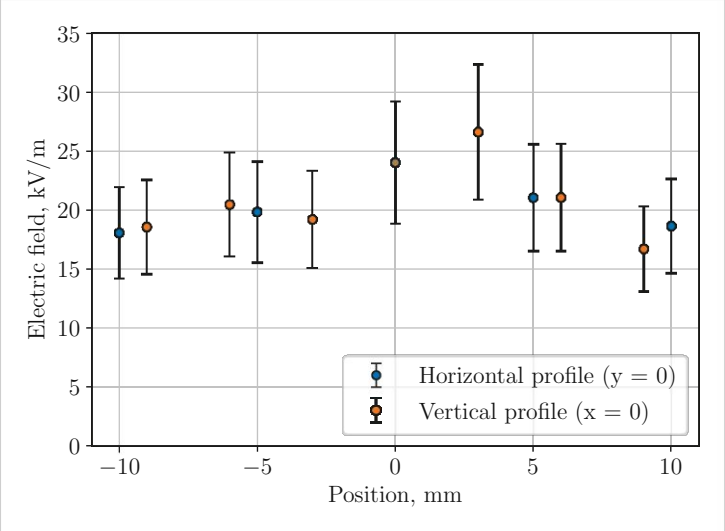

Figure 5.24: Peak electric field strength of CChDR for the horizontal (y = 0) and vertical profile (x = 0) for the data points depicted in fig. 5.23.

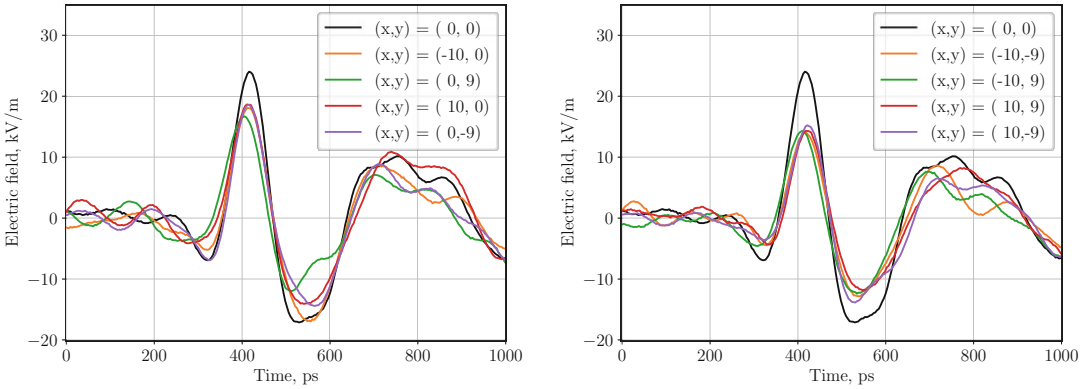

Figure 5.25: Average time traces at various locations after the exit surface of the radiator. On the left, the outermost points of the central horizontal and vertical row are shown. On the right, the corner points of the grid are depicted. The black trace at (x,y)=(0,0) is shown in both plots for reference.

corners of the grid are shown. For comparison, both plots show the time trace for the central point (0,0) of the 2D grid in black. In these plots, the attenuation of the CChDR pulse towards the edges is clearly observed, and the obtained curves show a symmetrical behaviour with respect to the centre of the radiator.

5.8 Findings based on Electro-optical Probes

The measurements performed with electro-optical probes elucidate various key results:

- The coherent nature of ChDR was confirmed by the proportionality of its electric field strength to the total bunch charge.
- The polarisation of CChDR after propagating through the radiator still retains the horizontal component of the radial polarisation as dictated by the electromagnetic field of the beam.
- The absolute value of the electric field strength of a CChDR signal was measured for the first time and agrees well with numerical simulations.
- The peak electric field strength was measured as a function of the impact parameter, and its behaviour shows good agreement with the 1/r decay of the beam field.
- The emitted signals are subject to multiple reflections within the radiator for observation times of tens of nanoseconds.
- The low-frequency cutoff of the radiator was measured for the first time and agrees well with the analytical prediction.
- The electric field strength of CChDR exhibits a uniform distribution at the exit surface of the radiator with a tendency of slightly higher amplitudes in the very centre of the radiator axis.

6

Experimental Characterisation using Electro-optical Spectral Decoding

This chapter introduces the measurement results obtained with the electro-optical spectral decoding setup as presented in section 4.6. The pulse response of the acquisition system for long and short time windows is analysed using coherent transition radiation (CTR). Afterwards, the CChDR signal in the time domain is presented, and various of its characteristics are discussed. The coherent nature of the signals for small bunch charges, the pulse response of the ChDR radiator, the contributions from diffraction radiation and the trailing fields behind the main CChDR pulse are shown. The obtained results are discussed with respect to the expectations from numerical simulations in chapter 3.

In chapter 5, several properties of ChDR were demonstrated using electro-optical probes. The coherent nature of the emission, the impact parameter dependence, the polarisation and the absolute value of the electric field strength were shown. The main drawback of the electro-optical probes is their sensitivity, which requires long integration times, the temporal jitter of the acquisition system and most importantly, the bandwidth limitation of 10 GHz. To overcome these limitations and analyse the temporal structure of CChDR, an experimental apparatus based on electro-optical spectral decoding (EOSD) was developed and introduced in section 4.6. All measurements presented in this chapter were conducted with the EOSD setup.

6.1 Temporal Alignment

The experimental apparatus used in the previous chapter 5 relies on a continuous wave laser for the measurements and does not require any temporal alignment procedure. As EOSD relies on short laser pulses of several ps in length, those laser pulses must be temporally aligned with the signal to be measured. In systems where the laser pulse travels in free space, the temporal overlap can be found by producing optical transition radiation with the particle bunch and letting the laser pulse reflect off the same screen. Using a streak camera or a fast photodiode, temporal alignment is achieved by delaying one pulse with respect to another. This procedure could not be performed with the given setup, as the laser pulses travel only in fibre throughout the accelerator hall. However, the benefit of the Mach-Zehnder intensity modulator is that it can be fed any RF signal. Therefore, the beam-generated transition radiation was directly collected with the horn antenna connected to the modulator. To find the temporal overlap, the transition radiation signal was read out using a continuous wave fibre-coupled laser source [96], a fast photodiode [114] and a 10 GHz oscilloscope [115]. The measured arrival time was noted, and the laser input was changed back to the pulsed laser source. The laser pulse was then delayed to the estimated arrival time of the transition radiation signal using the delay stage.

6.2 Calibration with Coherent Transition Radiation

As we are interested in measuring an ultra-short pulse, it is necessary to assess the performance of the whole detection chain of the EOSD setup. By just taking the values from the data sheets of the corresponding parts, we find that we are restricted by the low-frequency cutoff of 6.5 GHz and high-frequency cutoff of

18.0 GHz from the horn antenna. The low-cutoff frequency represents a hard limit, as the aperture dimensions of the antenna limit the input frequency. However, the high cutoff does not represent a hard limit, especially for receiving signals. The high-frequency cutoff of the intensity modulator is given as > 25 GHz. The transmission line from the signal capture within the antenna to the modulator input is only a few centimetres, which minimises the attenuation of the high-frequency components in the RF signal. To test the response of the EOSD setup, ideally, one would have a Dirac delta function at hand to feed into the system. This, by definition, would have a uniform power spectral density. Generating actual ultra-short testing pulses in the ps time scale is challenging. However, we have the advantage of having a particle beam available for testing CChDR, and the same particle beam is useful for generating ultra-short electromagnetic pulses. For this matter, we use coherent transition radiation (CTR). To expand the coherent part of the spectrum to higher frequencies, the bunch length was shortened to approximately 0.5 ps. The power spectrum of a Gaussian bunch with a standard deviation of $\sigma = 0.5$ ps is shown in fig. 6.1 in black. The power spectrum reaches frequencies up to several 100 GHz. Using the power spectrum, it is interesting to see how different frequency cutoffs influence the temporal distribution of the initial pulse. We consider the low-frequency cutoff of the antenna at 6.5 GHz and increase the high-frequency cutoff from 20 GHz (blue curve) to 40 GHz (orange curve) and 80 GHz (green curve). The low-frequency cutoff at 6.5 GHz corresponds to a time of 154 ps, and its influence on the temporal distribution is negligible for short pulses on the timescale of several ps. This is also visible by the baseline of the temporal signals depicted in fig. 6.1, which is similar to the one we obtained for Gaussian pulses without any low-frequency cutoff in fig. 5.6. However, the high-frequency cutoff substantially influences the achievable temporal resolution. As shown in fig. 6.1 a pulse of $\sigma = 0.5$ ps, is broadened to a standard deviation of 12.4 ps, 6.4 ps and 3.2 ps for cutoff frequencies of 20 GHz, 40 GHz and 80 GHz, respectively. This is to show intuitively that by measuring the short-pulse response of the system, we can estimate the maximum bandwidth of our system.

For short bunches, the energy of the electrons at CLEAR is typically less than the nominal 200 MeV, as the velocity bunching is performed with one of the accelerating structures. The energy was measured to be approximately 170 MeV during the measurements presented in this chapter, corresponding to a gamma value of $\gamma \approx 334$ for electrons.

6.2.1 Spectral and Angular Energy Distribution of CTR

The experimental configuration during the calibration is shown in fig. 6.2. The distance between the aperture of the horn antenna and the beam trajectory was

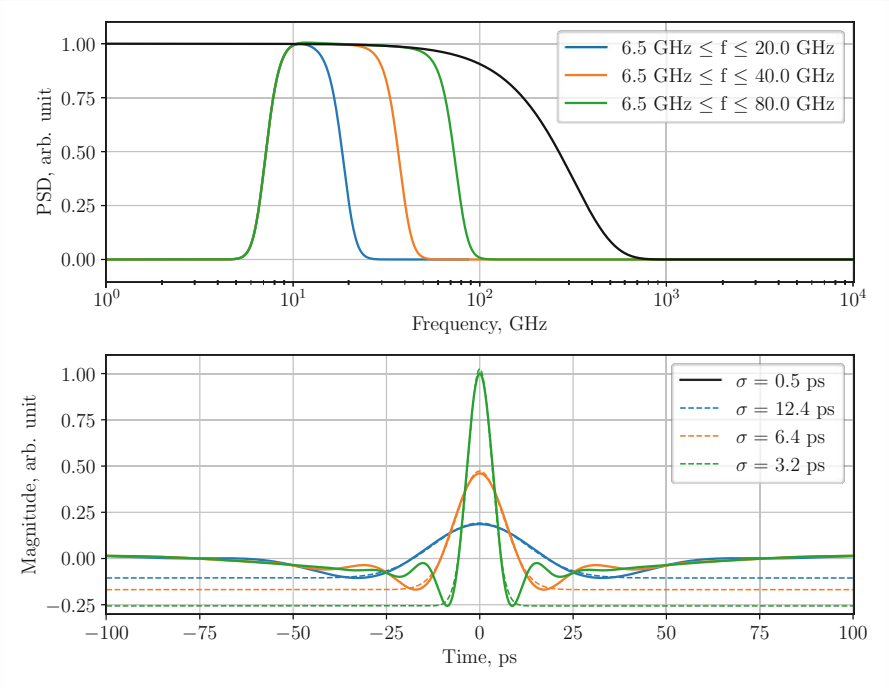

Figure 6.1: In the top plot, the power spectrum of a Gaussian pulse with a standard deviation of $\sigma = 0.5\,\text{ps}$ is shown in black. Various bandpass limited power spectra are represented in colour. The low cutoff arises from the horn antenna, while the high cutoff remains to be determined in the calibration measurement. In the bottom plot, the temporal signal of the bandpass-filtered Gaussian pulse is presented to illustrate the widening of the initial pulse. The temporal signals are fitted with a Gaussian function aligned to the minimum of each respective temporal signal and plotted in dashed lines.

fixed to a distance $d = 25\,\text{cm}$, whereas the distance to the waveguide of the horn antenna was $d + l = 35\,\text{cm}$ in total. The silicon wafer used as a transition screen had a diameter of 4 inches, corresponding to a radius of $a \approx 5.1\,\text{cm}$. The wafer was positioned at an angle of 45° with respect to the beam trajectory for the backward transition radiation to be emitted at 90° with respect to the beam.

After defining the beam parameters and the setup configuration, we estimate where the horn antenna should be placed to capture the CTR. As introduced in section 2.3, the spectral and angular energy distribution of backward transition radiation of a single particle is described by equation 2.11 for the near-field case and a limited transition radiation screen size. The angular distribution is then calculated for $\gamma = 334$, an observation distance of $L = 35\,\text{cm}$ and a transition

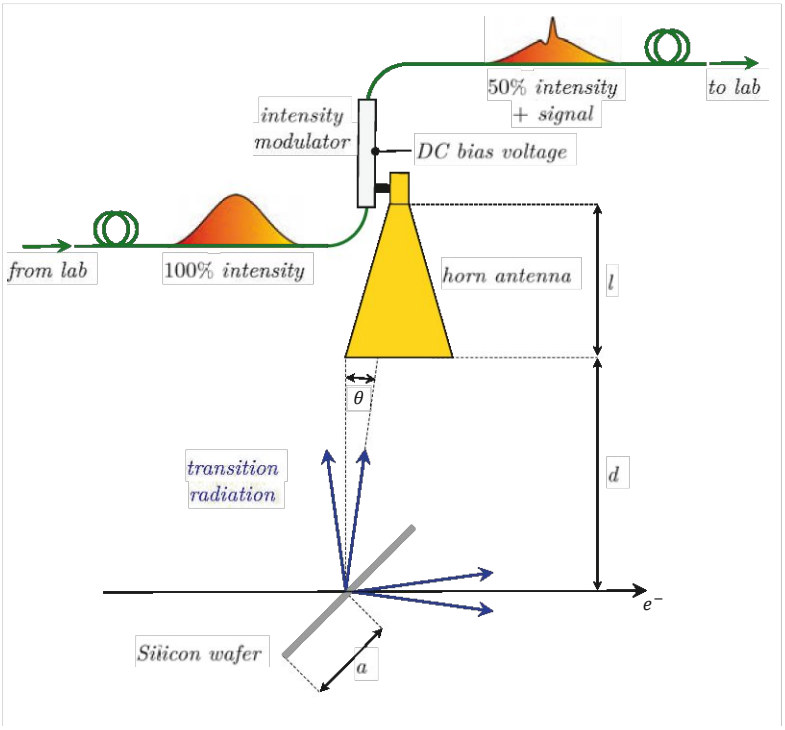

Figure 6.2: Schematic of the calibration setup with coherent transition radiation. The silicon wafer with a radius $a \approx 5.1\,\mathrm{cm}$ is placed at 45° with respect to the beam trajectory. The edge of the horn antenna aperture is aligned with the centre of the wafer. The backward transition radiation cone is centred around 90° with respect to the beam trajectory, and the angle θ denotes the deviation from this axis. The horn aperture was placed at a distance $d = 25\,\mathrm{cm}$ from the beam, with the horn having a length $l = 10\,\mathrm{cm}$.

screen radius of $a = 5.1\,\mathrm{cm}$. The obtained angular distribution for frequencies from 10 to 100 GHz is shown in fig. 6.3. The distribution is symmetric in θ, showing only one slice of the full circle. As expected, the peak of the angular distribution approaches smaller values of θ the higher the frequency. However, because the given configuration does not fulfil the Ginzburg-Frank condition of $a > r_{\mathrm{eff}}$ and $L > \gamma\, r_{\mathrm{eff}}$, the angular distribution deviates strongly from the Ginzburg-Frank equation. For comparison, the peak intensity for the Ginzburg-Frank distribution would be expected at $\theta \sim \gamma^{-1} \sim 0.2°$. The angular distribution at 100 GHz has its maximum at approximately 4.5°. Considering the distance of $L = 350\,\mathrm{mm}$, the horn antenna should be offset by approximately 2.7 cm to be aligned with the maximum. However, to ease alignment, the antenna was positioned for its outer edge to be flush with the centre of the silicon wafer, as shown in fig. 6.2. With the

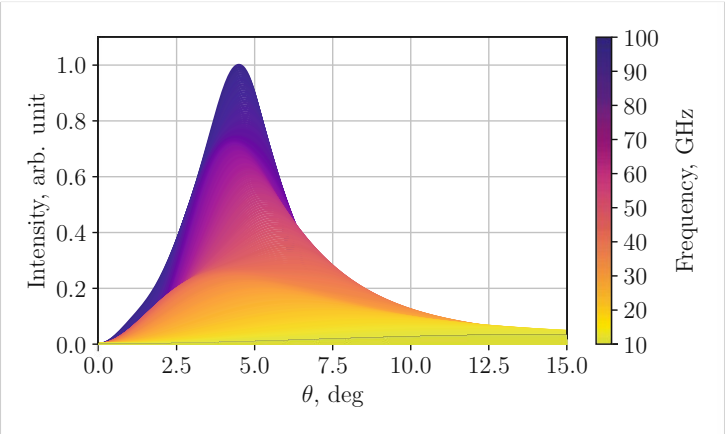

Figure 6.3: Angular energy distribution for the experimental setup used during the calibration measurement with CTR (cf. fig. 6.2). Calculated using equation 2.11 with parameters E = 170 MeV ($\gamma \approx 334$), distance to source $L = 35$ cm and disk radius $a = 5.1$ cm.

antenna's central axis being 3.3 cm from its edge, the waveguide entrance of the antenna is positioned at an angle $\theta \approx 5.4°$, with the horn collecting the radiation for angles $0° \leq \theta \leq 15.3°$. The angular distribution depicted in fig. 6.3 therefore represents the angular acceptance of the horn antenna in the given configuration.

In this configuration, we investigate the spectral distribution by integrating the intensity over θ in the range from 0° to 15° for each frequency. The obtained spectral energy distribution is depicted in fig. 6.4. The spectrum is continuous, with an increase in energy for higher frequencies. The spectrum flattens out for even higher frequencies. However, the coherent part of the power spectrum of a Gaussian bunch with a bunch duration of $\sigma = 0.5$ ps has substantial contributions only up to ~ 100 GHz, as presented in fig. 6.1. The coherent part of the power spectrum scales with $\sim N^2$ as presented in section 2.7 and CTR will therefore be highly dominated by frequencies up to ~ 100 GHz. Even though, ideally, one would prefer a flat frequency response, the CTR pulse exhibits suitable characteristics for measuring the short pulse response, given its continuous spectrum, which is dominated by higher frequencies and increases by less than 3 dB from 40 to 100 GHz.

6.2.2 Long Laser Pulse

The first set of measurements is performed with a long laser pulse. Details on stretching the laser pulse with a CFBG are presented in section 4.6.2. The pulse length of the long laser pulse just before entering the modulator was estimated as $\text{FHWM}_{long} \approx 280$ ps. It also has to be noted that the long laser pulse exhibits a

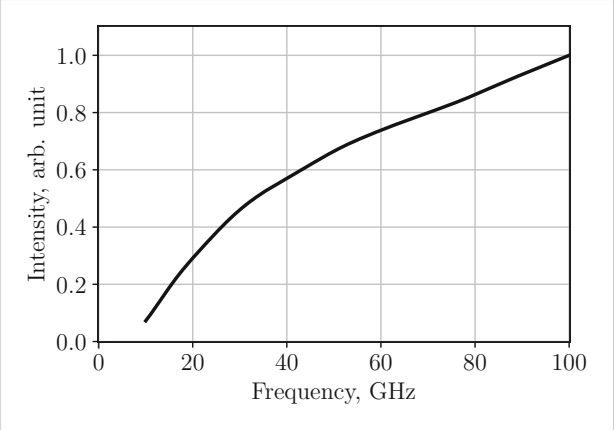

Figure 6.4: Spectral energy distribution of a single particle for angles $0 \leq \theta \leq 15$, corresponding to the θ acceptance of the horn antenna. The coherent part of the power spectrum of a Gaussian bunch of 0.5 ps ($1\,\sigma$) decays significantly for frequencies higher than ~ 100 GHz, as shown in fig. 6.1.

negative chirp at the location of the modulator. The leading edge, therefore, has shorter, and the trailing edge has longer wavelengths, as illustrated in fig. 4.7.

Transfer Function

Before conducting any measurements, the modulator's transfer function needs to be known. The transfer function is required to select the correct working point, which is crucial for interpreting the obtained signal correctly. As introduced in section 4.6.3, the linear regime of the transfer function corresponds to the quadrature point with 50% transmission of the incoming laser light. The quadrature point is reached by setting the bias voltage to the voltage V_{50}, which needs to be determined. As shown in section 4.6.3, the transfer function of the modulator is subject to drifts for changes in the working point. This led to the implementation of a procedure of switching the bias voltage so that the integrated voltage remains constant, as introduced in fig. 4.19. All transfer functions in this chapter have been obtained using this switching technique. The obtained transfer function of the modulator with the long laser pulse is shown in fig. 6.5. The obtained voltage $V_{50} = -0.84$ V is shown in the legend, together with the minimum bias voltage V_0 and maximum bias voltage V_{100}. It has to be noted that obtaining the transfer function is an iterative process in which V_{50} is progressively approached until a stable configuration is reached.

The stability of the transfer function, once it is relaxed into its final state, was

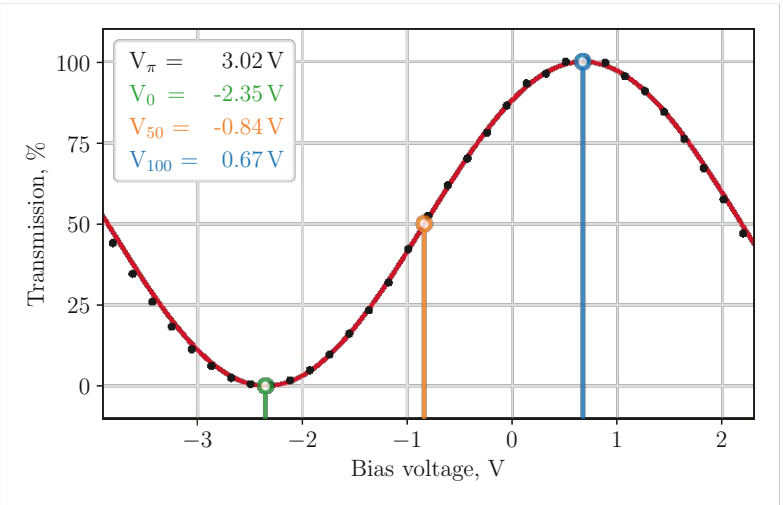

Figure 6.5: The transfer function is shown for the CTR measurement with long laser pulses. The data points were obtained by averaging the total intensity of several single laser pulses, as measured with the spectrometer. The bias voltages of interest are marked in green, orange and blue, with their respective values denoted in the legend.

already presented in section 4.6.3 for a continuous wave laser. However, the measurements in this chapter are performed with the pulsed laser source, so it is worth checking the stability of the system installed in the accelerator hall. In fig. 6.6, the laser stability of the pulsed laser source is provided for a repetition rate of 75 MHz, so integrated over 75×10^6 pulses per second. The top plot, with the data shown in red, depicts the normalised intensity of the laser source before going down to the accelerator hall. It exhibits a standard deviation of $\sigma = 0.9\%$ and is sufficiently stable during the acquisition window of 8 hours. The bottom plot, with the data shown in orange, depicts the normalised intensity of the laser source at the end of the acquisition system after it has been transmitted through the modulator and transmission fibres. During the acquisition, the modulator was set to a constant value of V_{50}. Even though the quadrature point is the most sensitive regarding intensity change caused by a drift of the transfer function, the intensity stayed reasonably stable, not indicating any significant drift, over the full measurement period of 8 hours. This stresses that the transfer function is stable for at least several hours once the modulator is set correctly and relaxed to the proper working point. The standard deviation of the transmitted laser power is $\sigma = 1.3\%$. The additional fluctuation introduced by the modulator is then estimated as $\sqrt{1.3^2 - 0.9^2}\,\% \approx 0.9\%$.

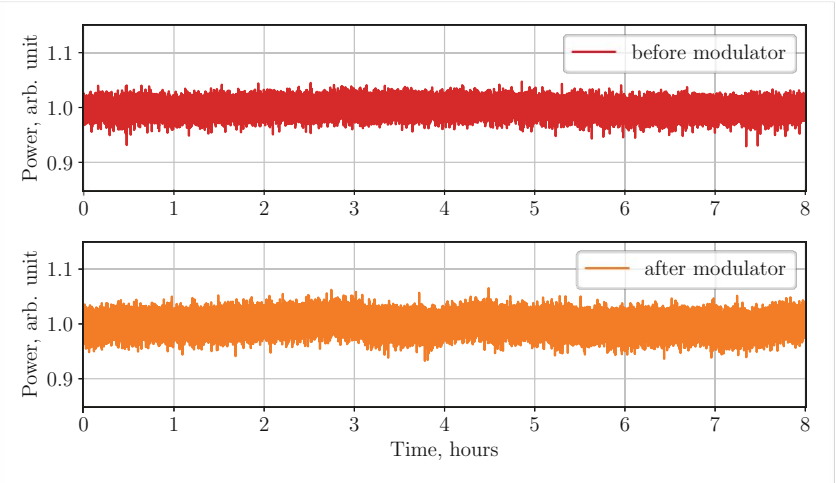

Figure 6.6: Before the modulator, the power of the laser system typically had a standard deviation of $\sigma = 0.9\%$. After the modulator operated at its most sensitive point at V_{50}, the laser power typically had a standard deviation of $\sigma = 1.3\%$. The additional fluctuation introduced by the modulator is estimated as $\sqrt{1.3^2 - 0.9^2}\% \approx 0.9\%$. Most importantly, the orange curve illustrates the long-term stability of the quadrature working point V_{50} over several hours of operation.

Charge Dependency

After correctly setting the working point, the setup is ready to measure the first signals. At the beginning, the input amplitude is unknown, which is problematic for interpreting the obtained signal, as too high input amplitudes will extend way out of the linear regime of the transfer function. If the input amplitudes exceed values in the order of $V_\pi/2$, the measured signal is subject to over-rotation. This behaviour is depicted in fig. 6.7. In the left graph, various Gaussian input signals are plotted normalised to V_π. The right graph displays the corresponding transmission through the modulator operating at V_{50} resulting from the various input signals. For values in the order of $V_\pi/2$, the transmitted intensity is already at its maximum, and the input signal is already distorted (blue curve). For even higher amplitudes of the input signal, the over-rotation of the input signals becomes evident. They saturate the transfer function and extend to the negative slope of the transfer function, leading to a negative imprint of the signal. The peak of the transmitted signals is folded down, leading to a double peak.

For this reason, it is important to start with small signal amplitudes and increase them until the transfer function saturates. The beam's bunch charge is modified to change the input signal amplitudes generated by the beam. The input signal

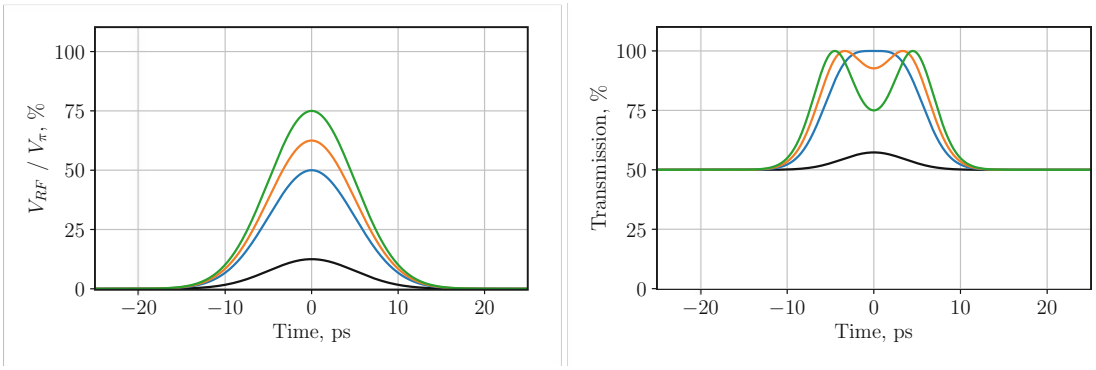

Figure 6.7: Illustration of the over-rotation of input signals with the modulator operated at V_{50}. Input signal amplitudes V_{RF} normalised to V_π are shown on the left, and the resulting transmission through the modulator is shown on the right. The transmitted signals are not distorted for signal amplitudes well below $V_\pi/2$ (black curve). For higher signal amplitudes, the transmitted signal is highly distorted, a behaviour which is also referred to as over-rotation.

is dominated by the coherent part of the power spectrum, which scales $\sim N^2$ for a large number of particles N. However, as with the modulator, we measure the electric field, the obtained signal scales with $\sim N$. Increasing the total bunch charge $Q = N \cdot e$, we expect a linear increase in the input signal. The transfer function at its positive slope at the V_{50} working point is given as:

$$T_{50}(V_{RF}) = \frac{1}{2} + \frac{1}{2}\sin\left(\frac{\pi V_{RF}}{V_\pi}\right) \tag{6.1}$$

where the first summand 1/2 stems from the V_{50} working point. The factor 1/2 before the second summand describes the total range of modulation, which is limited from -50% to +50% points as seen from the 50% baseline. For small input signal amplitudes V_{RF} the transfer function with respect to the 50% baseline is linear, and scales like

$$\frac{1}{2}\left(x - \frac{x^3}{6} + O(x^4)\right) \quad \text{with} \quad x = \frac{\pi V_{RF}}{V_\pi}\,. \tag{6.2}$$

With the input signal amplitude V_{RF} being proportional to the modulation of the laser intensity, the increase in total bunch charge Q is also proportional to the modulation of the laser intensity until the transmitted laser intensity saturates. In

fig. 6.8, the peak signal as a function of bunch charge is plotted. The background from the 50% baseline was removed, and the data was scaled to the maximum modulation of +50%. The smallest bunch charge achievable was approximately 10 pC, which was gradually increased to 35 pC. The first three data points show the expected linear behaviour until saturation is already reached for bunch charges above 20 pC. This is a fairly low bunch charge for CLEAR, considering that the nominal bunch charge varies from 0.01 to 1.5 nC. For conducting any measurements, a bunch charge of up to ~ 15 pC can be used to be well within the linear response of the modulator.

Even though we are only interested in the linear response of the modulator, it is still worth analysing the charge dependency in more detail. The graph in fig. 6.8 shows the peak signal of each acquisition, and it would therefore be expected that the values stay constant at 50% after reaching saturation. However, the peak signal amplitude clearly declines for values above 30 pC. This behaviour can be explained by the over-rotation as introduced before. For high input amplitudes, the signal experiences over-rotation, which is illustrated by the green curve in fig. 6.7. This over-rotation leads to a double peak, splitting the input signal into two shorter peaks. The resolution obtained with the long laser pulse is not high enough to resolve these two peaks, which leads to an underestimation of the signal amplitude. We will later see that the resolution obtained with the short laser pulse is sufficient to resolve them.

Time Conversion

As we now have a proper idea of which bunch charges lead to which modulation, we can interpret the obtained signals in a reliable way. We quantified the behaviour of the signal amplitude, so what is left is to establish the relation between the laser pulse spectrum and time. To do so, we use the laser delay stage as introduced in chapter 4. We gradually change the delay of the chirped laser pulse with respect to the CTR signal. The results of this measurement are shown in fig. 6.9. The traces are colour-coded from red on the left to yellow on the right to highlight the fact that the horizontal position refers to a certain wavelength. For details on the spectrometer setup, see section 4.6.4. The reduction in the path length of the laser pulse introduced by the delay stage is shown in the legend. To understand this graph, we must recall that the laser pulse exhibits a negative chirp with short wavelengths at the leading edge. The reduction in path length makes the laser pulse arrive earlier, shifting the detection of the signal to longer wavelengths. For the spectrometer, we have $d\lambda \propto -dx$, and we know that $dt \propto d\lambda$, which leads to the conclusion that we must have a negative time relation with respect to the pixel position on the spectrometer. This corresponds to what is shown in fig. 6.9.

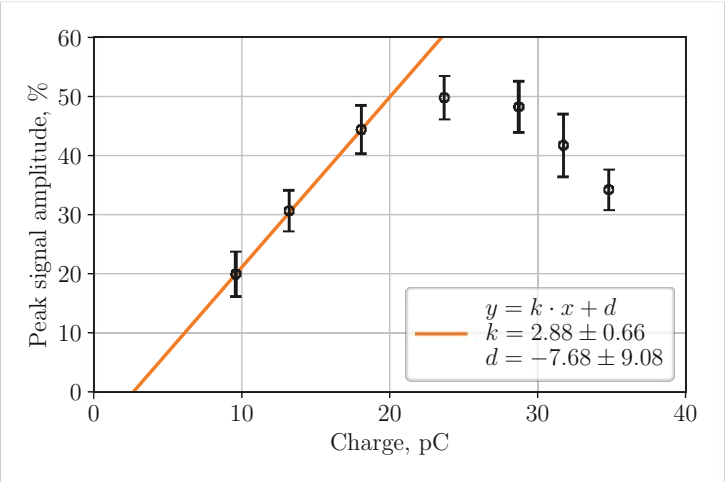

Figure 6.8: The peak signal amplitude is plotted as a function of bunch charge. The presented data was background subtracted and subsequently scaled so that the highest value corresponds to the saturation level of +50% transmission. The signal amplitude exhibits a linear dependence until the transfer function of the modulator saturates. With the modulator operating at V_{50}, the bunch charge must be kept well below 20 pC to obtain a linear response. The temporal resolution is insufficient to resolve the double peak caused by over-rotation (cf. fig. 6.7), leading to an underestimation of the saturation values above 30 pC.

A delay in arrival time corresponds to lower pixel values on the spectrometer. The various pulses are fitted with a Gaussian function to obtain their mean position. The diamond-shaped markers denote the mean position of each pulse.

The path difference introduced by the delay stage is converted to a temporal delay considering that the laser pulse travels with the speed of light in the air $c/n_{air} \sim c$. Plotting the temporal delay as a function of the mean position of each pulse, we obtain the time conversion as depicted in fig. 6.10. To convert the position on the spectrometer to the time domain, we obtain a factor of approximately -1.71 ps/px. As already mentioned above, we obtain a negative slope for the conversion. The linearity of the data points indicates that the pulse's frequency content is chirped linearly in time.

Time Domain Signal

After investing the amplitude of the transition radiation signals and the time conversion for the spectrometer, we perform a measurement of the time domain signals. From the charge dependency scan, we have seen that a charge up to

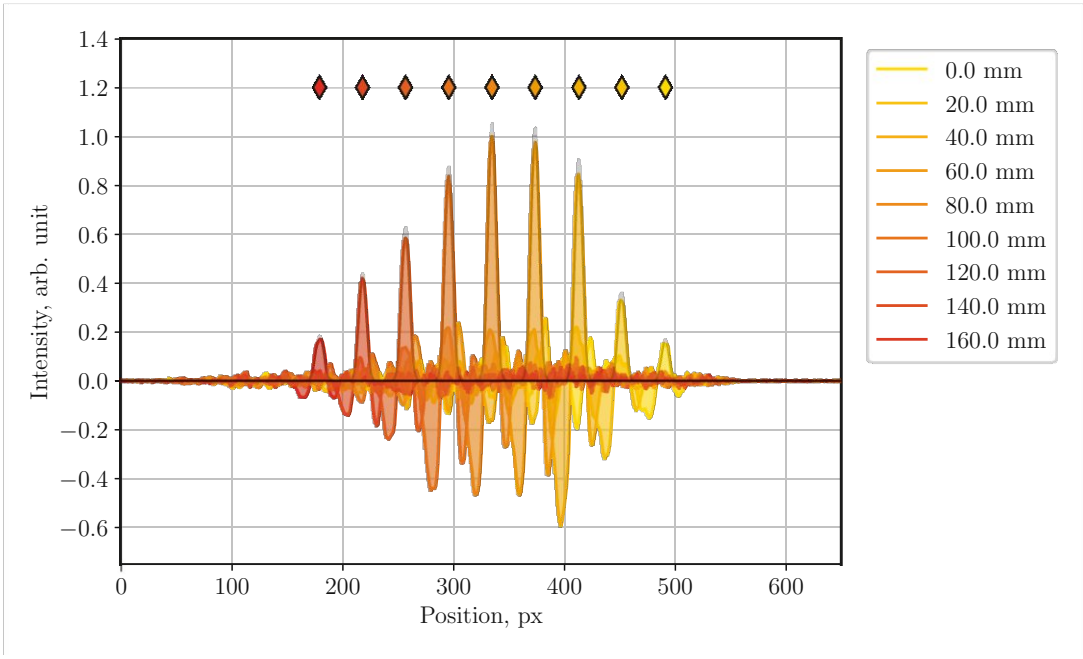

Figure 6.9: Time delayed transition radiation pulses as measured with the intensified spectrometer. The different motor positions of the delay stage are shown in the legend. The diamond-shaped markers denote the mean position of each pulse. From the presented data, the background was subtracted and then scaled to the peak intensity. Time increases from right to left as the laser pulse exhibits a negative chirp. The colour code of the signals indicates the spectrum of the laser pulse.

$\sim 15\,\mathrm{pC}$ leads to a linear modulator response. Moreover, we know that the time on the spectrometer increases from right to left. We, therefore, aim for a bunch charge below 15 pC and place the signal towards the right side of the spectrum so we can see a larger fraction of the trace behind the initial signal. The profiles obtained with the spectrometer are shown in fig. 6.11. To be able to scale the amplitudes properly, the background was measured at three different working points. In blue, the maximum transmission of the laser pulse at working point V_{100} without any signal modulation is shown. This curve represents the total laser intensity available for modulation. In orange, the 50% transmission of the laser pulse is shown, corresponding to the working point V_{50}. The green curve displays the minimum transmission of the laser pulse at working point V_0. The actual transition radiation signal is shown for a bunch charge of $13 \pm 2\,\mathrm{pC}$. As expected, the signal is well below the maximum transmission intensity. The signal trace was averaged over 1500 shots acquired within 2.5 minutes.

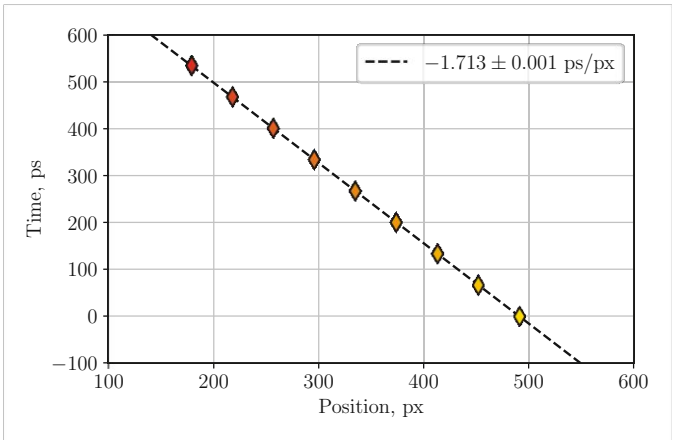

Figure 6.10: Time conversion using the mean position of the delayed signals on the spectrometer. The slope is negative due to the negative chirp of the laser pulse and $d\lambda$ of the spectrometer being $\propto -dx$, as indicated by the colour code. The linearity of the data points indicates that the frequency content within the laser pulse is linearly distributed.

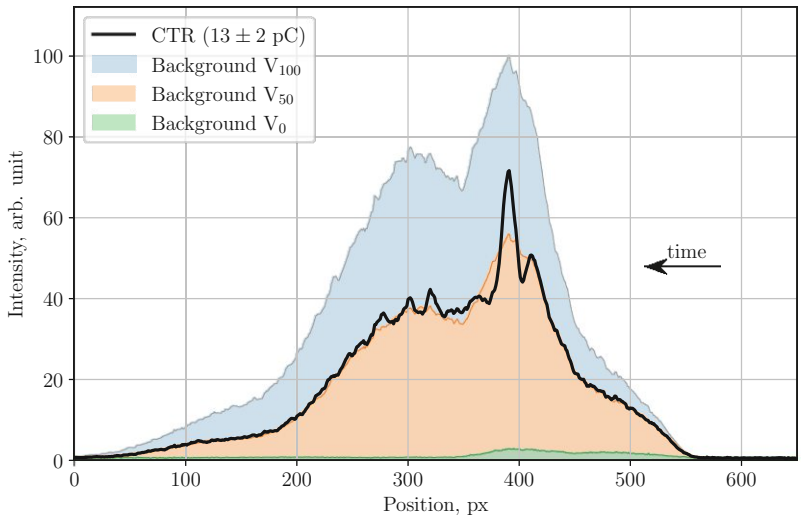

Figure 6.11: Four different profiles were measured with the spectrometer to obtain the normalised time trace of the signal. The three background levels at working points V_{100}, V_{50} and V_0 correspond to 100%, 50% and 0% laser light transmission of the modulator (cf. with the transfer function in fig. 6.5). The transition radiation signal is shown in black for an average bunch charge of $13 \pm 2\,\mathrm{pC}$ and at working point V_{50}. The profiles are then processed according to equation 6.3 to obtain the normalised time trace in fig. 6.12.

The acquired profiles from the spectrometer are then further processed to obtain the time trace of the signal. As summarised in equation 6.3, the background is subtracted from the signal and then normalised for the maximum range of modulation. The signal amplitude is then normalised to the modulation range from -50% to +50%. It is then only left with converting the spatial information from pixels to time information in seconds using the time conversion obtained before.

$$\begin{aligned} \text{Amplitude} &= \frac{\text{Signal}(V_{50}) - \text{Background}(V_{50})}{\text{Background}(V_{100}) - \text{Background}(V_0)} \\ \text{Time} &= \text{Position} \times \text{Time Conversion Factor} \end{aligned} \tag{6.3}$$

The final time trace of the CTR is shown in fig. 6.12. The peak signal amplitude was shifted to 500 ps to allow for convenient comparison between the various time traces presented in this chapter. The CTR signal is fitted with a Gaussian function, which yields a standard deviation of $\sigma = 8.4 \pm 0.1$ ps. The baseline of the Gaussian fit was set to the first minimum before the peak amplitude to have the same point of reference for all measurements presented in this chapter. As the time windows in this chapter are short with respect to the system's low-cutoff frequencies, it is impossible to have a reliable DC baseline for all time traces presented.

Spectrometer Resolution and Timing Jitter

During each experiment, the coupling of the laser pulse into the fibre and all along the pathway down to the modulator and back to the spectrometer is optimised. However, the laser intensity of the acquisition system varies for the various experimental setups. The laser intensity is influenced by the number of fibre connectors, the losses in the CFBG and the position of the delay stage. To compensate for these differences, the gain of the intensified camera is changed, which varies the spectrometer resolution slightly (cf. section 4.6.4). With a gain setting of 890 and considering the time conversion obtained, the spectrometer resolution is given as $\sigma_{\text{spec}} \approx 8.3$ ps. The timing jitter is calculated by acquiring 1000 single shot traces and binning the maxima of each trace into bins of 1 px width. After the time conversion, we obtain a standard deviation of the timing jitter of $\sigma_{\text{jitt}} \approx 5.0$ ps. The convolution of these two contributions is then given as $\sqrt{8.3^2 + 5.0^2}$ ps $= 9.7$ ps. We, therefore, cannot draw any conclusions on the input pulse length, as the total resolution of the setup is not high enough. However, the longer time trace still provides insight into the time response over several hundred ps. The noise floor after the main peak exhibits a peak-to-peak amplitude of $\sim 7.6\%$ of the full modulation range, whereas the pulse covers $\sim 23.6\%$ of the full modulation range.

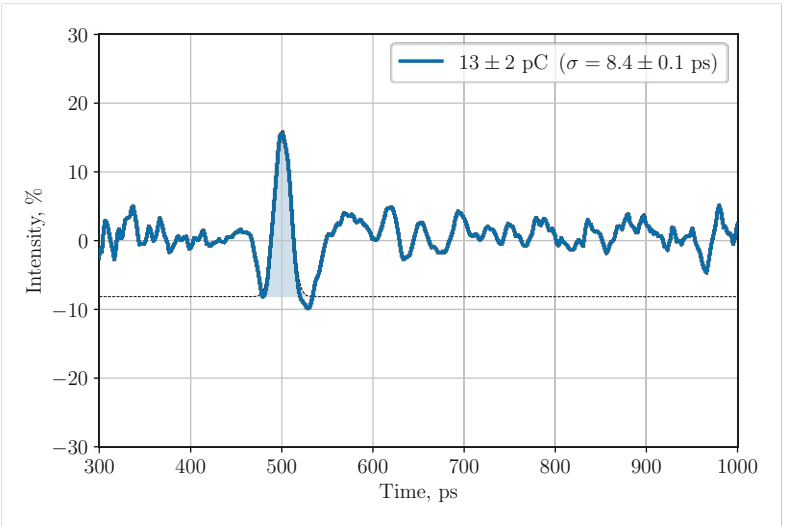

Figure 6.12: Time trace of the CTR pulse as measured with the long laser pulse at working point V_{50}. The Gaussian fit yields a standard deviation of $\sigma = 8.4 \pm 0.1$ ps. The trace is heavily affected by the spectrometer resolution and the timing jitter between the laser pulse and the CTR pulse.

The dominant frequency within the power spectrum is ~ 18.2 GHz, which is close to the nominal high-frequency cutoff of the antenna and corresponds to a time interval of approximately 55 ps.

6.2.3 Short Laser Pulse

The stretching to long laser pulses did not resolve the modulator's response to ultra-short input signals. There are two things to be optimised: the resolution of the spectrometer and the timing jitter. The spectrometer resolution was already minimised before, operating at the smallest slit width while still obtaining decent intensity levels. Optimising the laser light transmission through the system minimised the needed gain levels of the intensifier. The timing jitter is relatively high, and unfortunately, it was not possible to identify the source of this timing issue. However, the spectrometer resolution is obtained by applying the time conversion factor to the respective values given in pixels. So, to improve the resolution of the whole system, the time conversion factor must be reduced. This can be achieved by reducing the stretching of the laser pulse, which comes at the cost of reducing the time window available for measurements. This was achieved by removing the CFBG and stretching the laser pulse just in the transmission fibre. Details on stretching the laser pulse with the transmission fibre are presented in section 4.6.2. The pulse length of the short laser pulse just before entering the modulator was

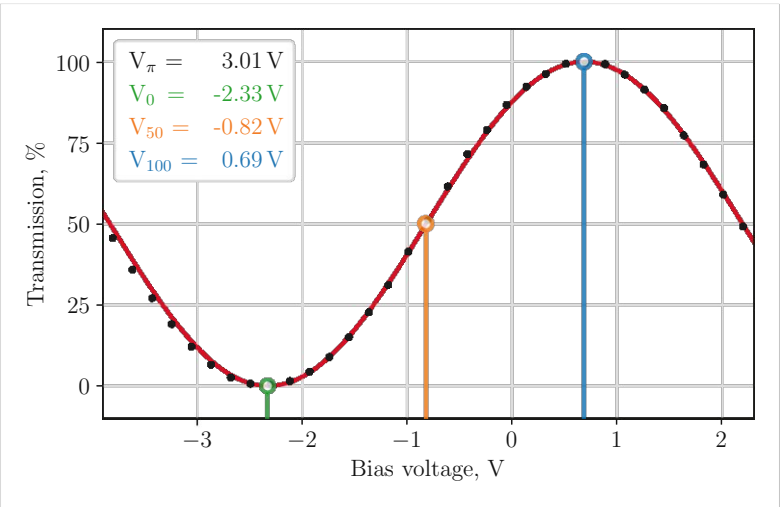

Figure 6.13: The transfer function is shown for the CTR measurement with short laser pulses. The data points were obtained by averaging the total intensity of several single laser pulses, as measured with the spectrometer. The bias voltages of interest are marked in green, orange and blue, with their respective values denoted in the legend.

estimated as $\mathrm{FHWM}_{long} \approx 61\,\mathrm{ps}$. In section 4.6.2 we have already shown that $\mathrm{FWHM}_{long}/\mathrm{FWHM}_{short} \approx 4.6$, so by reducing the laser pulse length the resolution of the spectrometer will be improved by this factor and at the same time the available time window will be shortened by this factor. It also has to be noted that the short laser pulse exhibits a positive chirp at the location of the modulator. The leading edge, therefore, has longer, and the trailing edge has shorter wavelengths, as illustrated in fig. 4.16. Therefore, the temporal distribution of the frequency content within the short laser pulse is opposite from the one in the long laser pulse.

Transfer Function

At the beginning of the measurement, the transfer function is measured in the same manner as explained in section 6.2.2. The results are displayed in fig. 6.13. The three working points V_{100}, V_{50} and V_0, which correspond to 100%, 50% and 0% transmission of the laser intensity, are displayed in green, orange and blue.

Charge Dependency

After obtaining the V_{50} working point, the peak signal amplitude is measured again as a function of bunch charge. The results are displayed in fig. 6.14. Just as for the long laser pulse, also with the short laser pulse, the measurement shows

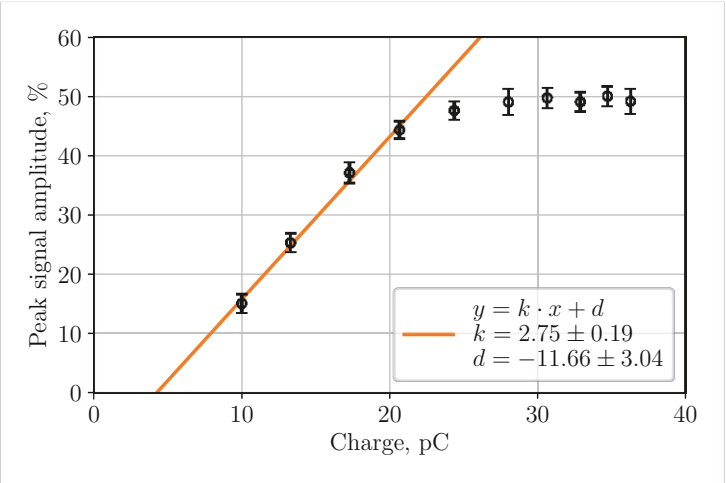

Figure 6.14: The peak signal amplitude is plotted as a function of bunch charge. The presented data was background subtracted and subsequently scaled so that the highest value corresponds to the saturation level of +50% transmission. The signal amplitude exhibits a linear dependence until the transfer function of the modulator saturates. With the modulator operating at V_{50}, the bunch charge must be kept well below 20 pC to obtain a linear response. The temporal resolution is sufficient to resolve the double peak caused by over-rotation (cf. fig. 6.7), leading to saturated values also above 30 pC.

a linear response up to ~ 20 pC before it starts saturating. However, for charges above 30 pC the measurement shows a different trend. As already mentioned in the corresponding paragraph on the charge dependency using the long laser pulse, this discrepancy can be explained by the difference in the resolution of the systems. Whereas the long laser pulse has insufficient temporal resolution to resolve the double peak caused by an over-rotation of the signal, the short laser pulse has a better temporal resolution. This resolution is high enough to resolve the over-rotation and when just plotting the peak signal amplitude of the signal, the graph stays saturated as expected.

Time Conversion

The charge dependency measurement already hinted towards a better total resolution of the system. Checking the time conversion will provide us with an exact value. The measurement of the CTR signal for different laser pulse delays is shown in fig. 6.15. The most obvious difference compared to the same plot for the long laser pulse (fig. 6.9) is that the pulses are significantly broader. As the laser pulse is much shorter, the CTR signal modulates a wider spectrum of the laser pulse,

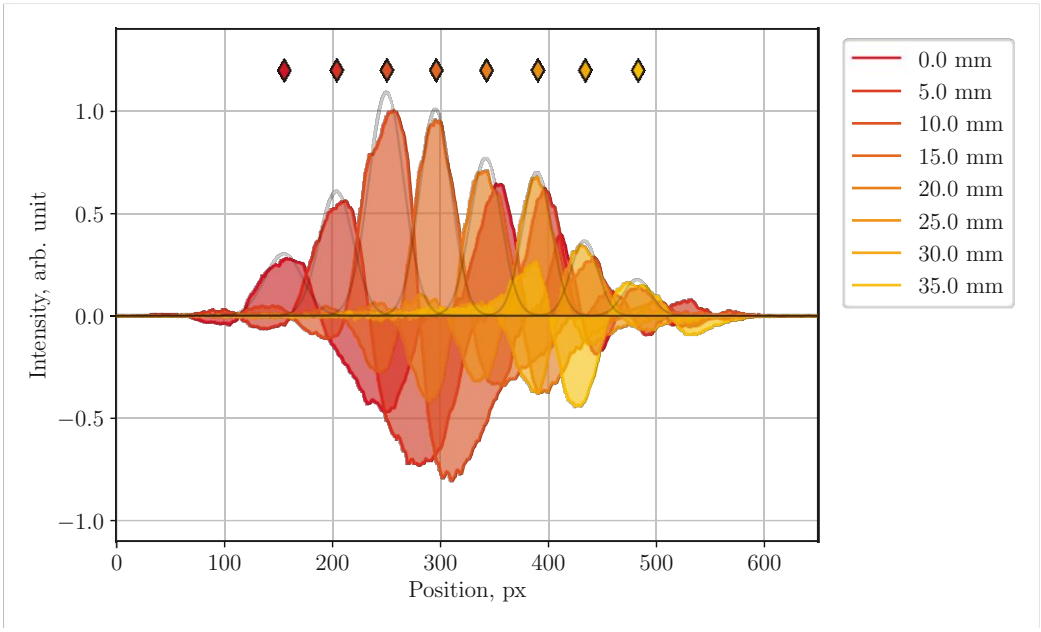

Figure 6.15: Time delayed transition radiation pulses as measured with the intensified spectrometer. The different motor positions of the delay stage are shown in the legend. The diamond-shaped markers denote the mean position of each pulse. From the presented data, the background was subtracted and then scaled to the peak intensity. Time increases from left to right as the laser pulse exhibits a positive chirp. The colour code of the signals indicates the spectrum of the laser pulse.

which is directly visible on the spectrometer by a broadening of the pulses. Also, the delay stage now only introduces a path length difference of 35 mm, compared to the 160 mm used before to cover the full laser pulse length. Just comparing these two motor positions, we already see that the pulse is compressed by roughly a factor of 4.6. The reduction in path length makes the laser pulse arrive earlier, shifting the detection of the signal to shorter wavelengths. For the spectrometer, we have $d\lambda \propto -dx$, and we know that $dt \propto -d\lambda$, which leads to the conclusion that we must have a positive time relation with respect to the pixel position on the spectrometer. This corresponds to what is shown in fig. 6.15. A delay in arrival time corresponds to higher pixel values on the spectrometer. The various pulses are fitted with a Gaussian function to obtain their mean position, and the diamond-shaped markers denote the mean position of each pulse.

The path difference introduced by the delay stage is again converted to a temporal delay. Plotting the temporal delay as a function of the mean position of each pulse, we obtain the time conversion as depicted in fig. 6.15. To convert the position on

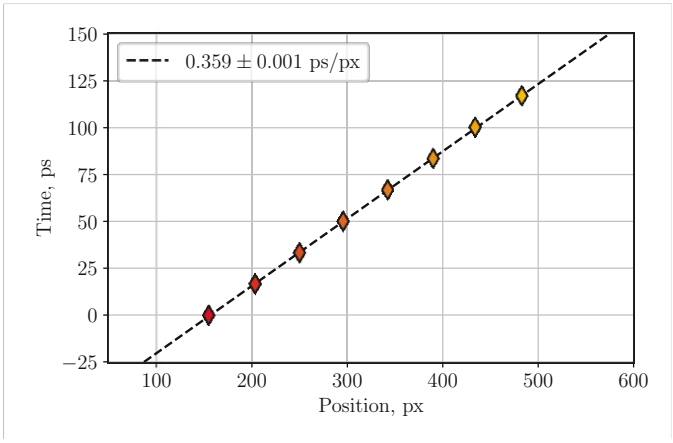

Figure 6.16: Time conversion using the mean position of the delayed signals on the spectrometer. The slope is positive due to the positive chirp of the laser pulse and $d\lambda$ of the spectrometer being $\propto -dx$, as indicated by the colour code. The linearity of the data points indicates that the frequency content within the laser pulse is linearly distributed.

the spectrometer to the time domain, we obtain a factor of 0.36 ps/px. As already mentioned above, we obtain a positive slope for the conversion. The linearity of the data points indicates that the pulse's frequency content is linearly chirped in time. Note that the signal span on the spectrometer is the same as for the long laser pulse, as the spectral content of the laser pulse did not change; only the compression in time and the chirp direction is different. Dividing the two obtained time conversion factors, we obtain a factor 4.77 for the difference in length between the short and long laser pulse, which is to be compared to the factor 4.6 estimated in chapter 4.

Time Domain Signal

Just as for the long laser pulse, we use the knowledge obtained from the charge scan, which yielded an optimal modulator response at bunch charges below 15 pC to perform the measurement of the time trace. Most importantly, the different direction of the chirp leads to a different direction in time on the spectrometer. We, therefore, place the signal peak more towards the left in the spectrometer to have a longer time window after the pulse has passed. The profiles as obtained with the spectrometer are shown in fig. 6.17.

The final time trace is shown in fig. 6.18. It was processed with the profiles shown in fig. 6.17 according to equation 6.3. The amplitude is, therefore, again normalised to the full modulation range from -50% to +50%. Interestingly, the signal span

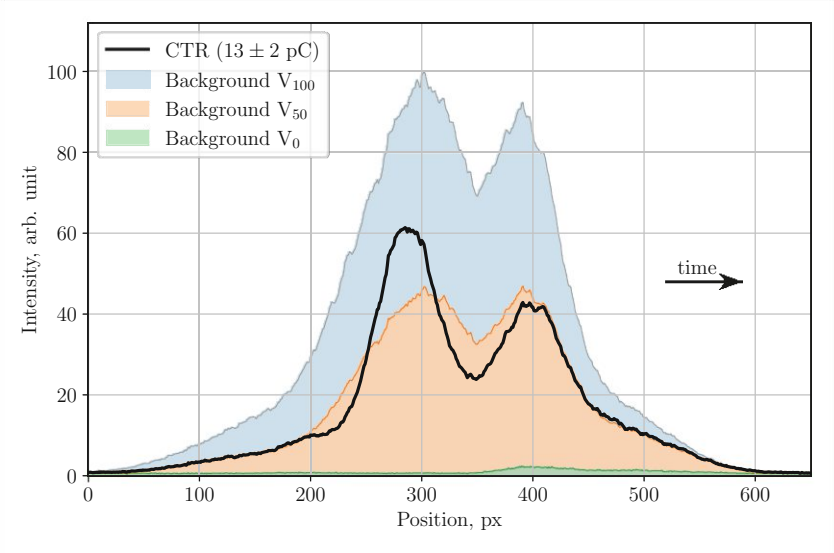

Figure 6.17: Four different profiles were measured with the spectrometer to obtain the normalised time trace of the signal. The three background levels at working points V_{100}, V_{50} and V_0 correspond to 100%, 50% and 0% laser light transmission of the modulator (cf. with the transfer function in fig. 6.13). The transition radiation signal is shown in black for an average bunch charge of $13 \pm 2\,\mathrm{pC}$ and at working point V_{50}. The profiles are then processed according to equation 6.3 to obtain the normalised time trace in fig. 6.18.

now covers 37.4% of the total modulation range, compared to a coverage of 23.6% with the long laser pulse, even though the bunch charge was the same. This also indicates that the resolution with the long laser pulse is insufficient for such short pulses. The CTR signal is again fitted with a Gaussian function, with the baseline being fixed to the first minimum before the pulse. We obtain a standard deviation of $\sigma = 7.9 \pm 0.1\,\mathrm{ps}$, which is only slightly shorter than the one obtained with the long laser pulse.

Spectrometer Resolution and Timing Jitter

With the laser pulse length being reduced by a factor of 4.77, also the spectrometer resolution will improve by this factor. During the measurement shown in fig. 6.18, the intensifier gain was set to a value of 860, which, considering the time conversion, leads to a spectrometer resolution of $\sigma_{\mathrm{spec}} \approx 1.7\,\mathrm{ps}$. The timing jitter is calculated by acquiring 1000 single shot traces and binning the maxima of each trace into bins of 1 px width. After the time conversion, we obtain a standard deviation of the timing jitter of $\sigma_{\mathrm{jitt}} \approx 5.3\,\mathrm{ps}$. The convolution of these two contributions is then

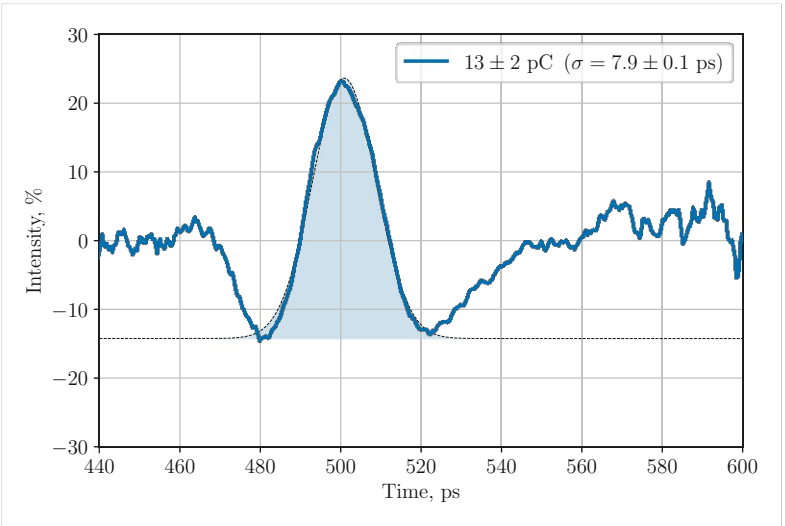

Figure 6.18: Time trace of the CTR pulse as measured with the short laser pulse at working point V_{50}. The Gaussian fit yields a standard deviation of $\sigma = 7.9 \pm 0.1\,\text{ps}$. The trace is affected by the timing jitter between the laser pulse and the CTR pulse, whereas the spectrometer resolution is improved compared to fig. 6.12.

given as $\sqrt{1.7^2 + 5.3^2}\,\text{ps} = 5.5\,\text{ps}$. This value is still quite close to the obtained standard deviation of the signal. However, we can now estimate the bandwidth of the whole system. The CTR input signal, corrected for the spectrometer resolution and timing jitter, is given as $\sqrt{7.9^2 - 5.5^2}\,\text{ps} = 5.6\,\text{ps}$. Considering that the temporal resolution of the system is very close to the obtained signal duration, this value is subject to large errors. For example, if we assume a 10% standard error on the spectrometer resolution and timing jitter, we obtain $5.6 \pm 0.8\,\text{ps}$, which is a standard error of more than 14% on the estimated input signal duration. The bandwidth BW of an acquisition system can be approximated by $BW \approx 1/(2\tau)$, with τ denoting the FWHM of the temporal pulse. The system's high-frequency cutoff is then given as approximately $38 \pm 5\,\text{GHz}$, which is substantially higher than the values provided in the datasheet for the antenna (18 GHz) and the modulator ($> 25\,\text{GHz}$). However, this measurement could be easily improved by reducing the timing jitter between the laser pulses and the beam signal. This is currently under investigation and will be optimised for future measurements.

6.3 Coherent Cherenkov Diffraction Radiation

In the previous section 6.2, we have performed a calibration measurement of the acquisition system by exposing it to ultra-short pulses generated by CTR. Using either the long or the short laser pulse, the available time duration for modulation is approximately 500 ps for the long pulse and around 100 ps for the short laser pulse. We demonstrated the different directions of the frequency chirp within the two laser pulses and obtained an estimation for the temporal resolution limit. After characterising the acquisition system with known pulse shapes, we move on to measure the time trace of the CChDR signal. The time trace is not completely unknown, as we have already measured it in chapter 5. However, the acquisition method in chapter 5 was subject to a high-frequency cutoff of 10 GHz and a timing jitter in the order of 50 ps. This significantly smeared out the time domain signal and led to the measurements presented in this chapter, where the bandwidth is improved to approximately 40 GHz and the timing jitter is reduced to several ps.

The experimental setup, as installed in the accelerator hall, is illustrated in fig. 6.19. The detection scheme is identical to the one used for the calibration measurement with CTR in fig. 6.2, except that it was moved from the in-air test stand to the location of the ChDR test stand (cf. fig. 4.1). The antenna aperture was centred along the radiator axis to be planar with the radiator exit surface and aligned to measure the horizontal polarisation of the emitted radiation. During the measurements, the distance between the exit surface of the radiator and the antenna aperture was set to $d = 7\,\mathrm{cm}$. This configuration was chosen to enable ChDR to propagate at the Cherenkov angle while simultaneously reducing the DR contributions captured by the horn antenna.

6.3.1 Long Laser Pulse

In the measurements performed with the electro-optical probes in chapter 5, the 20 ns-long time trace in fig. 5.18 showed substantial field strengths even after several nanoseconds after the main peak. The time window available for the EOSD measurements is much shorter, so care should be taken not to sample the wrong part of the signal. The first measurements are performed with a long laser pulse to facilitate this process. This will not provide us with enough resolution to measure the pulse width (cf. section 6.2.2); however, interpreting the obtained signal will be much easier with a longer time window. Also, we will gain better insight into the actual time structure of the trailing fields, as already observed with a lower resolution with the electro-optical probe and shown in fig. 5.18.

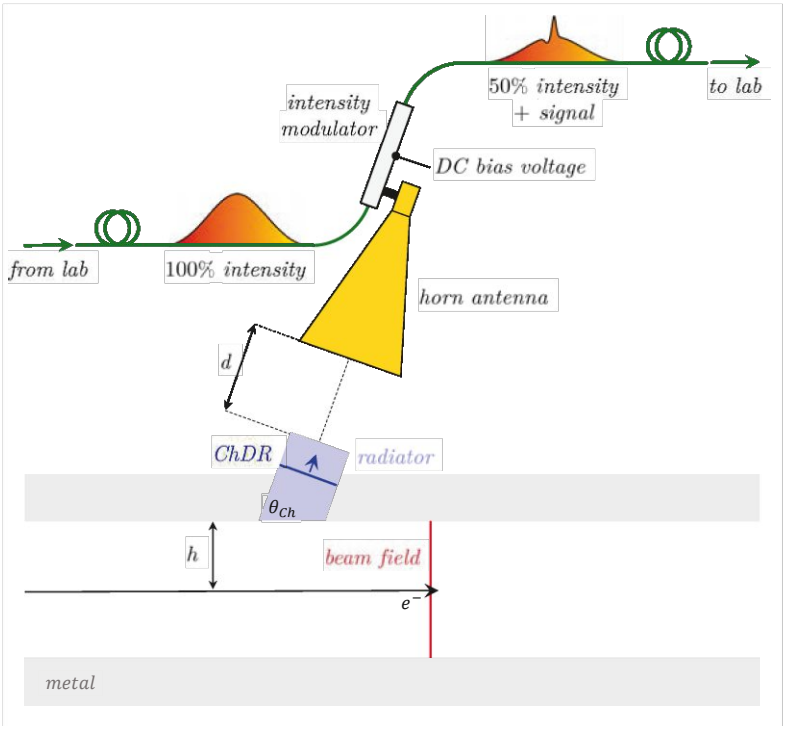

Figure 6.19: Schematic of the measurement setup for CChDR. The Cherenkov angle θ_{Ch} denotes the emission angle of CChDR. The horn antenna is placed at the Cherenkov angle, aligned with the central axis of the radiator. The horn aperture is placed at a distance $d = 7\,\text{cm}$ from the radiator exit surface.

Spectrometer Profiles

As the exact shape of the signal is unknown at such a short time scale, it is critical to understand the CChDR signal better. We will apply the knowledge obtained from the previous section 6.2 to identify the CChDR pulse. The first measurements of the CChDR are shown in fig. 6.20. It is important to recall that time increases from right to left, as also denoted in the figure. The CChDR pulse is placed on the right side of the spectrum to capture the trailing fields. The signal amplitude at a bunch charge of $23 \pm 3\,\text{pC}$ is well within the maximum and minimum laser intensity available for modulation. The signal trace also overlaps with the 50% transmission background at working point V_{50} for any time before the initial pulse, making sure that the captured signal is indeed the first pulse in time. Already in this plot, it is evident that the positive first pulse is followed by a negative second pulse, which was not the case during the calibration measurements presented in fig. 6.11. Also, the trailing field amplitudes are much more prominent. Both these characteristics

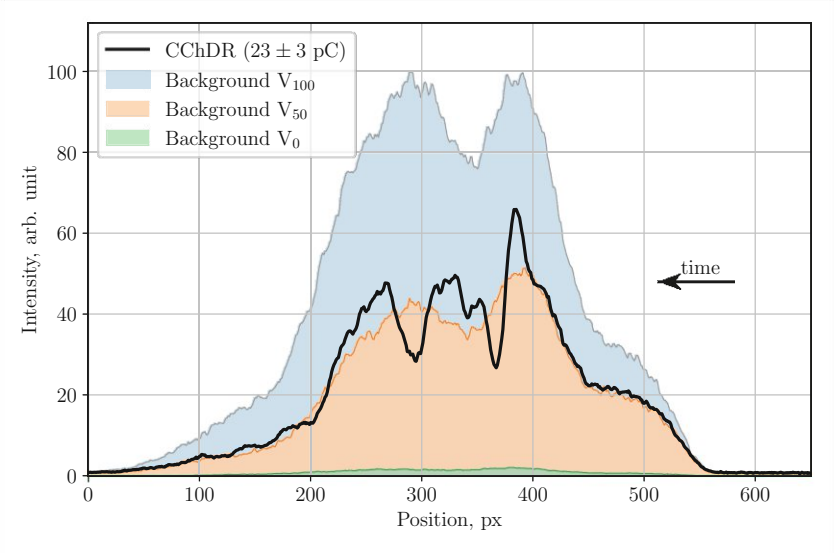

Figure 6.20: Four different profiles were measured with the spectrometer to obtain the normalised time trace of the signal. The three background levels at working points V_{100}, V_{50} and V_0 correspond to 100%, 50% and 0% laser light transmission of the modulator. The CChDR signal is shown in black for an average bunch charge of 23 ± 3 pC and at working point V_{50}. The profiles are then processed according to equation 6.3 to obtain the normalised time trace in fig. 6.23.

were already expected from the measurements with the electro-optical probe in fig. 5.18, but this time, they are captured with a much higher temporal resolution.

Time Conversion

To convert the profiles obtained in fig. 6.20, we need to measure the time conversion factor. The results of this measurement are presented in fig. 6.21. The delay stage was again moved up to 70 mm to introduce a maximum path length difference of 140 mm. The step size was cut in half compared to the previous measurement to obtain a fine scan. It also has to be noted that the working point for these measurements was changed to approximately V_{10} to be able to increase the first pulse's signal amplitude and decrease the second pulse's signal amplitude. At this working point, the negative amplitudes are strongly distorted. However, the linear part of the transfer function is increased for positive amplitudes. This allows for higher signal amplitudes and, consequently, a better signal-to-noise ratio. The various pulses are fitted with a Gaussian function to obtain their mean position. The diamond-shaped markers denote the mean position of each pulse. The path difference introduced by the delay stage is again converted to a temporal delay.

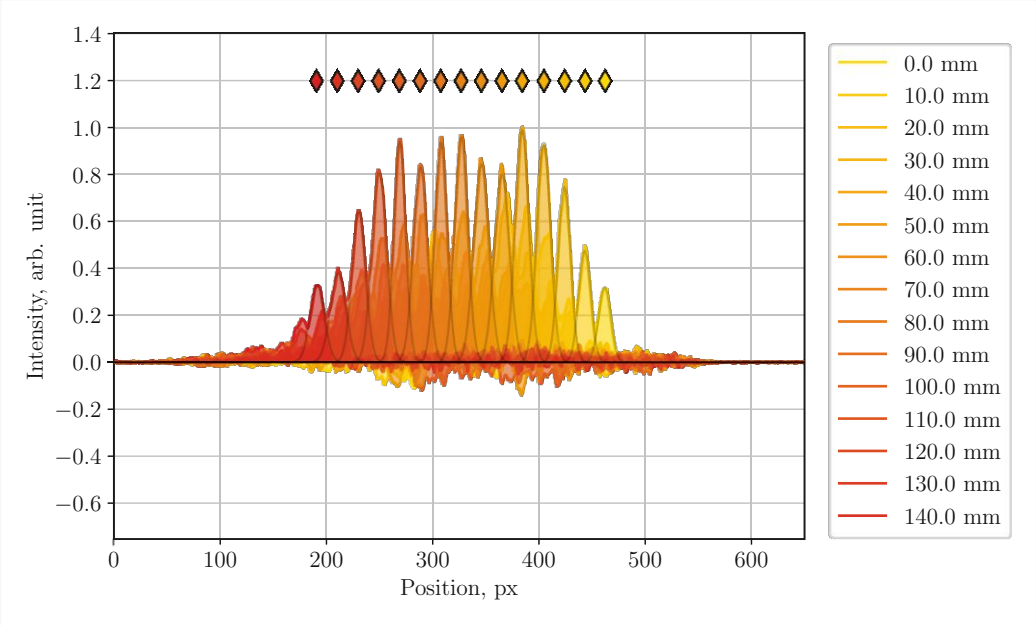

Figure 6.21: Time delayed CChDR pulses as measured with the intensified spectrometer. The different motor positions of the delay stage are shown in the legend. The diamond-shaped markers denote the mean position of each pulse. From the presented data, the background was subtracted and then scaled to the peak intensity. Time increases from right to left as the laser pulse exhibits a negative chirp. The colour code of the signals indicates the spectrum of the laser pulse. The profiles were obtained at working point V_{10} to increase the signal-to-noise ratio for the positive CChDR pulses.

Plotting the temporal delay as a function of the mean position of each pulse, we obtain the time conversion as depicted in fig. 6.22. We obtain a factor of approximately $-1.73\,\mathrm{ps/px}$, which differs by $\sim 10\,\mathrm{fs/px}$ from the earlier value. Again, the linearity of the frequency chirp within the laser pulse is confirmed as expected.

Time Domain Signal

After measuring the time delay, we convert the profiles acquired with the spectrometer as depicted in fig. 6.20 into the time domain. Equation 6.3 is used to normalise the signal's amplitude and the time information is reconstructed using the new time conversion factor. The final time trace of the CChDR signal is shown in fig. 6.23. The peak amplitude was shifted to 500 ps to ease comparison with the CTR signal shown in fig. 6.12. The Gaussian fit of the CChDR pulse yields a standard deviation

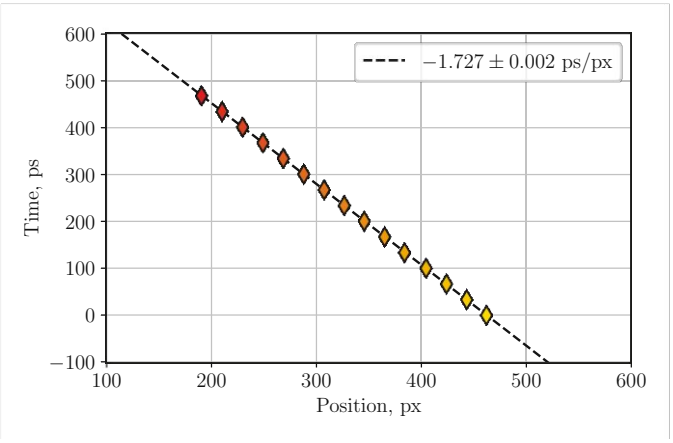

Figure 6.22: Time conversion using the mean position of the delayed signals on the spectrometer. The slope is negative due to the negative chirp of the laser pulse and $d\lambda$ of the spectrometer being $\propto -dx$, as indicated by the colour code. The linearity of the data points indicates that the frequency content within the laser pulse is linearly distributed.

of $\sigma = 9.4 \pm 0.2$ ps. However, we already know from the previous section that this value is very close to the resolution limit of the system itself. What is interesting to note is that the first negative peak exhibits a similar amplitude as the CChDR pulse. The trailing fields are much more prominent than suggested by simulations. This finding, however, agrees with the low-resolution measurement performed in chapter 5 and illustrated in fig. 5.18, which also shows much higher amplitudes of the trailing fields than predicted. Any reflection of the initial CChDR pulse within the radiator would need to travel for at least 900 ps in the alumina. All the trailing fields shown in fig. 6.23, therefore, cannot be caused by any reflections of the initial signal. The power spectrum has a maximum at approximately 7.2 GHz, which corresponds to approximately 140 ps. This periodicity of approximately 140 ps in the trailing fields is clearly visible in fig. 6.23. The high amplitude of the trailing fields might have several reasons. One of them could be that the amplitude calibration is only checked at the location of the CChDR pulse when performing the charge scan. Any amplitudes at a different location within the laser pulse might experience an error due to the normalisation method introduced in equation 6.3. However, this error should be small, as the same method was also used to measure the CTR signal in fig. 6.12, which resulted in negligible field amplitudes after the initial pulse. Another explanation would be that the coherent nature of the DR following the initial CChDR pulse leads to this strong modulation in intensity. The radiator can not be perfectly inserted, and its edge is also subject to imperfections. Moreover, the particles within the beam are not perfectly aligned

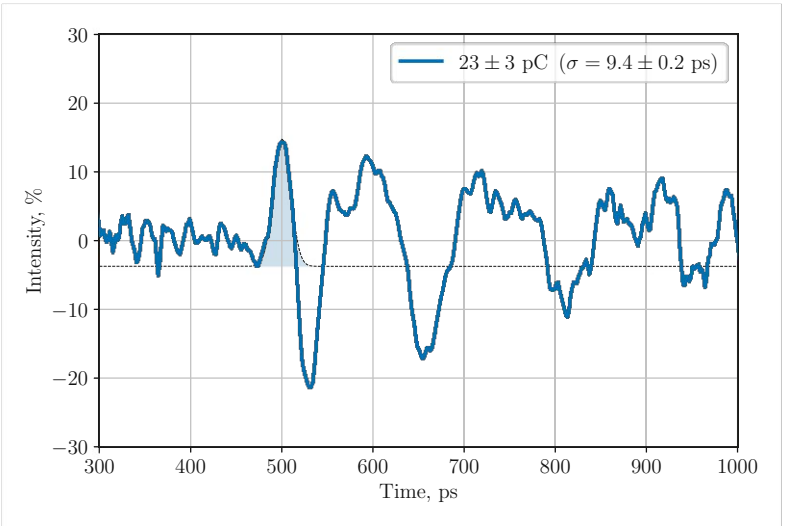

Figure 6.23: Time trace of the CChDR signal as measured with the long laser pulse at working point V_{50}. The Gaussian fit of the CChDR pulse yields a standard deviation of $\sigma = 9.4 \pm 0.2\,\mathrm{ps}$. The trace is heavily affected by the spectrometer resolution and the timing jitter between the laser pulse and the CChDR pulse.

with respect to the radiator edges. As DR is emitted all around the edge of the radiator and then interferes with those various contributions within the radiator, all these imperfections greatly affect the resulting DR signal. However, the prominent periodicity of approximately 140 ps indicates a rather systematic source. In vacuum, this frequency would correspond to a wavelength of 42 mm, which is close to the nominal impact parameter of 40 mm during the measurement and the vacuum chamber radius of 40 mm. Also, the low cutoff frequency of the horn antenna might play a role, as low-frequency components are highly suppressed in the CTR measurement, which could lead to the absence of this ringing in fig. 6.12. The real origin of these trailing fields is unknown at the moment and still requires further investigation.

Spectrometer Resolution and Timing Jitter

The trace shown in fig. 6.23 was acquired for an intensifier gain of 910, which leads to a spectrometer resolution of $\sigma_{\mathrm{spec}} \approx 8.7\,\mathrm{ps}$. After the time conversion, we obtain a standard deviation of the timing jitter of $\sigma_{\mathrm{jitt}} \approx 3.0\,\mathrm{ps}$. The convolution of these two contributions is then given as $\sqrt{8.7^2 + 3.0^2}\,\mathrm{ps} = 9.2\,\mathrm{ps}$. As expected from our findings in section 6.2, we cannot draw any conclusions on the input pulse length, as the resolution of the setup is not high enough.

6.3.2 Short Laser Pulse

The measurements with the short laser pulse follow the same procedure as described in section 6.2.3, and a schematic of the whole acquisition chain is shown in fig. 4.16. A closeup of the accelerator installation is depicted in fig. 6.19. The short laser pulse improves the spectrometer's resolution and is equivalent to changing the timescale on an oscilloscope. We basically magnify the time trace in fig. 6.23, whereas we are interested in the very first peak of the signal.

Spectrometer Profiles

After performing the measurements in section 6.3.1 with the long laser pulse and, therefore, with a longer time window, we already have a reasonable approximation of the time signal to be expected with the short laser pulse. The measurements of the CChDR using the short laser pulse are shown in fig. 6.24. It is important to recall that time increases from left to right, as also denoted in the figure. The CChDR pulse is placed on the left side of the spectrum also to capture the trailing fields. The signal amplitude at a bunch charge of $18 \pm 2\,\mathrm{pC}$ is well within the maximum and minimum laser intensity available for modulation. Again, a positive first pulse is followed by a negative second pulse, replicating the characteristics of the very first part of the signal obtained with the longer time window in fig. 6.23.

Time Conversion

For the time conversion, we delay the signal again using the delay stage. The change in path length is equivalent to the one used in fig. 6.15 and spans 35 mm, which delays the laser pulse by $\sim 117\,\mathrm{ps}$ in total, in steps of 5 mm, so $\sim 16.7\,\mathrm{ps}$. The measurement results are shown in fig. 6.25. The various pulses are fitted with a Gaussian function to obtain their mean position, and the diamond-shaped markers denote the mean position of each pulse. The path difference introduced by the delay stage is again converted to a temporal delay. Plotting the temporal delay as a function of the mean position of each pulse, we obtain the time conversion as depicted in fig. 6.26. We obtain a factor of approximately $0.36\,\mathrm{ps/px}$, which is identical to the value measured during the calibration measurement with CTR. Again, the chirp's linearity is confirmed as expected. However, in fig. 6.26, it is evident that the markers are not as accurately aligned as for the long laser pulse (cf. fig. 6.22). This is not due to non-linearities in the laser pulse spectrum but can be explained due to the timing jitter in the acquisition chain. As the timing jitter is in the order of 5 ps, it is already visible on this time scale, whereas these variations in position due to the timing jitter cannot be resolved with the long laser pulse.

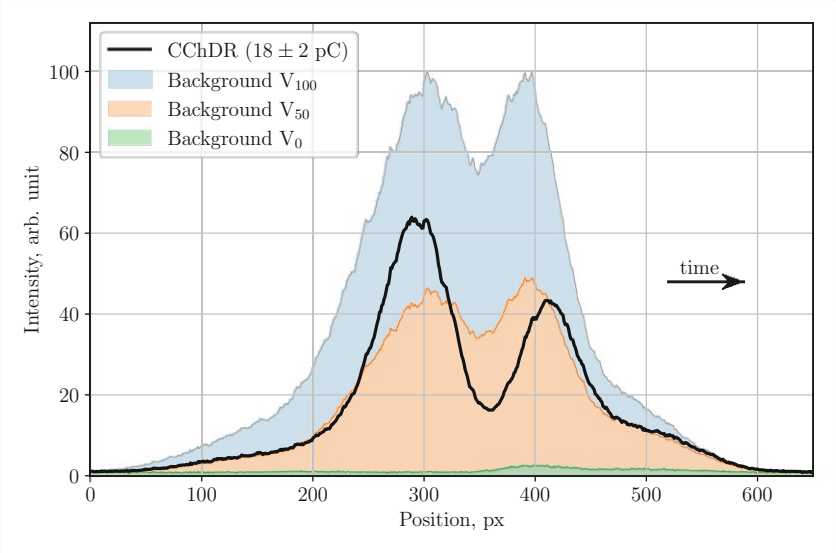

Figure 6.24: Four different profiles were measured with the spectrometer to obtain the normalised time trace of the signal. The three background levels at working points V_{100}, V_{50} and V_0 correspond to 100%, 50% and 0% laser light transmission of the modulator. The CChDR signal is shown in black for an average bunch charge of 18 ± 2 pC and at working point V_{50}. The profiles are then processed according to equation 6.3 to obtain the normalised time trace in fig. 6.31.

Charge Dependency

In chapter 5, we already presented the coherent nature of the ChDR signal in fig. 5.11 for bunch charges up to $\sim$ 400 pC. This measurement was performed with a high-frequency cutoff of 10 GHz. The EOSD setup has a higher bandwidth, and extrapolating from fig. 6.24, we can expect that the signals would saturate for approximately double the charge used in fig. 6.24, so roughly 40 pC. In this chapter, we perform a second charge scan to also confirm the coherent nature of the ChDR signal for small bunch charges in the order of tens of pC and a high-bandwidth acquisition system. As the previous charge scans in this chapter presented in section 6.2, the modulator is set to the working point V_{50}. After the background subtraction, the normalised signal amplitude may vary from -50% to +50%. In fig. 6.27, the peak signal amplitude is plotted as a function of the bunch charge. As we start the scan from the quadrature point of the modulator, a linear dependence is expected for small amplitudes. Increasing the bunch charge, the signal amplitude will saturate at +50% transmission. The peak signal amplitude shows a linear dependence up to $\sim$ 40 pC. This agrees with our expectations from the signal amplitude already obtained in fig. 6.24. A bunch charge up to around

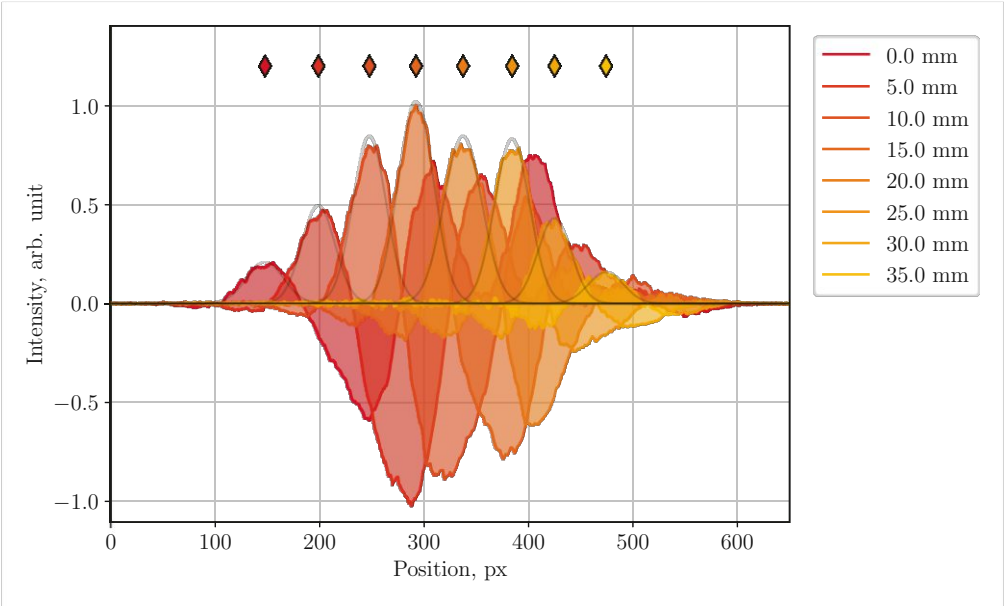

Figure 6.25: Time delayed CChDR pulses as measured with the intensified spectrometer. The different motor positions of the delay stage are shown in the legend. The diamond-shaped markers denote the mean position of each pulse. From the presented data, the background was subtracted and then scaled to the peak intensity. Time increases from left to right as the laser pulse exhibits a positive chirp. The colour code of the signals indicates the spectrum of the laser pulse.

approximately 25 pC keeps the amplitude well within the linear response of the modulator. During the CTR measurement, the slope obtained for the charge dependency was approximately 2.8 percentage points per pC. For CChDR, we obtain a shallower slope of approximately 1.2 percentage points per pC, indicating it produces lower signal levels than CTR.

Plotting the respective traces in the time domain can demonstrate the coherency of the whole signal rather than just the peak amplitude of the CChDR pulse. We, therefore, process the obtained profiles from the spectrometer as before by using equation 6.3. Additionally, we normalise the amplitude of each trace to a bunch charge of 20 pC. The normalised traces are presented in fig. 6.28. The initial bunch charge varied from 12 to 41 pC and is shown in the legend. After normalising all traces to the same charge, they overlap with each other. Except for the lowest bunch charge plotted in blue, which exhibits the lowest signal-to-noise ratio, the normalisation proves the coherent nature of the whole signal. The noise level increase for times after ~ 560 ps is due to the smaller laser intensity available for modulation and indicates the end of the laser pulse.

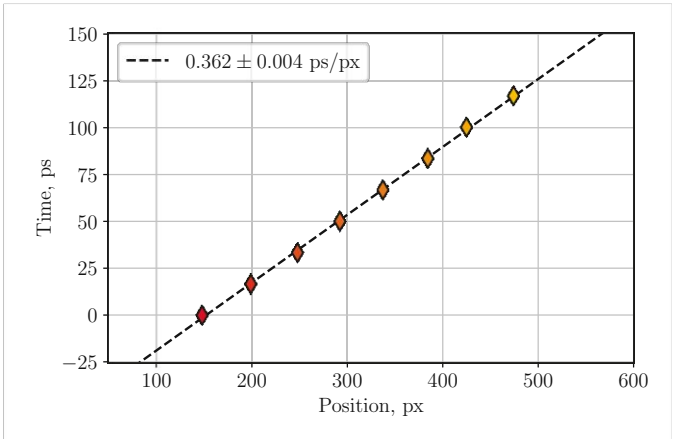

Figure 6.26: Time conversion using the mean position of the delayed signals on the spectrometer. The slope is positive due to the positive chirp of the laser pulse and $d\lambda$ of the spectrometer being $\propto -dx$, as indicated by the colour code. The linearity of the data points indicates that the frequency content within the laser pulse is linearly distributed. The timing jitter causes a small deviation from the linear fit.

In fig. 6.7, the principle behind the over-rotation of the input signal was introduced. It was shown that the signal is already distorted for signal amplitudes in the order of $V_\pi/2$, and for even higher signal amplitudes, the over-rotation becomes evident. To give an impression of this behaviour in actual measurements, we need to increase the bunch charge above the linear regime of the transfer function. The results are presented in fig. 6.29. The traces were again normalised to the maximum modulation amplitude by using equation 6.3. The graph spans the total modulation range from -50% to +50% as we saturate the transfer function of the modulator on purpose. The blue curve corresponds to a bunch charge of 63 pC, which is already above the linear response of the transfer function. This curve has two noteworthy aspects: It covers the full modulation range available. It reaches +50% and -50% transmission intensity in two different parts of the signal, which indicates that the normalisation method introduced in equation 6.3 works reasonably well for a wide fraction of the signal. Secondly, the signal shape is already strongly distorted, as we expected according to fig. 6.7. For even higher bunch charges, the over-rotation of the signal becomes evident. As the signal saturates for positive transmission (at ~ 500 ps) and negative transmission (at ~ 530 ps), the over-rotation is present for the positive and the negative pulse. The bunch charge is high enough for the three over-rotated signals shown in orange, green and red, for their signal peaks already entering the linear regime of the adjacent negative slope. This is visible by the equidistant offset between the peaks at ~ 500 ps and at ~ 530 ps.

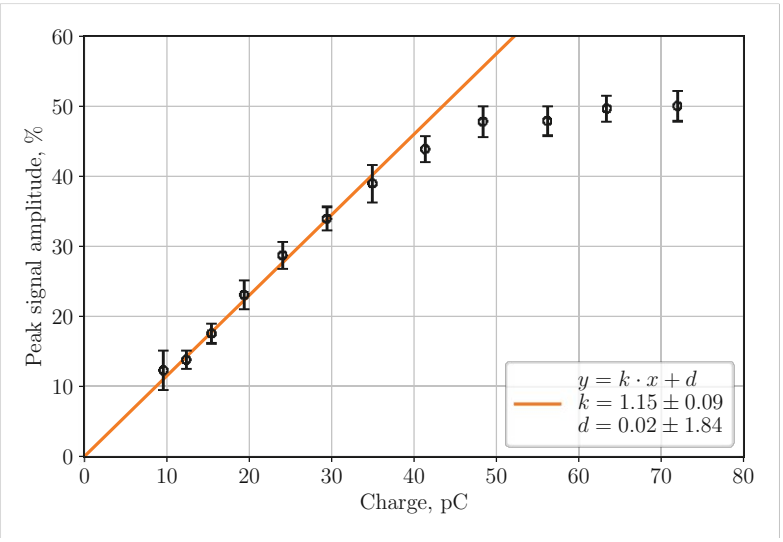

Figure 6.27: The peak signal amplitude is plotted as a function of bunch charge. The presented data was background subtracted and subsequently scaled so that the highest value corresponds to the saturation level of +50% transmission. The signal amplitude exhibits a linear dependence until the transfer function of the modulator saturates. With the modulator operating at V_{50}, the bunch charge must be kept well below 40 pC to obtain a linear response. The temporal resolution is sufficient to resolve the double peak caused by over-rotation (cf. fig. 6.7), leading to saturated values also for higher bunch charges.

Single Shot Acquisition

All traces shown so far have been averaged over hundreds of shots. The averaging is needed to obtain traces with a reasonable signal-to-noise ratio, as the acquisition system is optimised for temporal resolution rather than single-shot acquisition. The main limitation is the laser intensity, which is heavily reduced by the slit of the spectrometer to decrease the angular spread of the laser light and hence increase the spectrometer resolution. Given these restrictions, the single-shot profile suffers from significant noise levels, as shown in fig. 6.30. Especially at the beginning (< 460 ps) and the end of the trace (> 560 ps), the noise levels are even higher due to the laser intensity available for modulation being already low. However, when averaging several tens of traces, the CChDR signal already emerges from the noise floor, as shown by the green curve in fig. 6.30.

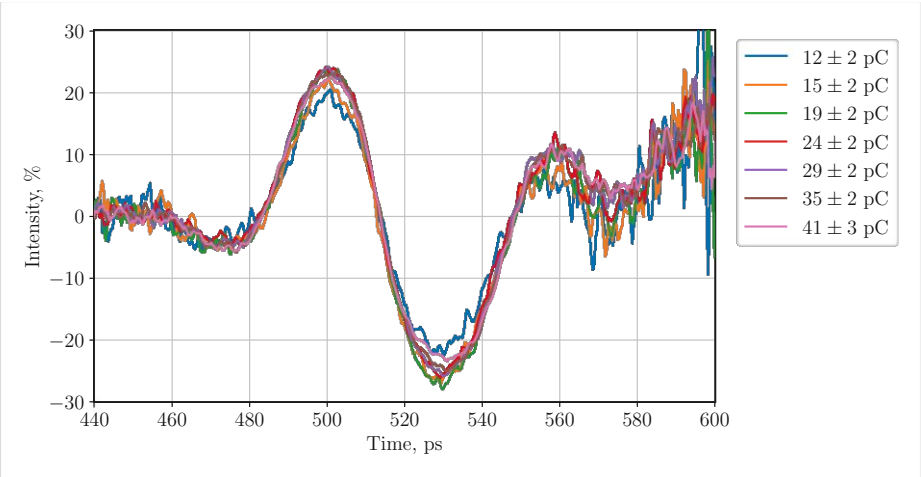

Figure 6.28: CChDR signals normalised to a bunch charge of 20 pC. The original bunch charges of the respective signals are displayed in the legend. The signal-to-noise ratio is higher for low bunch charges, as visible in the blue curve. The linearity is demonstrated for bunch charges up to $\sim$ 40 pC. The increase in noise after 560 ps is due to the normalisation of the amplitude and the decaying laser intensity available for modulation.

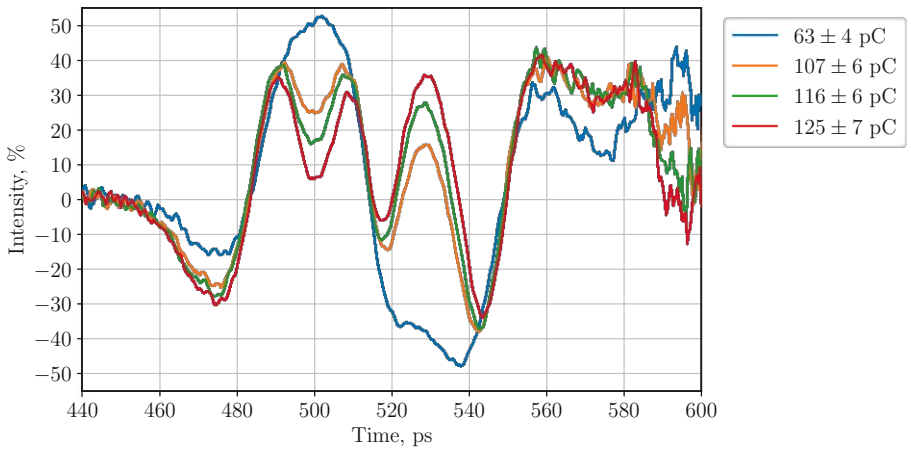

Figure 6.29: Demonstration of the over-rotation of signals due to too high bunch charges. The blue curve saturates the transfer function over the full range from -50% to +50% and already exhibits strong signal distortion. For even higher bunch charges, the signal's peak over-rotates and enters the linear regime on the negative slope of the transfer function. This is visible by the equidistant offset between the peaks at $\sim$ 500 ps and at $\sim$ 530 ps.

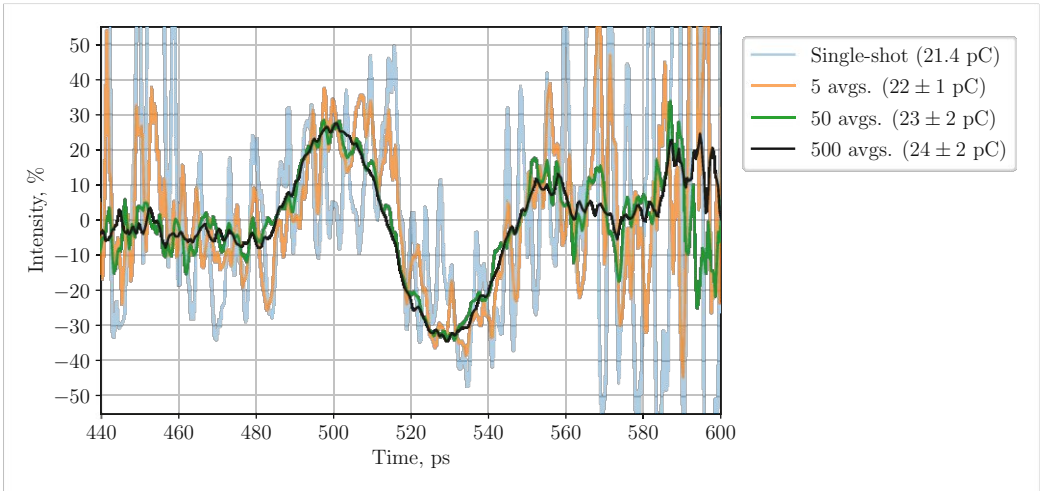

Figure 6.30: CChDR time traces for different numbers of shots acquired at working point V_{50}. The profiles were processed according to equation 6.3 with the different background levels averaged over 500 shots. The noise of the single-shot acquisition is highly amplified for times when the laser intensity available for modulation is low ($t < 460\,ps$ and $t > 560\,ps$).

Time Domain Signal

After measuring the signal amplitude as a function of bunch charge, we use a bunch charge of $\sim 18\,pC$ to be far within the linear modulator response to perform a high-resolution measurement of the CChDR time signal. The final time trace is shown in fig. 6.31 and was processed from the data shown in fig. 6.24 according to equation 6.3. The amplitude is, therefore, again normalised to the full modulation range from -50% to +50%. To increase this measurement's signal-to-noise ratio, the signal was averaged over 2500 shots, corresponding to an integration time of over 4 minutes. The CChDR pulse is fitted with a Gaussian function, with the baseline being fixed to the first minimum before the pulse. We obtain a standard deviation of $\sigma = 8.8 \pm 0.1\,ps$, which is slightly longer than the one obtained with the CTR pulse. As already observed in fig. 6.23, the first positive peak is followed by a negative peak. After the negative peak, the signal exhibits a second positive feature, which is also present in the long time trace. Recalling the results obtained from numerical simulations is convenient for interpreting the signal shape. In chapter 3, the electric field at the exit surface of the radiator was illustrated for areas (cf. fig. 3.15) and point probes (cf. fig. 3.14). In fig. 6.32, a closeup of these results is provided for the area A_4 and point probe P_4, located 30 mm from the radiator exit surface (cf. fig. 3.11). The simulated data was shifted - not scaled - in time to correspond to the timing as illustrated in fig. 6.31. It has to be noted that

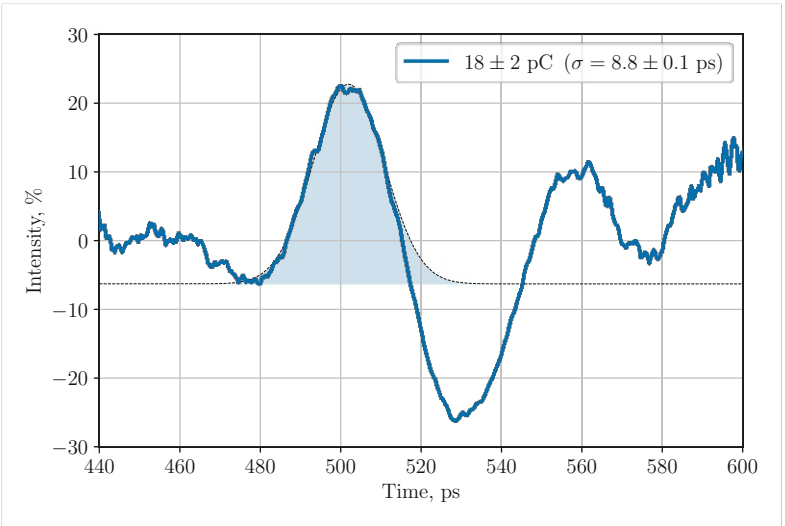

Figure 6.31: Time trace of the CChDR signal as measured with the short laser pulse at working point V_{50}. The Gaussian fit of the CChDR pulse yields a standard deviation of $\sigma = 8.8 \pm 0.1$ ps. The trace is affected by the timing jitter between the laser pulse and the CChDR pulse, whereas the spectrometer resolution is improved compared to fig. 6.23. The time trace exhibits the same features as predicted from numerical simulation, notably the positive CChDR pulse followed by the negative DR contributions.

this can only be a qualitative comparison, as the experimental parameters deviate from the simulations presented. In chapter 3, where the numerical simulations were discussed, the first positive pulse at 500 ps was clearly identified as the CChDR pulse. The negative pulse was identified as various DR contributions that interfere with each other and also lead to a second smaller positive pulse appearing later in time. The measured time domain signal resembles the simulated signal to a great extent, reflecting the characteristics as predicted from simulations. The first positive peak of the measured signal in fig. 6.31 is therefore identified as the CChDR pulse, which is followed by a negative pulse generated by DR. The trailing field is more prominent in the measured signal, which also agrees with the measurement obtained with the long laser pulse in fig. 6.23 and the electro-optical probes in fig. 5.18. The numerical simulation seems to underestimate the trailing fields systematically. As discussed in section 6.3.1, where the measurement with the long laser pulse was presented, this might be due to the coherent nature of the DR components and still requires further investigation.

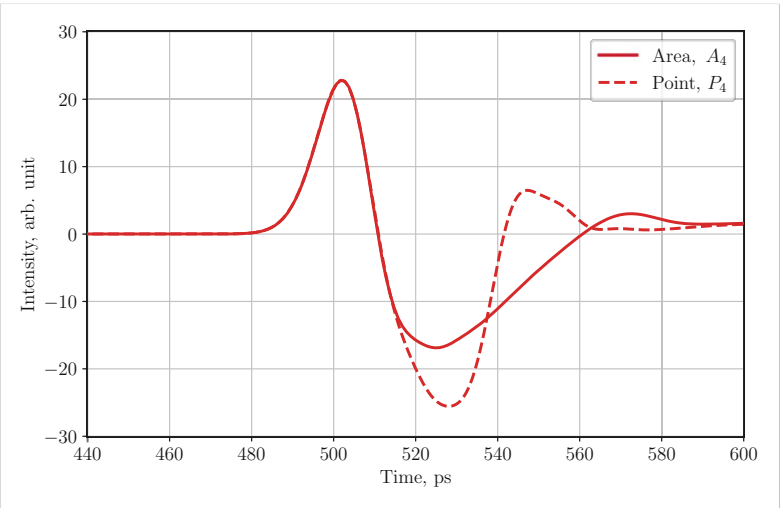

Figure 6.32: Close-up of the time domain signal from numerical simulations presented in chapter 3. The trace was scaled in amplitude and shifted - not scaled - in time for easier comparison with fig. 6.31. For the positioning of A_4 and P_4, see fig. 3.11.

Spectrometer Resolution and Timing Jitter

The trace shown in fig. 6.31 was acquired for an intensifier gain of 870, which leads to a spectrometer resolution of $\sigma_{\text{spec}} \approx 1.7\,\text{ps}$. After the time conversion, we obtain a standard deviation of the timing jitter of $\sigma_{\text{jitt}} \approx 4.7\,\text{ps}$. The convolution of these two contributions is then given as $\sqrt{1.7^2 + 4.7^2}\,\text{ps} = 5.0\,\text{ps}$. We can now estimate the pulse length of the CChDR pulse. The standard deviation of the CChDR pulse, corrected for the spectrometer resolution and timing jitter, is given as $\sqrt{8.8^2 - 5.0^2}\,\text{ps} = 7.2\,\text{ps}$. If we assume a 10% standard error on the spectrometer resolution and timing jitter, we obtain $7.2 \pm 0.5\,\text{ps}$. Again, one has to be cautious to draw definite conclusions from this bunch duration measurement, as the timing jitter would need to be improved for a more reliable measurement. Nevertheless, the signal indicates a slight broadening compared to the CTR measurement. The radiator geometry could explain this broadening, which has a curved surface for generating ChDR and a flat surface at the exit surface. This broadens the time signal when integrated over the full exit surface. Also, the dispersion within the radiator must be carefully investigated to draw any conclusions on the best time resolution achievable.

6.4 Findings based on Electro-optical Spectral Decoding

The measurements based on the EOSD setup with Mach-Zehnder intensity modulators elucidate various key results:

- The high-frequency cutoff of the acquisition system was measured as $\sim 40\,\mathrm{GHz}$. The linearity of the frequency chirp was confirmed for long laser pulses ($\sigma \sim 120\,\mathrm{ps}$) with a negative chirp, as well as for short laser pulses ($\sigma \sim 25\,\mathrm{ps}$) with a positive chirp. Once the $LiNbO_3$ intensity modulator was in a steady state, its performance stayed stable, not indicating any significant drift of the working point even without any active feedback.
- The acquisition system is sensitive to bunch charges in the order of 10 pC.
- The initial CChDR pulse is followed by trailing fields of substantial amplitude, which are still under investigation.
- The coherent nature of the ChDR was confirmed by the proportionality of its electric field strength to the total bunch charge, extending the measurement in chapter 5 to smaller bunch charges.
- The over-rotation of the output signal was demonstrated for high bunch charges.
- The shortest real-time measurement of the CChDR pulse was performed, with a Gaussian fit yielding a standard deviation of approximately 7.2 ps.
- For the first time, the CChDR pulse was temporally separated from the contributions of DR.
- For the first time, the prediction of the time domain signal from numerical simulations was verified in its basic characteristics in a real-time measurement.

7

Conclusion

This work proposes Cherenkov diffraction radiation (ChDR) as a novel beam-generated signal source for charged particle beam diagnostics. Its non-invasive nature, well-defined angle of emission, arbitrary radiator placement around the beam trajectory and its distinct emission mechanism, which is also suitable for straight sections, are the main characteristics which make it a promising tool for future accelerators. However, many properties of ChDR have not yet been tested in experiments. So far, investigations have primarily focused on the frequency domain, with no measurements conducted in the time domain. Analytical models describing ChDR are limited to the frequency domain and can only describe basic or unrealistic radiator geometries. To address these limitations, numerical simulations were performed to characterise a more realistic radiator design. The first vacuum-tight prototype for investigating the time domain signal was installed at a 200 MeV linear electron accelerator.

The ChDR radiator was characterised using two different experimental setups. The first setup used electro-optical probes to measure the absolute value of the electric field strength, impact parameter dependence, polarisation and field distribution. The second setup, using EOSD with Mach-Zehnder modulators, aimed to achieve a high temporal resolution. Both measurement campaigns sought to benchmark the numerical simulations with experimental data.

With the electro-optical probes, the coherent nature of the ChDR signal was demonstrated. The polarisation of the ChDR was shown to be aligned with the polarisation of the electromagnetic field of the beam, consistent with numerical simulations. The impact parameter dependence was measured to decay with $1/h$, where h represents the distance between the particle bunch and the inner surface of the radiator. This decay agrees with numerical simulations to a large extent

and can also be analytically explained by the $1/r$ decay of the electromagnetic field of the charged particle beam, which polarises the inner surface of the radiator. These are the first quantitative measurements of the peak electric field strength of the ChDR pulse as a function of impact parameter. After the main ChDR pulse, the trailing fields were found to decay only after tens of nanoseconds, which needs to be considered for bunch trains with a spacing close to that order of magnitude. The amplitude of the trailing fields was found to be higher than predicted by simulations. An analysis of the power spectrum showed substantial agreement with numerical simulations, with the strongest contributions stemming from reflections within the radiator. The trailing fields, therefore, undergo multiple reflections within the radiator. However, their high amplitude still requires further investigation. The power spectrum also revealed that the low cutoff frequency of the radiator corresponds to the cutoff frequency of the TE_{11} mode in a circular dielectric-loaded waveguide. The electric field distribution on the exit surface of the radiator was found to be highly uniform, which reflects the generation through surface polarisation and indicates the systematic emission of ChDR from the inner surface of the radiator. The absolute value of the peak electric field strength of the ChDR pulse at the exit surface of the radiator was measured to be in the order of 10 kV/m for a 200 MeV, 5 ps ($1\,\sigma$) long electron beam at an impact parameter of 40 mm. This value agrees with numerical simulations and represents the first measurement of the absolute value of the electric field strength of any ChDR signal.

The EOSD setup was calibrated using transition radiation pulses, demonstrating a high cutoff frequency of approximately 40 GHz. The coherent nature of the ChDR signal was also demonstrated for small bunch charges up to 40 pC, complementing the measurement with the electro-optical probes. The EOSD setup exhibited high sensitivity, with averaged signals obtained for bunch charges in the order of 10 pC with the radiator placed 40 mm from the bunch trajectory. The trailing fields right after the initial wavefront were found to be of the same order of magnitude and higher than expected from simulations. However, this finding agrees with the experimental results obtained with the electro-optical probes. The ChDR pulse in the time domain was measured to exhibit a standard deviation of $\sigma \approx 7.2 \pm 0.5$ ps. The time domain signal shows the same characteristics as predicted by numerical simulations, with the first positive ChDR pulse being followed by a negative pulse from diffraction radiation. This represents the shortest measurement of a ChDR pulse in the time domain and demonstrates for the first time the temporal separation between the ChDR pulse and the contributions from diffraction radiation.

8

Future Perspectives

The results of this work represent a significant advancement towards the development of beam instrumentation devices utilising the time domain signal of ChDR. It was demonstrated that the experiments examining the absolute value of the electric field strength, polarisation, impact parameter dependence and temporal characteristics closely align with numerical simulations. This opens up the possibility of designing and optimising reliable ChDR radiators specific to beam diagnostics needs for the first time. The time domain signal of the ChDR pulse was observed to have a duration in the order of several picoseconds for the given radiator design. This temporal resolution is constrained by the bandwidth of the acquisition system and the geometry of the radiator. It represents a limit that can be surpassed through advanced acquisition techniques and improved radiator designs.

A better-engineered radiator for the FCC-ee would need to minimise contributions from diffraction radiation and ideally also increase the temporal delay with respect to the ChDR pulse. Moreover, multiple reflections within the radiator would need to be carefully controlled to reduce the contributions of trailing fields, which could affect the following bunch with the given bunch spacing of 25 ns. Even though the intrinsic temporal resolution of ChDR remains to be precisely determined, it is believed to be of the order of atomic polarisability in the sub-femtosecond range. Additionally, the dispersion characteristics of the radiator material, whether alumina or other dielectrics, must be carefully investigated to achieve optimal time response. A first step to higher temporal resolution could be to measure the ChDR time domain signal with EOSD techniques utilising crystals directly exposed to the ChDR field, potentially extending the bandwidth to hundreds of gigahertz. As simulations of the electric field strength of ChDR were successfully benchmarked, the development of improved detection setups can be pursued more predictably.

Exploiting ChDR instead of the direct beam field would ease the integration into the accelerator complex, as the probing laser does not need to traverse into the vacuum chamber. Moreover, the impedance of a carefully engineered radiator might be lower than that of a probing crystal protruding inside the vacuum chamber. A thorough impedance study of an optimised radiator design for implementation at the FCC-ee would still need to be performed.

Furthermore, the flexibility in positioning radiators for generating ChDR signals at any location around the beam chamber facilitates seamless integration into large-scale accelerators such as the FCC-ee. Contrary to exploiting synchrotron radiation to measure the longitudinal beam profile, this would avoid the need for dedicated magnets to utilise the visible spectrum of synchrotron radiation as well as the need to implement long extraction lines into the accelerator layout.

The EOSD scheme with Mach-Zehnder modulators, developed for high-resolution time domain measurements of the ChDR signal, may find broader utility beyond ChDR detection. The modulator's versatility in accepting various RF signal sources, coupled with the fibre-based transmission of laser pulses within the accelerator hall, enhances security and streamlines installation procedures. The modulator's high bandwidth from DC to $\sim 40\,\mathrm{GHz}$ could be extended to an even higher bandwidth available for modulators based on a wavelength of 1550 nm. The system's operation on pulsed signal sources, typically present in particle accelerators, makes it especially suitable for this use case. Sensing high-frequency signals in particle accelerators is a challenge on its own, and EOSD with Mach-Zehnder modulators might be a valuable option for transmitting high-frequency signals over long distances. This feature is of particular interest for very large-scale facilities like the FCC-ee.

The EOSD setup presented in this study suffered from a significant timing jitter between the laser pulses and the generated signals in the order of several picoseconds. Addressing this issue is imperative, particularly for averaged measurements. The reduction of light intensity on the spectrometer due to the narrow slit width was essential to improve the temporal resolution. These issues - the significant timing jitter and the low light yield - made it necessary to average all presented data over several hundred shots. Employing photonic time-stretch techniques and thereby substituting the spectrometer with a fast photodiode could pave the way towards a simplified setup capable of single-turn acquisition that would be suitable for the FCC-ee beam diagnostic needs. The performance of such a single-turn acquisition system still requires further studies.

9

Acknowledgements

I am truly honoured and thankful for the possibility of conducting my research on Cherenkov diffraction radiation at CERN. It goes without saying that the results presented in this thesis would not have been possible without the tremendous efforts of people from all over the world contributing to such a large-scale facility - not only during my stay but since its founding nearly 70 years ago. However, even though it is impossible to thank every single person directly or indirectly involved in making this thesis a reality, there are several people I want to mention in particular.

I want to thank Prof. Michael Benedikt for enabling and supporting my journey at CERN, which started already more than five years ago when I joined the organisation during my master's programme. I am particularly thankful for his Fingerspitzengefühl in placing me into the beam instrumentation group and endorsing my path at CERN throughout the years.

I want to thank Stefano for always being there, teaching, and mentoring me with his detailed knowledge and outstanding patience. Thanks for the tremendous support throughout the last three years, whether in Switzerland or on the other side of the globe. Your guidance made this thesis much more successful and enjoyable to work on.

I want to thank Thibaut for accepting me as a student at CERN in the very first place. Without your passion and constant support, this project could not have been realised. Thanks for all the interest and optimism, especially during times when success was not granted. Allowing enough room for failure definitely made this thesis possible.

I am grateful to the ChDR research group for all their support and input during numerous meetings. I am genuinely thankful for all your help, particularly as the pandemic made cross-border cooperation difficult. I especially thank Pavel for his encouraging discussions and for sharing his equipment. Many thanks to Eugenio for sharing all his expertise and office space. Many thanks to Kacper for his mathematical support and fruitful discussions. Many thanks to Daniele for always providing a helping hand and for his genuine interest. Many thanks to Can for the great company and exchange on ChDR. Many thanks to Collette for the input on numerical simulations. Many thanks to Marek, Ole, Manfred and Tom for helping me out with anything RF-related.

Many thanks to the whole operation team of CLEAR for always stepping in to provide the best particle beam possible. Many thanks to Roberto, Wilfrid, Pierre, Avni, Alexander, Vilde, Joe and Cameron. Many thanks to Edu and Miguel for all their support during measurements and in between. Many thanks to Nicolas and Candy for the technical drawings and to Fritz, Morad, Ashley and Lewis for the mechanical integration. Many thanks to Lionel for offering his expertise during the electro-optical probe measurements and providing much more support than I could have requested.

Many thanks to Michal, Antonio, Alberto and Stephen for all the discussions on electro-optical systems. Also, many thanks to Gudrun, Bastian and Micha for sharing their expertise. Many thanks to all the section members who made working on this thesis so enjoyable every day. I especially want to thank Federico, Enrico, Stephane, Karim, Ondrej, Miguel, Petr, Sara and Jose for directly or indirectly contributing to this thesis.

Many thanks to everyone who encouraged me during all the small breaks from work, especially Jacqueline, Bernd, and Joanna. Also, many thanks to Marie-Laure, Peter, Diana, Anthony, Estelle, Eddy, Caterina, Michele, Lily, Dariush, Lidia and Hazel for making the Pays de Gex and France a second home.

Ich möchte mich auch bei all meinen Freunden in Österreich, die mich während dieser Reise unterstützt haben, bedanken. Ein besonderes Danke an Alexander und Nandor für ihre Freundschaft über mehrere Ländergrenzen hinweg.

Danke an meine ganze Familie. Vielen lieben Dank an meine Eltern für all die wertvolle Unterstützung. Ohne euch wäre all dies nicht möglich gewesen. Auch vielen lieben Dank an meine beiden Schwestern und ihre eigenen Familien. Ich könnte mir keine bessere Familie wünschen. Vielen lieben Dank auch an meine Schwiegerfamilie für ihre Unterstützung.

Wie kann man sich über die Welt freuen,
außer wenn man zu ihr flüchtet?

— Franz Kafka

Eine Dissertation fordert nicht nur ihren Verfasser. Ich darf mich unglaublich glücklich schätzen, meine Partnerin Elli in meinem Leben zu haben. Ich kann dir nicht genug danken, für deine Unterstützung in jeder Hinsicht und deine richtigen Worte zur richtigen Zeit. Danke besonders für deinen unerschütterlichen Optimismus und, dass du mit mir zu dieser wundervollen Welt flüchtest.

List of Figures

List of Tables

Symbols and Acronyms

$\mathbf{Al_2O_3}$	Aluminium oxide, also alumina
$\mathbf{Bi_{12}SiO_2}$ / **BSO**	Bismuth silicone oxide
GaP	Gallium phosphide
$\mathbf{LiNbO_3}$	Lithium niobate
ZnTe	Zinc telluride
$\boldsymbol{F(\omega)}$	Bunch form factor
$\boldsymbol{H}$	Higgs boson
$\boldsymbol{J_\alpha}$	Bessel function of the first kind
$\boldsymbol{K_\alpha}$	Modified Bessel function of the second kind
$\boldsymbol{N}$	Number of particles
$\boldsymbol{Q}$	Total bunch charge
$\boldsymbol{S_{1D}}$	Normalised longitudinal particle density distribution
$\boldsymbol{V_0, V_{50}, V_{100}}$	Bias voltage for 0%, 50% and 100% intensity transmission
$\boldsymbol{V_\pi}$	Half-wave voltage of Mach-Zehnder modulator
$\boldsymbol{W^\pm}$	W bosons
$\boldsymbol{Z^0}$	Z boson
$\boldsymbol{\beta}$	Relative velocity v/c
$\boldsymbol{\gamma}$	Lorentz factor
$\boldsymbol{\lambda}$	Wavelength
$\boldsymbol{\mu_0}$	Vacuum permeability

μ_r	Relative permeability
ω	Angular frequency
π	number π
σ_z	Bunch length of Gaussian bunch
σ	Standard deviation of Gaussian distribution
θ_{Ch}	Cherenkov angle
ε_0	Vacuum permittivity
ε_r	Relative permittivity
$\vec{B}$	Magnetic field vector
$\vec{E}$	Electric field vector
c	Speed of light in vacuum
e^-/e^+	Electron / Positron
e	Elementary charge
f	Frequency
h	Impact parameter
i	Imaginary unit
k	Wavenumber
n	Refractive index
q	Single particle charge
r_{eff}	Effective radius
$t\bar{t}$	Top quark and top antiquark
v	Particle velocity
AC	Alternating current
AF	Antenna factor
AWAKE	Advanced proton-driven plasma wakefield acceleration experiment
BPM	Beam position monitor
BS	Beam strahlung

BW	Bandwidth
CCD	Charge-coupled device
CChDR	Coherent Cherenkov diffraction radiation
CDR	Conceptual design report
CERN	European organisation for nuclear research (Conseil européen pour la recherche nucléaire)
CFBG	Chirped fibre Bragg grating
ChDR	Cherenkov diffraction radiation
ChR	Cherenkov radiation
CLEAR	CERN linear electron accelerator for research
CLIC	Compact Linear Collider
CST	Computer Simulation Technology
CTF	CLIC test facility
CTR	Coherent transition radiation
CW	Continuous wave
DC	Direct current
DESY	Deutsches Elektronen-Synchrotron
DN	Nominal diameter (diamètre nominal)
DR	Diffraction radiation
EO	Electro-optical
EOS	Electro-optical sampling
EOSD	Electro-optical spectral decoding
FC/APC	Fibre connector angled physical contact
FC/PC	Fibre connector physical contact
FCC	Future Circular Collider
FCC-ee	Future Circular Collider for electrons and positrons

FCC-hh	Future Circular Collider for hadrons (proton-proton collider)
FWHM	Full width at half maximum
HL-LHC	High-Luminosity Large Hadron Collider
ICT	Integrating current transformer
IP	Interaction point
KIT	Karlsruhe Institute of Technology
LDM	Longitudinal density monitor
LEP	Large Electron-Positron Collider
LHC	Large Hadron Collider
LINAC	Linear particle accelerator
MM	Multi-mode
NIR	Near infrared
PM	Polarisation maintaining
PSI	Paul Scherrer Institute
RF	Radio frequency
SM	Single-mode
TR	Transition radiation
VESPER	Very energetic electron facility for space planetary exploration missions in harsh radiative environments

Bibliography

[1] M. Benedikt *et al.*, "Future Circular Collider study, Volume 2: The Lepton Collider (FCC-ee). Conceptual Design Report," *Eur. Phys. J. Special Topics*, vol. 228, pp. 261–623, 2019.

[2] R. Heuer, "Future Circular Collider (FCC) Study, Kickoff Meeting 2014." URL: https://indico.cern.ch/event/282344/contributions/1630764/, Feb. 2014.

[3] M. Mangano *et al.*, "Future Circular Collider study, Volume 1: FCC Physics Opportunities. Conceptual Design Report," *Eur. Phys. J. C*, vol. 79, p. 474, 2019.

[4] F. Zimmermann *et al.*, "Future Circular Collider study, Volume 3: The Hadron Collider (FCC-hh). Conceptual Design Report," *Eur. Phys. J. Special Topics*, vol. 228, p. 755–1107, 2019.

[5] F. Zimmermann *et al.*, "Future Circular Collider study, Volume 4: The High-Energy Large Hadron Collider (HE-LHC). Conceptual Design Report," *Eur. Phys. J. Special Topics*, vol. 228, p. 1109–1382, 2019.

[6] M. Benedikt, "FCC Feasibility Study Status, FCC Week 2023." URL: https://indico.cern.ch/event/1202105/contributions/5423504/, June 2023.

[7] F. Gianotti, "Introductory Remarks, FCC Week 2023." URL: https://indico.cern.ch/event/1202105/contributions/5423451/, June 2023.

[8] T. Raubenheimer, "FCC Accelerator, FCC Week 2023." URL: https://indico.cern.ch/event/1202105/contributions/5423512/, June 2023.

[9] K. Oide, "Layout, optics, parameters, FCC Week 2023." URL: https://indico.cern.ch/event/1202105/contributions/5408583/, June 2023.

[10] K. Hanke, "Technical infrastructure, FCC Week 2023." URL: https://indico.cern.ch/event/1202105/contributions/5423514/, June 2023.

[11] T. Lefèvre, "Beam instrumentation for FCC-ee, FCC Week 2023." URL: https://indico.cern.ch/event/1202105/contributions/5385371/, June 2023.

[12] Swiss Federal Office of Energy SFOE, "Electricity production and consumption in 2022." URL: https://www.newsd.admin.ch/newsd/message/attachments/77291.pdf, April 2023.

[13] M. Masaki, S. Takano, M. Takao, and Y. Shimosaki, "X-ray Fresnel diffractometry for ultralow emittance diagnostics of next generation synchrotron light sources," *Phys. Rev. ST Accel. Beams*, vol. 18, p. 042802, April 2015.

[14] J. Corbett *et al.*, "Transverse Beam Profiling and Vertical Emittance Control with a Double-Slit Stellar Interferometer," in *Proceedings, 5th International Beam Instrumentation Conference (IBIC 2016), Barcelona, Spain*, Sept. 2017.

[15] T. Mitsuhashi, K. Oide, and F. Zimmermann, "Conceptual Design for SR Monitor in the FCC Beam Emittance (Size) Diagnostic," in *Proceedings, 7th International Particle Accelerator Conference (IPAC 2016), Busan, Korea*, May 2016.

[16] M. Siano *et al.*, "Two-dimensional electron beam size measurements with X-ray heterodyne near field speckles," *Phys. Rev. Accel. Beams*, vol. 25, p. 052801, May 2022.

[17] A. J. Burns and H. Schmickler, "Bunch Length Measurements in LEP," in *Proceedings DIPAC: Chester, United Kingdom*, Sept. 1999.

[18] M. Uesaka, T. Ueda, T. Kozawa, and T. Kobayashi, "Precise measurement of a subpicosecond electron single bunch by the femtosecond streak camera," *Nuclear Instruments and Methods in Physics Research Section A: Accelerators, Spectrometers, Detectors and Associated Equipment*, vol. 406, no. 3, pp. 371–379, 1998.

[19] A. Jeff *et al.*, "Longitudinal density monitor for the LHC," *Phys. Rev. ST Accel. Beams*, vol. 15, p. 032803, March 2012.

[20] J. Rossbach, J. R. Schneider, and W. Wurth, "10 years of pioneering X-ray science at the Free-Electron Laser FLASH at DESY," *Physics Reports*, vol. 808, pp. 1–74, 2019. 10 years of pioneering X-ray science at the Free-Electron Laser FLASH at DESY.

[21] D. F. Nelson and E. H. Turner, "Electro-optic and Piezoelectric Coefficients and Refractive Index of Gallium Phosphide," *Journal of Applied Physics*, vol. 39, pp. 3337–3343, Nov. 2003.

[22] K. Tada and M. Aoki, "Linear Electrooptic Properties of ZnTe at 10.6 Microns," *Japanese Journal of Applied Physics*, vol. 10, p. 998, Aug. 1971.

[23] E. Turner, "High-frequency electro-optic coefficients of lithium niobate," *Applied Physics Letters*, vol. 8, no. 11, pp. 303–304, 1966.

[24] D. Eimerl, L. Davis, S. Velsko, E. K. Graham, and A. Zalkin, "Optical, mechanical, and thermal properties of barium borate," *Journal of Applied Physics*, vol. 62, pp. 1968–1983, Sept. 1987.

[25] Q. Wu and X. Zhang, "Free-space electro-optic sampling of terahertz beams," *Applied Physics Letters*, vol. 67, pp. 3523–3525, Dec. 1995.

[26] D. Oepts and G. M. Knippels, "Direct Measurement of the Shape of Short Electron Bunches," in *Proceedings, 20th International Free Electron Laser Conference (FEL98), Williamsburg, Virginia, Unites States*, Aug. 1998.

[27] M. J. Fitch, A. C. Melissinos, and P. L. Colestock, "Picosecond electron bunch length measurement by electro-optic detection of the Wakefield," in *Proceedings, 18th Particle Accelerator Conference (PAC 1999), New York City, New York, United States*, March 1999.

[28] X. Yan, A. M. MacLeod, W. A. Gillespie, G. M. H. Knippels, D. Oepts, A. F. G. van der Meer, and W. Seidel, "Subpicosecond Electro-optic Measurement of Relativistic Electron Pulses," *Phys. Rev. Lett.*, vol. 85, pp. 3404–3407, Oct. 2000.

[29] Z. Jiang and X.-C. Zhang, "Electro-optic measurement of THz field pulses with a chirped optical beam," *Applied Physics Letters*, vol. 72, pp. 1945–1947, April 1998.

[30] B. Steffen *et al.*, "Electro-optic time profile monitors for femtosecond electron bunches at the soft X-ray free-electron laser FLASH," *Phys. Rev. ST Accel. Beams*, vol. 12, p. 032802, March 2009.

[31] I. Wilke, A. M. MacLeod, W. A. Gillespie, G. Berden, G. M. H. Knippels, and A. F. G. van der Meer, "Single-Shot Electron-Beam Bunch Length Measurements," *Phys. Rev. Lett.*, vol. 88, p. 124801, March 2002.

[32] B. Steffen *et al.*, "Compact single-shot electro-optic detection system for THz pulses with femtosecond time resolution at MHz repetition rates," *Review of Scientific Instruments*, vol. 91, April 2020.

[33] A. Borysenko *et al.*, "Electron Bunch Shape Measurements Using Electro-optical Spectral Decoding," *Physics Procedia*, vol. 77, pp. 3–8, March 2015. International Conference on Laser Applications at Accelerators (LA3NET 2015), Mallorca, Spain.

[34] N. Hiller *et al.*, "Single-shot electro-optical diagnostics at the ANKA storage ring," in *Proceedings, 3rd International Beam Instrumentation Conference (IBIC 2014), Monterey, California, United States*, Sept. 2014.

[35] S. Funkner *et al.*, "Revealing the dynamics of ultrarelativistic non-equilibrium many-electron systems with phase space tomography," *Scientific Reports*, vol. 13, March 2023.

[36] E. Roussel *et al.*, "Phase Diversity Electro-optic Sampling: A new approach to single-shot terahertz waveform recording," *Light: Science and Applications*, vol. 11, Jan. 2022.

[37] M. Reißig *et al.*, "Status of a monitor design for single-shot electro-optical bunch profile measurements at FCC-ee," in *Proceedings, 11th International Beam Instrumentation Conference (IBIC 2022), Kraków, Poland*, Dec. 2022.

[38] L. Rota *et al.*, "KALYPSO: Linear array detector for high-repetition rate and real-time beam diagnostics," *Nuclear Instruments and Methods in Physics Research Section A: Accelerators, Spectrometers, Detectors and Associated Equipment*, vol. 936, pp. 10–13, Aug. 2019. Frontier Detectors for Frontier Physics: 14th Pisa Meeting on Advanced Detectors.

[39] M. M. Patil *et al.*, "An Ultra-Fast and Wide-Spectrum Linear Array Detector for High Repetition Rate and Pulsed Experiments," in *Proceedings, 10th International Particle Accelerator Conference (IPAC 2019), Melbourne, Australia*, May 2019.

[40] E. Roussel *et al.*, "Observing microscopic structures of a relativistic object using a time-stretch strategy," *Scientific Reports*, vol. 5, May 2015.

[41] C. Szwaj *et al.*, "High sensitivity photonic time-stretch electro-optic sampling of terahertz pulses," *Review of Scientific Instruments*, vol. 87, p. 103111, Oct. 2016.

[42] T. Lefèvre *et al.*, "Cherenkov diffraction radiation as a tool for beam diagnostics," in *Proceedings, International Beam Instrumentation Conference (IBIC 2019), Malmö, Sweden*, Oct. 2019.

[43] R. Kieffer *et al.*, "Direct Observation of Incoherent Cherenkov Diffraction Radiation in the Visible Range," *Phys. Rev. Lett.*, vol. 121, p. 054802, Aug. 2018.

[44] R. Kieffer *et al.*, "Generation of incoherent Cherenkov diffraction radiation in synchrotrons," *Phys. Rev. Accel. Beams*, vol. 23, p. 042803, April 2020.

[45] A. Curcio *et al.*, "Beam-based sub-THz source at the CERN linac electron accelerator for research facility," *Phys. Rev. Accel. Beams*, vol. 22, no. 2, p. 020402, 2019.

[46] A. Curcio *et al.*, "Noninvasive bunch length measurements exploiting Cherenkov diffraction radiation," *Phys. Rev. Accel. Beams*, vol. 23, p. 022802, Feb. 2020.

[47] E. Senes *et al.*, "Beam Position Monitoring of a Short Electron Bunch in the Presence of a Longer and More Intense Proton Bunch for the AWAKE Experiment," in *Proceedings, 10th International Beam Instrumentation Conference (IBIC 2018), Pohang, Korea*, Sept. 2021.

[48] C. Pakuza *et al.*, "A beam position monitor for electron bunch detection in the presence of a more intense proton bunch for the AWAKE Experiment," *Journal of Physics: Conference Series*, vol. 2420, p. 012067, Jan. 2023.

[49] C. Davut, O. Apsimon, P. Karataev, T. Lefèvre, S. Mazzoni, and G. Xia, "Optimization Study of Beam Position and Angular Jitter Independent Bunch Length Monitor for Awake Run 2," in *Proceedings, 11th International Beam Instrumentation Conference (IBIC 2022), Kraków, Poland*, Sept. 2022.

[50] E. Adli *et al.*, "Acceleration of electrons in the plasma wakefield of a proton bunch," *Nature*, vol. 561, p. 363–367, 2018.

[51] G. Stupakov and P. Baxevanis, "Wakefields and Collective Beam Instabilities." URL: `https://uspas.fnal.gov/materials/19Knoxville/Knoxville-Wakefields.shtml`, Jan. 2019.

[52] J. D. Jackson, *Classical electrodynamics*. New York, NY: Wiley, 3rd ed., 1999.

[53] J. Stöhr and H. Siegmann, *Magnetism: From Fundamentals to Nanoscale Dynamics*. Springer Series in Solid-State Sciences, Springer Berlin Heidelberg, 2007.

[54] M. Ferrario, M. Migliorati, and L. Palumbo, "Space Charge Effects," in *Proceedings, CAS - CERN Accelerator School: Advanced Accelerator Physics Course, Trondheim, Norway*, pp. 331–356, 2014.

[55] V. Ginzburg and V. Tsytovich, "Several problems of the theory of transition radiation and transition scattering," *Physics Reports*, vol. 49, no. 1, pp. 1–89, 1979.

[56] S. Casalbuoni, B. Schmidt, P. Schmüser, V. Arsov, and S. Wesch, "Ultrabroadband terahertz source and beamline based on coherent transition radiation," *Phys. Rev. ST Accel. Beams*, vol. 12, p. 030705, March 2009.

[57] M. Castellano, A. Cianchi, G. Orlandi, and V. Verzilov, "Effects of diffraction and target finite size on coherent transition radiation spectra in bunch length measurements," *Nuclear Instruments and Methods in Physics Research Section A: Accelerators, Spectrometers, Detectors and Associated Equipment*, vol. 435, no. 3, pp. 297–307, 1999.

[58] A. Potylitsyn, "Transition radiation and diffraction radiation. Similarities and differences," *Nuclear Instruments and Methods in Physics Research Section B: Beam Interactions with Materials and Atoms*, vol. 145, no. 1, pp. 169–179, 1998.

[59] M. Castellano, "A new non-intercepting beam size diagnostics using diffraction radiation from a slit," *Nuclear Instruments and Methods in Physics Research Section A: Accelerators, Spectrometers, Detectors and Associated Equipment*, vol. 394, no. 3, pp. 275 – 280, 1997.

[60] U. Happek, A. J. Sievers, and E. B. Blum, "Observation of coherent transition radiation," *Phys. Rev. Lett.*, vol. 67, pp. 2962–2965, Nov. 1991.

[61] Z. Wu *et al.*, "Intense terahertz pulses from SLAC electron beams using coherent transition radiation," *Review of Scientific Instruments*, vol. 84, p. 022701, Feb. 2013.

[62] Q. Tian *et al.*, "Single-shot spatial-temporal electric field measurement of intense terahertz pulses from coherent transition radiation," *Phys. Rev. Accel. Beams*, vol. 23, p. 102802, Oct. 2020.

[63] G. Naumenko *et al.*, "Spectrum of coherent transition radiation generated by a modulated electron beam," *Jetp Lett.*, vol. 106, pp. 127—130, 2017.

[64] M. Castellano, "A new non-intercepting beam size diagnostics using diffraction radiation from a slit," *Nuclear Instruments and Methods in Physics Research Section A: Accelerators, Spectrometers, Detectors and Associated Equipment*, vol. 394, no. 3, pp. 275–280, 1997.

[65] P. Karataev *et al.*, "Beam-Size Measurement with Optical Diffraction Radiation at KEK Accelerator Test Facility," *Phys. Rev. Lett.*, vol. 93, p. 244802, Dec. 2004.

[66] M. Bergamaschi, *Development of a combined transition and diffraction radiation station for non-invasive beam size monitoring on linear accelerators*. PhD thesis, Royal Holloway, University of London, 2018.

[67] P. A. Čerenkov, "Visible Radiation Produced by Electrons Moving in a Medium with Velocities Exceeding that of Light," *Phys. Rev.*, vol. 52, pp. 378–379, Aug. 1937.

[68] *Nobel Lectures, Physics 1942-1962*. Elsevier Publishing Company, Amsterdam, 1964.

[69] I. Frank and I. Tamm, "Coherent visible radiation of fast electrons passing through matter," *Compt. Rend. Acad. Sci. URSS*, vol. 14, no. 3, pp. 109–114, 1937.

[70] K. Łasocha, *Non-Invasive Beam Diagnostics with Schottky Signals and Cherenkov Diffraction Radiation*. PhD thesis, Jagiellonian U., 2022. Presented 12 December 2022.

[71] R. Ulrich, "Zur Cerenkov-Strahlung von Elektronen dicht über einem Dielektrikum," *Zeitschrift für Physik*, vol. 194, April 1966.

[72] J. G. Linhart, "Čerenkov Radiation of Electrons Moving Parallel to a Dielectric Boundary," *Journal of Applied Physics*, vol. 26, pp. 527–533, May 2004.

[73] A. Schloegelhofer, "Čerenkov-Diffraktionsstrahlung in der Strahldiagnostik," Master's thesis, TU Wien, 2021.

[74] A. P. Potylitsyn and S. Y. Gogolev, "Radiation Losses of the Relativistic Charge Moving Near a Dielectric Radiator," *Russian Physics Journal*, vol. 62, pp. 2187–2193, April 2020.

[75] O. Grimm and P. Schmüser, "Principles of longitudinal beam diagnostics with coherent radiation," in *Proceedings, 10th European Particle Accelerator Conference (EPAC 2006), Edinburgh, United Kingdom*, April 2006.

[76] R. Lai and A. J. Sievers, "Determination of bunch asymmetry from coherent radiation in the frequency domain," *AIP Conference Proceedings*, vol. 367, no. 1, pp. 312–326, 1996.

[77] E. Senes, *Development of a beam position monitor for co-propagating electron and proton beams*. PhD thesis, Oxford University, 2020. Presented 08 December 2020.

[78] 3DS, "CST Studio Suite Help." URL: https://space.mit.edu/RADIO/CST_online/general/welcome_de.htm, 2020.

[79] T. Weiland and R. Wanzenberg, "Wake fields and impedances," *Lect. Notes Phys.*, vol. 400, pp. 39–79, 1992.

[80] Morgan Advanced Materials, "AL300 (Mac-A976W)." URL: https://www.morgantechnicalceramics.com/en-gb/datasheets/material-datasheets/.

[81] D. Gamba *et al.*, "The CLEAR user facility at CERN," *Nucl. Instrum. Meth. A*, vol. 909, pp. 480–483, 2018.

[82] K. Sjøbæk *et al.*, "Status of the CLEAR electron beam user facility at CERN," in *Proceedings, 10th International Particle Accelerator Conference (IPAC 2019), Melbourne, Australia*, July 2019.

[83] KAPTEOS, "Electric Field Probe EL5." URL: https://en.kapteos.com/eoprobe-datasheet.

[84] Thorlabs, "Linear Stage LNR502/M." URL: https://www.thorlabs.com.

[85] Keysight, "UXR0702A Infiniium UXR-Series Oscilloscope." URL: https://www.keysight.com.

[86] Keysight, "34461A Digital Multimeter." URL: https://www.keysight.com.

[87] Thorlabs, "Spectrometer CCS175/M." URL: https://www.thorlabs.com.

[88] Leysop Ltd, "KD*P Pockels Cell EM508." URL: https://www.leysop.com/EM500M%20Pockels%20cell.html.

[89] Thorlabs, "Fiberport PAF2-5B." URL: https://www.thorlabs.com.

[90] FEMTOCHROME Research, Inc., "FR-103MN Autocorrelator." URL: https://www.femtochrome.com/fr-103mn.html.

[91] Hamamatsu Photonics, "Femtosecond Streak Camera C6138." URL: https://www.hamamatsu.com.

[92] I. H. Malitson, "Interspecimen comparison of the refractive index of fused silica," *J. Opt. Soc. Am.*, vol. 55, pp. 1205–1209, 1965.

[93] Thorlabs, "Fibres 780-HP, PM-780-HP and 630-HP." URL: https://www.thorlabs.com.

[94] Exail, "Introduction to Exail Modulator Bias Controller." URL: https://www.ixblue.com/wp-content/uploads/2021/12/introduction-to-ixblue-mbc-2019.pdf.

[95] W. Chang, ed., *RF Photonic Technology in Optical Fiber Links*. Cambridge University Press, 2002.

[96] Thorlabs, "S1FC780PM Fiber-Coupled Laser Source." URL: https://www.thorlabs.com.

[97] Thorlabs, "PDA10A2 Si Amplified Fixed Gain Detector." URL: https://www.thorlabs.com.

[98] Keysight, "33600A Series Trueform Waveform Generators." URL: https://www.keysight.com.

[99] Binder, "Climate Chamber Model MKF 240." URL: https://www.binder-world.com.

[100] J.-P. Salvestrini, L. Guilbert, M. Fontana, M. Abarkan, and S. Gille, "Analysis and control of DC drift in LiNbO3-based Mach-Zehnder modulators," *Journal of Lightwave Technology*, vol. 29, pp. 1522–1534, 2011.

[101] A-INFO, "Multi Octave Horn Antenna LB-65180-15-C-SF." URL: https://www.ainfoinc.com.

[102] Johnson Cinch Connectivity, "2.92 mm plug to SMA plug, 134-1010-003." URL: https://www.belfuse.com/cinch.

[103] R. Pan, *Electro-Optic Diagnostic Techniques For The CLIC Linear Collider*. PhD thesis, University of Dundee, 2015.

[104] Thorlabs, "Air-Spaced Doublet Collimator F810FC-780." URL: https://www.thorlabs.com.

[105] Hamamatsu Photonics, "High-speed gated image intensifier unit, C9547-04." URL: https://www.hamamatsu.com.

[106] Hamamatsu Photonics, "Relay lens (2:1), A2098." URL: https://www.hamamatsu.com.

[107] Basler, "Camera ace acA1920-40gm." URL: https://www.baslerweb.com.

[108] Thorlabs, "Adjustable mechanical slit VA100." URL: https://www.thorlabs.com.

[109] E. G. Loewen and E. A. Popov, *Diffraction gratings and applications*. New York, NY: Dekker, 1997.

[110] Newport, "Holographic reflection grating 53006BK01-230H." URL: https://www.newport.com.

[111] Oriel Instruments, "Spectral calibration lamp, Krypton 6031." URL: https://www.newport.com.

[112] National Institute of Standards and Technology, "Atomic Spectra Database." URL: https://www.nist.gov/pml/atomic-spectra-database.

[113] A. Schloegelhofer *et al.*, "Characterisation of Cherenkov Diffraction Radiation Using Electro-Optical Methods," in *Proceedings, International Beam Instrumentation Conference (IBIC 2023), Saskatoon, Canada*, Sept. 2023.

[114] Thorlabs, "DXM12 Ultrafast Fiber Optic Photodetectors." URL: https://www.thorlabs.com.

[115] Tektronix, "MSO64B 6-Series B MSO Oscilloscope." URL: https://www.keysight.com.